6-17-2019 10:00 AM

An apodized-aperture x-ray detector design for improved image quality in mammography

Tomi F. Nano
The University of Western Ontario

Supervisor
Cunningham, Ian A.
Robarts Research Institute

Graduate Program in Medical Biophysics
A thesis submitted in partial fulfillment of the requirements for the degree in Doctor of Philosophy

Recommended Citation

Nano, Tomi F., "An apodized-aperture x-ray detector design for improved image quality in mammography" (2019). *Electronic Thesis and Dissertation Repository*. 6233.
https://ir.lib.uwo.ca/etd/6233

Abstract

X-ray imaging for early cancer detection, such as screening mammography, requires images with high signal-to-noise ratio (SNR) using low levels of radiation exposure. Conventional detectors consist of a matrix of sensor elements, producing images where each pixel corresponds to a single sensor element. This imposes a fundamental limitation on image contrast and SNR for imaging fine detail for a given exposure. The work presented here reconsiders x-ray image formation using a new x-ray detector design that synthesizes image pixels from a large number of very small sensor elements with the goal of optimizing contrast and SNR.

Our new detector design, called apodized-aperture pixel (AAP), makes use of recent technology developments of complementary metal-oxide semiconductor (CMOS) sensors with directly deposited selenium to produce images with a desired pixel size of 50 - 100μm from sensor elements of 5 – 25μm. The "over-sampled" sensor signal is used to synthesize image pixels while suppressing both signal and noise aliasing to improve the modulation transfer function (MTF) and detective quantum efficiency (DQE).

Signal and noise performance of the AAP approach is described theoretically using a cascaded-systems analysis. This approach preserves the MTF of the small sensor elements up to the image sampling cut-off frequency where the MTF is increased by up to 53%. Frequencies above the cut-off are suppressed, eliminating both signal and noise aliasing artifacts and corresponding to a high-frequency DQE increase by 2.5×. X-ray interactions in a scintillator introduce signal and noise correlations, including x-ray reabsorption and converter blur, resulting in reduced aliasing and decreased improvement in DQE. Best results with the AAP design were obtained using a high-resolution converter, such as selenium (Se), with little impact from reabsorption.

Implementation on a Se/CMOS micro-sensor prototype with 7.8μm element size with image pixel size approximately 50μm showed a flat DQE curve (ideal) up to 10cycles/mm. AAP images of resolution test patterns, mammography phantoms, and specimen imaging of micro-calcifications from biopsies showed the expected improvements in SNR and visibility of fine-detail.

It is concluded that synthesizing image pixels from small physical sensor elements can increase MTF and DQE, and eliminate aliasing artifacts, for a desired image pixel size. The resulting increase in SNR may benefit all forms of radiography, and in particular mammography, where accurate visualization of fine detail is important for early cancer detection.

Keywords: Apodized aperture pixel (AAP), x-ray detector design, detective quantum efficiency (DQE), noise aliasing, high frequency, signal to noise ratio, cascaded system analysis

Co-Authorship

The main-body thesis chapters are composed of three manuscripts that are either published, submitted or in preparation for submission to scientific journals. I was the primary contributor to all aspects of manuscript preparation, including: study design, data acquisition, data processing, analysis and manuscript writing. The first and last chapter in this thesis were prepared only by myself, and specific contributions to all other chapters by all other co-authors are listed below.

Chapter 2 is an original research article entitled "MTF and DQE enhancement using an apodized-aperture x-ray detector design" and was published in Medical Physics in 2017. This manuscript was co-authored by T. F. Nano, T. Escartin, E. Ismailova, K. S. Karim, J. Lindström, H. K. Kim, and I. A. Cunningham. My specific contributions were developing the theoretical model, developing MATLAB and C++ code for Monte Carlo simulations, acquiring experimental data, processing data in MATLAB and C++, analysis of data, preparation of figures and writing the manuscript. Mr. Escartin assisted with experimental data acquisition and analysis of results. Ms. Ismailova assisted with the theoretical modeling of x-ray detector design. Dr. Karim and Dr. Lindstrom helped with data acquisition and Dr. Kim helped with interpretation of results.

Chapter 3 is an original research article entitled "Impact of x-ray reabsorption and converter blur on MTF and DQE improvements using the apodized-aperture pixel (AAP) x-ray detector design" and was submitted for publication to Physics in Medicine and Biology in March 2019. This manuscript was co-authored by K. S. Karim and I. A. Cunningham. My specific contributions were developing the theoretical model, developing MATLAB code for model validation, acquiring experimental data, processing data in MATLAB and C++, analysis of data, preparation of figures and writing the manuscript. Dr. Karim provided x-ray detector expertise and helped with data interpretation.

Chapter 4 is an original research article entitled "Performance evaluation of a Se/CMOS prototype x-ray detector with the apodized-aperture x-ray detector design" and is in preparation for submission to Journal of Medical Imaging. This manuscript was co-authored by K. S. Karim, J. Lindström and I. A. Cunningham. My specific contributions were acquiring experimental data, processing data in MATLAB and C++, analysis of data, preparation of figures and writing the manuscript. Dr. Karim and Dr. Lindström provided x-ray detector expertise and helped with data interpretation.

Chapter 5 is an original research article entitled "Signal-to-noise ratio criteria to suppress Gibbs ringing with the apodized-aperture x-ray detector design" and is in preparation for submission to Physics in Medicine and Biology. This manuscript was co-authored by I. A. Cunningham. My specific contributions were developing the theoretical model, developing MATLAB code for model validation, acquiring experimental data, processing data in MATLAB and C++, analysis of data, preparation of figures and writing the manuscript.

Acknowledgments

This work would not have been possible without the help of many individuals and support from funding sources. I would like to acknowledge my supervisor Dr. Ian Cunningham, who provided guidance throughout all research matters and set the scholarly standard which I aim for in research. In conjunction with my supervisor, I acknowledge the mentorship of my advisory committee: Dr. Jerry Battista, Dr. Maria Drangova, Dr. George Hajdok, Dr. Anat Kornecki and Dr. Paul Picot.

The Department of Medical Biophysics supplied resources during my graduate studies. I acknowledge contributions from individuals in leadership and admin roles, such as: Dr. Aaron Ward, Dr. Rob Stodilka, Dr. Jeff Frisbee, Dr. Grace Parraga, Wendy Hough, Kathleen Petts, Jennifer Devlin and many others.

Members of the Cunningham lab have helped make my studies productive and enjoyable. I am grateful for helpful discussions I've had with: Terenz Escartin, Dr. Christiane Burton, Mike McDonald, and Sam Laxer. In addition, I acknowledge contributions from collaborating labs, including: Dr. Karim Karim at University of Waterloo (Waterloo, Ontario), Dr. Ho Kyung Kim at Pusan National University (Busan, South Korea), and Dr. Jan Lindström at Karolinska University (Stockholm, Sweden).

Most importantly, I would like to thank my family and friends for their unconditional support. To my family and loved ones, thank you for your continuous encouragement and for always helping me achieve new goals. To my friends, thank you for sharing good times and sticking with me through challenging ones.

Funding support was received from: Canadian Institutes of Health Research (CIHR), Natural Sciences and Engineering Research Council of Canada (NSERC), Translational Breast Cancer Research Unit (TBCRU) with the Breast Cancer Society of Canada, and Western Graduate Research Stipend (WGRS) from the Schulich School of Medicine.

Contents

List of Figures

List of Tables

List of Abbreviations

1D	One-dimensional
2D	Two-dimensional
3D	Three-dimensional
AAP	Apodized-aperture pixel
SNR	Signal-to-noise ratio
MLO	Mediolateral oblique
CC	Craniocaudal
BIRADS	Breast imaging, reporting and data system
DBT	Digital breast tomosynthesis
US	Ultrasound
MRI	Magnetic resonance imaging
OBSP	Ontario breast screening programs
KERMA	Kinetic energy released in medium (A)
ESAK	Entrance skin air-KERMA
PSF	Point-spread function
LSF	Line-spread function
MTF	Modulation transfer function
NPS, NNPS	Noise power spectrum, normalized NPS
DQE	Detective quantum efficiency
NEQ	Noise equivalent quanta

Chapter 1

Introduction

1.1 Thesis motivation

This thesis is motivated by the ubiquity of x-ray imaging in medicine and the importance of producing high quality images while using an acceptable level of radiation. The crux of the problem is that striking the desired balance between image quality and x-ray exposure is a difficult challenge. Ultimately, it is limited by the performance of the x-ray detector design. Unfortunately, while many x-ray detectors used at present are very effective at producing high-quality images using low levels of radiation exposure that show large structures such as masses and bones, they are less effective at producing images showing fine details such as small lesions and calcifications. We describe a new x-ray detector design that overcomes some limitations of conventional detectors to increase image quality of fine detail without increasing radiation exposure with the implication being that this will result in improved detection of cancer. The proposed x-ray detector may be useful for many imaging applications, although we think the most direct and greatest impact will be in mammography screening because high dose-efficiency and image quality of fine-detail is crucial for early cancer detection.

Since implementation of screening mammography in mid-1980s, breast cancer mor-

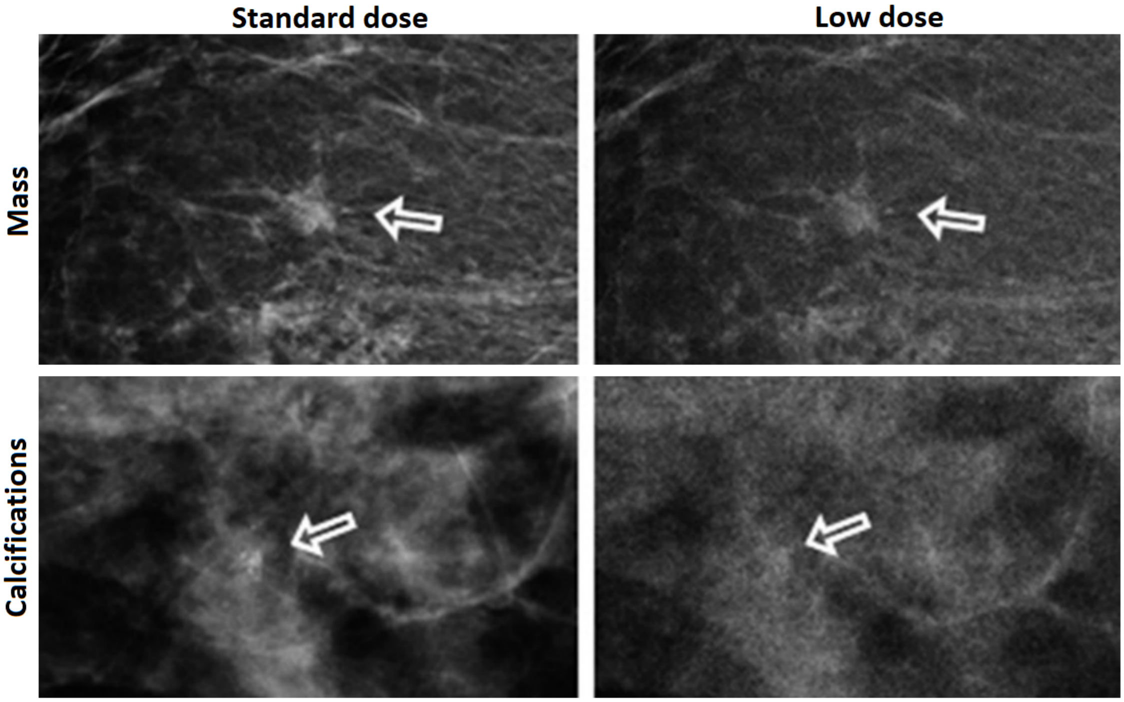

Figure 1.1: Image regions from a mammogram acquired with a clinical detector (Hologic Inc., 70μm pixel size) of a mass (top) and a calcification cluster (bottom) at a standard dose (left) and ∼10× lower dose (right). At low dose, visibility of the mass slightly decreases and the calcifications are almost completely undetectable. Modified from Bluekens et. al., BJR, 88 (1047), 2015. Permission to reproduce for PhD dissertation provided in Appendix.

tality rates have been reduced by 40-50% and attributed to improved treatment following earlier detection[1, 2]. However, early cancer detection depends on x-ray image quality in terms of signal-to-noise ratio (SNR).[3, 4] Image quality is low for low exposures because image SNR depends on the number of quanta incident on the detector, as was first shown by Rose in optical imaging.[5, 6] Figure 1.1 shows mammograms containing a mass and calcifications acquired an x-ray exposure giving 4mGy average glandular dose and reduced dose by ∼15×. This image has inverted pixel values, meaning that bright areas correspond to higher x-ray attenuation. Between standard and low doses, there are differences in SNR of the mass and even greater differences for calcifications − they are easily missed in the low-dose image. This is due to current x-ray detectors having low "dose efficiency" at producing high SNR of small structures and fine detail.[7, 8] Low

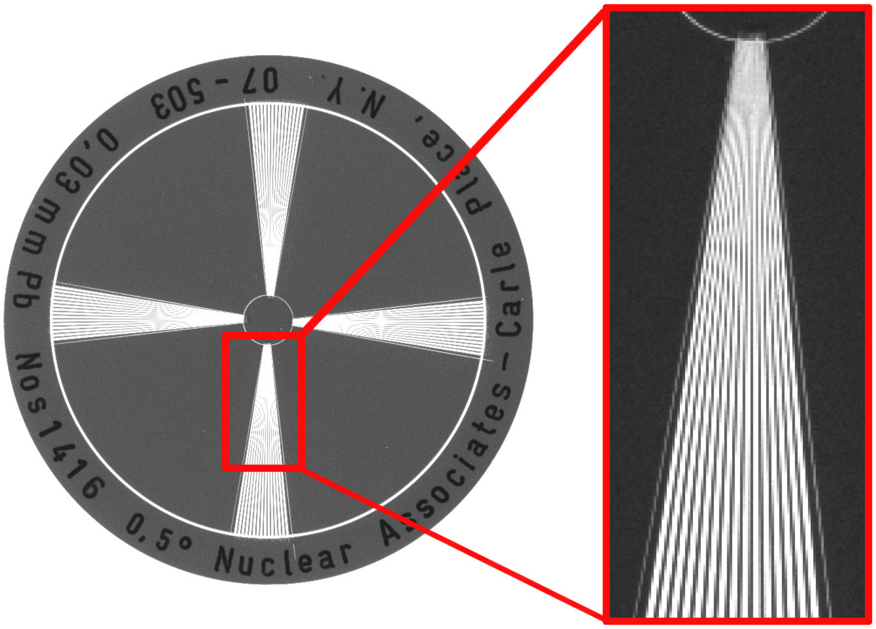

Figure 1.2: An example of signal aliasing in an x-ray image of a star-pattern acquired with a clinical mammography system. At the center of the image where spacing between bars is less than the pixel size, a distinct Moire pattern is caused by aliasing. Additionally, there are aliasing artifacts producing steps along the spoke edges caused. The x-ray image of the star pattern was provided courtesy of Dr. Jan Linsdström.

exposures are important to minimize radiation risk when screening a large asymptomatic population and obtaining high SNR of fine-detail (such as micro-calcifications) is crucial for early detection. One aim of the work in this thesis is to develop an x-ray detector design with improved x-ray detector "dose efficiency" when imaging fine-detail structures.

The resolution capabilities of a mammography system can be measured using a bar-pattern, as shown in Figure 1.2, by testing the ability to discern closely spaced high-contrast features. Dark pixel values in this image correspond to higher x-ray attenuation (opposite of Figure 1.1). X-ray images acquired using conventional detectors, where one pixel represents the output from one detector element, are prone to an image artifact called aliasing. Aliasing is a misrepresentation of fine-detail and it is further described in Section 1.6. An example using a clinical mammography system is shown in Figure 1.2, where aliasing misrepresents the test object as having ripples between bars and sometimes contrast inversion. This is concerning because health related decisions are made assuming that x-ray images provide an accurate representation of the object being imaged. Another aim of the work in this thesis is to design a detector design that is insensitive to aliasing and ensures accurate representation of objects in x-ray images.

The overarching goal of this thesis is to reconsider x-ray image formation and overcome limitations of conventional x-ray detectors which suffer from poor "dose efficiency" of fine-detail and aliasing artifacts. Such an approach could improve cancer detection in mammography screening where high performing x-ray detectors and identification of certain hard-to-see details of microcalcification morphology is important for improved patient outcomes.[9, 10, 11]

1.2 Burden of breast cancer

The Canadian Cancer Society estimated that 1 in 8 Canadian women will develop breast cancer during their lifetime and 1 in 31 will die from it.[12] In men, the disease is less common with the occurrence rate being approximately 1% of all cases.[12] The economic burden attributable to breast cancer is on average $30,000 per patient, and total yearly cost of treatment is estimated to be $450 million in Canada.[13, 14] These statistics are alarming and depict the burden that breast cancer has on both our society and individuals.

1.2.1 Incidence, prevalence and risk factors

Within the global female population, breast cancer is the most commonly diagnosed cancer and the leading cause of cancer death at 11.6%.[15] In 2018, it was estimated there would be 2.1 million newly diagnosed female breast cancer cases, accounting for almost 1 in 4 of all (male and female) cancer cases world-wide.[15] In the Canadian population,

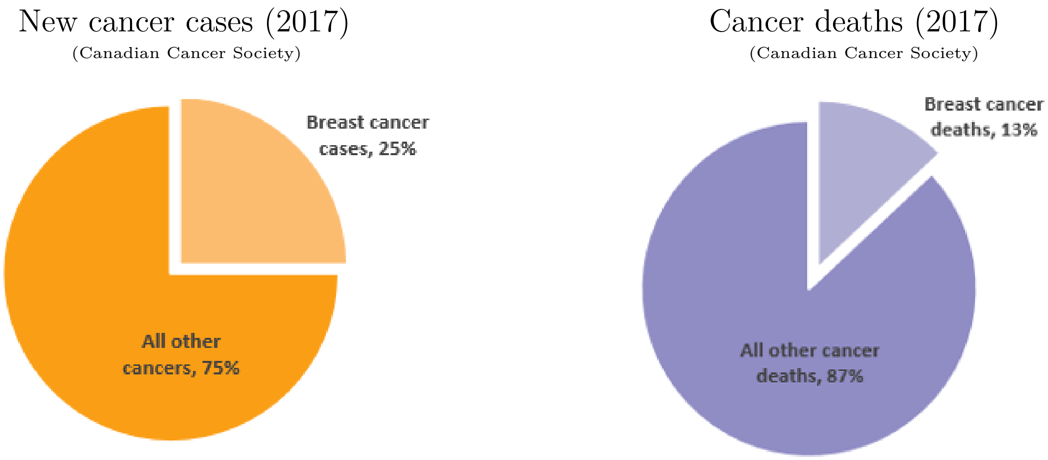

Figure 1.3: In 2017, an estimate 26,300 Canadian women were diagnosed with breast cancer (25% of all new cancer cases in women) and 5,000 women died from breast cancer (13% of all cancer deaths in women). This figure was adapted from the Canadian Cancer Society (2018).[12]

similar trends were observed in 2017 at 13% of all cancer deaths in Canadian women, as shown in Figure 1.3.[12] Over the last decades, incidence rates of breast cancer have been rising for most low-income countries due to a combination of demographic, social and economic factors (including postponement of childbearing, having fewer children, greater levels of obesity and physical inactivity).[15] In contrast, several high-income countries (ie. United States, Canada, United Kingdom, France and Australia) have observed a decrease in incidence since the early 2000s, partly attributable to declines in the use of postmenopausal hormonal treatment and increases in mammographic screening.[15, 16]

Much of the worldwide increase in breast cancer has been linked to the increasing prevalence of a number of breast cancer risk factors. Almost 1% of women are estimated to be at high risk (up to 85%) for developing breast cancer, compared to the 10-12% risk for the general population of women.[12] Survival varies with stage of the disease, as 5-year net survival is 87% but late-stage is 22%.[12, 17] This highlights the importance of early detection and effective treatments. Risk factors associated with the etiology of breast cancer can be classified as hereditary and non-hereditary. Hereditary and genetic factors account for 5-10% of breast cancer cases. These factors include personal and family history of breast or ovarian cancer; inherited mutations (ie. BRCA1, BRCA2, HER2) and epigenetics.[18] Non-hereditary factors are: menstruation (early age at menarche, later age at menopause), reproduction (nulliparity, late age at first birth, and fewer children), exogenous hormone intake (via oral contraceptive use and hormone replacement therapy), lifestyle and nutrition (alcohol intake), and anthropometry (greater weight, weight gain during adulthood, and body fat distribution).[15, 19] Non-hereditary factors are the major drivers of breast cancer incidence rates.[15] Prevention of breast cancer remains a challenge and recommendations include management of obesity, alcohol consumption, and encouragement to breastfeed (or increase duration of breastfeeding).[15, 16]

1.2.2 Breast anatomy and disease

In order to accurately identify the pathological state of disease in imaging studies, it is important to understand normal breast anatomy and disease. The human breast is a cutaneous exocrine gland that consists of subcutaneous tissue, breast parenchyma (ducts, lobules, and supporting fibrous tissue), and supporting stroma, including fat interposed in a complex network of ligaments, nerves, blood and lymph vessels.[20, 21] Figure 1.4 illustrates female breast anatomy and its major components. Each breast extends from the second rib superiorly to the 6th rib inferiorly, with the sternum medially and the midaxillary line laterally.[21] Approximately two-thirds of the breast lies over the pectoralis major muscle superiorly, and the remainder contacts the serratus anterior muscle laterally and upper abdominal oblique muscles inferiorly.[21, 22]. The female breast is usually larger than the male breast and contains a larger volume of fibroglandular tissue, whereas the male breast is almost entirely composed of fat.[21] The breast consists of two fascial layers: (i) superficial fascia that lies deep to the dermis and where the breast tissue can be found and (ii) the deep fascia that lies anterior to the pectoralis major muscle fascia.[22] Breast tissue is attached to skin by the ligaments of Cooper (fibrous connective tissue). It consists of epithelial parenchymal elements (10-

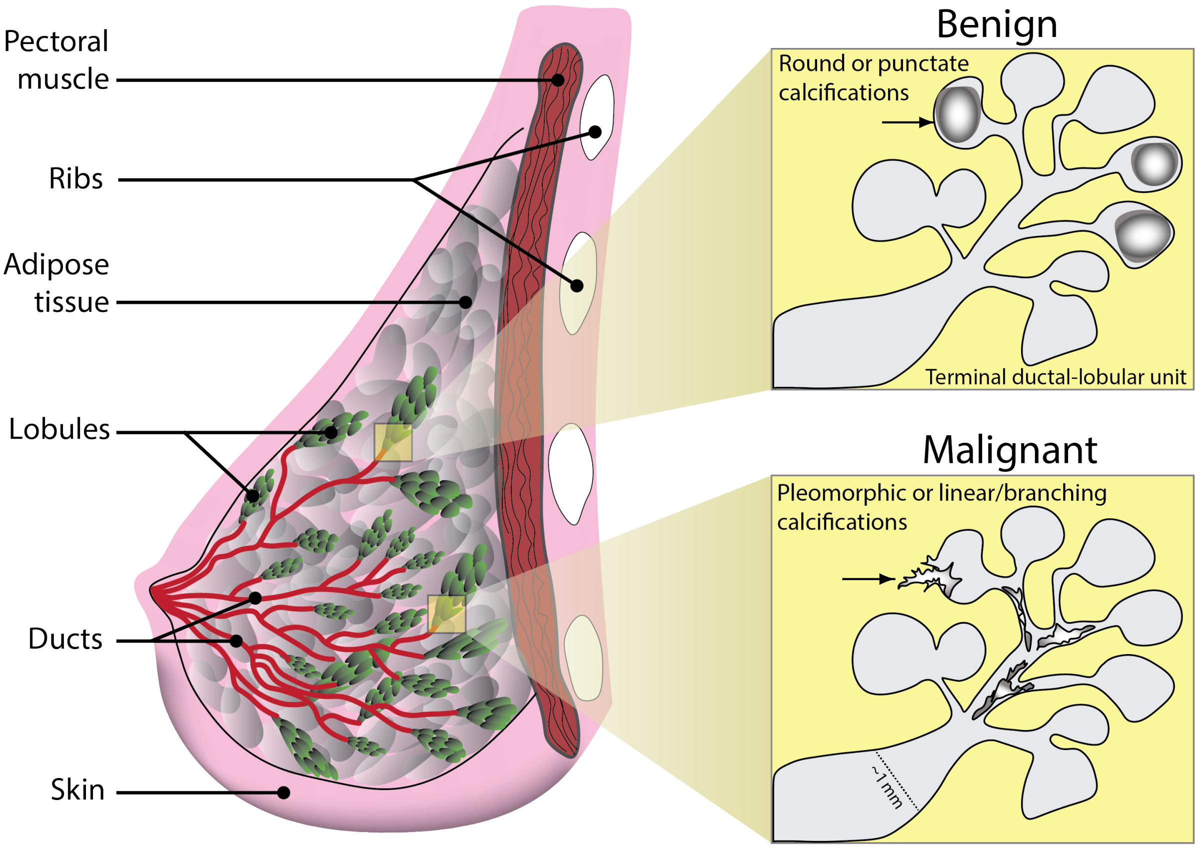

Figure 1.4: Breast anatomy showing glandular tissue with calcification deposits forming in the mammary ducts and lobules. Typically, round or punctate shaped calcifications develop in benign cancer and form in the lobules (top-right), where pleomorphic or branching shaped calcifications develop in malignant cancer and are found in the ducts (bottom-right).

15% of the volume) and stroma. The breast parenchyma consists of ducts and lobules. Terminal ductal lobules are where milk is formed and drains into a major lactiferous duct which carries the milk from the lobules into a sinus beneath the areola and then open through the nipple. Deposits of minerals (such as calcium) can crystallize and harden into microcalcifications as illustrated in Figure 1.4. Each breast has 15-20 lobules, which further branch out into 20-40 lobules, and the space between the lobules is filled with adipose tissue.[22]

Breast disease can be classified into benign and malignant (predominantly carcinomas). Three subtypes of benign breast disease include: non-proliferative lesions, proliferative lesions without atypia (excessive growth of normal-looking cells) and atypical hyperplasia (excessive growth of abnormal cells).[23, 24] Non-proliferative lesions include cysts, papillary apocrine change, epithelial-related calcifications, mild epithelial hyperplasia, as well as ductal ectasia, nonsclerosing adenosis, and periductal fibrosis. Proliferative lesions without atypia include moderate or florid ductal hyperplasia of the usual type, sclerosing adenosis, radial scar, and intraductal papilloma or papillomatosis. Proliferative lesions with atypia include atypical ductal and lobular hyperplasia.[24] Benign breast disease is diagnosed following abnormal imaging or palpable lesions felt during a physical exam. Although benign, they are considered an important risk factor for the development of breast cancer later on, having strongest association with the proliferative subtypes with atypical hyperplasia.[23, 25]

Two common types of breast carcinoma are: non-invasive (or *in situ*) and invasive breast carcinoma.[26] Two major carcinomas *in situ*, which are both precursors of the invasive counterpart, have been identified: ductal carcinoma and lobular carcinoma *in situ*.[26, 27] The most common presentation of invasive breast carcinoma, accounting for the 70-75% of cases, is ductal carcinoma.[26] Lobular carcinoma is associated to a lower risk of recurrence compared to ductal carcinoma in the first 6 years after diagnosis but confers a significantly higher risk after.[28] In addition to carcinomas, non-epithelial tumours (including sarcoma), which originate from the connective and fat tissue surrounding the breast gland, while significantly less prevalent (accounting for fewer than 5% of all breast neoplasms), can also occur.[29]

Common abnormalities associated with breast disease are masses and microcalcifications. Large masses are often palpable and one goal of screening mammography is to detect small masses and early disease. Another goal of sceening mammography is to determine shape and distribtion morphology of microcalcifications which are important indicators of aggressive cancers (see Fig. 1.4).[30, 31, 11]

1.2.3 Importance of early detection

The decline in breast cancer death rate since the mid-1980s likely reflects the impact of screening and improvements in adjuvant therapies for breast cancer.[2] This is important because generally there are better outcomes when cancer is diagnosed earlier, with the 5-year survival rate of early-stage cancer being close to 100%.[12] According to the Canadian Cancer Society report (June 2018), more than 80% of female breast cancers were diagnosed early (stage 1 or 2). This is believed to be attributed to early detection through organized breast cancer screening programs. Less than 5% of the cases were diagnosed at late stage (stage 4).[12]

1.3 Early detection with breast imaging

Mammography screening is the main tool shown to be effective for early breast cancer detection.[12] According to the Canadian Task Force on Preventive Health Care and the Ontario Breast Screening Program, it is recommended for women over 50 years old (and that are not at increased risk of cancer) to participate in mammography screening.[32, 17] Although, there is strong evidence showing that starting screening at 40 years old would be more beneficial.[33] In addition to mammography, other imaging modalities are useful for breast cancer detection (such as tomosynthesis, ultrasound, magnetic resonance imaging and contrast-enhanced methods) as they provide additional information that may be advantageous. Below is a summary of common imaging modalities used to detect cancer and Table 1.1 lists some advantages and disadvantages for each modality.

1.3.1 Breast imaging

a. Mammography

A mammography system, as shown in Figure 1.5, consists of an x-ray tube, compression paddle and an x-ray detector that acquires x-ray images that are interpreted by a

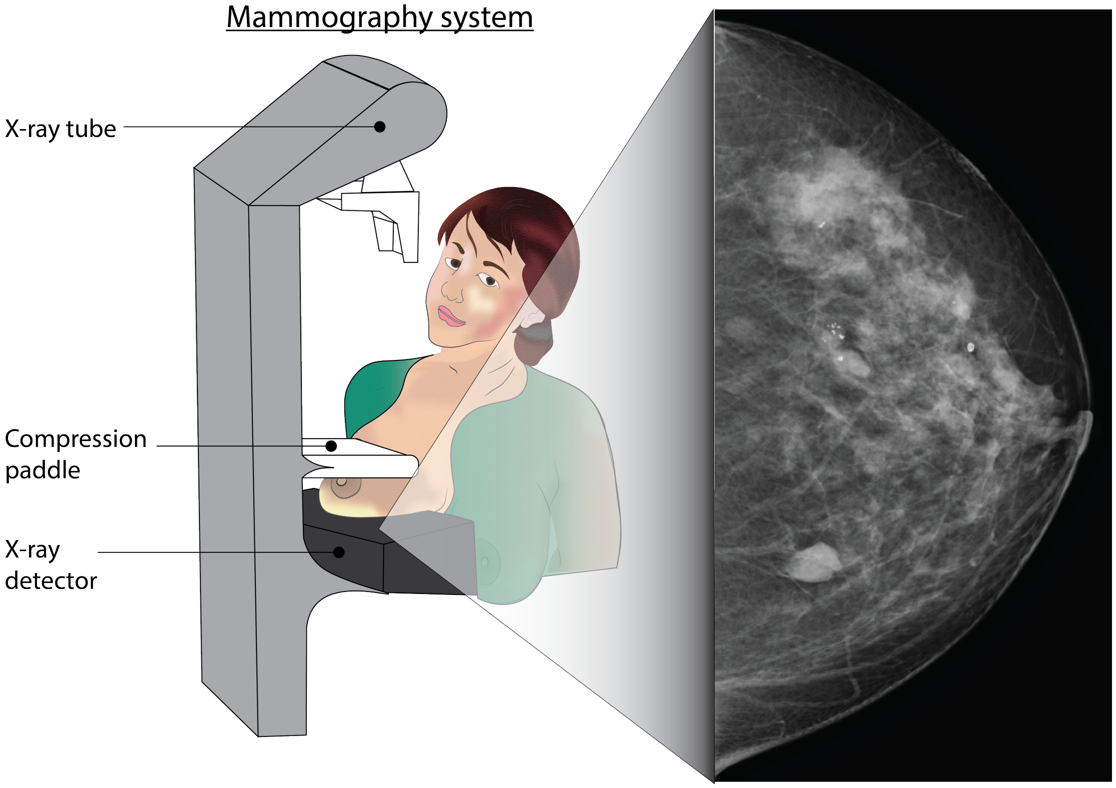

Figure 1.5: An illustration showing a mammography system with a patient, and labeled is the x-ray tube (source for x-rays), compression paddel (for immoblization) and x-ray detector that acquires an image. Case courtesy of Dr Alexandra Stanislavsky, Radiopedia.org, rID: 33698.

radiologist.[34] The x-ray tube outputs x-rays, and the transmitted x-rays through breast tissue are detected for acquiring an image. The compression paddle is used to immobilize and spread breast tissue to reduce overlap that might obstruct visibility in an x-ray projection. Other attachments are used: a spot-compression paddle compresses the breast at a local area and is used to acquire a magnified view,[35] and a anti-scatter grid is used to reduce detection of scattered radiation and improve tissue contrast from the primary x-rays.[36, 37] X-rays that are transmitted through the breast and interact in the x-ray detector contribute to detector output and final image.

A routine mammography screening comprises of 4 images at two different views acquired at different projection angles, called medio-lateral oblique (MLO) and craniocaudal (CC), for left and right breasts.[38] Breast positioning is a key factor for assuring optimum image quality and conclusive mammographic results.[39] Optimal MLO and CC projections should show pectoralis major muscle on the posterior edge of the breast followed anteriorally by the retromammary space, corpus mammae, subcutaneous space and nipple-areolar complex.

Most radiologists use a standardized method of reporting mammograms, as established by the American College of Radiology called the Breast Imaging Reporting and Data System (BIRADS).[40] This BIRADS system provides a lexicon and assessment categories for risk stratification. Mammography lexicon includes breast composition based on overall density, mass descriptors (shape, margin and density), asymmetry, architectural distortion, calcifications (morphology and distribution) and associated features.

b. Digital breast tomosynthesis (DBT)

Tomosynthesis as a methodology has been around since the 1970s, but recent advancement of digital x-ray detectors has brought it into mammography clinics with the first digital breast tomosynthesis (DBT) device receiving FDA clearance in 2011.[41] To better visualize breast features that may be blocked by overlapping tissue, multiple low-dose projections (typically 10-25) over a limited angular range (typically 10-35 degrees) are acquired in DBT. Using these projections, a 3D volume is reconstructed consisting of an asymmetric “volume slab” with z thickness and x-y resolution along the detector plane having the same pixel size as mammography. Therefore, multiple low-dose projections are used to reconstruct a DBT volume with approximately the same total exposure as a single mammography image.[42]

Tomosynthesis has been included in clinical studies as a screening tool in combination with mammography. The combination of both modalities was found to out perform just mammography alone by improving detection of masses and architectural distortion in dense breast thereby reducing false positive rates.[43]

c. Ultrasound

Ultrasound (US) imaging consists of a transducer array that generates and receives pressure waves to acquire images showing acoustic properties of tissue. Typical clinical setting use pressure waves with frequency 5-15 MHz. Image contrast based on acoustic properties of tissue allow for better soft-tissue visibility because their interfaces are visible. Ultrasound images are frequently used in breast imaging as an augmentation to mammography for verifying the presence of a previously detected mass and ensuring that it is not a benign fluid-filled cyst.[44] US has been shown to reduce false-positive rates when supplementing screening mammography.[45]

Important advantages of US imaging are that it: provides good soft-tissue contrast; can be used for real-time imaging for biopsy guidance; is widely available due to relatively low cost compared to other imaging modalities; and is safe as it does not use ionizing radiation (acoustic intensity is also monitored to not cause tissue damage).[46] Disadvantages include: higher false positive rates when used for screening (although it is effective at separating masses from cysts); poor visibility of microcalcifications; poor detection of deep-seated tumours because sound waves are less penetrating than x-rays; and skill level of the operator greatly impacts ultrasound image quality.[47, 48, 49]

d. Magnetic resonance imaging

Magnetic resonance imaging (MRI) uses a strong magnetic field, magnetic field gradients, and radiofrequency pulses to acquire an image showing contrast from relaxation of perturbed magnetic moment of nuclei (usually hydrogen).[50] Breast MRI provides good soft-tissue information that is useful for diagnosis. As a supplement to mammography, MRI is used to screen high-risk patients who have family history of cancer and is useful to determine the aggressiveness of cancer by imaging metabolism/vascularization.[51] For patients with dense breast or implants, MRI helps visualize cancers that are difficult to see in mammography and US.

The advantages of MRI imaging are that it provides contrast of soft-tissue, it can help identify aggressive cancers and angiogenesis which is helpful in assessing treatment response.[52, 53] The disadvantages are that MRI is not widely available and early indications of breast cancer, such as microcalcifications, are not visible.[54, 55]

e. Contrast-enhanced imaging

Contrast enhanced imaging with various modalities (mammography, US, MRI) are typically acquired using an intravenous injection of a contrast agent. The most common contrast agents used are: gadolinium or iodine for mammography, micro-bubbles for US, and gadolinium for MRI. These agents are manufactured to be safe for patients in low-doses, having minimal side-effects. Contrast agents are commonly used to evaluate cancer vascularization as an indication of aggressiveness.[56, 57]

Contrast imaging provides high sensitivity for detecting hard to see cancers based on functional tissue information. It can enhance visualization of hard-to-see aggressive tumours, but may be limited for patients with pre-existing renal toxicity or very dense breast.[58]

1.3.2 Impact of mammography screening

Mammography is the main screening tool for detecting breast cancer early and it is recommended that women older than 50 years participate in regular screening programs.[59, 17] The Ontario Breast Screening Program (OBSP) provides high-quality breast cancer screening to Ontarians and it recommends biannual screening for women ages 50 to 74 years old and annual screening for women ages 30 to 69 who are confirmed to be at high risk of developing breast cancer.[60] The reduction of breast cancer mortality has been largely attributed to early detection that leads to improved treatment.[1]

The OBSP found 30% greater cancer detection rates in centers that used higher performing x-ray detectors (producing higher image SNR) than centers that used lower performing systems.[3] As a result of this study, lower performing systems were recalled and replaced.[61] This is an example of the importance of high performing x-ray detectors required to provide effective early detection of breast cancer.

	Advantage	Disadvantage
Mammography	- High-resolution imaging (0.07-0.1 mm pixel size) - Fast imaging for screening large populations	- Limited by 2D projection and overlapping tissue - Patient discomfort due to compression of the breast
DBT	- Reduces obstruction of overlapping tissue - Similar dose and equipment as mammography	- Poor resolution in the z direction causes artifacts - Longer radiologist reading time and workflow
Ultrasound	- Real-time imaging - Good soft-tissue contrast that allows for differentiation between a cyst and a mass	- User-dependent due to hand-held transducer - Long imaging sessions (20min) makes screening difficult
MRI	- Good soft-tissue contrast - Able to identify aggressive tumours and screen young women who are at high-risk	- Expensive and therefore not widely available - Poor spatial resolution for early detection of calcifications
Contrast-enhanced imaging	- Can be added to current imaging using contrast loader - Able to identify aggressive tumours	- Some patients are intolerant to exogenous agents - Requires additional time, making sessions long

Table 1.1: Summary of advantages and disadvantages of common breast imaging modalities. DBT = digital breast tomosynthesis; MRI = magnetic resonance imaging.

1.3.3 Importance of x-ray detector performance

Image SNR in mammography depends on x-ray dose, detector efficiency, scattered radiation emerging from the patient and artifacts.[62] Detector performance and image SNR is further defined in Section 1.4.2. A standard entrance skin air-KERMA (ESAK) in mammography is approximately 10mGy with 100μGy air-KERMA incident on the detector. Approximately 3 - 5% of incident exposure is transmitted, and the average absorbed glandular dose is approximately 1 mGy.[63] Since only a small percentage of the incident x-rays are transmitted through the breast, the detector needs to be very high-performing to keep patient dose at a minimum while acquiring a high SNR image.

1.4 X-ray detector performance

Image SNR and detector performance are intimately connected. An absolute scale of image quality is quantified by the noise equivalent quanta (NEQ) which gives the number of Poisson-distributed quanta that would produce the same SNR given an ideal detector.[64, 65] For a given number of quanta $\bar{q}_\text{o}$ incident on the detector per unit area, a measure of system performance as a function of spatial frequency is given by the detective quantum efficiency (DQE) where $\text{DQE} = {}^{\text{NEQ}}/_{\bar{q}_\text{o}}$.[65]

To understand x-ray detector performance, one must consider the physics involved in x-ray production, interactions and detection.

1.4.1 X-ray physics

a. X-ray production

The x-rays produced from an x-ray tube are polyenergetic and x-ray spectrum depends on the tube settings, as shown in Figure 1.6. X-rays are created by accelerating electrons (current setting mA) to a peak energy ranging 25-35 keV (kilovoltage setting kV) towards a high-Z target (typically molybdenum or tungsten) producing Bremsstrahlung radiation and characteristic x-rays. Filter material attenuate the x-ray beam and remove low-energy x-rays, which are are less likely to be transmitted through the patient and therefore not contribute to the image. The tube output air-KERMA is controlled by changing mA

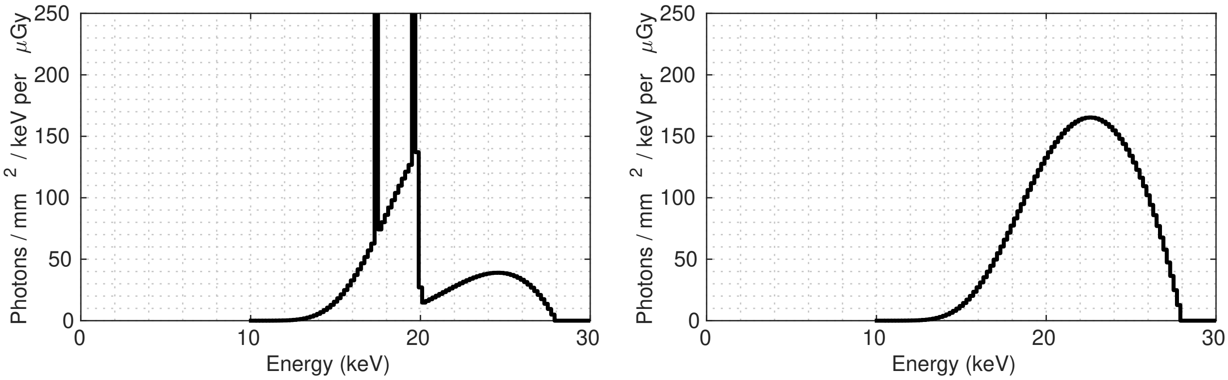

Figure 1.6: Mammography x-ray spectra from molybdenum (left) and tungsten (right) x-ray tubes.

and kV settings to ensure that a satisfactory image is obtained and is dependent on factors such as breast thickness.

b. X-ray interactions

X-rays transfer their energy by interacting with orbital electrons in matter. X-ray interactions are important because differences between x-ray interactions in tissues produce image contrast. An x-ray passing through matter can either be absorbed (an x-ray interacts and transfers all of its energy locally), scattered (an x-ray interacts but does not transfer all of its energy locally) or transmitted (does not interact). Figure 1.7 shows the x-ray spectra incident on breast tissue (A), incident on the detector (B) and absorbed in the detector (C). There is a change in y-axis scale between (A) and (B) because approximately only 3 - 5 % of the x-rays are transmitted through the breast.

At diagnostic energies, x-rays undergo either photoelectric, coherent or incoherent (Compton) interactions.[66] During photoelectric interactions, an x-ray transfers all its energy to an inner-shell electron that is ejected from the atom. The vacancy created is filled by a higher shell electron producing a characteristic photon. The energy of the characteristic photon depends on the binding energy of the levels in the absorbing material. Photoelectric interaction in the patient is important for medical imaging because it produces the desirable contrast in images. During coherent interaction, an x-ray inter-

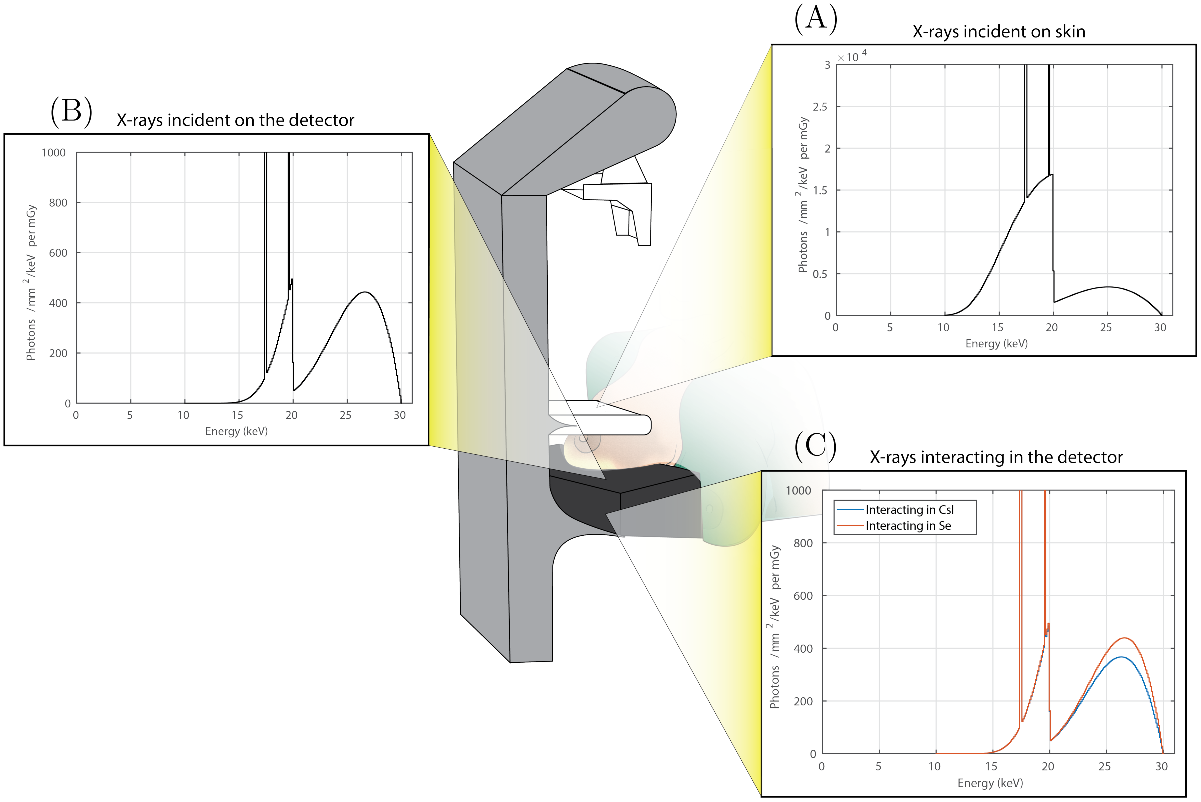

Figure 1.7: X-ray spectra at different stages in mammography. Incident x-rays on the breast tissue (A) that are transmitted fall incident on the detector (B) and are absorbed in the x-ray converter layer (C).

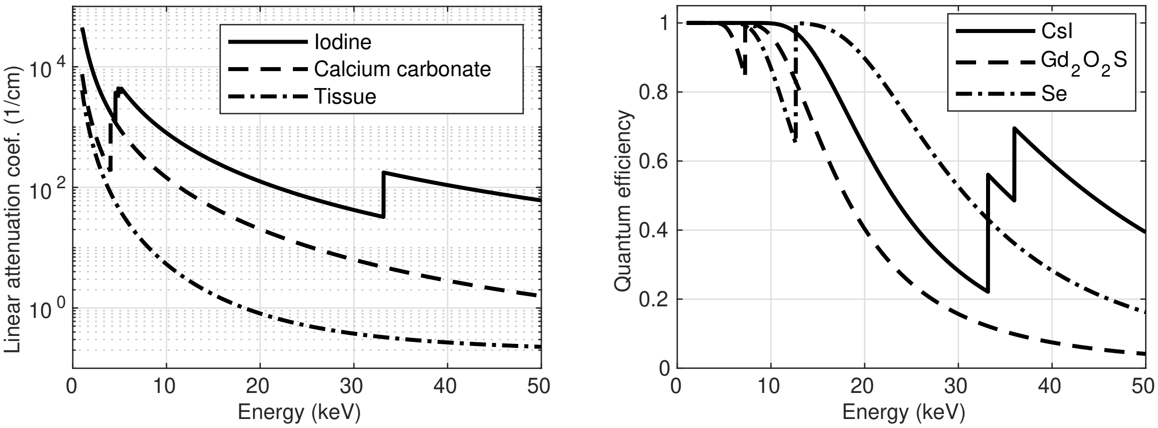

Figure 1.8: Linear x-ray coefficients (left) for iodine, calcium carbonate and breast tissue (ICRU-44). Quantum efficiency (right) of different x-ray converters in mammography: caesium iodide (CsI), gadolinium oxysulfide (Gd2O2S) and selenium (Se).

acts with an outershell electron and does not deposit energy while it changes direction. Coherent scatter is forward-peaked, leads to x-ray diffraction effects and has a higher probability of occurring at lower keV. During incoherent interaction, the incident x-ray changes direction, energy and ejects an electron. Incoherent and coherent scatter from surrounding tissue in the patient is usually not desirable because it reduces contrast of features in an image.[67]

X-ray transmission through an attenuator is described by energy-dependent interaction coefficients, $\mu(E) = \mu_{\mathrm{PE}}(E)+\mu_{\mathrm{COH}}(E)+\mu_{\mathrm{INC}}(E)$. Transmission of a spectrum $q_o(E)$ through a material having uniform linear attenuation coefficient $\mu(E)$ and thickness x results in the transmitted spectrum $q(E)$ where

$$q(E) \quad = \quad q_o(E)e^{-\mu(E)x}.$$

Linear attenuation coefficients of some materials are shown in Figure 1.8 (left) with discontinuities at absorption edges.

c. X-ray detection

Quantum efficiency of a detector α is given by

$$\alpha(E) = 1 - e^{-[\mu_{\mathrm{PE}}(E)+\mu_{\mathrm{INC}}(E)]x_d}$$

where x_d is the thickness of the detector converter material. Figure 1.8 (right) shows quantum efficiency of some x-ray converter material with 0.2mm thicknesses. Modern digital x-ray detectors typically function in three steps: 1) conversion of x-ray energy into secondary quanta using a conversion layer, such as phosphor or photoconductor; 2) liberation of secondary quanta such as optical photons or electrical charges; 3) collection of secondary quanta using a sensor array that measures the number of liberated secondaries. Figure 1.9 shows a cross-section of an x-ray detector with a converter layer and sensor array.

The detector's converter layer is where x-ray energy is detected by either an indirect or direct converter. In an indirect converter (such as caesium iodide, CsI), x-rays deposit energy in the converter that liberates optical photons that must be detected by the detector.[68] In a direct converter (such as amorphous selenium, *a*-Se), x-rays liberate electron/hole pairs and they are detected electronically in the same material.[69, 70] The choice of converter material type depends on the imaging application to provide the greatest quantum efficiency of x-rays with the greatest resolution (ie. minimal blurring).

The detector's sensor array collect secondary quanta liberated in the converter resulting in the electronic readout of the detector. Large-area flat-panel detectors can be manufactured using various sensor technology. Charge-coupled devices (CCD) detect focused optical photons from a scintillator with low readout noise and high resolution. Active-matrix flat-panel imagers, based on thin-film transistor (TFT) electronics using amorphous silicon, consist of a charge-collection electrode and storage capacitors for electronic readout of detector elements. Complimentary-metal-oxide semiconductors (CMOS) sensors have direct readout of each element and wafers can be tiled into an array

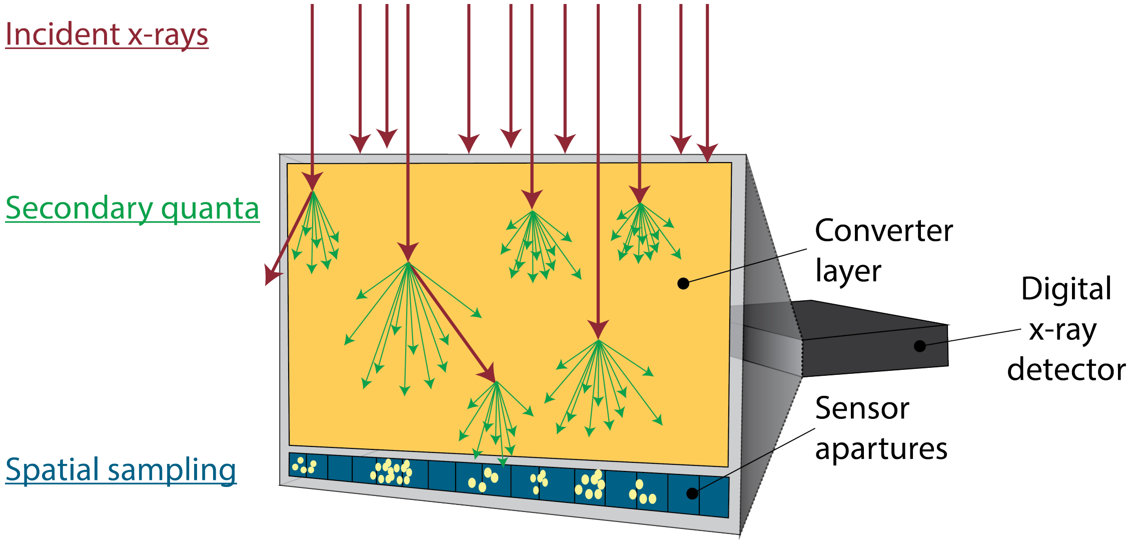

Figure 1.9: A cross-sectional view of an x-ray detector showing x-ray interactions (red arrows), secondary quanta liberation (green arrows) and electronic charge collection (yellow dots in the sensor apartures).

for a large area detector.[70, 71] Polycrystalline silicon and CMOS can be used to create sensors with extremely low readout noise, very high bandwidth performance and small element size (microns).[70, 72] CMOS wafers are maximum 6-inches in size which poses challenges for large area manufacturing (with high yield rates), but small area prototypes have been manufactured and new applications are being developed. [73, 74, 75]

In this thesis, we aim to take advantage of recent advancements of low readout noise and small element size x-ray sensor technology (such as CMOS) to improve x-ray detector performance.

1.4.2 Detector performance metrics

X-ray detector performance is commonly characterized in terms of Fourier-based metrics that are spatial-frequency dependent.[76] Signal transfer is quantified in terms of the modulation transfer function (MTF) that describes the change in amplitude of a sinusoidal input to a system output. Noise is quantified by the Wiener noise power spectrum (NPS) which is a spectral-decomposition of the variance. It can be intuitively useful to think of noise "transfer" describing the change in amplitude variations of a sinusoidal input to a system output. Similarly, SNR "transfer" is quantified by the detective quantum efficiency (DQE) as illustrated in Figure 1.10.

Fourier-based metrics of digital systems assume that a system is linear and shift-invariant (LSI) and that noise processes are wide-sense stationary (WSS).[65] A system that satisfies LSI conditions has an output that is proportional to the input and the same impulse-response function regardless of image position. Noise in an imaging system that is WSS has mean, auto-covariance and second-order statistics that are stationary in image space. These theoretical model properties are useful tools for quantifying theoretical detector performance and understanding experimental measurements, even if these assumptions are not always true.[77]

The point-spread function (PSF) describes the 2D response of a system in the spatial domain. It is the output function of a LSI system when the input is an impulse function (δ-function). For a 1D analysis response of the system, the line-spread function (LSF) describes the response of the system to a "line" of δ-functions normalized to unity.[65] The LSF in one direction averages out the details of the detector response in the orthogonal direction. In the frequency domain, the 1D MTF is the magnitude of the Fourier transform of the LSF. By definition since the LSF has unity area, the zero-frequency MTF value is unity. The Wiener NPS of a WSS random variable (fluctuations in pixel about its mean) is the Fourier transform of the autocovariance function of the random variable. Therefore, according to the Wiener-Khinchin theorem, the NPS and autocovariance function are Fourier pairs. A normalized NPS (NNPS) can be defined as the NPS normalized to the mean number of quanta incident on the detector.

The DQE can be measured and modeled based on the MTF, $\mathrm{T}(u)$, the NNPS, $\mathrm{W}^{(n)}(u)$, and is given by, Signal transfer

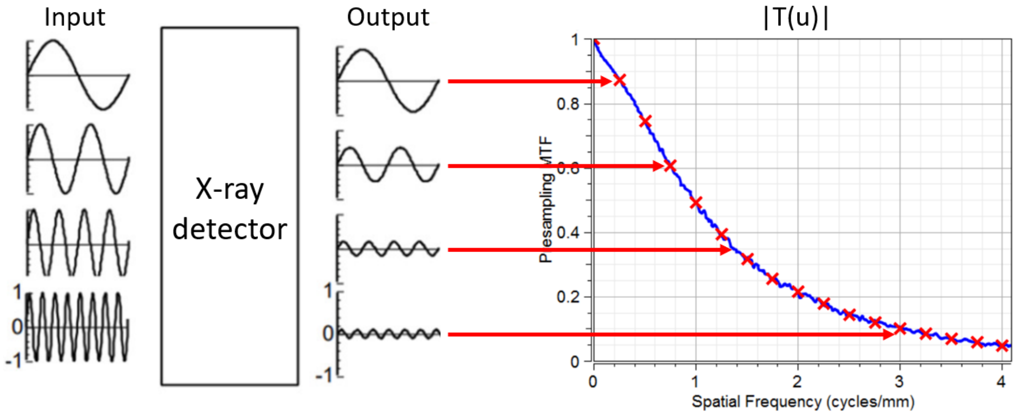

Noise

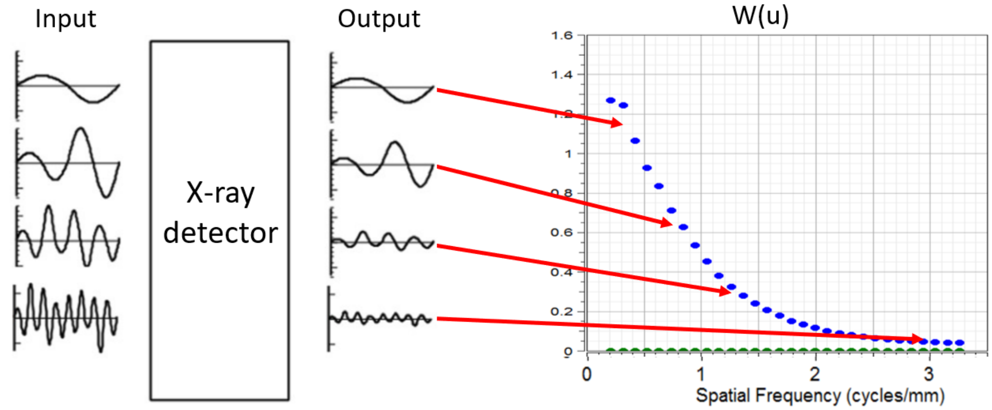

SNR ”transfer”

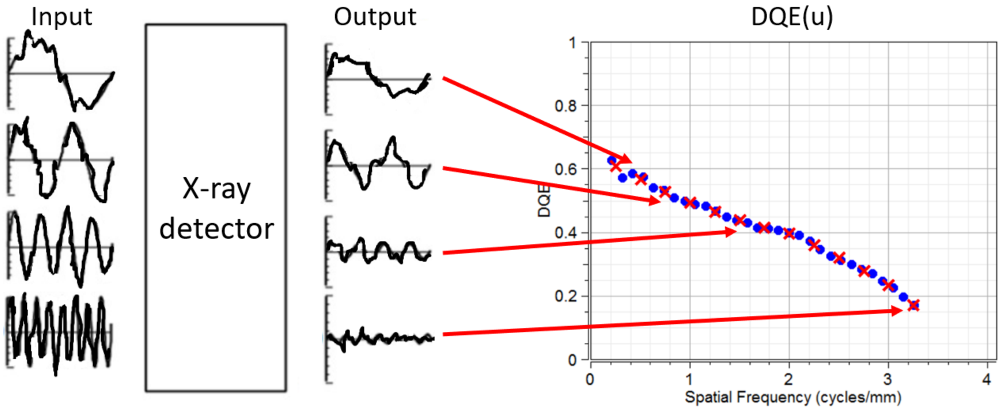

Figure 1.10: An illustration of signal, noise and SNR in an x-ray detector as quantified by the T(u) (modulation transfer function), W(u) (Wiener noise power spectrum) and DQE(u) (detective quantum efficiency). The quotes in SNR “transfer” are used because this is a transfer only for a special case of uncorrelated Poisson input x-ray quanta.

$$\mathrm{DQE}(u) = \frac{|\mathrm{T}(u)|^2}{\mathrm{W}^{(n)}(u)}.$$

The International Electrotechnical Commission (IEC) has standardized techniques for MTF, NPS and DQE measurement of x-ray detectors.[78, 79]

1.4.3 Modeling x-ray detector design

Models of x-ray detector designs are useful for predicting theoretical performance metrics (MTF, NPS and DQE) for complex imaging systems. While models usually do not perfectly describe real detectors, they provide a deep and intuitive understanding of overall performance and limiting cases that may be of interest. These models are useful tools for imaging physicists because they allow for optimization of x-ray detector parameters to achieve the maximum possible performance.

a. Elementary processes

At the most fundamental level, all quantum-based imaging systems (not just x-rays) deal with the discrete nature of quanta. This can be described theoretically using stochastic point-process theory.[80] However, these processes can quickly become complicated even for simple imaging systems. Fortunately, a useful approximation can be taken by assuming a system has LSI response under conditions of WSS noise properties.[76, 81] Furthermore, it has been shown that imaging systems can be broken-down to a linear cascade of elementary processes that describe signal and noise transfer with simple expressions.[80, 82]

Elementary processes used to describe point-processes and physics in x-ray detectors are: quantum gain, quantum selection, quantum scatter, deterministic blur, sampling and additive noise.[80, 83]

1. Quantum gain describes the process of converting each input quanta into a random number of secondary quanta at the same location, resulting in a gain from mean input number quanta to output.[84] Random variable $\tilde{g}$ describes the process with mean $\bar{g}$ and variance $\sigma_{\tilde{g}}^2$. An example of this process is conversion deposited x-ray energy into secondary quanta (optical light photons or electron/hole pairs) in the detector converter layer.

2. Quantum selection describes the process of randomly selecting whether each input quantum contributes (or not) to the output quanta distribution with probability β. This is a special case of quantum gain when the gain value is either 0 or 1, with mean value β. An example of this process is the selection of secondary quanta that interact in the sensor array.

3. Quantum scatter describes the stochastic process of relocating an input quanta from its initial location to its output location.[85] The relocation process is characterized by a normalized scatter point-spread function, $\mathrm{s}(x)$, as a redistribution of probabilities represented by the operator $*_s$.[86] The Fourier transform of $\mathrm{s}(x)$ is given by $\mathrm{T_s}(u)$, describing the quantum scatter transfer function. Examples of this process include relocation of x-rays after scatter and relocation of secondary quanta from their point of release to interaction in the sensor array.

4. Deterministic blur describes image blur that can be expressed as a convolution, $*$, of the input with a point-spread function. The input can be a quantum distribution or continuous function, but the output can only be a continuous signal. Examples of this process include spatial integration of interacting quanta in a sensor array.

5. Sampling describes the process of selecting discrete values at discrete locations of an input continuous signal. An example of this process includes obtaining discrete output signals, that represent a digital image, from each detector element from a sensor array. In imaging, where sampling occurs at fixed spacings apart, sampling

Process	**Mean signal transfer**	**Noise transfer**
Quantum gain $\tilde{g}$, $\bar{g}$, $\sigma_{\bar{g}}^2$	$\bar{q}_{\text{out}} = \bar{g}\bar{q}_{\text{in}}$	$\mathrm{W}_{\text{out}}(u) = \bar{g}^2\mathrm{W}_{\text{in}}(u) + \sigma_{\bar{g}}^2\bar{q}_{\text{in}}$
Quantum selection β	$\bar{q}_{\text{out}} = \beta\bar{q}_{\text{in}}$	$\mathrm{W}_{\text{out}}(u) = \beta^2\left[\mathrm{W}_{\text{in}}(u) - \bar{q}_{\text{in}}\right] + \beta\bar{q}_{\text{in}}$
Quantum scatter $\mathrm{s}(x)$, $\mathrm{T}_{\mathrm{s}}^2(u)$	$\bar{q}_{\text{out}} = \bar{q}_{\text{in}}$	$\mathrm{W}_{\text{out}}(u) = \left[\mathrm{W}_{\text{in}}(u) - \bar{q}_{\text{in}}\right]\left\|\mathrm{T}_{\mathrm{s}}(u)\right\|^2 + \bar{q}_{\text{in}}$
Deterministic blur $\mathrm{b}(x)$, $\mathrm{T}_{\mathrm{b}}^2(u)$	$\bar{q}_{\text{out}} = \bar{q}_{\text{in}}$	$\mathrm{W}_{\text{out}}(u) = \mathrm{W}_{\text{in}}(u)\left\|\mathrm{T}_{\mathrm{b}}(u)\right\|^2$
Sampling at spacings x_a	$\bar{q}_{\text{out}} = \frac{1}{x_a}\bar{q}_{\text{in}}$	$\mathrm{W}_{\text{out}}(u) = \frac{1}{x_a}\mathrm{W}_{\text{in}}(u) + \frac{1}{x_a}\sum_{j=1}^{\infty}\mathrm{W}_{\text{in}}(u \pm \frac{j}{x_a})$
Additive noise $\tilde{\mathrm{n}}(x)$, $\sigma_{\tilde{\mathrm{n}}}^2$	$\bar{q}_{\text{out}} = \bar{q}_{\text{in}}$	$\mathrm{W}_{\text{out}}(u) = \mathrm{W}_{\text{in}}(u) + \sigma_{\tilde{\mathrm{n}}}^2$

Table 1.2: Summary of mean signal and noise transfer through each elementary process.

is often described as the input multiplied by a train of Dirac-delta functions equally spaced apart.

6. Additive noise describes the process of additional noise added to an input. An example of this process includes read-out noise during the discretization of the output signal, such as in sampling.

Equations describing transfer of signal and noise through each process have been developed previously using point-process theory and are summarized in Table 1.2 in terms of the average number of quanta $\bar{q}$ and Wiener noise power spectrum $\mathrm{W}(u)$.[87]

Elementary processes have been used to describe signal and noise transfer through various systems. An important complex process for x-ray imaging is the interaction of x-rays in a detector's converter layer that deposits energy and liberates quanta. A cascade of processes can be used to model x-ray interactions.

b. Generalized x-ray interaction model

A generalized "simple-atom" model having only one atomic transition (K edge) can be used to describe photoelectric, coherent and incoherent interactions.[88, 89] The model consists of three paths: 1) describes generation of secondary quanta when no emitted/scattered photon is released, resulting in all energy deposited locally; 2) describes the case when emitted/scattered photons are released but they are absorbed locally too; and 3) describes the case when emitted/scattered photons are reabsorbed at a different location from the initial interaction location. Each path is a linear cascade of simple processes and the sum of all three paths in parallel is considered a parallel process.[82]

The generalized x-ray interaction model utilizing parallel-cascades and the simple-atom model has been shown to describe MTF and DQE, including effects from x-ray reabsorption and achieve agreement within 2% with more complex Monte Carlo models.[89, 83]

1.5 Conventional x-ray detector design

In addition to understanding the elementary processes as described in the previous section, it is often necessary to determine signal and noise transfer through a combination of processes. X-ray detector performance in terms of MTF, NPS and DQE can be accurately predicted by cascaded system analysis.

1.5.1 Cascaded system analysis

An x-ray detector is modeled as a cascade of six linear stages, as illustrated in Figure 1.11. The input is a uniform distribution of x-ray quanta represented as $\tilde{\mathrm{q}}_0(x)$. Stage 1 is a quantum selection elementary process of x-ray quanta that will undergo a given interaction type. Stage 2 is a generalized x-ray interaction process for each interaction type that results in the total liberated secondary quanta distribution $\tilde{\mathrm{q}}_r(x)$. Stage 3 is a quantum scattering elementary process of secondary quanta being relocated from point of liberation to point of interaction. Stage 4 is a quantum selection elementary process of secondary quanta interacting in the sensor array resulting in the interacting secondary

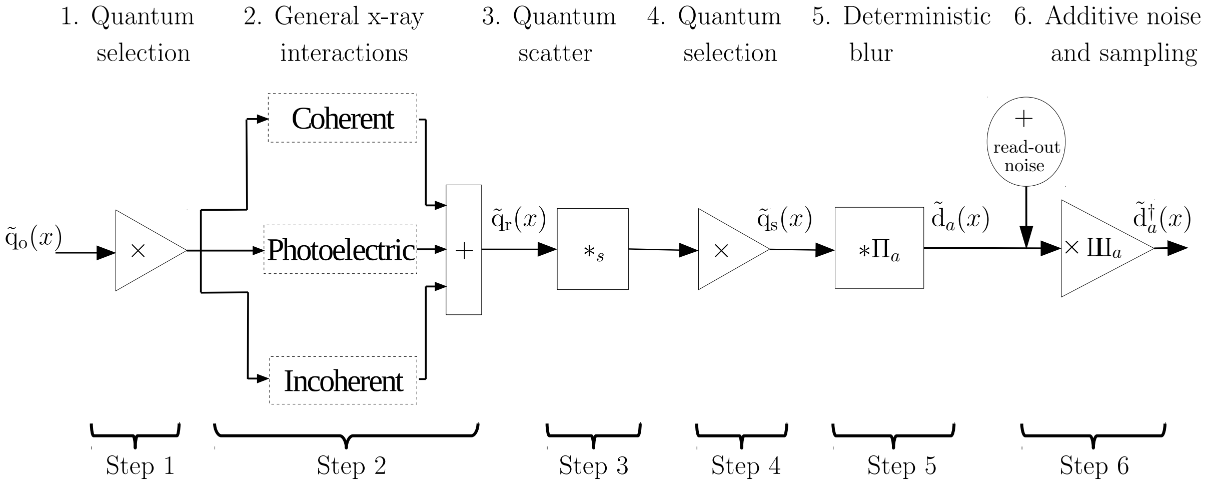

Figure 1.11: CSA model of a conventional detector design. Incident x-ray distribution $\tilde{q}_o(x)$ undergoes: (1) quantum selection in the converter layer, (2) x-ray interactions, (3) quantum scatter, (4) quantum selection in the sensor array, (5) deterministic blur by the sensor aparture, and (6) additive noise and sampling.

quanta distribution $\tilde{q}_s(x)$. Stage 5 is a deterministic blur elementary process of spatial integration of interacting quanta by sensor elements resulting in continuous signal $\tilde{d}_a(x)$. Stage 6 is a combination of sampling and additive noise elementary processes resulting in an output of discrete values $\tilde{d}^\dagger_a(x)$.

1.5.2 Causes of DQE loss

The DQE of an x-ray detector can be reduced by lack of initial interaction quantum efficiency, x-ray reabsorption, converter blur and secondary quantum sinks.[90] It is important to have high DQE across all spatial-frequencies that pertain to a certain imaging task. Reasons for DQE loss are shown in Figure 1.12 that include non-unity quantum efficiency, Swank noise,[91, 92] x-ray reabsorption[88] converter blur,[92, 87] secondary quantum sinks[7] and noise aliasing.[93] Cascaded systems can be used to model the effects of each factor (solid line) and show good agreement with experiment (data points).

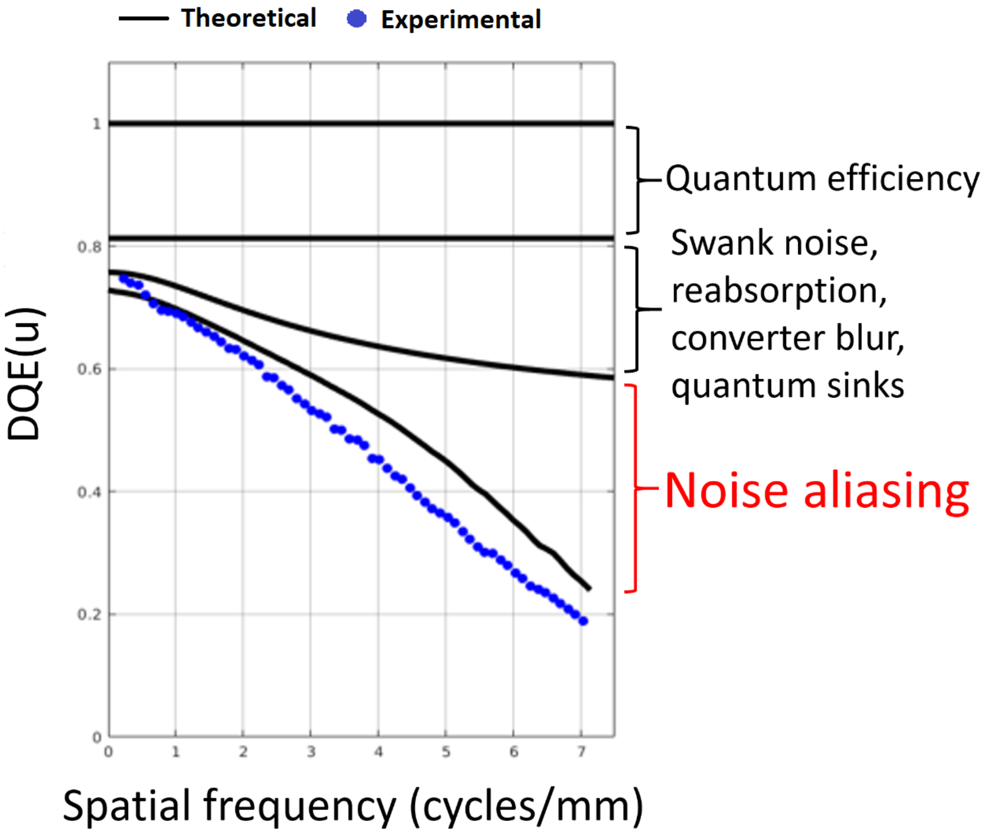

Figure 1.12: DQE loss caused by different factors showing the compounding effects with each curve. At high frequencies, the primary cause loss is noise aliasing for a high resolution detector. Theoretical DQE curves (solid line) were modeled using CSA having good agreement with experiment (data points) for a clinical mammography detector.

1.5.3 Methods of improving performance

New x-ray detector designs have been developed to overcome some limitations of conventional detectors.[94] For example, a high gain avalanche rushing photoconductor (HARP) has been developed for low-dose x-ray imaging when a conventional detector might not produce enough secondary quanta and have quantum sinks.[95] Another example of a new x-ray detector design is a pixelated (or partially pixelated) scintillator which can improve MTF at high-frequencies but at the expense of reduced DQE.[96] These designs provide improvement by addressing issues such as secondary quantum sinks or MTF loss at high-frequencies. However, there is still no solution for noise aliasing which is the main cause of DQE loss at high frequencies with a high resolution converter layer.

Previous methods of reducing noise aliasing were studied when selenium was first being developed as a converter layer for digital x-ray imaging.[97] Some of these methods removed aliasing by attenuating frequencies below the image cut-off frequency using a post-processing filtering or adding an insulating layer between *a*-Se and the sensor array.[98, 99, 100] Although these methods may reduce aliasing in an image, they achieve this by attenuating both signal and noise that does not result in improved DQE. In addition, these methods reduce presampling MTF below the image cut-off frequency which is typically undesirable.

1.6 Aliasing

In digital imaging, a continuous function (representing the object being imaged) is evaluated at uniform spacings as shown in Figure 1.13. Nyquist showed that the maximum frequency in a discrete signal with spacings a is $^{1}/_{2a}$ – this is known as the Nyquist cut-off frequency $u_c = {}^{1}/_{2a}$.[101] The Fourier transform of the presampling signal $\tilde{\mathrm{d}}_a$ is given by $\tilde{\mathrm{D}}_a$ and if it has frequencies above u_c this will result in **aliasing**. The sampled signal $\tilde{\mathrm{d}}^{\dagger}_a$ will have frequency power above u_c “folded” into lower frequencies as shown by

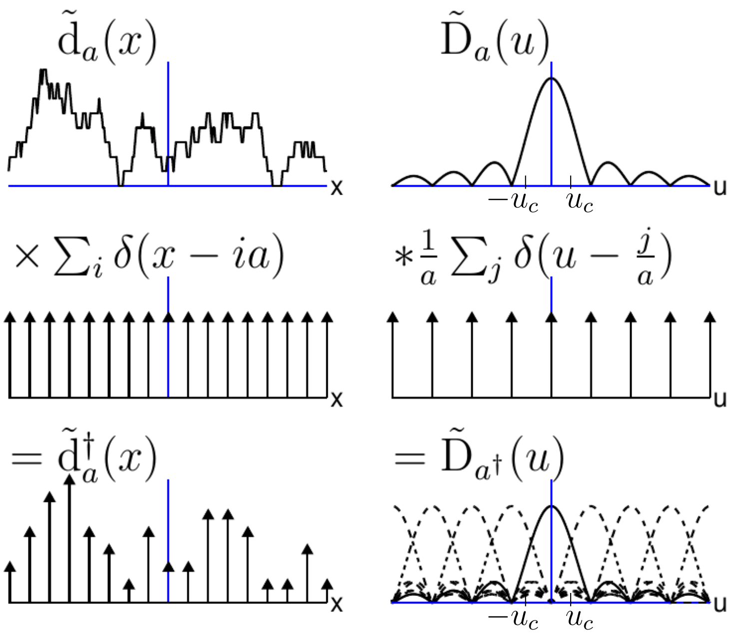

Figure 1.13: A continuous signal $\tilde{\mathrm{d}}_a$ that has frequencies $\tilde{\mathrm{D}}_a$ past the image sampling cut-off frequency u_c will result in aliasing. The sampled signal $\tilde{\mathrm{d}}_a^\dagger$ has frequencies $\tilde{\mathrm{D}}_{a^\dagger}$ that are a summation of the fundamental (solid line) and aliased frequencies (dashed lines).

the dashed line in Figure 1.13 for $\tilde{\mathrm{D}}_{a^\dagger}$. We classify aliasing into two types: signal and noise aliasing.

Signal aliasing may result in image artifacts and degradation because it misrepresents the object being imaged.[102] Since signal aliasing is not linear or shift-invariant, it is not included in MTF calculations or modeling.[65] To overcome this issue, the presampling MTF which does not include aliasing is used to quantify system signal transfer. However, we are careful when describing performance of digital systems because there could be aliasing present.

Noise aliasing occurs when noise components are folded into image frequencies. Noise aliasing can be modeled with CSA for noise properties that are wide-sense cyclo-stationary (WSCS).[65] Cyclo-stationary processes exhibit periodic behaviour but have statistical properties that are invariant to shifts of any multiple of that period. Stationary noise properties are often satisfied in imaging tasks of low-contrast features. Noise aliasing has the greatest impact on frequencies near the cut-off frequency and results in degradation of low-contrast fine-detail features.[93] For high-resolution imagers, where resolution is limited by pixel size and not converter blur, quantum noise is uncorrelated and noise aliasing has a large effect on DQE at high-frequencies.

1.7 Thesis overview

1.7.1 Research problem

While much effort has been invested in improving DQE of x-ray detectors, DQE values at high-frequencies are still much lower than at low-frequencies. We have identified that noise aliasing reduces high-frequency DQE by as much as 60% when using a high-resolution converter layer and a conventional detector design. This indicates that low DQE values at high-frequencies are a design limitation of high-resolution conventional detectors.

These issues lead to the following research questions:

1. Can we design a new x-ray detector approach that eliminates (signal and noise) aliasing and results in increased high-frequency DQE?
2. How will x-ray detector physics affect the performance of this new x-ray detector, and how will different detector conditions affect DQE improvement?
3. Can we implement the new detector design on a small-area prototype and show MTF and DQE improvements with image pixels similar in size to mammography.

These questions are important because once answered we will know if we can overcome a current limitation of conventional designs, making it possible to achieve a “perfect” detector in terms of MTF and DQE. Answering these questions requires a thorough understanding of image formation in x-ray detectors and how detector design modifications may affect detector performance and x-ray image quality.

1.7.2 Research hypothesis

The overarching hypothesis of this thesis is that image SNR can be improved through MTF and DQE at high-frequency using a new detector design that has a sensor array with physical elements much smaller than the desired image pixel size. We refer to this new design as apodized-aperture pixel (AAP) because of the apodization in the frequency response. An anti-aliasing filter can be applied to the "over-sampled" sensor output to eliminate aliasing and an image can be created by resampling to synthesize desired pixel size. This approach takes advantage of new technology by using very small sensor elements (7.8 μm in our lab prototype) without the associated large image files (one 24×30 cm mammography image would be 2.3 GB) where such file sizes would be too large to handle and display with a busy conventional PACS system, or where there may be negligible diagnostic value gained from higher resolution.

1.7.3 Research objectives

The objectives of this thesis are:

1. Design an x-ray detector that uses smaller element size and develop a method to synthesize pixels which suppress aliasing for improved MTF and DQE at high-frequencies.

2. Determine the impact of x-ray detector physics on the new x-ray detector design.

3. Demonstrate implementation of the AAP design using a small-area prototype and show improvements in fine-feature visualization.

4. Determine optimum AAP anti-aliasing filter shape that reduces artifacts while maintaining AAP benefit in MTF and DQE.

1.7.4 Outline

The goal of this thesis is addressed in a series of 4 manuscripts (Chapter 2 to 5), where each chapter corresponds to a specific thesis objective.

Chapter 2: MTF and DQE Enhancements using an apodized-aperture pixel (AAP) x-ray detector design

While DQE values at low frequencies can be as high as 0.8 for high-performing detectors, high-frequency DQE values remain much lower and therein lies the most potential for improvement. Current high-performing x-ray detectors with high-resolution converter layers have reduced DQE values by 60% due to noise aliasing. We propose developing a new x-ray detector design, called apodized-aperture pixel (AAP), that eliminates noise aliasing by using sensor elements smaller than desired pixel size.

Chapter 2 describes the AAP approach using a simple cascaded model of an x-ray detector with an ideal converter. MTF and DQE comparisons are made between conventional and AAP designs using proof-of-concept experiments. It is shown that the AAP approach preserves the MTF of the small sensor elements and attenuates frequencies above the image sampling cut-off frequency. This has the double benefit of improving the MTF while reducing both signal and noise aliasing, resulting in a DQE increase at high spatial frequencies.

[This chapter was published in Medical Physics: Tomi F. Nano, Terenz Escartin, Elina Ismailova, Jan Linström, Karim K. Karim, Ho Kyung Kim and Ian A. Cunningham, "MTF and DQE enhancements with an apodized-aperture pixel x-ray detector design", Medical Physics, 44(9), 2017]

Chapter 3: Impact of x-ray reabsorption and converter blur MTF and DQE improvements using an apodized-aperture pixel (AAP) x-ray detector design

Chapter 2 showed a proof-of-concept demonstration of the AAP design with improvement high-frequency MTF and DQE, and image SNR of fine detail using the same patient exposure. However, analysis of the AAP approach was done using an ideal detector model and therefore did not consider x-ray physics in a general converter layer. We developed a cascaded system analysis using a simple-atom model of x-ray interactions that includes effects of stochastic energy-deposition, x-ray reabsorption, quantum scattering and quantum selection in the detector converter layer.

Chapter 3 describes the impact of x-ray physics on MTF and DQE using cascaded-systems analysis (CSA) on conventional and AAP x-ray detector designs. X-ray reabsorption and converter blur were identified as important factors to consider because they may affect aliasing, and it is shown that reabsorption has negligible effect on the AAP whereas converter blur reduces the AAP benefit depending on the amount of blur. Therefore, the AAP design should be implemented with a high-resolution converter.

This chapter was submitted to Physics in Medicine and Biology: Tomi F. Nano, Karim S. Karim and Ian A. Cunningham, "Impact of x-ray reabsorption and converter blur MTF and DQE improvements using an apodized-aperture pixel (AAP) x-ray detector design".

Chapter 4: Performance evaluation of a Se/CMOS prototype x-ray detector with the apodized-aperture x-ray detector design

Chapter 3 investigated the x-ray physics effects on the AAP design and showed that a high-resolution converter layer with little blur provides the most improvement with the AAP approach, such as a high-resolution converter layer like selenium deposited directly on a complementary metal-oxide semiconductor (CMOS) sensor. We implemented the AAP design on a small-area prototype and developed a cascaded system analysis using a simple-atom model of x-ray interactions that includes effects of stochastic energy-deposition, x-ray reabsorption, quantum scattering and quantum selection in the detector converter layer.

Chapter 4 describes implementation of the AAP approach on a Se/CMOS prototype with 7.8 μm element size and compare AAP and conventional (binned) images with 47 μm pixel size. It is shown that the AAP design has 1.5× greater MTF near the image cut-off frequency ($u_c = 10.6$ cyc/mm) than conventional design and 2.5× greater DQE. In addition, the AAP approach removes signal aliasing that causes partial volume effects that cause inconsistent visibility of small structures (such as breast calcifications).

This chapter is being submitted to Journal of Medical Imaging: Tomi F. Nano, Chris C. Scott, Yunzhe Li, Celon Con, Jan Linström, Karim K. Karim and Ian A. Cunningham, "An x-ray detector prototype using Se/CMOS and the apodized-aperture pixel (AAP) design to reduce aliasing".

Chapter 5: Anti-aliasing filter with minimal Gibbs ringing using an apodized-aperture pixel (AAP) x-ray detector design

Chapter 4 investigated performance of the AAP approach on a Se/CMOS prototype and showed that the AAP design has 1.5× greater MTF near the image cut-off frequency ($u_c = 10.6$ cyc/mm) than conventional design and 2.5× greater DQE. Additionally, inconsistent visualization of specs in mammography phantoms is eliminated with the AAP approach by eliminating signal aliasing that cause partial volume artifacts. However, elimination of signal aliasing requires application of a low-pass filter in the spatial-frequency domain that may cause Gibbs ringing (an undesired image artifact) in the spatial domain. We investigated the impact of Gibbs ringing on image quality with the AAP design using an anti-aliasing filter that is implemented directly on the detector and improvements on MTF and DQE.

Chapter 5 describes how AAP anti-aliasing filter shape affects Gibbs ringing and benefits with the AAP design. We define conditions when Gibbs ringing is visible and describe AAP filter shapes that reduce Gibbs ringing.

This chapter is in preparation to be submitted to Physics in Medicine and Biology:

Tomi F. Nano and Ian A. Cunningham, "Anti-aliasing filter with minimal Gibbs ringing using an apodized-aperture pixel (AAP) x-ray detector design".

Chapter 6: Conclusions and future work

An overview and summary of conclusions and important findings of Chapter 2-5 is provided. Study limitations are discussed and preliminary direction of future work as shown.

Future work 1: Observer performance of AAP vs conventional image frequencies

Future work 2: Ultrahigh-resolution imaging of microcalcifications in mammography

Future work 3: Impact of the AAP design tomosynthesis and computed tomography

Bibliography

[1] D. A. Berry, K. A. Cronin, S. K. Plevritis, D. G. Fryback, L. Clarke, M. Zelen, J. S. Mandelblatt, A. Y. Yakovlev, J. D. F. Habbema, and E. J. Feuer, "Effect of screening and adjuvant therapy on mortality from breast cancer," *New England Journal of Medicine*, vol. 353, no. 17, pp. 1784–1792, 2005. PMID: 16251534.

[2] C. E. DeSantis, J. Ma, A. Goding Sauer, L. A. Newman, and A. Jemal, "Breast cancer statistics, 2017, racial disparity in mortality by state," *CA: A Cancer Journal for Clinicians*, vol. 67, no. 6, pp. 439–448, 2017.

[3] M. J. Yaffe, A. K. Bloomquist, D. M. Hunter, G. E. Mawdsley, A. M. Chiarelli, D. Muradali, and J. G. Mainprize, "Comparative performance of modern digital mammography systems in a large breast screening program," *Medical Physics*, vol. 40, no. 12, pp. 121915–n/a, 2013. 121915.

[4] A. M. Chiarelli, S. A. Edwards, M. V. Prummel, D. Muradali, V. Majpruz, S. J. Done, P. Brown, R. S. Shumak, and M. J. Yaffe, "Digital compared with screen-film mammography: Performance measures in concurrent cohorts within an organized breast screening program," *Radiology*, vol. 268, pp. 684–93, Sep 2013.

[5] A. Rose, "Quantum and noise limitations of the visual process," *Journal of the Optical Society of America*, vol. 43, pp. 715–6, 1953.

[6] A. Rose, *Vision: Human and Electronic*. New York: Plenum Press, 1974.

[7] I. A. Cunningham, M. S. Westmore, and A. Fenster, "A spatial-frequency dependent quantum accounting diagram and detective quantum efficiency model of signal and noise propagation in cascaded imaging systems.," *Med Phys*, vol. 21, no. 3, pp. 417–427, 1994.

[8] J. H. Siewerdsen and L. E. Antonuk, "DQE and system optimization for indirect-detection flat-panel imagers in diagnostic radiology," in *Medical Imaging 1998: Physics of Medical Imaging*, vol. 3336, pp. 546–556, International Society for Optics and Photonics, 1998.

[9] S. Weigel, T. Decker, E. Korsching, D. Hungermann, W. BÃP cker, and W. Heindel, "Calcifications in digital mammographic screening: Improvement of early detection of invasive breast cancers?," *Radiology*, vol. 255, no. 3, pp. 738–745, 2010. PMID: 20501713.

[10] H.-J. Langen, S. Koehler, J. Bielmeier, R. Jocher, D. Kranzfelder, N. Jagusch, G. Treutlein, T. Wetzler, J. Müller, and G. Ott, "Microradiography of microcalcifications in breast specimen: a new histological correlation procedure and the effect of improved resolution on diagnostic validity," *Radiology research and practice*, vol. 2012, 2012.

[11] M. Lanyi, *Diagnosis and differential diagnosis of breast calcifications.* Springer Science & Business Media, 2012.

[12] Canadian Cancer Statistics Advisory Committee, "Canadian cancer statistics 2018," *Toronto, ON: Canadian Cancer Society*, 2018. Available at: cancer.ca/Canadian-Cancer-Statistics-2018-EN (accessed Dec. 10th 2018).

[13] N. Mittmann, J. Porter, J. Rangrej, S. Seung, N. Liu, R. Saskin, M. Cheung, N. Leighl, J. Hoch, M. Trudeau, W. Evans, K. Dainty, C. DeAngelis, and C. Earle,

"Health system costs for stage-specific breast cancer: a population-based approach," *Current Oncology*, vol. 21, no. 6, 2014.

[14] B. Will, J.-M. Berthelot, C. L. Petit, E. Tomiak, S. Verma, and W. Evans, "Estimates of the lifetime costs of breast cancer treatment in canada," *European Journal of Cancer*, vol. 36, no. 6, pp. 724 – 735, 2000.

[15] F. Bray, J. Ferlay, I. Soerjomataram, R. L. Siegel, L. A. Torre, and A. Jemal, "Global cancer statistics 2018: Globocan estimates of incidence and mortality worldwide for 36 cancers in 185 countries," *CA: A Cancer Journal for Clinicians*, vol. 68, no. 6, pp. 394–424, 2018.

[16] M. M. Fidler, I. Soerjomataram, and F. Bray, "A global view on cancer incidence and national levels of the human development index," *International Journal of Cancer*, vol. 139, no. 11, pp. 2436–2446, 2016.

[17] Cancer Care Ontario, "Screening guidelines and program eligibility," *Cancer Care Ontario*, 2018. Retrieved Dec. 10th, 2018, from https://archive.cancercare.on.ca/pcs/screening/.

[18] X. R. Yang, M. E. Sherman, D. L. Rimm, J. Lissowska, L. A. Brinton, B. Peplonska, S. M. Hewitt, W. F. Anderson, N. Szeszenia-Dkabrowska, A. Bardin-Mikolajczak, W. Zatonski, R. Cartun, D. Mandich, G. Rymkiewicz, M. Ligaj, S. Lukaszek, R. Kordek, and M. Garcia-Closas, "Differences in risk factors for breast cancer molecular subtypes in a population-based study," *Cancer Epidemiology and Prevention Biomarkers*, vol. 16, no. 3, pp. 439–443, 2007.

[19] H. D. Nelson, B. Zakher, A. Cantor, R. Fu, J. Griffin, E. S. OMeara, D. S. Buist, K. Kerlikowske, N. T. van Ravesteyn, A. Trentham-Dietz, J. S. Mandelblatt, and D. L. Miglioretti, "Risk Factors for Breast Cancer for Women Aged 40 to 49 Years:

A Systematic Review and Meta-analysis," *Annals of Internal Medicine*, vol. 156, pp. 635–648, 05 2012.

[20] C. Haagensen, *Disease of the breast.* W. B. Saunders Co.; 3rd edition, 1986.

[21] R. A. Jesinger, "Breast anatomy for the interventionalist," *Techniques in Vascular and Interventional Radiology*, vol. 17, no. 1, pp. 3 – 9, 2014. Breast Interventions.

[22] S. Pandya and R. G. Moore, "Breast development and anatomy," *Clinical obstetrics and gynecology*, vol. 54, no. 1, pp. 91–95, 2011.

[23] L. C. Hartmann, T. A. Sellers, M. H. Frost, W. L. Lingle, A. C. Degnim, K. Ghosh, R. A. Vierkant, S. D. Maloney, V. S. Pankratz, D. W. Hillman, V. J. Suman, J. Johnson, C. Blake, T. Tlsty, C. M. Vachon, L. J. Melton, and D. W. Visscher, "Benign breast disease and the risk of breast cancer," *New England Journal of Medicine*, vol. 353, no. 3, pp. 229–237, 2005. PMID: 16034008.

[24] M. Guray and A. A. Sahin, "Benign breast diseases: Classification, diagnosis, and management," *The Oncologist*, vol. 11, no. 5, pp. 435–449, 2006.

[25] J. A. Tice, E. S. OMeara, D. L. Weaver, C. Vachon, R. Ballard-Barbash, and K. Kerlikowske, "Benign Breast Disease, Mammographic Breast Density, and the Risk of Breast Cancer," *JNCI: Journal of the National Cancer Institute*, vol. 105, pp. 1043–1049, 06 2013.

[26] H.-P. Sinn and H. Kreipe, "A brief overview of the who classification of breast tumors," *Breast care*, vol. 8, no. 2, pp. 149–154, 2013.

[27] B. A. Virnig, T. M. Tuttle, T. Shamliyan, and R. L. Kane, "Ductal carcinoma in situ of the breast: A systematic review of incidence, treatment, and outcomes," *JNCI: Journal of the National Cancer Institute*, vol. 102, no. 3, pp. 170–178, 2010.

[28] B. C. Pestalozzi, D. Zahrieh, E. Mallon, B. A. Gusterson, K. N. Price, R. D. Gelber, S. B. Holmberg, J. Lindtner, R. Snyder, B. ThÃŒrlimann, E. Murray, G. Viale, M. Castiglione-Gertsch, A. S. Coates, and A. Goldhirsch, “Distinct clinical and prognostic features of infiltrating lobular carcinoma of the breast: Combined results of 15 international breast cancer study group clinical trials,” *Journal of Clinical Oncology*, vol. 26, no. 18, pp. 3006–3014, 2008. PMID: 18458044.

[29] C. Acevedo, C. Amaya, and J.-L. López-Guerra, “Rare breast tumors: review of the literature,” *Reports of Practical Oncology & Radiotherapy*, vol. 19, no. 4, pp. 267–274, 2014.

[30] E. A. Sickles, “Breast calcifications: mammographic evaluation.,” *Radiology*, vol. 160, no. 2, pp. 289–293, 1986.

[31] E. Lazarus, M. B. Mainiero, B. Schepps, S. L. Koelliker, and L. S. Livingston, “Bi-rads lexicon for us and mammography: interobserver variability and positive predictive value,” *Radiology*, vol. 239, no. 2, pp. 385–391, 2006.

[32] C. T. F. on Prevention Health Care, “Breast cancer update,” 2018.

[33] M. J. Yaffe, N. Mittmann, O. Alagoz, A. Trentham-Dietz, A. N. Tosteson, and N. K. Stout, “The effect of mammography screening regimen on incidence-based breast cancer mortality,” *Journal of medical screening*, vol. 25, no. 4, pp. 197–204, 2018.

[34] E. D. Pisano and M. J. Yaffe, “Digitla mammography,” *Radiology*, 2005.

[35] E. A. Sickles, K. Doi, and H. K. Genant, “Magnification film mammography: Image quality and clinical studies,” *Radiology*, vol. 125, no. 1, pp. 69–76, 1977. PMID: 897191.

[36] W. J. Veldkamp, M. A. Thijssen, and N. Karssemeijer, "The value of scatter removal by a grid in full field digital mammography," *Medical Physics*, vol. 30, no. 7, pp. 1712–1718, 2003.

[37] J. M. Boone, K. K. Lindfors, V. N. Cooper III, and J. A. Seibert, "Scatter/primary in mammography: comprehensive results," *Medical physics*, vol. 27, no. 10, pp. 2408–2416, 2000.

[38] D. B. Kopans, "Breast imaging," in *Classic Papers in Breast Disease*, pp. 162–180, CRC Press, 2004.

[39] M. B. Popli, R. Teotia, M. Narang, and H. Krishna, "Breast positioning during mammography: Mistakes to be avoided," *Breast cancer : basic and clinical research*, vol. 8, pp. 119–124, July 2014.

[40] L. Liberman and J. H. Menell, "Breast imaging reporting and data system BI-RADS," *Radiologic Clinics*, vol. 40, no. 3, pp. 409–430, 2002.

[41] J. S. Greenberg, M. C. Javitt, J. Katzen, S. Michael, and A. E. Holland, "Clinical performance metrics of 3d digital breast tomosynthesis compared with 2d digital mammography for breast cancer screening in community practice," *American Journal of Roentgenology*, vol. 203, no. 3, pp. 687–693, 2014.

[42] D. Kopans, S. Gavenonis, E. Halpern, and R. Moore, "Calcifications in the breast and digital breast tomosynthesis," *The breast journal*, vol. 17, no. 6, pp. 638–644, 2011.

[43] P. Skaane, A. I. Bandos, E. B. Eben, I. N. Jebsen, M. Krager, U. Haakenaasen, U. Ekseth, M. Izadi, S. Hofvind, and R. Gullien, "Two-view digital breast tomosynthesis screening with synthetically reconstructed projection images: comparison with digital breast tomosynthesis with full-field digital mammographic images," *Radiology*, vol. 271, no. 3, pp. 655–663, 2014.

[44] C. H. Lee, D. D. Dershaw, D. Kopans, P. Evans, B. Monsees, D. Monticciolo, R. J. Brenner, L. Bassett, W. Berg, S. Feig, E. Hendrick, E. Mendelson, C. D'Orsi, E. Sickles, and L. W. Burhenne, "Breast cancer screening with imaging: Recommendations from the society of breast imaging and the acr on the use of mammography, breast mri, breast ultrasound, and other technologies for the detection of clinically occult breast cancer," *Journal of the American College of Radiology*, vol. 7, no. 1, pp. 18 – 27, 2010.

[45] C. K. Kuhl, S. Schrading, C. C. Leutner, N. Morakkabati-Spitz, E. Wardelmann, R. Fimmers, W. Kuhn, and H. H. Schild, "Mammography, breast ultrasound, and magnetic resonance imaging for surveillance of women at high familial risk for breast cancer," *Journal of Clinical Oncology*, vol. 23, no. 33, pp. 8469–8476, 2005. PMID: 16293877.

[46] W. A. Berg, J. D. Blume, J. B. Cormack, E. B. Mendelson, D. Lehrer, M. Böhm-Vélez, E. D. Pisano, R. A. Jong, W. P. Evans, M. J. Morton, *et al.*, "Combined screening with ultrasound and mammography vs mammography alone in women at elevated risk of breast cancer," *Jama*, vol. 299, no. 18, pp. 2151–2163, 2008.

[47] C. M. Sehgal, S. P. Weinstein, P. H. Arger, and E. F. Conant, "A review of breast ultrasound," *Journal of Mammary Gland Biology and Neoplasia*, vol. 11, pp. 113–123, Apr 2006.

[48] A. Izumori, K. Takebe, and A. Sato, "Ultrasound findings and histological features of ductal carcinoma in situ detected by ultrasound examination alone," *Breast Cancer*, vol. 17, no. 2, pp. 136–141, 2010.

[49] H. Q. Ontario *et al.*, "Ultrasound as an adjunct to mammography for breast cancer screening: a health technology assessment," *Ontario health technology assessment series*, vol. 16, no. 15, p. 1, 2016.

[50] S. Lord, W. Lei, P. Craft, J. Cawson, I. Morris, S. Walleser, A. Griffiths, S. Parker, and N. Houssami, “A systematic review of the effectiveness of magnetic resonance imaging (mri) as an addition to mammography and ultrasound in screening young women at high risk of breast cancer,” *European Journal of Cancer*, vol. 43, no. 13, pp. 1905 – 1917, 2007.

[51] C. D. Lehman, J. D. Blume, P. Weatherall, D. Thickman, N. Hylton, E. Warner, E. Pisano, S. J. Schnitt, C. Gatsonis, and M. a. Schnall, “Screening women at high risk for breast cancer with mammography and magnetic resonance imaging,” *Cancer*, vol. 103, no. 9, pp. 1898–1905, 2005.

[52] M. O. Leach, “Breast imaging technology application of magnetic resonance imaging to angiogenesis in breast cancer,” *Breast Cancer Research*, vol. 3, no. 1, p. 22, 2000.

[53] J. Seely and T. Alhassan, “Screening for breast cancer in 2018: What should we be doing today?,” *Current Oncology*, vol. 25, no. Suppl 1, p. S115, 2018.

[54] R. M. Mann, C. K. Kuhl, K. Kinkel, and C. Boetes, “Breast mri: guidelines from the european society of breast imaging,” *European Radiology*, vol. 18, pp. 1307–1318, Jul 2008.

[55] M. B. Mainiero, A. Lourenco, M. C. Mahoney, M. S. Newell, L. Bailey, L. D. Barke, C. D’Orsi, J. A. Harvey, M. K. Hayes, P. T. Huynh, *et al.*, “Acr appropriateness criteria breast cancer screening,” *Journal of the American College of Radiology*, vol. 13, no. 11, pp. R45–R49, 2016.

[56] E. M. Fallenberg, C. Dromain, F. Diekmann, F. Engelken, M. Krohn, J. M. Singh, B. Ingold-Heppner, K. J. Winzer, U. Bick, and D. M. Renz, “Contrast-enhanced spectral mammography versus mri: Initial results in the detection of breast cancer

and assessment of tumour size," *European Radiology*, vol. 24, pp. 256–264, Jan 2014.

[57] S. Sree, E. Ng, R. Archarya, and O. Faust, "Breast imaging: A survey," *W. J. of Clin. Onc.*, vol. 2, no. 4, pp. pp. 171–178, 2011.

[58] C. Dromain and C. Balleyguier, *Contrast-Enhanced Digital Mammography*, pp. 187–198. Berlin, Heidelberg: Springer Berlin Heidelberg, 2010.

[59] E. D. Pisano, C. Gatsonis, E. Hendrick, M. Yaffe, J. K. Baum, S. Acharyya, E. F. Conant, L. L. Fajardo, L. Bassett, C. D'Orsi, R. Jong, and M. Rebner, "Diagnostic performance of digital versus film mammography for breast-cancer screening," *New England Journal of Medicine*, vol. 353, no. 17, pp. 1773–1783, 2005.

[60] C. C. Ontario, "Ontario breast screening program 2011 report," *Toronto, Canada*, 2013.

[61] C. Health, "Ontario to swap mammogram devices based on study," May 2013.

[62] N. W. Marshall, P. Monnin, H. Bosmans, F. O. Bochud, and F. R. Verdun, "Image quality assessment in digital mammography: part i. technical characterization of the systems," *Physics in Medicine and Biology*, vol. 56, pp. 4201–4220, jun 2011.

[63] A. Kawaguchi, Y. Matsunaga, T. Otsuka, and S. Suzuki, "Patient investigation of average glandular dose and incident air kerma for digital mammography," *Radiological Physics and Technology*, vol. 7, pp. 102–108, Jan 2014.

[64] R. Shaw, "The equivalent quantum efficiency of the photographic process," *J. Photogr. Sc.*, vol. 11, pp. 199–204, 1963.

[65] I. A. Cunningham, "Applied linear-systems theory," in *Handbook of Medical Imaging: Vol 1, Physics and Psychophysics* (J. Beutel, H. L. Kundel, and R. V. Metter, eds.), Ch 2, pp. 79–159, SPIE Press, 2000.

[66] H. E. Johns, *Physics of radiology.* Charles River Media, 1983.

[67] G. T. Barnes, "Contrast and scatter in x-ray imaging.," *Radiographics*, vol. 11, no. 2, pp. 307–323, 1991.

[68] J. Yorkston, "Recent developments in digital radiography detectors," *Nuclear Instruments and Methods in Physics Research Section A: Accelerators, Spectrometers, Detectors and Associated Equipment*, vol. 580, no. 2, pp. 974 – 985, 2007. Imaging 2006.

[69] M. J. Yaffe and J. G. Mainprize, "Detectors for digital mammography," *Technology in Cancer Research & Treatment*, vol. 3, no. 4, pp. 309–324, 2004. PMID: 15270582.

[70] S. Kasap, J. B. Frey, G. Belev, O. Tousignant, H. Mani, J. Greenspan, L. Laperriere, O. Bubon, A. Reznik, G. DeCrescenzo, *et al.*, "Amorphous and polycrystalline photoconductors for direct conversion flat panel x-ray image sensors," *Sensors*, vol. 11, no. 5, pp. 5112–5157, 2011.

[71] S. Abbaszadeh, N. Allec, and K. S. Karim, "Improving amorphous selenium photodetector performance using an organic semiconductor," *Key Eng. Mat.*, vol. 543, pp. 451–54, 2013.

[72] K. S. Karim, A. Nathan, and J. A. Rowlands, "Amorphous silicon active pixel sensor readout circuit for digital imaging," *IEEE transactions on electron devices*, vol. 50, no. 1, pp. 200–208, 2003.

[73] C. C. Scott, S. Abbaszadeh, S. Ghanbarzadeh, G. Allan, M. Farrier, I. A. Cunningham, and K. S. Karim, "Amorphous selenium direct detection CMOS digital x-ray imager with 25 micron pixel pitch," *Proc. SPIE: Physics of Medical Imaging*, vol. 9033, 2014.

[74] C. C. Scott, A. Parsafar, A. El-Falou, P. M. Levine, and K. S. Karim, "High dose efficiency, ultra-high resolution amorphous selenium/CMOS hybrid digital X-ray imager," *IEEE Int. Electron Devices Meet.*, vol. 30.6.1, pp. 1–4, 2015.

[75] A. Parsafar, C. C. Scott, A. El-Falou, P. M. Levine, and K. S. Karim, "Direct-conversion CMOS x-ray imager with 5.6um x 6.25um pixels," *IEEE Electron Device Lett.*, vol. 36, pp. 481–483, May 2015.

[76] J. C. Dainty and R. Shaw, *Image Science: Principles, Analysis, and Evaluation of Photographic-Type Image Processing.* Academic Press, 1974.

[77] A. E. Burgess, B. Worthington, C. E. Metz, C. J. Taylor, C. R. Hill, D. C. Barber, D. E. Kuhl, D. G. Brown, K. J. Myers, M. A. Smith, P. Sharp, P. Wells, R. Brooks, and R. F. Wagner, "Report 54," *Journal of the International Commission on Radiation Units and Measurements*, vol. os28, pp. NP–NP, 04 2016.

[78] "Medical electrical equipment - Characteristics of digital x-ray imaging devices - Part 1-2: Determination of the detective quantum efficiency - Detectors used in mammography," Medical electrical equipment IEC 62220-1-2, International Electrotechnical Commission, 2007.

[79] "Medical electrical equipment - Characteristics of digital x-ray imaging devimaging Part 1-1: Determination of the detective quantum efficiency - Detectors used in radiographic imaging," Medical Electrical Equipment IEC 62220-1-1, International Electrotechnical Commission, 2015.

[80] H. H. Barrett and K. J. Myers, *Foundations of Image Science.* New Jersey: John Wiley & Sons, Inc., 2004. Chapter 11, pg. 651-655.

[81] C. E. Metz and K. Doi, "Transfer function analysis of radiographic imaging systems," *Physics in Medicine & Biology*, vol. 24, no. 6, p. 1079, 1979.

[82] J. Yao and I. A. Cunningham, "Parallel cascades: New ways to describe noise transfer in medical imaging systems," *Med. Phys.*, vol. 28, pp. 2020–2038, October 2001.

[83] S. Yun, J. Tanguay, H. K. Kim, and I. A. Cunningham, "Cascaded-systems analyses and the detective quantum efficiency of single-Z x-ray detectors including photoelectric, coherent and incoherent interactions," *Med. Phys.*, vol. 40, no. 4, p. 041916, 2013.

[84] M. Rabbani, R. Shaw, and R. V. Metter, "Detective quantum efficiency of imaging systems with amplifying and scattering mechanisms," *J. Opt. Soc. Am. A*, vol. 4, pp. 895–901, May 1987.

[85] M. Rabbani and R. V. Metter, "Analysis of signal and noise propagation for several imaging mechanisms," *J. Opt. Soc. Am. A*, vol. 6, pp. 1156–1164, August 1989.

[86] I. A. Cunningham, "Linear-systems modeling of parallel cascaded stochastic processes: The NPS of radipgraphic screen with reabsorption of characteristic x radiation," *Proc. SPIE: Medical Imaging*, vol. 3336, pp. 220–231, 1998.

[87] I. A. Cunningham and R. Shaw, "Signal-to-noise optimization of medical imaging systems," *J. Opt. Soc. Am. A.*, vol. 16, no. 3, pp. 621–32, 1999.

[88] C. E. Metz and C. J. Vyborny, "Wiener spectral effects of spatial correlation between the site of characteristic x-ray emission and reabsorption in radiographic screen-film systems," *Phys. Med. Biol.*, vol. 28, no. 5, pp. 547–564, 1983.

[89] G. Hajdok, J. Yao, J. J. Battista, and I. A. Cunningham, "Signal and noise transfer properties of photoelectric interactions in diagnostic x-ray imaging detectors," *Med. Phys.*, vol. 33, no. 10, pp. 3601–3610, 2006.

[90] I. A. Cunningham, J. Yao, and V. Subotic, “Cascaded models and the dqe of flat-panel imagers: Noise aliasing, secondary quantum noise and reabsorption,” *Proc. of SPIE: Physics of Medical Imaging*, vol. 4682, pp. 61–72, 2002.

[91] R. K. Swank, “Absoprtion and noise in x-ray phosphorha,” *Journal of Applied Physics*, vol. 44, no. 9, pp. 4199–4203, 1973.

[92] G. Hajdok, J. J. Battista, and I. A. Cunningham, “Fundametnal x-ray interaction limits in diagnostic imaging detectors: Frequency-dependent Swank noise,” *Med. Phys.*, vol. 35, no. 7, pp. 3194–3204, 2008.

[93] M. F. Kijewski and P. F. Judy, “The noise power spectrum of ct images,” *Physics in Medicine & Biology*, vol. 32, no. 5, p. 565, 1987.

[94] L. Antonuk, K.-W. Jee, Y. El-Mohri, M. Maolinbay, S. Nassif, X. Rong, Q. Zhao, J. Siewerdsen, R. Street, and K. Shah, “Strategies to improve the signal and noise performance of active matrix, flat-panel imagers for diagnostic x-ray applications,” *Medical physics*, vol. 27, no. 2, pp. 289–306, 2000.

[95] W. Zhao, D. Li, A. Reznik, B. J. M. Lui, D. C. Hunt, J. A. Rowlands, Y. Ohkawa, and K. Tanioka, “Indirect flat-panel detector with avalanche gain: Fundamental feasibility investigation for sharp-amfpi (scintillator harp active matrix flat panel imager),” *Medical Physics*, vol. 32, no. 9, pp. 2954–2966, 2005.

[96] H. K. Kim, S. M. Yun, J. S. Ko, G. Cho, and T. Graeve, “Cascade modeling of pixelated scintillator detectors for x-ray imaging,” *IEEE Transactions on Nuclear Science*, vol. 55, pp. 1357–1366, June 2008.

[97] J. Rowlands, D. Hunter, and N. Araj, “X-ray imaging using amorphous selenium: A photoinduced discharge readout method for digital mammography,” *Medical physics*, vol. 18, no. 3, pp. 421–431, 1991.

[98] W. G. Ji, W. Zhao, and J. A. Rowlands, "Digital x-ray imaging using amorphous selenium: Reduction of aliasing," *Med. Phys.*, vol. 25, pp. 2148–62, November 1998.

[99] W. Zhao, W. G. Ji, and J. A. Rowlands, "Effect of characterisitic xrays on the noise power spectra and detective quantum efficiency of photoconductive x-ray detectors," *Med. Phys.*, vol. 28, October 2001.

[100] W. Zhao, W. G. Ji, A. Debrie, and J. A. Rowlands, "Imaging performance of amorphous selenium based flat-panel detectors for digital mammography: Characterization of a small area prototye detector," *Med. Phys.*, vol. 30, no. 2, pp. 254–263, 2003.

[101] J. Abdul, "The shannon sampling theorem: lts various extensions and applications," *Proceedings of the IEEE*, vol. 65, no. 11, p. 1565, 1977.

[102] P. R. Granfors and R. Aufrichtig, "Performance of a 41× 41-cm amorphous silicon flat panel x-ray detector for radiographic imaging applications," *Medical physics*, vol. 27, no. 6, pp. 1324–1331, 2000.

Chapter 2

MTF and DQE Enhancement using an Apodized-Aperture X-Ray Detector Design

We describe a novel apodized-aperture pixel (AAP) design which makes a separation of physical sensor elements from image pixels by using very small sensor elements (e.g. 0.010-0.025 mm) to synthesize desired larger image pixels (e.g. 0.1-0.2 mm). It is shown that the AAP approach preserves the MTF of the small sensor elements and attenuates frequencies above the image sampling cut-off frequency. This has the double benefit of improving the MTF while reducing both signal and noise aliasing, resulting in an increase of the DQE at high spatial frequencies.

This chapter is based on a manuscript published in Medical Physics: TF Nano, T Escartin, E Ismailova, KS Karim, J Lindstrom, HK Kim, and IA Cunningham, Medical Physics, 44(9), 2017. Permission to reproduce this article is included in the Appendix.

2.1 Introduction

The need to produce high-quality medical images while minimizing risks associated with radiation exposure [1, 2] is a key motivator for the development of new x-ray detector technologies. Two critical detector-performance metrics are the modulation transfer function (MTF) and detective quantum efficiency (DQE), expressed as a function of spatial frequency. The MTF describes spatial resolution and the appearance of high contrast and high signal-to-noise ratio (SNR) structures. The DQE describes image SNR for a given number of x-ray quanta incident on the detector with an ideal photon-counting detector having unity DQE.[3, 4, 5]

Not all systems are able to produce equivalent image quality and SNR for a given exposure, due to differences in DQE.[6] For example, DQE can be reduced by: i) reabsorption and escape of characteristic and scatter photons from photoelectric and Compton interactions; ii) inadequate number of secondary quanta collected (optical photons in a phosphor or charges in a photoconductor); iii) scatter of secondary quanta (optical scatter or charge migration); iv) noise aliasing; and v) electronic read-out noise.[7, 8, 9, 10, 11, 12] When read-out noise is sufficiently small, noise aliasing is the primary cause of DQE degradation relative to the zero-frequency value in *a*-Se detectors.[13, 8, 14]

Several investigators have studied methods of reducing signal and noise aliasing. For example, aliasing artifacts can be minimized by preferentially suppressing frequencies where aliasing may be expected. The "effective presampling filter" described by Ji *et al.*[15] is a linear filter that suppresses both signal and noise, resulting in reduced aliasing artifacts but no improvement in the DQE. Rowlands described a method of charge sharing between elements in a sensor array to reduce aliasing.[16, 17] This approach reduced the MTF slightly, but increased the DQE at frequencies where noise is reduced more than the squared MTF.

We describe a method of suppressing both signal and noise aliasing while improving the MTF and DQE at high frequencies.[18, 19] The method requires a detector consisting

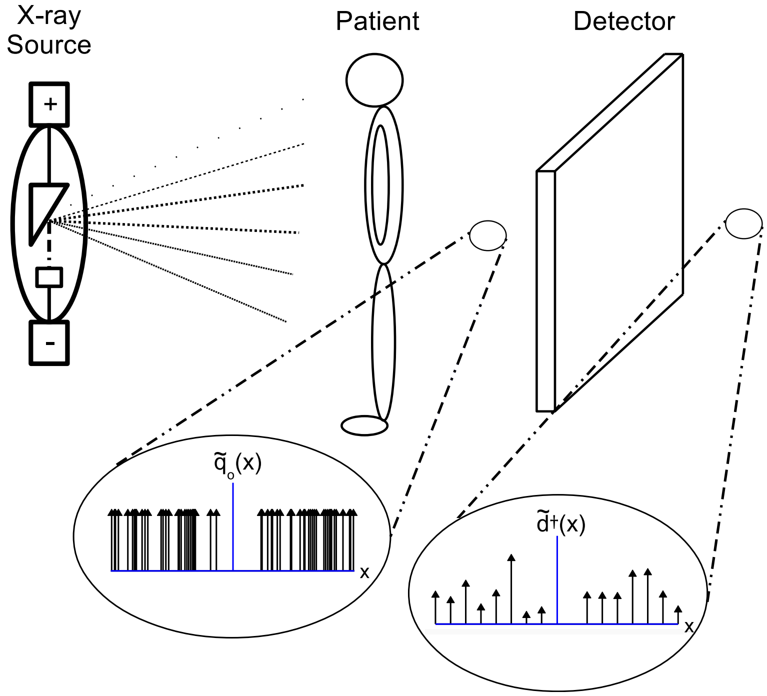

Figure 2.1: Input to the cascaded model is $\tilde{\mathrm{q}}_o(x)$, a random point process consisting of δ-functions representing x-ray quanta incident on the detector. The output is $\tilde{\mathrm{d}}^{\dagger}(x)$, a uniformly-spaced sequence of δ-functions scaled by associated discrete image pixel values.

of an array of sensor elements that are smaller than the desired image pixel size. This provides an "over-sampled" image signal that is used to synthesize image pixels while maximizing the MTF and suppressing aliasing. The goal is to develop an approach of improving the DQE by taking advantage of new technologies (e.g. CMOS) that can be used to manufacture sensor elements so small they may have no clinical importance as image pixels directly, or result in image files too large for modern PACS and display systems. The result is a detector with an apodized aperture pixel (AAP) design in which pixels have a weighted and overlapping aperture response rather than conventional non-overlapping pixel apertures. The converter layer must also be very high resolution, such as amorphous selenium deposited on a CMOS sensor array.[20, 21, 22] In this article we present a theoretical description of the AAP design and describe improvements in detector performance in terms of the MTF and DQE. Results are validated with a simple Monte Carlo simulation and experimental proof-of-concept studies.

2.2 Theory

The SNR performance of the AAP design is described using a cascaded systems analysis (CSA) that quantifies signal and noise properties of quantum-based imaging systems using a linear-systems approach.[5, 14, 12] It describes propagation of image signal and noise in the spatial frequency domain through a cascade of simple physical processes.

Input to the CSA model is a random point process[23] describing a spatial distribution of x-ray quanta $\tilde{\mathrm{q}}_o(x)$ incident on the detector as illustrated in Fig. 2.1, consisting of the superposition of a Dirac δ-function for each incident x-ray photon. The overhead tilde ($\tilde{}$) is used to indicate a random variable (RV) or function, and overhead bar ($\bar{}$) indicates an expectation value. We use one-dimensional illustrations for simplicity but results are easily generalized to two-dimensional space. The model output is $\tilde{\mathrm{d}}^{\dagger}(x)$, a sequence of uniformly-spaced δ-functions scaled by associated discrete numerical values representing image pixel data where the superscript $\dagger$ is used to indicate a sampled function.

Cascaded models of both a simple conventional detector and an AAP detector are compared in Fig. 2.2. For each, the three columns represent: i) image signal in the spatial domain; ii) image signal in the spatial frequency domain (magnitude only); and iii) Wiener noise power spectrum. The letter q is used to indicate a random point process describing a spatial distribution of quanta (δ functions), d a detector numerical value, and n an additive detector readout noise term. In the frequency domain, dashed lines indicate aliased terms whereas solid lines indicate fundamental components (in the 2nd column) and sum of harmonics (in the 3rd column).

The input to step 1 is $\tilde{q}_o(x)$ representing x-ray quanta incident on the detector:[24]

$$\tilde{\mathrm{q}}_o(x) = \sum_{n=1}^{\tilde{N}_o} \delta(x - \tilde{x}_n), \tag{2.1}$$

where $\tilde{x}_n$ is a vector RV describing the coordinate of the nth of $\tilde{N}_o$ photons. In practice,

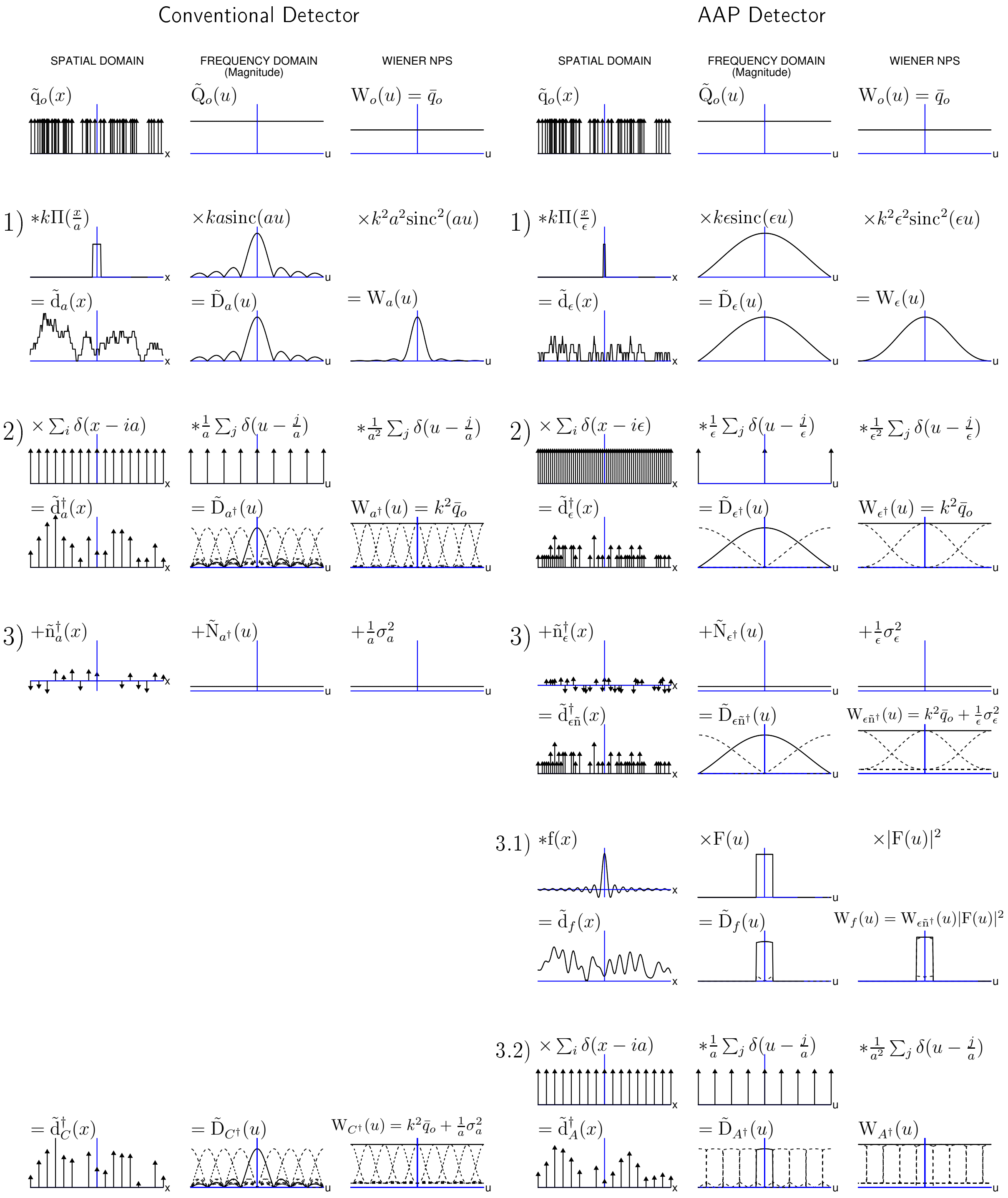

Figure 2.2: Graphical illustration of the CSA model comparing signal and noise transfer through conventional (left) and AAP (right) detectors. The three columns illustrate spatial domain signal, Fourier domain signal (magnitude only plotted) and Wiener NPS. The input at the top consists of a random spatial distribution of x-ray quanta interacting in each detector. The detector output at the bottom consists of a sequence of δ-functions scaled by discrete pixel values representing the final digital image. Dashed lines indicate aliased contributions.

$\tilde{x}_n$ is not uniformly distributed to reflect non-uniform x-ray transmission through the patient, but for Fourier metrics of noise we must assume wide-sense stationary noise processes, requiring that $\tilde{x}_n$ be uniformly distributed over an infinite detector that we represent as having width L in the limit $L \rightarrow \infty$ and $\bar{N}_o = \bar{q}_o L$.

The Fourier transform (FT) of $\tilde{\mathrm{q}}_o(x)$ is $\tilde{\mathrm{Q}}_o(u)$, the superposition of the FT of many shifted δ-functions. Application of the Fourier shift theorem gives:

$$\tilde{\mathrm{Q}}_o(u) = \mathscr{F}\left\{\tilde{\mathrm{q}}_o(x)\right\} = \sum_{n=1}^{\tilde{\mathrm{N}}_o} e^{-i2\pi\tilde{x}_n u} \tag{2.2}$$

and $|\tilde{\mathrm{Q}}_o(u)| = \tilde{\mathrm{N}}_o$ which is independent of frequency. The Wiener NPS of a Poisson random distribution[25], $\tilde{\mathrm{q}}_o(x)$, is therefore $\mathrm{W}_{q_o}(u) = \bar{q}_o$. It is assumed that all incident x-ray quanta interact (unity quantum efficiency) in an ideal converter layer such that each sensor element is an ideal energy-integrating sensor.

2.2.1 Conventional Detector

As illustrated in step 1) of Fig. 2.2, the number of photons interacting in the ith element of width a of a conventional detector, scaled by constant k representing detector gain, is given by:

$$\tilde{d}_{a,i} = \tilde{\mathrm{d}}_a(x)\Big|_{x=ia} = k\tilde{\mathrm{q}}_o(x) * \prod\left(\frac{x}{a}\right)\Big|_{x=ia} \tag{2.3}$$

where $*$ represents a convolution operation and $\tilde{\mathrm{d}}_a(x)$ is the detector presampling signal describing the sensor signal that would be obtained for an element centered at x. The FT of $\tilde{\mathrm{d}}_a(x)$ is given by:

$$\mathscr{F}\left\{\tilde{\mathrm{d}}_a(x)\right\} = \tilde{\mathrm{D}}_a(u) = ka\tilde{\mathrm{Q}}_o(u)\mathrm{sinc}(au) \tag{2.4}$$

where $\mathrm{sinc}(au) \equiv \sin(\pi au)/\pi au$ and the Wiener NPS by

$$\mathrm{W}_a(u) = k^2 a^2 \bar{q}_o \mathrm{sinc}^2(au). \tag{2.5}$$

The process of evaluating $\tilde{\mathrm{d}}_a(x)$ to obtain the set of discrete signal values from all elements is illustrated in step 2):

$$\tilde{\mathrm{d}}_a^\dagger(x) = \tilde{\mathrm{d}}_a(x) \sum_{i=-\infty}^{\infty} \delta(x - ia) = \sum_{i=-\infty}^{\infty} \tilde{d}_{a,i} \delta(x - ia), \tag{2.6}$$

resulting in a series of δ-functions scaled by values $\tilde{\mathrm{d}}_{a,i}$ where the δ-functions give positional significance to the discrete values. The FT of $\tilde{\mathrm{d}}_a^\dagger(x)$ is given by

$$\tilde{\mathrm{D}}_{a^\dagger}(u) = k\tilde{\mathrm{Q}}_o(u)\mathrm{sinc}(au) + \sum_{j=1}^{\infty} k\tilde{\mathrm{Q}}_o(u \pm \frac{j}{a})\mathrm{sinc}(au \pm j). \tag{2.7}$$

The Wiener NPS is determined by noting that $\tilde{\mathrm{d}}_a^\dagger(x)$ is a wide-sense cyclostationary random process since the mean and autocovariance are stationary with shifts of ia.[26, 9] Thus, while signal aliasing is described as a convolution of $\tilde{\mathrm{D}}_a(u)$ with $\frac{1}{a}\sum_j \delta(u - \frac{j}{a})$, noise aliasing is described as a convolution of $\mathrm{W}_{d_a}(u)$ with $\frac{1}{a^2}\sum_j \delta(u - \frac{j}{a})$, giving:

$$\begin{aligned}
\mathrm{W}_{a^\dagger}(u) &= \frac{1}{a^2}\mathrm{W}_a(u) + \frac{1}{a^2}\sum_{j=1}^{\infty} \mathrm{W}_a(u \pm \frac{j}{a}) && (2.8)\\
&= k^2 \bar{q}_o \left[\mathrm{sinc}^2(au) + \sum_{j=1}^{\infty} \mathrm{sinc}^2(au \pm j)\right] && (2.9)\\
&= k^2 \bar{q}_o. && (2.10)
\end{aligned}$$

The last result comes from the property that an infinite sequence of $\mathrm{sinc}^2(au)$ functions, shifted by integer multiples of a^{-1}, sum to unity.[13]

Detector electronic additive readout noise is represented as the addition of $\tilde{\mathrm{n}}_a^\dagger(x)$, a sequence of δ-functions scaled by a discrete zero-mean Gaussian RV $\tilde{n}_{a,i}$ having variance σ_a^2:

$$\tilde{\mathrm{n}}_a^\dagger(x) = \sum_{i=-\infty}^{\infty} \tilde{n}_{a,i}\delta(x - ia). \tag{2.11}$$

With additive noise, the conventional detector signal is shown at step 3):

$$\tilde{\mathrm{d}}_{\mathrm{C}}^\dagger(x) = \tilde{\mathrm{d}}_a^\dagger(x) + \tilde{\mathrm{n}}_a^\dagger(x) \tag{2.12}$$

having NPS given by

$$\mathrm{W}_{\mathrm{C}^\dagger}(u) = k^2\bar{q}_o + \frac{1}{a}\sigma_a^2. \tag{2.13}$$

It is convenient to express the NPS as a normalized NPS, $\mathrm{W}_{\mathrm{C}^\dagger}^{(n)}(u) \equiv \mathrm{W}_{\mathrm{C}^\dagger}(u)\bar{q}_o / \left\langle \tilde{\mathrm{d}}_{\mathrm{C}}^\dagger(x) \right\rangle^2$, giving:

$$\mathrm{W}_{\mathrm{C}^\dagger}^{(n)}(u) = 1 + \frac{\sigma_a^2}{k^2 a \bar{q}_o}, \tag{2.14}$$

where the average of scaled δ-functions with spacing a is $\left\langle \tilde{\mathrm{d}}_a^\dagger(x) \right\rangle = \frac{1}{a}\bar{d}_a$. This form is helpful for understanding performance characteristics since an ideal detector in this model has $\mathrm{W}_{\mathrm{C}^\dagger}^{(n)}(u) = 1$.

The presampling MTF is determined as the ratio of the output to input mean signal in the spatial frequency domain, normalized to unity at $u = 0$:

$$\mathrm{MTF}_{\mathrm{C}}(u) = \frac{\left|\bar{\mathrm{D}}_a(u)\right|}{\bar{\mathrm{D}}_a(0)} = |\mathrm{sinc}(au)| \tag{2.15}$$

and DQE by

$$\mathrm{DQE_C}(u) = \frac{\mathrm{MTF}^2_{\mathrm{C}}(u)}{\mathrm{W}^{(n)}_{\mathrm{C}^\dagger}(u)} = \frac{\mathrm{sinc}^2(au)}{1+\frac{\sigma_a^2}{k^2 a \bar{q}_o}}. \tag{2.16}$$

2.2.2 AAP Detector

The AAP detector is represented as an array of sensor elements of size ϵ, where ϵ is smaller than a. With this difference, the cascaded model of the AAP detector in Fig. 2.2 is similar to that of the conventional detector up to and including step 3). The synthesis of image pixel values from sensor data is expressed as a discrete convolution and resampling operation, corresponding to a convolution integral in step 3.1) giving $\tilde{\mathrm{d}}_{\mathrm{f}}(x) = \tilde{\mathrm{d}}^\dagger_{\epsilon\tilde{\mathrm{n}}}(x) * \mathrm{f}(x)$ where $\mathrm{f}(x)$ is the kernel of the presampling AAP filter, followed by evaluation of the result at uniform spacings a in step 3.2). Similar to $\tilde{\mathrm{d}}_a(x)$, $\tilde{\mathrm{d}}_\epsilon(x)$ and $\tilde{\mathrm{d}}_{\mathrm{f}}(x)$ are presampling functions that are not physically accessible. The output from the AAP detector is therefore given by [mm^{-1}]:

$$\tilde{\mathrm{d}}^\dagger_A(x) = \left[\tilde{\mathrm{d}}^\dagger_{\epsilon\tilde{\mathrm{n}}}(x) * \mathrm{f}(x)\right] \times \sum_{i=-\infty}^{\infty} \delta(x - ia) \tag{2.17}$$

and

$$\begin{aligned}\tilde{\mathrm{D}}_{A^\dagger}(u) &= \frac{1}{a}\tilde{\mathrm{D}}_{\epsilon\tilde{\mathrm{n}}^\dagger}(u)\mathrm{F}(u) \\ &\quad + \frac{1}{a}\sum_{j=1}^{\infty}\tilde{\mathrm{D}}_{\epsilon\tilde{\mathrm{n}}^\dagger}(u \pm \frac{j}{a})\mathrm{F}(u \pm \frac{j}{a})\end{aligned} \tag{2.18}$$

where $\mathrm{F}(u)$ is the FT of $\mathrm{f}(x)$ and the NPS of $\tilde{\mathrm{d}}_{\mathrm{f}}(x)$ is given by [mm]:

$$\mathrm{W_f}(u) = \left[k^2\bar{q}_o + \frac{1}{\epsilon}\sigma_\epsilon^2\right] \times \left|\mathrm{F}(u)\right|^2. \tag{2.19}$$

The NPS of the AAP detector is [mm^{-1}]:

$$\begin{aligned}\mathrm{W}_{A^\dagger}(u) &= \frac{1}{a^2}\mathrm{W}_f(u) + \frac{1}{a^2}\sum_{j=1}^{\infty}\mathrm{W}_f(u \pm \frac{j}{a}) \\ &= \frac{1}{a^2}\left[k^2\bar{q}_o + \frac{1}{\epsilon}\sigma_\epsilon^2\right]\left\{|\mathrm{F}(u)|^2 + \sum_{j=1}^{\infty}\left|\mathrm{F}(u \pm \frac{j}{a})\right|^2\right\} \qquad (2.20)\end{aligned}$$

and the corresponding normalized NPS [unitless]:

$$\begin{aligned}\mathrm{W}_{A^\dagger}^{(n)}(u) &= \mathrm{W}_{A^\dagger}(u)\bar{q}_o / \left\langle \tilde{\mathrm{d}}_A^\dagger(x)\right\rangle^2 \qquad (2.21) \\ &= \left[1 + \frac{\sigma_\epsilon^2}{k^2\epsilon\bar{q}_o}\right]\left\{\frac{|\mathrm{F}(u)|^2}{\mathrm{F}^2(0)} + \sum_{j=1}^{\infty}\frac{\left|\mathrm{F}(u \pm \frac{j}{a})\right|^2}{\mathrm{F}^2(0)}\right\}\end{aligned}$$

where $\mathrm{F}(0)$ is the zero-frequency value of $\mathrm{F}(u)$ and $\mathrm{F}(0) \neq 0$.

The MTF of the AAP detector is therefore given by:

$$\mathrm{MTF_A}(u) = \frac{\left|\bar{\mathrm{D}}_\epsilon(u)\mathrm{F}(u)\right|}{\bar{\mathrm{D}}_\epsilon(0)\mathrm{F}(0)} = \frac{|\mathrm{F}(u)|}{\mathrm{F}(0)}\left|\mathrm{sinc}(\epsilon u)\right|. \qquad (2.22)$$

The DQE is more subtle due to the combined effects of noise aliasing from sampling at spacings of both a and ϵ:

$$\begin{aligned}\mathrm{DQE_A}(u) &= \frac{\mathrm{MTF_A^2}(u)}{\mathrm{W_{A^\dagger}^{(n)}}(u)} \\ &= \frac{|\mathrm{F}(u)\mathrm{sinc}(\epsilon u)|^2}{\left[1 + \frac{\sigma_\epsilon^2}{k^2\epsilon\bar{q}_o}\right]\left\{|\mathrm{F}(u)|^2 + \sum_{j=1}^{\infty}\left|\mathrm{F}(u \pm \frac{j}{a})\right|^2\right\}} \\ &= \frac{|\mathrm{sinc}(\epsilon u)|^2}{\left[1 + \frac{\sigma_\epsilon^2}{k^2\epsilon\bar{q}_o}\right]\left\{1 + \frac{\sum_{j=1}^{\infty}\left|\mathrm{F}(u \pm \frac{j}{a})\right|^2}{|\mathrm{F}(u)|^2}\right\}}. \qquad (2.23)\end{aligned}$$

Inspection of Eq. (2.23) suggests that a good choice for $\mathrm{F}(u)$ is a low-pass filter that blocks all frequencies above the sampling cut-off frequency $u_c = 0.5/a$. This ensures image content at frequencies above $u = u_c$ (in samples with spacings ϵ) is not aliased below the image sampling cut-off frequency u_c, and the DQE simplifies to:

$$\mathrm{DQE_A}(u) = \frac{\mathrm{sinc}^2(\epsilon u)}{1 + \frac{\sigma_\epsilon^2}{k^2 \epsilon \bar{q}_o}}. \tag{2.24}$$

2.2.3 MTF and DQE Improvement

The presampling MTF, normalized NPS and DQE curves predicted by the CSA model for conventional (binned) and AAP detectors (ideal converter-layer with unity quantum efficiency, rectangular low-pass AAP filter, $\epsilon = 0.05\,\mathrm{mm}$ and $a = 0.2\,\mathrm{mm}$) having the same pixel size are compared in Fig. 2.3. The conventional presampling MTF follows the $\mathrm{sinc}(au)$ shape given by Eq. (2.15) while the AAP presampling MTF follows $\mathrm{sinc}(\epsilon u)$ up to the cut-off frequency $u_c = 0.5/a$ and suppresses frequencies above u_c as described by Eq. (2.22). Thus, while the AAP method results in an MTF increase by the factor $\mathrm{sinc}(\epsilon u)/\mathrm{sinc}(au)$, giving a 53% increase at the cut-off frequency (regardless of converter-layer blur), it also removes aliasing from the image if present.

Comparison of $\mathrm{W_{C^\dagger}}(u)$ and $\mathrm{W_{A^\dagger}}(u)$ at step 3) shows the AAP approach reduces noise aliasing by suppressing frequencies $0.5/a < u < 0.5/\epsilon$. As illustrated in Fig. 2.3, the NPS is independent of frequency for both conventional and AAP detectors when used with an ideal (no blur) x-ray converter layer.

Equations (2.23) and (2.24) show the DQE is independent of AAP filter $\mathrm{F}(u)$ shape as long as it describes a low-pass filter with cut-off frequency $u_c = 0.5/a$ and readout noise is negligible. Under these conditions, the DQE-improvement factor is $\mathrm{sinc}^2(\epsilon u)/\mathrm{sinc}^2(au)$, equal to a 2.3× increase at the image sampling cut-off frequency. Also, comparison of Eqs. (2.16) and (2.24) shows the AAP approach will generally be less tolerant of

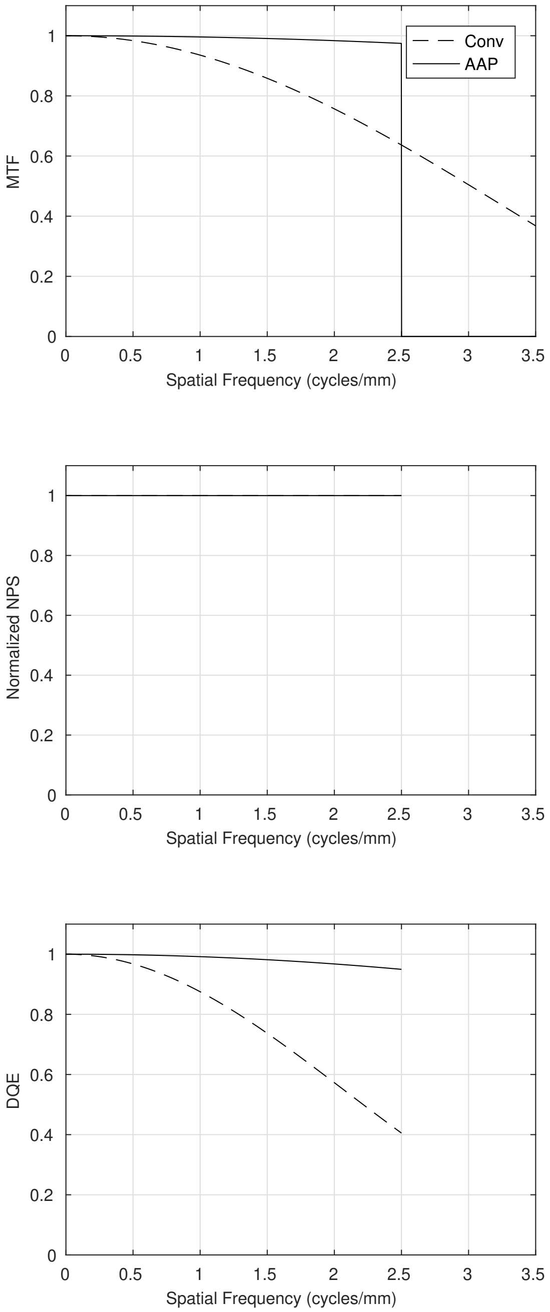

Figure 2.3: Theoretical MTF, normalized NPS, and DQE, comparing an AAP detector with a conventional detector having the same pixel size, assuming negligible read-out noise and ideal x-ray converter layer with unity quantum efficiency and no spatial blur. The normalized NPS of conventional and AAP detectors overlap.

readout noise, requiring $\sigma_\epsilon^2 = \frac{\epsilon}{a}\sigma_a^2$ for the same effect on the DQE, due to the smaller sensor size. In two-dimensions, the read-out noise requirement scales with the square of the element-to-pixel size ratio, $\sigma_\epsilon^2 = (\frac{\epsilon}{a})^2\sigma_a^2$. Achieving lower readout noise may not be trivial. Reducing sensor area may decrease the required storage capacitance in each element, which may reduce noise, but the corresponding reduced signal size and increased number of sensors on each dataline will place greater demands on the electronics. These may be difficult to achieve with some technologies.

2.2.4 Simulated Sinusoidal Patterns

The visual impact of the expected MTF and DQE improvements is illustrated with a simple simulation comparing conventional with AAP images. An oversampled image (representing micro-elements with $\epsilon = 0.05\,\text{mm}$) was created to synthesize both conventional (4×4 binned, $a = 0.2\,\text{mm}$) and AAP ($a = 0.2\,\text{mm}$) images assuming no read-out noise. The AAP approach was implemented in the frequency domain using a low-pass filter with unity height up to the sampling cut-off frequency $u_c = 0.5/a$. Other AAP images (open field, edge, star-pattern and rat leg) where synthesized similarly differing only in pixel size.

Each image has 15 two-dimensional sinusoidal patterns in three rows of differing contrast and five columns of differing spatial frequency (1.0, 1.5, 2.0, 2.4 and 3.0 cycles/mm) chosen to be below, just below, and above the sampling cut-off frequency of 2.5 cycles/mm. Patterns in the rows from top to bottom have amplitudes of 60, 100, and 140 pixel values. Gaussian noise (standard deviation of 100) was added to each pixel in the oversampled image to simulate quantum-noise.

2.3 Materials and Methods

2.3.1 Experimental Star-Pattern and Biological Images

Proof-of-concept images for the AAP design were obtained using a star-pattern (Tielung, 0.05 mm Pb thickness, 45 mm diameter, with 2° angled bars) and clinical mammography system (Hologic Inc.) having a Se converter layer and 0.07 mm sensor elements. Both conventional (4 × 4 binning) and AAP images were synthesized to create images with $a = 0.28$ mm.

With a similar Hologic detector, an image of a rat leg perfused with a lanthanide-based vascular contrast agent was acquired in accordance with the protocol (#2015-018) approved by The University of Western Ontario Council on Animal Care. The raw image was log-transformed and gray-scale inverted. Conventional and AAP images were synthesized as described above. While this results in relatively low-resolution (0.28 mm pixel) images, they are used to experimentally demonstrate the relative MTF improvement with the AAP approach.

2.3.2 Experimental MTF and DQE

Experimental validation of the AAP theory was performed using both lab-based and clinical imaging systems. The lab system consisted of a CMOS-based panel having 0.05 mm sensor elements (Xmaru, Rayence Co. Ltd., Seoul Korea) with a 0.5-mm CsI converter layer. Conventional images were generated with 4×4 binning (0.2 mm pixels) and AAP images were synthesized as described in section IID. The MTF and DQE were determined using both conventional and AAP images with a detector exposure of 4 μGy air KERMA and IEC RQA-5 spectrum (70 kV, 21.0 mm added Al, 6.4 mAs, 7.1 mm Al HVL, 150 cm source-image distance) using a DQE-testing instrument (DQE*Pro*, DQE Instruments Inc., London Canada) following IEC 62220-1 guidelines [27]. Additive read-out noise was verified to be negligible relative to x-ray quantum noise.

The same MTF and DQE comparison was made using a Hologic detector with a Se converter layer. Images having 0.28 mm pixels were synthesized for both AAP and 4 × 4 binning methods as described above. The MTF and DQE were measured using 90 μGy air KERMA with an IEC W/Rh spectrum (28 kV, 2 mm added Al, 24 mAs, 0.75 mmAl HVL, 65 cm source-image distance, no grid).

2.4 Results

2.4.1 Simulated Sinusoidal Patterns

The simulated images in Fig. 2.4 compare the visual appearance of conventional (binned, upper) and AAP (lower) methods. The first observation is that noise in both images is indistinguishable. This is expected as they each have a flat NPS and images are shown with the same display windows. The conventional image shows decreasing contrast with increasing frequency in the first four columns as expected, and the fifth column shows a pattern that has been aliased to a lower frequency. In comparison, the AAP image shows very little loss of contrast with frequency in the first four columns, consistent with the expected flatter MTF, and the fifth-column pattern has been removed completely as it contains only frequencies above the sampling cut-off frequency u_c. This observation gives confidence in the ability of the AAP method to suppress both signal and noise frequencies above u_c.

2.4.2 Experimental Star-Pattern and Biological Images

Star-pattern images in Fig. 2.5 show obvious difference between the conventional (left) and AAP (right) images. The conventional image contains the distinct Moiré pattern artifact due to interference effects from undersampled signals (aliasing) resulting in a misrepresentation of the star-pattern with contrast reversal near the image sampling cut-off frequency (near the circle). The AAP image shows improved contrast, particularly at

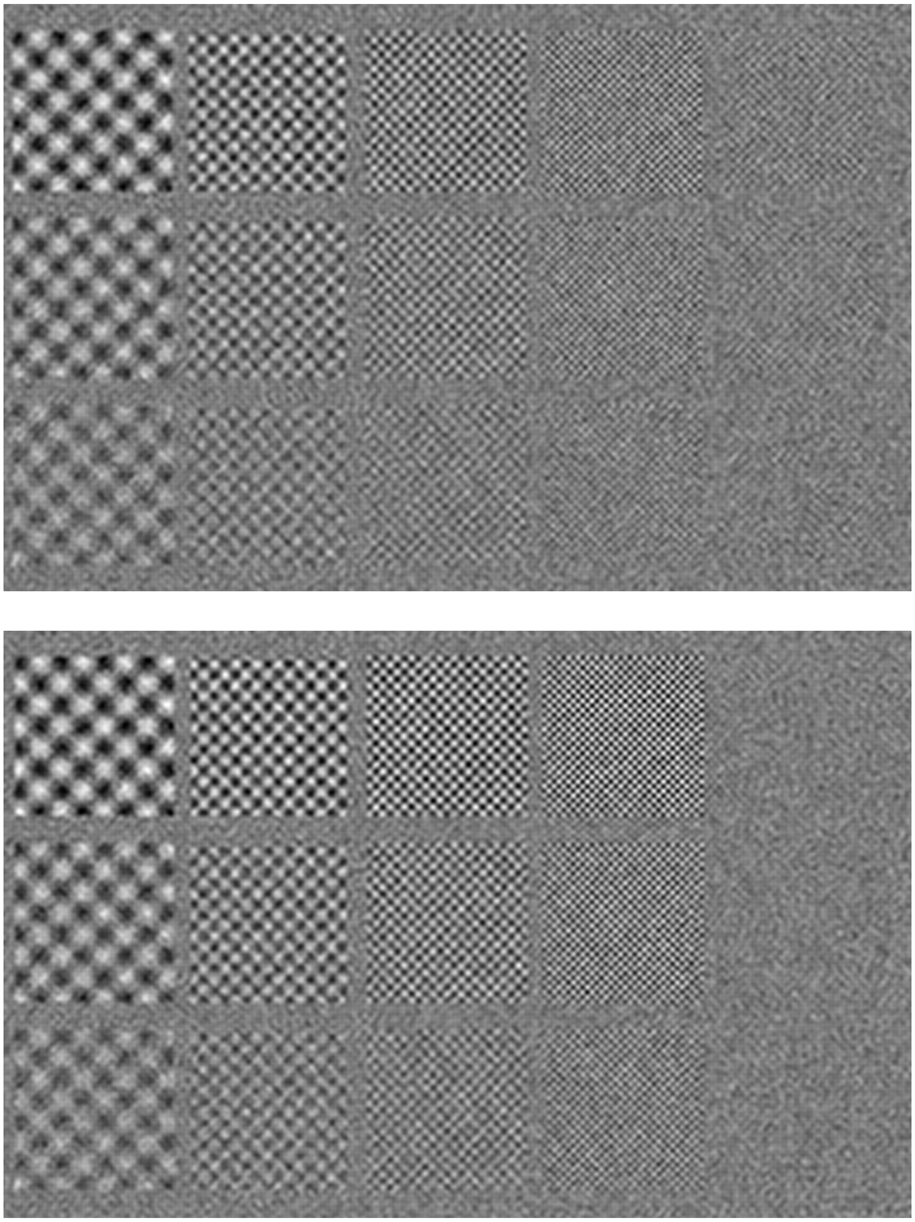

Figure 2.4: Simulated sinusoidal pattern images with frequencies 1.0, 1.5, 2.0 2.4 and 3.0 cycles/mm illustrating the visual difference in conventional (upper) and AAP (lower) images ($\epsilon = 0.05\,\mathrm{mm}$, $a = 0.2\,\mathrm{mm}$, $u_c = 2.5$ cycles/mm). Noise has a similar appearance in conventional and AAP images. The conventional image shows decreasing contrast with increasing frequency as expected in the first four columns and aliased pattern in the fifth (which is above the sampling cut-off frequency). The AAP image shows less change in contrast with increasing frequency in the first four columns and no (aliased) pattern in the fifth. Images are sinc interpolated (4× oversampling) for display purposes and best viewed on high-resolution display.

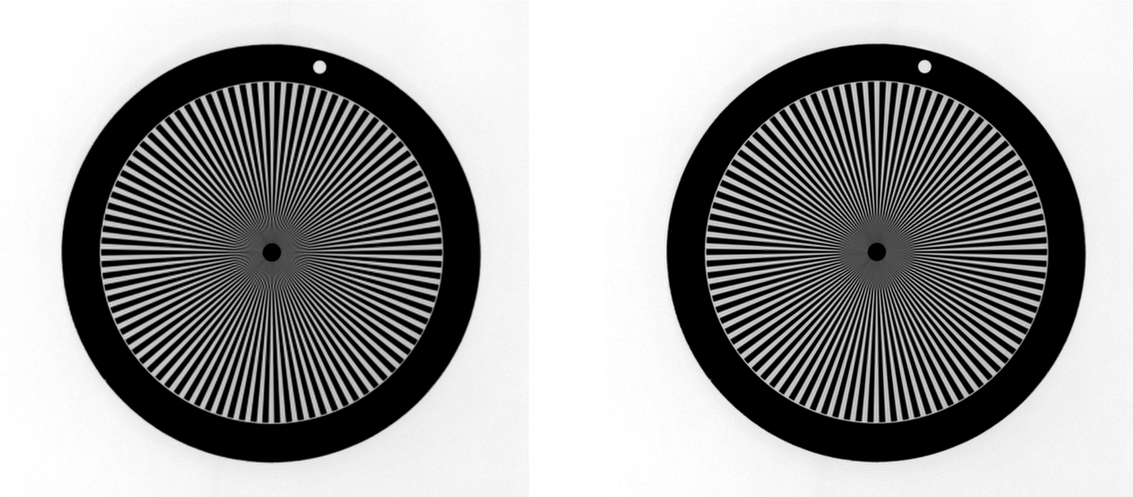

Figure 2.5: Conventional (left) and AAP (right) images of a star-pattern acquired with a clinical mammography Se detector. The image pixel size is 4x the detector element size and the image sampling cut-off frequency is 1.8 cycles/mm (red circle). In the conventional image there are aliasing artifacts (Moiré pattern) at high frequencies near the center of the pattern. The AAP image shows suppression of the Moiré pattern and increased contrast of the bar patterns at higher frequencies.

high frequencies, and removal of aliasing artifacts.

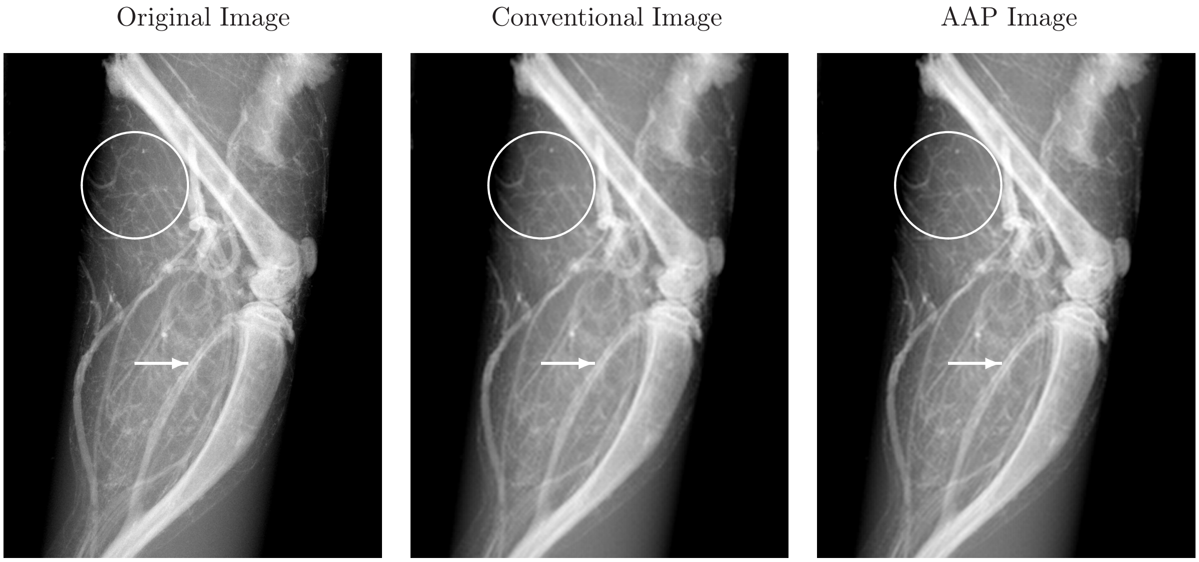

Figure 2.6: Comparison of conventional and AAP images of a contrasted rat leg. The original image (left) was acquired with $a-$Se detector and used to synthesize conventional (middle) and AAP (right) images. The AAP image has sharper bone edges (white arrow), finer detail of vasculature (white circle) and more accurately shows original image features.

The AAP image of the biological specimen in Fig. 2.6 shows sharper bone edges (white arrow) and finer vasculature detail (white circle) than the conventional image. This is due to improved high-frequency response with the AAP approach. The AAP image preserves high-frequency content up to the cut-off frequency while the conventional image appears blurred. Also, the AAP image has no visible ringing. Both conventional and AAP images were sinc interpolated (4 x oversampling) to ensure all three images have the same number of pixels in the publication to allow for direct comparison.

2.4.3 Experimental MTF and DQE

2.4.3.1 CMOS/CSI Detector

The experimental presampling MTF, normalized NPS, and DQE curves obtained with the CMOS/CsI detector are shown in Fig. 2.7, comparing conventional (binned) and AAP methods. This detector has extremely low readout noise. The measured normalized readout NPS for both conventional and AAP methods was approximately 0.003 over all frequencies which is considered negligible compared to the total NPS as shown. Optical scatter in the CsI converter layer reduces spatial resolution and hence the measured MTF decreases with frequency more quickly than the theoretical model of Eq. (2.15) which does not include a converter. The AAP MTF shows a modest improvement only, still consistent with the expected 53% increase, and the low-pass characteristic of the AAP method as frequencies above $u_c = 0.5/a$ are suppressed. The CsI converter also suppresses high-frequency noise, and hence there is less noise aliasing than predicted by the theoretical model. As a consequence, while the DQE is still improved by a factor of two (from 0.2 to 0.4) near the cut-off frequency, it is less than what is predicted by Eq. 2.24.

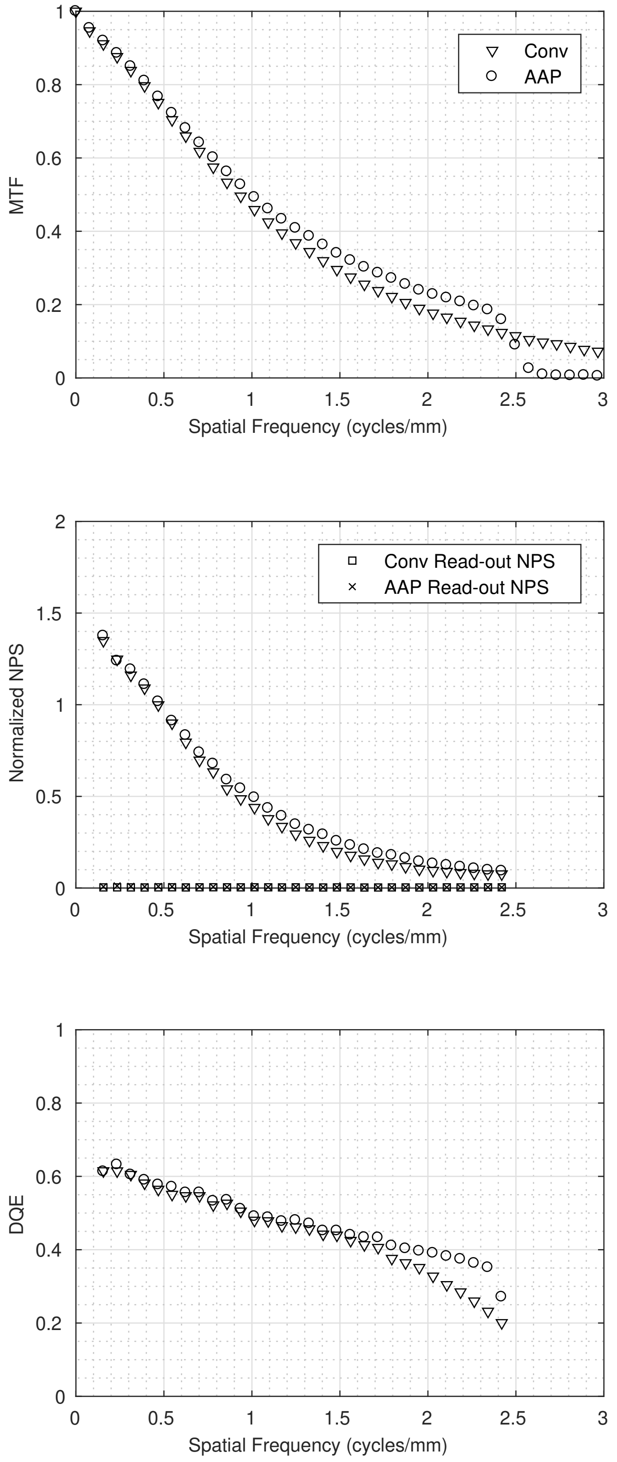

Figure 2.7: Presampling MTF, normalized NPS and DQE curves obtained with the CMOS/CsI detector comparing conventional (binned) and AAP approaches. While these results demonstrate an increase in high spatial frequency DQE, the improvement is not as great as predicted by the CSA model due to resolution limitations of the CsI.

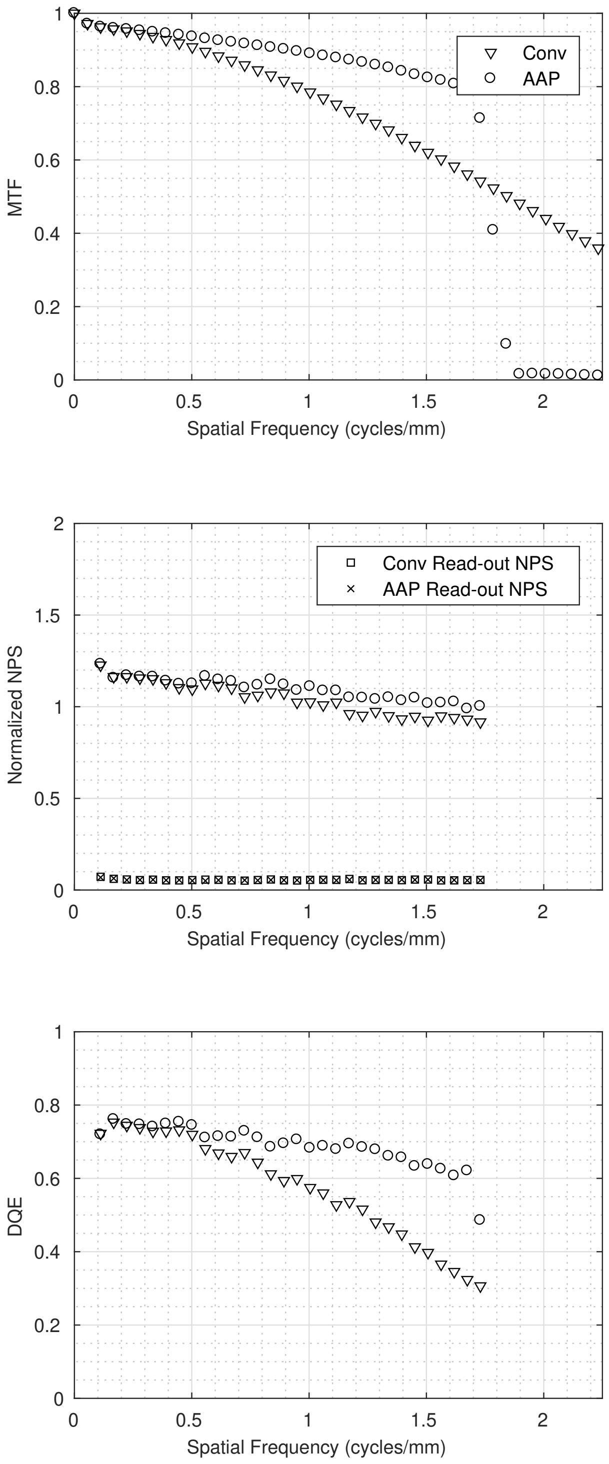

Figure 2.8: Measured presampling MTF, normalized NPS, and DQE curves from an $a-$Se detector in which 0.28 mm (a) pixels are synthesized from 0.07 mm (ϵ) sensors, comparing conventional (binned) pixels of the same size with the AAP approach.

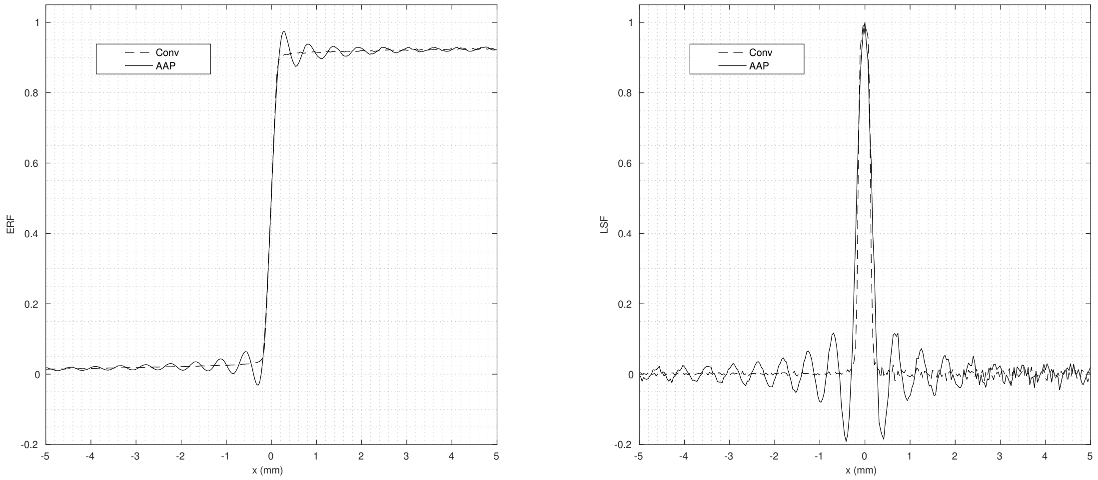

Figure 2.9: Edge-response function (ERF) and line-spread function (LSF) measured with $a-$Se detector comparing conventional and AAP designs. The AAP profiles show the Gibbs ringing phenomenon due to sharp truncation of frequencies. Oscillations in both AAP profiles have zero-crossings with exactly one pixel spacing apart (0.28 mm).

2.4.3.2 Se Detector

Results obtained with the Se detector are closer to the theoretical prediction as the Se converter layer results in very little loss of spatial resolution [28]. Figure 2.8 shows measured presampling MTF, normalized NPS, and DQE curves comparing conventional (binned) and AAP methods using the Se detector. The conventional MTF is similar to the theoretical curve of Eq. (2.15) and the AAP MTF is closer to Eq. (2.22) including the low-pass cut-off frequency of $u_c = 0.5/a \approx 1.8$ cycles/mm. Readout noise is negligible compared to the total image noise as shown and the NPS is relatively flat for both conventional and AAP images. The DQE near u_c is approximately doubled from 0.3 to 0.6, resulting in a DQE that is less dependent of frequency up to the sampling cutoff frequency.

The AAP response in the spatial domain is shown in the edge-response function (ERF), and its derivative the line-spread function (LSF), in Fig. 9 for both conventional and AAP approaches. The AAP curves, particularly the LSF, shows Gibbs ringing due to our use of a rectangular filter with sharp truncation in the frequency domain.

2.5 Discussion

The approach described in this work is the first description of how high-frequency DQE values can be increased by reducing spectral aliasing without simply suppressing content at frequencies where aliasing may occur. Spectral aliasing can be the primary cause of DQE degradation at high frequencies for Se-based detectors and for CsI-based detectors at x-ray energies below the K-edge energies of Cs and I (∼33 keV). The AAP method improves both the MTF and DQE, but may be less effective when other factors such as additive detector noise, secondary quantum sinks[7] or scatter reabsorption[11] are the main cause of SNR degradation. Spatial-resolution limitations of the converter material explains the underwhelming improvement in DQE of the CMOS/CsI detector shown here, and illustrates the need for very high resolution converter materials to make this successful. For example, a Se/CMOS combination may be near optimal [20, 21, 22]. Also, the sharp low-pass filter used in this demonstration results in slight Gibbs ringing around edges, as shown in the edge-response function and the star-pattern image. This can likely be reduced with a less-abrupt filter cutoff, but maybe at the expense of a reduced benefit on the MTF and DQE. Filters with a sharp-cutoff in the frequency domain result in a detector impulse response that is not "local", such as off-center oscillations in the spatial domain as shown in the AAP line-spread function. This could potentially result in visible ringing artifacts near sharp-edges, but it preserves image contrast and improves visibility of features in noise-limited low-contrast regions.

Conventional and AAP approaches would have the same DQE if aliasing did not occur, but images from conventional high-resolution converter layer detectors usually have noise aliasing. Removing noise aliasing improves high-frequency DQE and provides greater visibility of high-frequency features present in noise-limited low-contrast regions as shown in Fig. 2.4. For images that are not noise-limited, modest contrast improvement is expected from MTF improvement at high-frequencies with the AAP approach as observed in Fig. 2.6. This proof-of-concept experiment demonstrates sharper edges and finer detail in AAP images, even though the image is contrast-limited so we only expect a 50% improvement at high frequencies. Greater improvement in visibility of high-frequency content in noise-limited regions is expected.

We view the AAP approach as having a role to play on detectors having substantial computational ability and where sensor elements can be manufactured smaller than what might be of practical value for clinical imaging. For example, the high-frequencies available with full-size detectors having 0.025 mm sensors (20 cycles/mm) may have no direct clinical value, and the resulting file sizes ($\approx$ 1 TByte) may be too large for practical display, transmission and storage at present. The AAP method may provide an architectural approach in which image pixels are separated from physical sensor elements. On CMOS and other new detector designs with very small sensors this may be a way to improve the DQE at frequencies of practical importance. The synthesis of larger pixel values could take place in real time, directly on the detector, eliminating the need for very high data-transfer bandwidths in the readout systems. As illustrated here, the AAP approach may be useful for CMOS/CsI systems, but would likely have a greater impact on CMOS/Se or related technologies having very high resolution converter layers that are currently under development.[20, 22] Development of x-ray sensors with micro-element sizes for clinical use requires a converter layer that achieves a desirable quantum detective efficiency without reducing spatial resolution. The low noise performance of CMOS sensor arrays might best satisfy the read-out noise requirement for AAP implementation due to reduced signal strength in each sensor and the need for multiple readouts per image pixel.

2.6 Conclusion

A method is described in which high-frequency MTF and DQE performance of x-ray detectors can be improved through the use of detectors with physical sensor elements that are smaller than the desired image pixels. It is shown theoretically that the method works by preserving the superior aperture MTF of the smaller physical sensor elements and reducing noise aliasing by implementing a low-pass filter that eliminates frequencies above the image sampling cut-off frequency $u_c = 0.5/a$ where a is the image pixel size. This has the additional benefit of removing signal aliasing from the image. The result is a potential 53% increase in the MTF and more than a doubling of the DQE at the sampling cut-off frequency when used with a high-resolution converter layer.

Bibliography

[1] E. J. Hall and D. J. Brenner, "Cancer risks from diagnostic radiology," *Br. J. Radiol.*, vol. 81, pp. 362–78, May 2008.

[2] A. Berrington de Gonzalez and S. Darby, "Risk of cancer from diagnostic x-rays: estimates for the UK and 14 other countries," *Lancet*, vol. 363, pp. 345–51, Jan 2004.

[3] R. Shaw, "The equivalent quantum efficiency of the photographic process," *J. Photogr. Sc.*, vol. 11, pp. 199–204, 1963.

[4] "Medical Imaging - The Assessment of Image Quality," ICRU 54, International Commission of Radiation Units and Measurements, 1996.

[5] I. A. Cunningham and R. Shaw, "Signal-to-noise optimization of medical imaging systems," *J. Opt. Soc. Am. A.*, vol. 16, no. 3, pp. 621–32, 1999.

[6] A. M. Chiarelli, S. A. Edwards, M. V. Prummel, D. Muradali, V. Majpruz, S. J. Done, P. Brown, R. S. Shumak, and M. J. Yaffe, "Digital compared with screen-film mammography: Performance measures in concurrent cohorts within an organized breast screening program," *Radiology*, vol. 268, pp. 684–93, Sep 2013.

[7] I. A. Cunningham, M. S. Westmore, and A. Fenster, "A spatial-frequency dependent quantum accounting diagram and detective quantum efficiency model of signal and noise propagation in cascaded imaging systems.," *Med. Phys.*, vol. 21, no. 3, pp. 417–427, 1994.

[8] I. A. Cunningham, "Degradation of the detective quantum efficiency due to a non-unity detector fill factor," *Proc. SPIE*, vol. 3032, pp. 22–31, May 1997.

[9] I. Cunningham, *Handbook of Medical Imaging, Volume 1. Physics and Psychophysics, Chapter 2.* SPIE Press, 2002.

[10] G. Hajdok, J. Yao, J. J. Battista, and I. A. Cunningham, "Signal and noise transfer properties of photoelectric interactions in diagnostic x-ray imaging detectors.," *Med. Phys.*, vol. 33, no. 10, pp. 3601–20, 2006.

[11] G. Hajdok, J. J. Battista, and I. A. Cunningham, "Fundamental x-ray interaction limits in diagnostic imaging detectors: frequency-dependent Swank noise," *Med. Phys.*, vol. 35, no. 7, pp. 3194–204, 2008.

[12] S. Yun, J. Tanguay, H. K. Kim, and I. A. Cunningham, "Cascaded-systems analyses and the detective quantum efficiency of single-z x-ray detectors including photoelectric, coherent and incoherent interactions," *Med. Phys.*, vol. 40, no. 4, 2013.

[13] W. Z. Zhao and J. A. Rowlands, "Digital radiology using active matrix readout of amorphous selenium: Theoretical analysis of detective quantum efficiency," *Med. Phys.*, vol. 24, pp. 1819–33, December 1997.

[14] I. A. Cunningham, J. Yao, and V. Subotic, "Cascaded Models and the DQE of Flat-Panel Imagers: Noise Aliasing, Secondary Quantum Noise and Reabsorption," *Proc. SPIE*, vol. 4682, pp. 61–72, 2002.

[15] W. G. Ji, W. Zhao, and J. A. Rowlands, "Digital x-ray imaging using amorphous selenium: Reduction of aliasing," *Med. Phys.*, vol. 25, pp. 2148–62, November 1998.

[16] J. A. Rowlands, W. G. Ji, W. Zhao, and D. L. Lee, "Direct-conversion flat panel x-ray imaging: reduction of noise by presampling filtration," *Proc. SPIE*, vol. 446, 2000.

[17] W. Zhao, W. G. Ji, A. Debrie, and J. A. Rowlands, "Imaging performance of amorphous selenium based flat-panel detectors for digital mammography: Characterization of a small area prototye detector," *Med. Phys.*, vol. 30, no. 2, pp. 254–263, 2003.

[18] E. Ismailova, K. Karim, and I. A. Cunningham, "Apodized-aperture pixel design to increase high-frequency DQE and reduce noise aliasing in x-ray detectors," *Proc. SPIE*, vol. 9412, May 2015.

[19] T. Nano, T. Escartin, K. Karim, and I. A. Cunningham, "A novel x-ray detector design with higher DQE and reduce aliasing: Theoretical analysis of x-ray reabsorption in detector converter material," *Proc. SPIE*, vol. 9783, 2016.

[20] S. Abbaszadeh, N. Allec, and K. S. Karim, "Improving amorphous selenium photodetector performance using an organic semiconductor," *Key Eng. Mat.*, vol. 543, pp. 451–54, 2013.

[21] Y. Fang, A. Badal, A. Badano, and K. S. Karim, "Spatial resolution characteristics of a-Se imaging detectors using spatiotemporal Monte Carlo methods with detailed transport of x rays, electrons and electron-hole pairs under applied bias," *Proc. SPIE*, vol. 8668, 2013.

[22] C. C. Scott, S. Abbaszadeh, S. Ghanbarzadeh, G. Allan, M. Farrier, I. A. Cunningham, and K. S. Karim, "Amorphous selenium direct detection CMOS digital x-ray imager with 25 micron pixel pitch," *Proc. SPIE*, 2014.

[23] D. L. Snyder and M. I. Miller, *Random Point Processes in Time and Space.* New York: Springer-Verlag, 1991.

[24] H. H. Barrett and W. Swindell, *Radiological Imaging: The Theory of Image Formation, Detection, and Processing.* Academic Press, 1996.

[25] H. H. Barrett and K. J. Myers, *Foundations of Image Science.* New Jersey: John Wiley & Sons, Inc., 2004. Chapter 11, pg. 651-655.

[26] A. Papoulis, *Systems and Transforms with Application in Optics.* McGraw-Hill Book Company, 1968.

[27] "Medical electrical equipment - characteristics of digital x-ray imaging devimaging Part 1-1: Determination of the detective quantum efficiency - Detectors used in radiographic imaging," Medical Electrical Equipment IEC 62220-1-1, International Electrotechnical Commission, 2015.

[28] G. Hajdok, J. J. Battista, and I. A. Cunningham, "Fundamental x-ray interaction limits in diagnostic imaging detectors: spatial resolution," *Med. Phys.*, vol. 35, no. 7, pp. 3180–93, 2008.

Chapter 3

Impact of x-ray reabsorption and converter blur on MTF and DQE improvements using the apodized-aperture pixel (AAP) x-ray detector design

We investigate converter blur and x-ray reabsorption with the AAP x-ray detector design. A ceasium-iodide detector was used to measure DQE of synthesized conventional and AAP images for cases with and without x-ray reabsorption and converter blur. It is shown that reabsorption and converter blur do not effect MTF improvement with the AAP design (1.5× greater MTF near the image cut-off frequency u_c) whereas DQE improvements depend on noise aliasing. Converter blur reduces noise aliasing with the consequence of also reducing MTF, and therefore reduces the improvement with the AAP design to 1-2.5× depending on the blur.

The contents of this chapter are submitted to the journal of Physics in Medicine and Biology: TF Nano, KS Karim and IA Cunningham.

3.1 Introduction

The need to produce high-quality images using low radiation exposures motivates the development of new detector designs that give the best possible image quality for a given patient exposure. The detective quantum efficiency (DQE) describes image signal-to-noise ratio (SNR) for a specified number of x-ray quanta incident on the detector,[1, 2] and is a surrogate for the "dose efficiency" of a detector. High DQE is particularly important in applications such as mammography screening programs where a large assumed-healthy population is exposed to radiation and increased image SNR is known to improve cancer detection rates.[3, 4]

Most detector designs use either a scintillator (eg. CsI or Gd_2O_2S) or photoconductor (eg. Se) to convert x-ray energy into optical quanta or liberate charges, coupled to a sensor array, with each sensor element corresponding to an image pixel. We recently described an "apodized-aperture pixel" (AAP) design that uses very small sensor elements to synthesize pixels of a desired size using a weighted combination of signals from these "micro elements".[5, 6, 7] With a sufficiently high resolution converter, this approach preserves the broad spectral shape of the aperture modulation transfer function (MTF) corresponding to the micro elements while eliminating signal and noise aliasing, resulting in a $\sim$40% increase in MTF and more than doubling of DQE values at the image sampling cut-off frequency.[5, 6, 7] This approach can be implemented using a sensor array such as CMOS, which can have very low noise and small sensor elements, coupled to a high-resolution converter layer such as selenium.[8, 9, 10] The AAP design takes advantage of some benefits of using very small sensor elements (7.8 μm in our lab prototype) without the associated large image files (one 24×30 cm mammography image would be 2.3 GB)

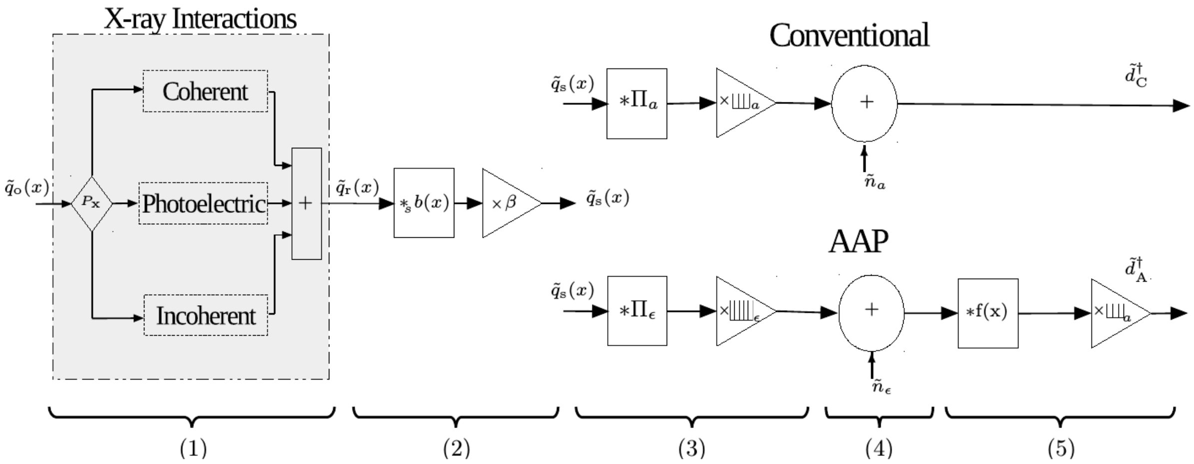

Figure 3.1: Illustration of the simple-atom CSA model for conventional and AAP designs. The model input $\tilde{q}_o$ is a random point distribution representing x-ray quanta incident on the detector. Outputs $\tilde{d}^{\dagger}_{C}$ and $\tilde{d}^{\dagger}_{A}$ consist of uniformly-spaced δ-functions scaled by discrete output signals from conventional and AAP detectors respectively. The distribution of secondary quanta after reabsorption and converter blur is $\tilde{q}_s$ and $\tilde{n}$ is readout noise in the output signal.

where such file sizes would be too large to handle and display with a busy conventional PACS system, or where there may be negligible diagnostic value gained from higher resolution.

Our previous work[7] assumed an ideal x-ray detector where each element is an ideal photon-counting sensor. That work is generalized here to accommodate the random processes of energy deposition from photoelectric interactions, Compton scatter and coherent scatter, including the resulting noise correlations and converter blur. We develop, and experimentally validate, a cascaded systems analysis (CSA) of signal and noise transfer to determine conditions for which the AAP design will improve the MTF and DQE.

3.2 Methods

3.2.1 CSA model of the AAP design with reabsorption and blur

A cascaded-systems analysis is used to characterize signal and noise transfer in the conversion of incident x-ray quanta to secondary quanta liberated in a converter layer and collected in a sensor array. With reference to Fig. 3.1, the input $\tilde{\mathrm{q}}_{\mathrm{o}}(x)$ is a random point distribution describing x-ray quanta incident on the detector, with each quantum represented as a Dirac δ function:[11]

$$\tilde{\mathrm{q}}_{\mathrm{o}}(x) = \sum_{i=1}^{\tilde{\mathrm{N}}} \delta(x - \tilde{x}_i), \tag{3.1}$$

where $\tilde{x}_i$ is the random location of the ith of $\tilde{\mathrm{N}}$ photons. We use one-dimensional expressions for simplicity but results are easily generalized to two-dimensional space, and a notation where overhead ˜ indicates a random variable or function.

3.2.1.1 X-ray interactions in converter layer and detector signal

The model consists of five steps. Step 1 describes conversion of incident x-ray quanta $\tilde{\mathrm{q}}_{\mathrm{o}}(x)$ to secondary quanta $\tilde{\mathrm{q}}_{\mathrm{r}}(x)$ (light quanta generated in a scintillator or charges liberated in a photoconductor) where selection between interaction types is determined by x-ray interaction coefficients and described as a random branch point[12, 13] with probabilities P_{x} where x indicates interaction type.[14] A single generalized "simple-atom" model with only one atomic transition (ie. K edge)[12, 15, 14] is used to accommodate photoelectric, coherent and incoherent interactions including the effect of emission and scatter photon reabsorption.[16, 17, 18]

Step 2 describes converter blur caused by random relocation of secondary quanta, such as optical scatter, by the scatter operator $*_s$ and scatter point spread function $b(x)$,[19, 20, 21] followed by a random selection with probability β to identify secondary quanta that are coupled and detected in the sensor array to generate $\tilde{\mathrm{q}}_{\mathrm{s}}(x)$, a distribution of interacting secondary quanta. Step 3 describes collection of secondary quanta by ideal sensor elements as a convolution with the (reversed[21]) aperture function for both conventional and AAP detectors, followed by multiplication by a train of Dirac δ functions at uniform spacings $\text{III}(x/x_a)$ or $\text{III}(x/x_\epsilon)$. Step 4 describes detector additive electronic

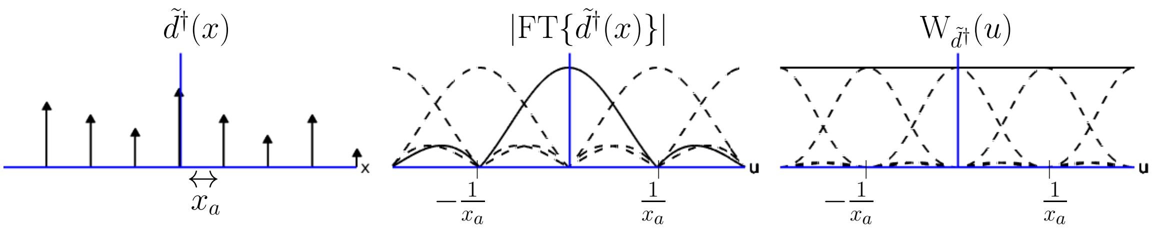

Figure 3.2: Illustration of detector output expressed as $\tilde{\mathrm{d}}^\dagger(x)$, a sequence of scaled δ functions on spacings x_a, in the spatial domain, spatial-frequency domain (solid line showing fundamental), and corresponding Wiener NPS (solid line showing sum of all aliases).

noise as addition of a discrete zero-mean Gaussian random variable $\tilde{\mathrm{n}}_a$ or $\tilde{\mathrm{n}}_\epsilon$ with variance σ_a^2 or σ_ϵ^2. Figure 3.2 illustrates a detector output $\tilde{d}^\dagger(x)$ expressed as a sequence of scaled δ functions on spacings x_a in the spatial domain, spatial-frequency domain, and corresponding Wiener noise-power spectrum (NPS). The AAP algorithm in step 5 requires filtering with the kernel $\mathrm{f}(x)$ and sub-sampling on spacings x_a to produce an output consisting of a sequence of δ-functions scaled by discrete detector output values. Details of the AAP method have been described previously.[7] Superscript † indicates a discrete output consisting of a sequence of scaled δ functions on uniform spacings and subscripts C and A indicate conventional and AAP detectors. Important signal and noise transfer properties of the secondary quanta distribution $\tilde{\mathrm{q}}_s(x)$ are summarized in App. 3.7.1 in terms of the optical transfer function (OTF) $\mathrm{T_s}(u)$ and Wiener NPS $\mathrm{W_s}(u)$.

3.2.1.2 Conventional detector

The output from the conventional detector is represented as:[7]

$$\tilde{\mathrm{d}}_{\mathrm{C}}^\dagger(x) \;=\; \sum_{i=-\infty}^{\infty} \left[\tilde{\mathrm{d}}_{a,i} + \tilde{\mathrm{n}}_{a,i}\right] \delta(x - i x_a) \tag{3.2}$$

where $\tilde{\mathrm{d}}_{a,i} = \tilde{\mathrm{d}}_a(x)\Big|_{x=ix_a} = k_{\mathrm{C}}\tilde{\mathrm{q}}_{\mathrm{s}}(x) * \prod(x/a)\Big|_{x=ix_a}$ and $\tilde{\mathrm{d}}_a(x)$ is the conventional detector presampling signal. While the presampling signal is not physical, it is a convenient construct that, when evaluated at element centers, gives the x-ray contribution to element signals (excluding electronic noise in this case). Detector gain k_{C} relates the sensor element signal to the number of interacting secondary quanta. Mean detector output is $\bar{d}_a = k_{\mathrm{C}}\bar{q}_s a \mathrm{T}_a(0) = k_{\mathrm{C}}\bar{q}_{\mathrm{s}} a$, where $\mathrm{T}_a(u) = \mathrm{sinc}(au)$ is the aperture OTF of the sensors, and the detector presampling OTF is therefore $\mathrm{T}_{\mathrm{C}}(u) = \mathrm{T}_{\mathrm{s}}(u)\mathrm{T}_a(u)$, where $\mathrm{T}_{\mathrm{s}}(u)$ is the OTF associated with conversion from incident x-ray quanta to interacting secondary quanta described in App. 3.7.1. The frequency response of the conventional detector is therefore given by:

$$\mathrm{T}_{\mathrm{C}^\dagger}(u) = \underbrace{\mathrm{T}_{\mathrm{s}}(u)\,\mathrm{T}_a(u)}_{\text{fundamental}} + \underbrace{\sum_{j=1}^{\infty} \mathrm{T}_{\mathrm{s}}\left(u \pm \frac{j}{x_a}\right) \mathrm{T}_a\left(u \pm \frac{j}{x_a}\right)}_{\text{aliases at spacings } 1/x_a} \tag{3.3}$$

and the NPS by:

$$\mathrm{W}_{\mathrm{C}^\dagger}(u) = \underbrace{k_{\mathrm{C}}^2 \frac{a^2}{x_a^2} \mathrm{W}_{\mathrm{s}}(u) \left|\mathrm{T}_a(u)\right|^2}_{\text{fundamental}} + \underbrace{k_{\mathrm{C}}^2 \frac{a^2}{x_a^2} \sum_{j=1}^{\infty} \mathrm{W}_{\mathrm{s}}\left(u \pm \frac{j}{x_a}\right) \left|\mathrm{T}_a\left(u \pm \frac{j}{x_a}\right)\right|^2}_{\text{aliases at spacings } 1/x_a} + \underbrace{\frac{a}{x_a^2}\sigma_a^2}_{\text{readout noise}}, \tag{3.4}$$

where $\mathrm{W}_{\mathrm{s}}(u)$ is the secondary quanta NPS described in Appendix 3.7.1.

3.2.1.3 AAP detector

Analogous to above, output from the AAP detector is also discrete on spacings x_a:[7]

$$\tilde{\mathrm{d}}_{\mathrm{A}}^\dagger(x) = \sum_{i=-\infty}^{\infty} \left[\tilde{\mathrm{d}}_{\mathrm{f},i} + \tilde{\mathrm{n}}_{\mathrm{f},i}\right] \delta(x - ix_a) \tag{3.5}$$

where the discrete values $\tilde{\mathrm{d}}_{\mathrm{f},i} = \left\{k_{\mathrm{A}}\left[\tilde{\mathrm{q}}_s(x) * \prod(x/\epsilon)\right] \times \sum_i \delta(x - ix_\epsilon)\right\} * \mathrm{f}(x)\Big|_{x=ix_a}$ are based on micro elements of size ϵ and spacing x_ϵ, filtered with $\mathrm{f}(x)$, and resampled on spacings x_a. Readout noise, which is also filtered by $\mathrm{f}(x)$, contributes values $\tilde{\mathrm{n}}_{\mathrm{f},i} = \{\sum_i \tilde{\mathrm{n}}_{\epsilon,i}\delta(x - ix_\epsilon)\} * \mathrm{f}(x)\big|_{x=ix_a}$ to the output.

Mean AAP detector output is $\bar{d}_{\mathrm{f}} = k_{\mathrm{A}}\bar{q}_{\mathrm{s}}\frac{\epsilon}{x_\epsilon}\mathrm{F}(0)$ where $\mathrm{F}(u)$ is the Fourier transform of $\mathrm{f}(x)$. The AAP method produces the same signal as the conventional detector when $\mathrm{f}(x)$

is chosen to sum micro elements over distance x_a. In that case, $\mathrm{f}(x)$ is a rectangle with width x_a and unity height, giving $\mathrm{F}(0) = x_a$ and average output $\bar{d}_{\mathrm{f}} = k_{\mathrm{A}}\bar{q}_{\mathrm{s}}\frac{\epsilon}{x_\epsilon}x_a$. In the following, the filter is described as $\mathrm{F}(u) = x_a\mathrm{T}_{\mathrm{f}}(u)$ where $\mathrm{T}_{\mathrm{f}}(u)$ is normalized to unity at $u = 0$.

As shown in Sec. 3.7.2, the DQE is optimized when a low-pass filter satisfying $\mathrm{T}_{\mathrm{f}}(u) = \mathrm{T}_{\mathrm{f}}(u)\Pi(x_a u)$ is used so that frequencies above the sampling cut-off frequency $u_c = {}^1\!/_{2x_a}$ are suppressed, eliminating noise aliasing and resulting in:

$$\mathrm{T}_{\mathrm{A}^\dagger}(u) = \underbrace{\mathrm{T}_{\mathrm{s}}(u)\mathrm{T}_\epsilon(u)\mathrm{T}_{\mathrm{f}}(u)}_{\mathrm{band-limited\ fundamental}} + \underbrace{\sum_{j=1}^{\infty}\mathrm{T}_{\mathrm{s}}\left(u \pm \frac{j}{x_\epsilon}\right)\mathrm{T}_\epsilon\left(u \pm \frac{j}{x_\epsilon}\right)\mathrm{T}_{\mathrm{f}}(u)}_{\mathrm{band-limited\ micro-element\ aliases\ at\ spacings\ {}^1\!/x_\epsilon}}\ . \tag{3.6}$$

The NPS of $\tilde{\mathrm{d}}_{\mathrm{A}}^\dagger$ is given by:

$$\begin{aligned}\mathrm{W}_{\mathrm{A}^\dagger}(u) \quad &= \quad \underbrace{k_{\mathrm{A}}^2\frac{\epsilon^2}{x_\epsilon^2}\mathrm{W}_{\mathrm{s}}(u)\left|\mathrm{T}_\epsilon(u)\right|^2\left|\mathrm{T}_{\mathrm{f}}(u)\right|^2}_{\mathrm{band-limited\ fundamental}} \\ &+ \quad \underbrace{k_{\mathrm{A}}^2\frac{\epsilon^2}{x_\epsilon^2}\sum_{j=1}^{\infty}\mathrm{W}_{\mathrm{s}}\left(u \pm \frac{j}{x_\epsilon}\right)\left|\mathrm{T}_\epsilon\left(u \pm \frac{j}{x_\epsilon}\right)\right|^2\left|\mathrm{T}_{\mathrm{f}}(u)\right|^2}_{\mathrm{band-limited\ micro-element\ aliases\ at\ spacings\ {}^1\!/x_\epsilon}} + \underbrace{\frac{\epsilon}{x_\epsilon^2}\sigma_\epsilon^2\left|\mathrm{T}_{\mathrm{f}}(u)\right|^2}_{\mathrm{band-limited\ readout\ noise}}\end{aligned} \tag{3.7}$$

3.2.2 MTF, NPS and DQE

3.2.2.1 Conventional detector

The conventional detector presampling MTF is given by

$$\mathrm{MTF}_{\mathrm{C}}(u) \quad = \quad \left|\mathrm{T}_{\mathrm{s}}(u)\mathrm{T}_a(u)\right| \tag{3.8}$$

and normalized NPS (NNPS), $\frac{\bar{q}_{\mathrm{o}}}{\bar{d}_a^2}x_a^2\mathrm{W}_{\mathrm{C}^\dagger}(u)$ where $\mathrm{W}_{\mathrm{s}}^{(n)}(u) = \frac{1}{\bar{q}_{\mathrm{o}}\bar{g}_{\mathrm{s}}^2}\mathrm{W}_{\mathrm{s}}(u)$, by:

$$\mathrm{W}_{\mathrm{C}^\dagger}^{(n)}(u) \quad = \quad \underbrace{\mathrm{W}_{\mathrm{s}}^{(n)}(u)\left|\mathrm{T}_a(u)\right|^2}_{\mathrm{normalized\ fundamental}} + \underbrace{\sum_{j=1}^{\infty}\mathrm{W}_{\mathrm{s}}^{(n)}\left(u \pm \frac{j}{x_a}\right)\left|\mathrm{T}_a\left(u \pm \frac{j}{x_a}\right)\right|^2}_{\mathrm{normalized\ aliases\ at\ spacings\ {}^1\!/x_a}} + \underbrace{\frac{1}{\bar{q}_{\mathrm{o}}\bar{g}_{\mathrm{s}}^2k_{\mathrm{C}}^2a}}_{\mathrm{normalized\ readout\ noise}}\sigma_a^2 \tag{3.9}$$

where $\bar{g}_\mathrm{s} = \bar{q}_\mathrm{s}/\bar{q}_\mathrm{o}$ is the number of secondary quanta collected in the sensor elements per incident x-ray photon. This normalization is convenient as the NNPS of an ideal photon-counting detector is unity and the inverse of the zero-frequency value is therefore equal to the quantum efficiency. The DQE of a conventional detector, $\mathrm{MTF}_\mathrm{C}^2(u)/\mathrm{W}_{C^\dagger}^{(n)}(u)$ is therefore given by:

$$\mathrm{DQE}_\mathrm{C}(u) = \frac{\left|\mathrm{T_s}(u)\mathrm{T}_a(u)\right|^2}{\mathrm{W}_\mathrm{s}^{(n)}(u)\left|\mathrm{T}_a(u)\right|^2 + \sum_{j=1}^{\infty}\mathrm{W}_\mathrm{s}^{(n)}\left(u \pm \frac{j}{x_a}\right)\left|\mathrm{T}_a\left(u \pm \frac{j}{x_a}\right)\right|^2 + \frac{1}{\bar{q}_\mathrm{o}\bar{g}_\mathrm{s}^2 k_\mathrm{C}^2 a}\sigma_a^2}. \tag{3.10}$$

3.2.2.2 AAP detector

The presampling MTF of the AAP detector is given by:

$$\mathrm{MTF_A}(u) = \left|\mathrm{T_s}(u)\mathrm{T}_\epsilon(u)\mathrm{T_f}(u)\right| \tag{3.11}$$

and NNPS by:

$$\begin{aligned}\mathrm{W}_\mathrm{A}^{(n)}(u) = & \underbrace{\mathrm{W}_\mathrm{s}^{(n)}(u)\left|\mathrm{T}_\epsilon(u)\right|^2\left|\mathrm{T_f}(u)\right|^2}_{\mathrm{normalized\ band-limited\ fundamental}} \\ & \underbrace{+\sum_{j=1}^{\infty}\mathrm{W}_\mathrm{s}^{(n)}\left(u \pm \frac{j}{x_\epsilon}\right)\left|\mathrm{T}_\epsilon\left(u \pm \frac{j}{x_\epsilon}\right)\right|^2\left|\mathrm{T_f}(u)\right|^2}_{\mathrm{normalized\ band-limited\ micro-element\ aliases\ at\ spacings\ ^1/x_a}} + \underbrace{\frac{1}{\bar{q}_o\bar{g}_\mathrm{s}^2 k_\mathrm{A}^2\epsilon}\sigma_\epsilon^2\left|\mathrm{T_f}(u)\right|^2}_{\mathrm{normalized\ band-limited\ readout\ noise}}\end{aligned} \tag{3.12}$$

where again $\mathrm{T_f}(u) = \mathrm{T_f}(u)\Pi(x_a u)$ is band-limited to $u = 1/2x_a$. Therefore, the DQE of the AAP detector is given by:

$$\mathrm{DQE_A}(u) = \frac{\left|\mathrm{T_s}(u)\mathrm{T}_\epsilon(u)\right|^2}{\mathrm{W}_\mathrm{s}^{(n)}(u)\left|\mathrm{T}_\epsilon(u)\right|^2 + \sum_{j=1}^{\infty}\mathrm{W}_\mathrm{s}^{(n)}\left(u \pm \frac{j}{x_\epsilon}\right)\left|\mathrm{T}_\epsilon\left(u \pm \frac{j}{x_\epsilon}\right)\right|^2 + \frac{1}{\bar{q}_o\bar{g}_\mathrm{s}^2 k_\mathrm{A}^2\epsilon}\sigma_\epsilon^2} \tag{3.13}$$

Equations (3.10) and (3.13) show that while it is important to have a low-pass AAP filter that suppresses frequencies $|u| > \frac{1}{2x_a}$, the shape of the filter in other regards affects the shape of the MTF and NPS but not the DQE. Further implications of these results are discussed below.

3.2.3 MTF and DQE change with AAP approach

Changes in MTF and DQE with the AAP approach is investigated using ratios of MTF, NPS and DQE relative to conventional. The MTF ratio is given by:

$$\frac{\mathrm{MTF_A}(u)}{\mathrm{MTF_C}(u)} = \frac{|\mathrm{T_s}(u)\mathrm{T}_\epsilon(u)\mathrm{T_f}(u)|}{|\mathrm{T_s}(u)\mathrm{T}_a(u)|} = \frac{|\mathrm{T}_\epsilon(u)|}{|\mathrm{T}_a(u)|}\,|\mathrm{T_f}(u)|\,, \tag{3.14}$$

where $\mathrm{T_s}(u) = \mathrm{T_r}(u)\mathrm{T_b}(u)$ is the product of the OTFs associated with liberation and scatter of secondary quanta (App. 3.7.1), showing the ratio depends only on sensor element OTF and AAP filter. This means that relative MTF improvement with the AAP design is independent of x-ray reabsorption and converter blur. However, absolute improvement ($\mathrm{MTF_A} - \mathrm{MTF_C}$) is proportional to $\mathrm{T_s}(u)$ and hence is substantial only with a high-resolution converter where converter blur is less than pixel width a.

The ratio of AAP to conventional NNPS is given by:

$$\frac{\mathrm{W_A^{(n)}}(u)}{\mathrm{W_C^{(n)}}(u)} \tag{3.15}$$

$$= \frac{\mathrm{W_s}(u)\left|\mathrm{T}_\epsilon(u)\right|^2\left|\mathrm{T_f}(u)\right|^2 + \sum_{j=1}^{\infty}\mathrm{W_s}\left(u \pm \frac{j}{x_\epsilon}\right)\left|\mathrm{T}_\epsilon\left(u \pm \frac{j}{x_\epsilon}\right)\right|^2\left|\mathrm{T_f}(u)\right|^2 + \frac{\sigma_\epsilon^2}{k_\mathrm{A}^2\epsilon}\left|\mathrm{T_f}(u)\right|^2}{\mathrm{W_s}(u)\left|\mathrm{T}_a(u)\right|^2 + \sum_{j=1}^{\infty}\mathrm{W_s}\left(u \pm \frac{j}{x_a}\right)\left|\mathrm{T}_a\left(u \pm \frac{j}{x_a}\right)\right|^2 + \frac{\sigma_a^2}{k_\mathrm{C}^2 a}} \tag{3.16}$$

which depends on, and is therefore affected by, both x-ray reabsorption and converter blur.

The DQE ratio of AAP to conventional is given by:

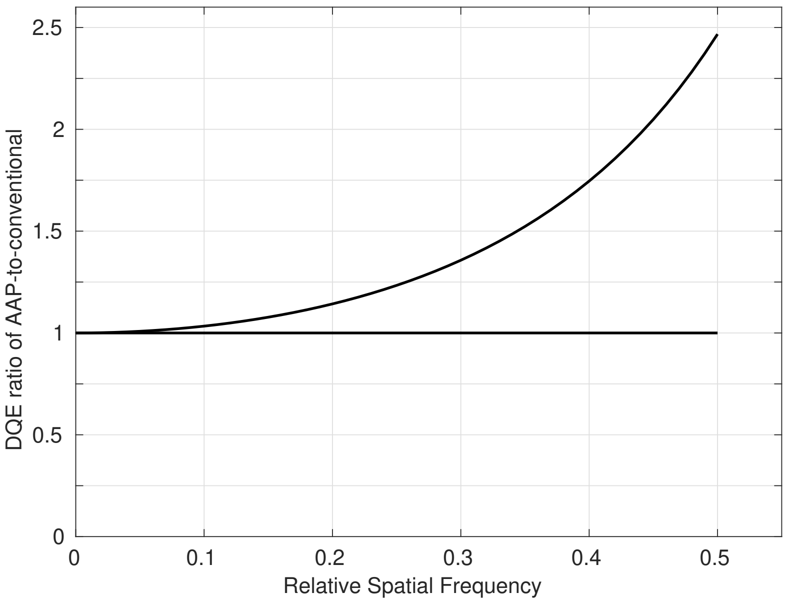

Figure 3.3: Upper limit (top curve) in DQE improvement with AAP occurs with a high-resolution converter and lower limit (bottom curve) occurs with low resolution converter than suppresses noise aliasing.

$$\frac{\mathrm{DQE_A}(u)}{\mathrm{DQE_C}(u)} = \frac{|\mathrm{T}_\epsilon(u)|^2}{|\mathrm{T}_a(u)|^2} \frac{\mathrm{W_s}(u)\,|\mathrm{T}_a(u)|^2 + \sum_{j=1}^{\infty} \mathrm{W_s}\left(u \pm \frac{j}{x_a}\right)\left|\mathrm{T}_a\left(u \pm \frac{j}{x_a}\right)\right|^2 + \frac{\sigma_a^2}{k_\mathrm{C}^2 a}}{\mathrm{W_s}(u)\,|\mathrm{T}_\epsilon(u)|^2 + \sum_{j=1}^{\infty} \mathrm{W_s}\left(u \pm \frac{j}{x_\epsilon}\right)\left|\mathrm{T}_\epsilon\left(u \pm \frac{j}{x_\epsilon}\right)\right|^2 + \frac{\sigma_\epsilon^2}{k_\mathrm{A}^2 \epsilon}} \tag{3.17}$$

As indicated in Eq. (3.17) and shown previously,[7] the AAP approach requires lower readout noise than conventional to prevent DQE loss, given by $\sigma_\epsilon^2 = \frac{k_\mathrm{A}^2}{k_\mathrm{C}^2}\frac{\epsilon}{a}\sigma_a^2$. The noise aliasing term due to micro-element sampling, $\sum_{j=1}^{\infty} \mathrm{W_s}\left(u \pm \frac{j}{x_\epsilon}\right)\left|\mathrm{T}_\epsilon\left(u \pm \frac{j}{x_\epsilon}\right)\right|^2$, degrades the DQE by less than one percent when $x_\epsilon < x_a/4$, suggesting there may be little benefit of using micro-elements that are less than a quarter of the desired pixel size, even with a high-resolution converter.

For the idealized limiting case of negligible readout noise and detectors with unity fill factor, Eq. (3.17) becomes:

$$\frac{\mathrm{DQE_A}(u)}{\mathrm{DQE_C}(u)} \simeq 1 + \frac{\sum\limits_{j=1}^{\infty} \mathrm{W_s}(u \pm \tfrac{j}{a})\, |\mathrm{sinc}(au \pm j)|^2}{\mathrm{W_s}(u)\, |\mathrm{sinc}(au)|^2}, \tag{3.18}$$

showing the AAP design improves DQE in proportion to aliased noise power present in a conventional detector having the same pixel size. Thus, impact of the AAP approach is determined only by the extent of noise aliasing, and indirectly on the effects of reabsorption and converter blur on aliasing. The ratio of AAP to conventional DQE in Eq. (3.18) has a lower (no aliasing) and upper bound (uncorrelated sensor elements) as shown in Fig. 3.3.

These model results identify noise aliasing as the primary consideration affecting AAP improvement on DQE. The conditions under which the AAP will impact on performance are therefore largely determined by converter blur spread function $b(x)$ with mean width b_o, reabsorption spread function $r(x)$ with mean width r_o, and image pixel size a, as illustrated in Fig. 3.4(a). For example, a low-resolution converter ($b_\mathrm{o} > a$) will suppress noise aliasing giving $\sum_{j=1}^{\infty} \mathrm{W_s}(u \pm \frac{j}{a})\, |\mathrm{sinc}(au \pm j)|^2 = 0$ for $|u| \leq {}^{1}/_{2x_a}$ with a unity DQE ratio. On the other hand, a high-resolution converter ($b_\mathrm{o} < a$) resulting in uncorrelated noise gives $\sum_{j=1}^{\infty} \mathrm{W_s}(u \pm \frac{j}{a})\, |\mathrm{sinc}(au \pm j)|^2 = \mathrm{W_s} \sum_{j=1}^{\infty} |\mathrm{sinc}(au \pm j)|^2 = \mathrm{W_s}(1 - |\mathrm{sinc}(au)|^2)$, and a DQE ratio equal to $1/|\mathrm{sinc}(au)|^2$. Reabsorption of scatter photons introduces correlated noise with a corresponding decrease in noise aliasing and slightly reduced DQE ratio. It is most important at energies just above the K-shell binding energy and only when the reabsorption distance is substantially greater than pixel size. These conditions are summarized in Fig. 3.4(b).

3.2.4 Experimental validation

Experimental validation of model predictions was performed by isolating the effects of scatter reabsorption and converter blur separately as described below using a CsI/CMOS-

(a)

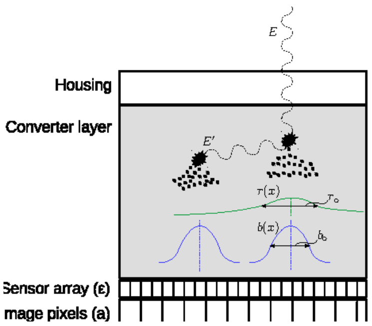

(b)

X-ray Reabsorption	Converter Blur: Without ($b_{\mathrm{o}} < a$)	Converter Blur: With ($b_{\mathrm{o}} \gg a$)
Without ($E < E_{\mathrm{K}}$ or $r_{\mathrm{o}} \ll a$)	i) +++++ eg. Se mammography	ii) +++ CsI mammography
With ($E > E_{\mathrm{K}}$ and $r_{\mathrm{o}} \geq a$)	iii) ++++ eg. CsI fluoroscopy	iv) ++ eg. CsI radiography

Figure 3.4: (a) Schematic illustration showing converter blur $b(x)$ with average width b_{o} and reabsorption spread function $r(x)$ with average width r_{o} from an interacting x-ray of energy E with scatter photon with energy E'. (b) Summary of limiting cases of converter blur, scatter reabsorption that impact on AAP performance. Plus signs indicate positive MTF and DQE improvement (with 5 signs being maximum).

based detector (Xmaru-1215CF, Vatech Inc.) having 0.0495-mm elements. We first validate the CSA model for this detector using a low and high energy x-ray beam, then we compare effects of reabsorption and converter blur on conventional and AAP performance.

3.2.4.1 CSA model validation

The CSA model describes the effect of x-ray conversion gain variability from poly-energetic x-ray spectra, x-ray reabsorption of K characteristic photons and converter blur of secondary quanta. Spectra and x-ray physics were modeled using an in-house open-source software library.[24] Known detector properties and fundamental constants are listed in Table 3.1. Converter blur $\mathrm{T_b}(u)$ was determined empirically as the ratio of the measured OTF using the low-energy beam (no reabsorption) to the theoretical $\mathrm{sinc}(au)$ aperture OTF. Two remaining unknown parameters, effective housing cover material and thickness (in mm of Al) and secondary quanta coupling efficiency β, were determined

CsI thickness, density, packing fraction	0.50 mm, 4.51 g/cm^3, 0.8	
Element size	0.0495 mm	
Relative interaction probability in CsI:	at 30 keV	at
Photoelectric	90.5 %	40 keV
Coherent	8.4 %	96.5 %
Incoherent	1.1 %	2.7 %
		0.8 %
Probability of characteristic emission, s_{pe}	0.726 [22]	
Effective work energy (keV), w	0.018 [23]	
Probability of reabsorption, $r_{\mathrm{pe}}(E)$	App. 3.7.1.	
Relocation transfer function of x-ray emission, $\mathrm{R_K}(u)$	App. 3.7.1.	

Table 3.1: Detector properties used in CSA model. Average energies of low and high energy spectra were approximately 30 and 40 keV.

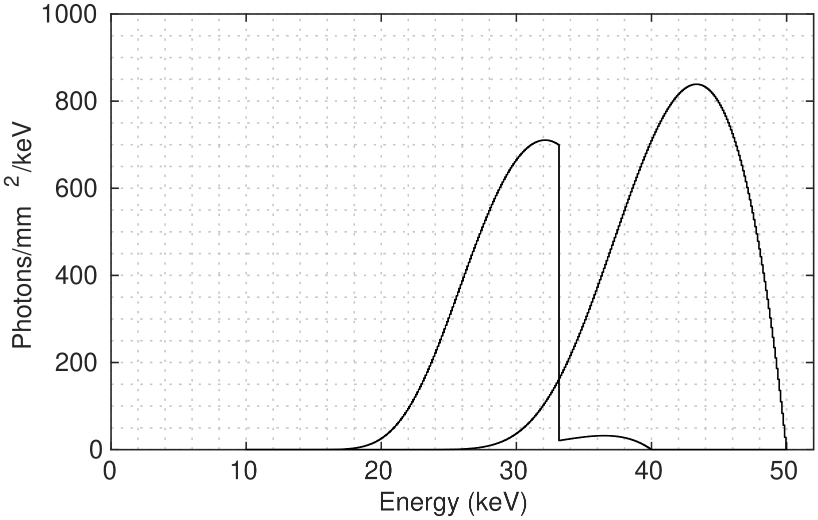

Figure 3.5: X-ray spectra below and above iodine K-edge energy.

using a non-linear least-squares fit to NNPS measurements for each spectrum.

3.2.4.2 Reabsorption

Reabsorption was isolated using two narrow x-ray spectra as illustrated in Fig. 3.5, one above the iodine K-edge energy (33 keV) to include reabsorption, and one below, corresponding to conditions (ii) and (iv) in Fig. 3.4(b). The high-energy spectrum was a 50 kV beam with 21.0 mm added Al having 4.6 mm Al HVL and 42 keV average energy, which has 96% of all photon energies above the K-edge energy. The low-energy spectrum was obtained using 40 kV with a 0.12-cm^2/g iodine filter having 1.9mm Al HVL and 30 keV average energy, giving 97% of all photons below the K-edge energy. Incident air KERMA used was 4.6 μGy for all image acquisitions.

3.2.4.3 Converter-layer blur

Converter blur depends on the width of $b(x)$ relative to pixel size a. We isolated the effect of blur by adjusting pixel size a by binning to achieve conditions (i) and (ii) in Fig. 3.4(b). Detector pixels were used directly as micro-elements ($\epsilon = 0.0495$ mm) having converter blur, and 3×3 binned pixels as micro-elements ($\epsilon = 0.148$ mm) with less blur. While this approach uses micro elements with different sizes, it isolates the effect of converter blur when MTF, NPS and DQE results are expressed as a function of spatial frequency relative to the sampling frequency. The same low-energy spectrum from the previous section was used to ensure negligible generation of K-characteristic emissions. For all cases, conventional images were created using 4×4 binned elements and AAP images synthesized for the same pixel size.

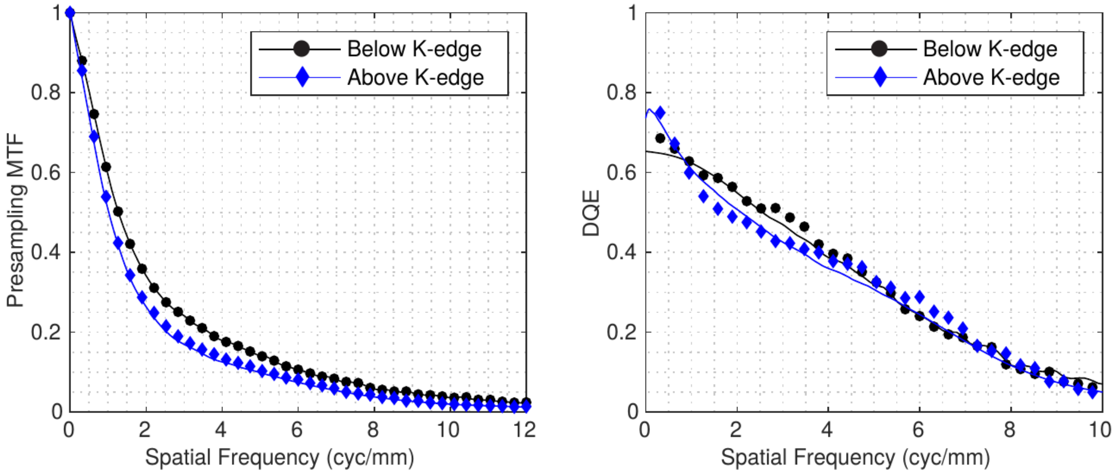

Figure 3.6: MTF and DQE results for x-ray spectra below (black) and above (blue) the converter K-edge energy. Empirically determined CSA model parameters for the case without reabsorption shows excellent agreement on measurements with reabsorption, giving confidence in the model.

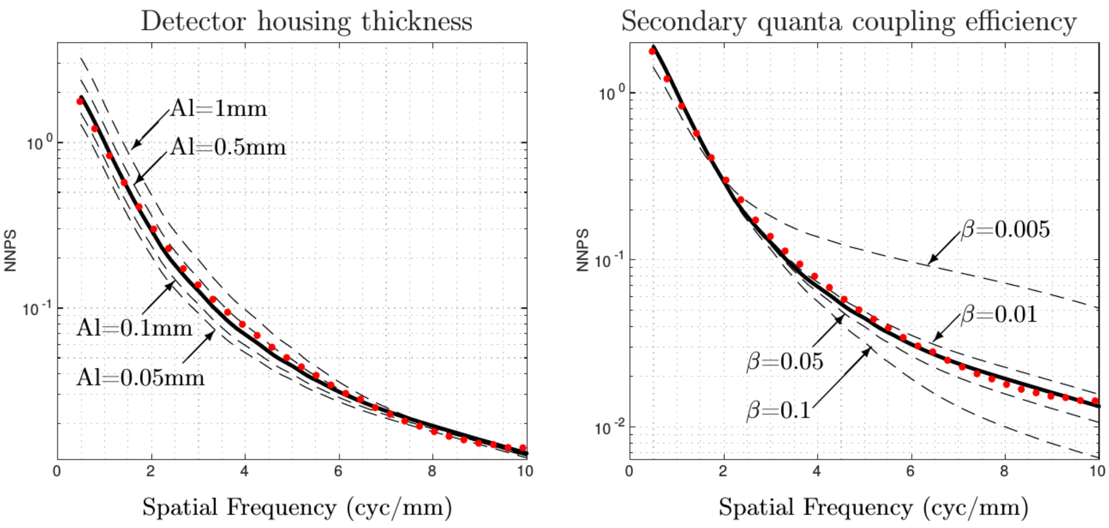

Figure 3.7: Detector housing thickness and secondary quanta coupling efficiency were determined using least-squares fit between theoretical model (solid curve) and NNPS measurement (red points). An effective Al thickness of 0.26 mm and coupling efficiency of 2.3 % give the best fit. Perturbations of Al thickness (left) affect low frequency values and high frequencies are affected by changes in β values (right). Poor fitting (dashed lines) of non-optimum values shows confidence in CSA parameters.

	Below K-edge Energy	Above K-edge Energy
Housing, mm Al	0.26	0.26
Secondary quanta coupling, β	0.023	0.023

Table 3.2: Housing thickness (mm Al) and secondary quanta coupling probability (β) as determined by a non-linear least-squares fit of the CSA NNPS to measured data for the two spectra.

3.3 Results

3.3.1 CSA model validation

Figure 3.6 shows results of presampling MTF and DQE obtained below and above the K-edge energy. Close agreement of the fit values for cover Al thickness and secondary quanta coupling probability β for both spectra gives important confidence on the accuracy of model results. In particular, Fig. 3.7 as poor fits are obtained for small perturbations in these parameters. Detector housing material thickness affects the quantum efficiency of the detector, and therefore impacts NNPS values over all frequencies, where as β affects higher frequencies. In all cases, CSA model results closely match experimental results. This is particularly significant since two different x-ray spectra are used while conversion gain in each branch of the theoretical model is assumed proportional to absorbed energy with the same constant of proportionality, and the OTF obtained with the low-energy spectrum was used for both energies. The close agreement for both spectra gives confidence in the model accuracy. Reduction in MTF with increasing frequency is observed with reabsorption as expected, and differences in DQE measurements for both cases are followed by the model.

3.3.2 Reabsorption

Figure 3.8 illustrates presampling MTF, NNPS and DQE results obtained below and above the K-edge energy. MTF results (Fig. 3.8 top row) show a 50% increase with AAP at the cut-off frequency both above and below the K-edge energy; however, this

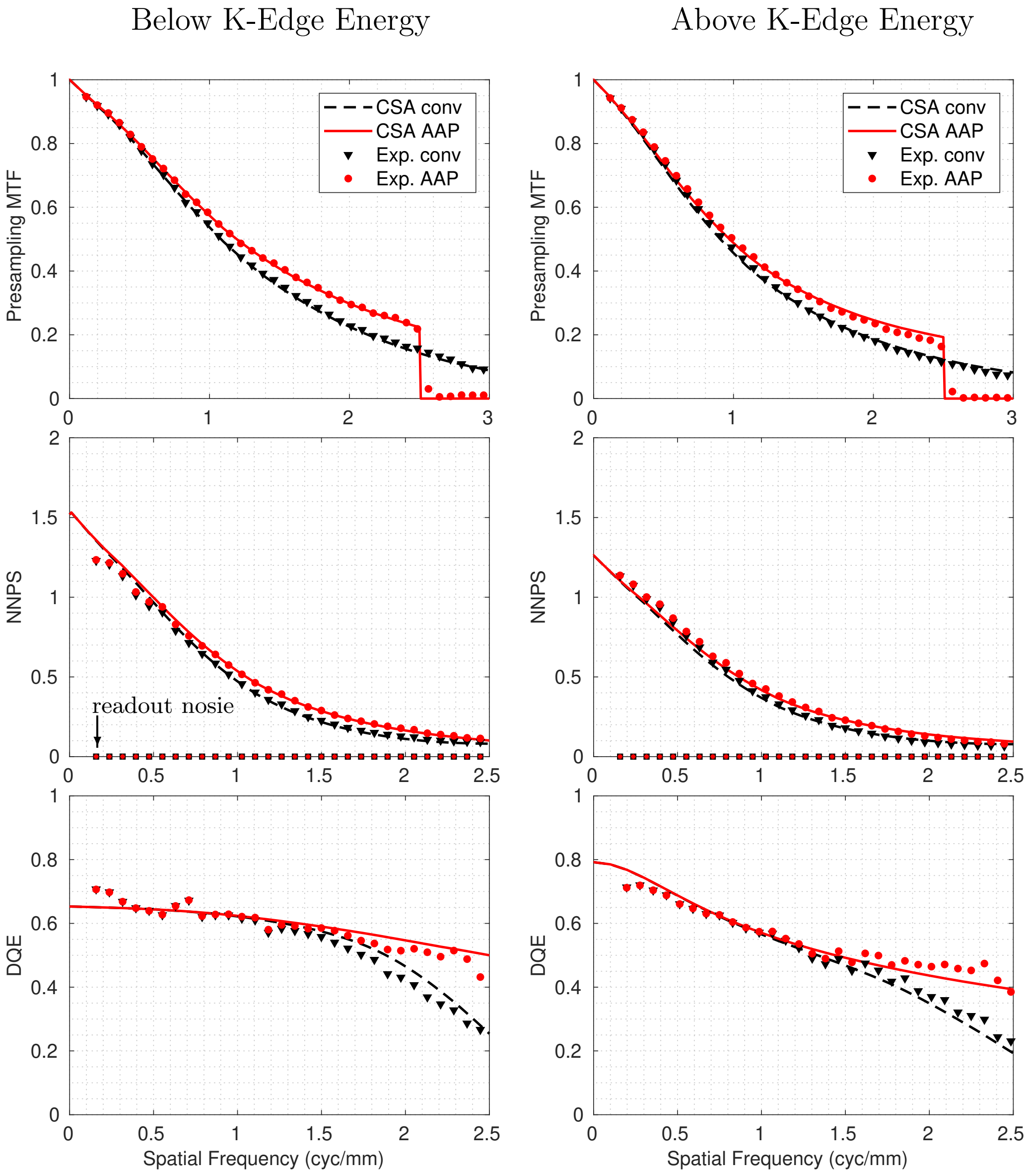

Figure 3.8: Theoretical (CSA) and experimental results of presampling MTF, NNPS and DQE of conventional (binned) and AAP designs under conditions without reabsorption (left) and with (right). Both cases show approximately the same modest increase in MTF and DQE near the image cut-off frequency.

increase is modest due to the low MTF value caused by converter blur. Converter blur also causes the NNPS to drop substantially with increasing frequency, resulting in very little noise aliasing and therefore very little change with AAP. Below the K-edge energy, the conventional DQE decreases near u_c due to slight noise aliasing. The AAP increases high-frequency DQE values by approximately 75%, resulting in a near-flat DQE curve, although the over-all increase in area under the DQE curve remains modest. Above the K-edge energy, DQE is greater due to increased quantum efficiency and shows the characteristic decrease with frequency due to reabsorption. Relative improvement with AAP is similar for both spectra, indicating that reabsorption has little effect on the AAP improvement.

3.3.3 Converter-layer blur

Figure 3.9 shows results for cases with less blur (left column) using larger image pixels and more blur (right column) using smaller image pixels. The MTF of the AAP design is 1.5× that of the conventional design near the cut-off frequency $u_\mathrm{c} = 0.84$ and $u_\mathrm{c} = 2.5$ cycles/mm for large and small pixels respectively. Minimal converter blur results in a flatter NNPS with large pixels, as expected for less correlated noise, resulting in approximately 2.5× greater DQE at high frequencies with the AAP design. Converter blur with smaller pixels reduces MTF and NPS with increasing frequency, therefore reducing the amount of noise aliasing in conventional images. Less DQE improvement is observed with the AAP design for the case with converter blur.

3.3.4 Impact of reabsorption and blur on AAP

Figure 3.10 shows results for MTF, NNPS and DQE ratios between conventional and AAP designs of cases with and without reabsorption in Sec. 3.3.2 (left column) and converter blur in Sec. 3.3.3 (right column). The MTF ratio is the same for all cases, as predicted by Eq. 3.14 showing that it does not depend on reabsorption or blur. With

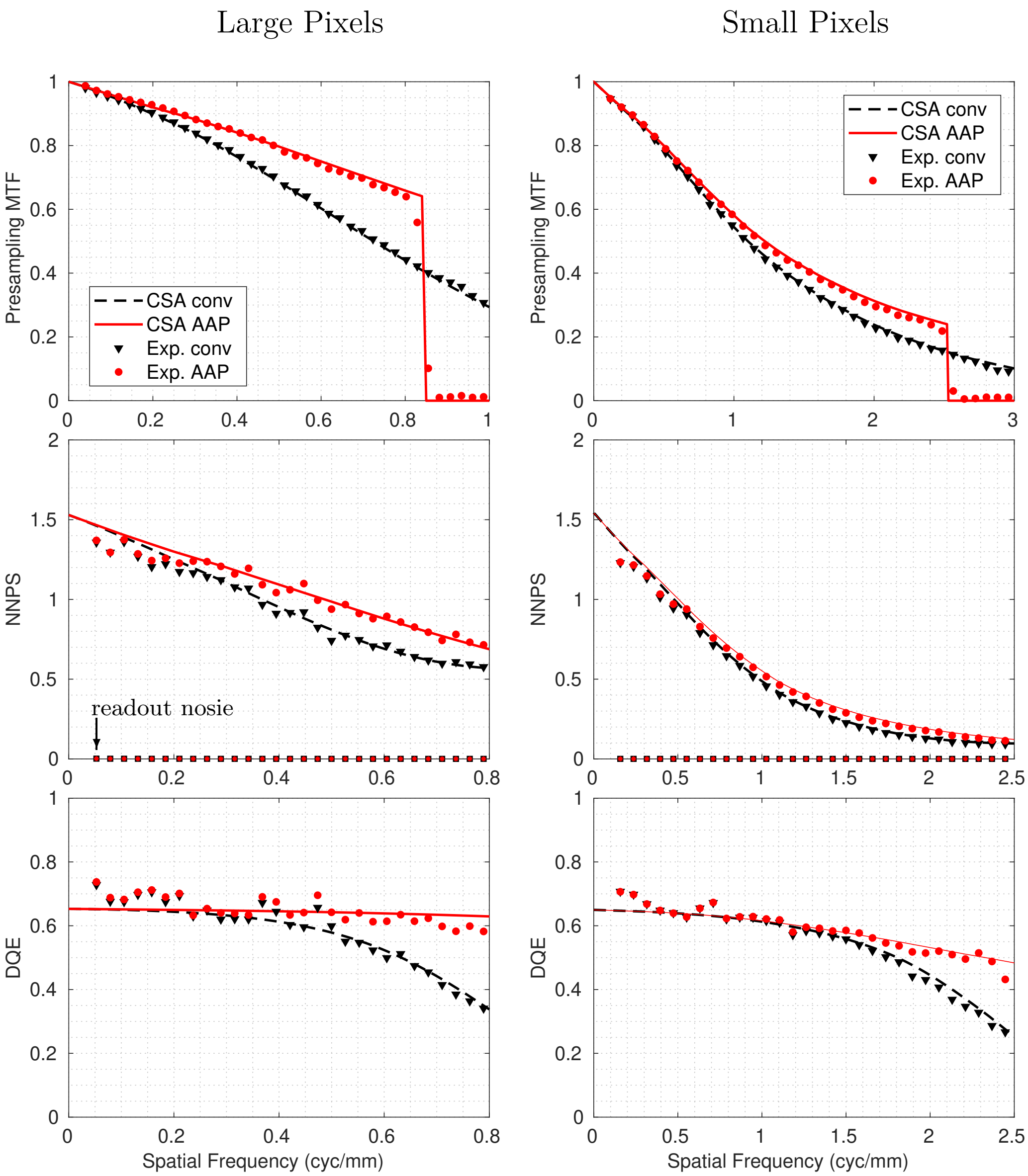

Figure 3.9: Theoretical and experimental results of presampling MTF, NNPS and DQE of conventional (binned) and AAP designs using large pixels (0.594mm) and small pixels (0.198mm). The AAP design shows the same 1.5× relative increase in MTF near u_c for both cases with and without blur, but greater DQE improvement with the AAP approach is possible without converter blur (left).

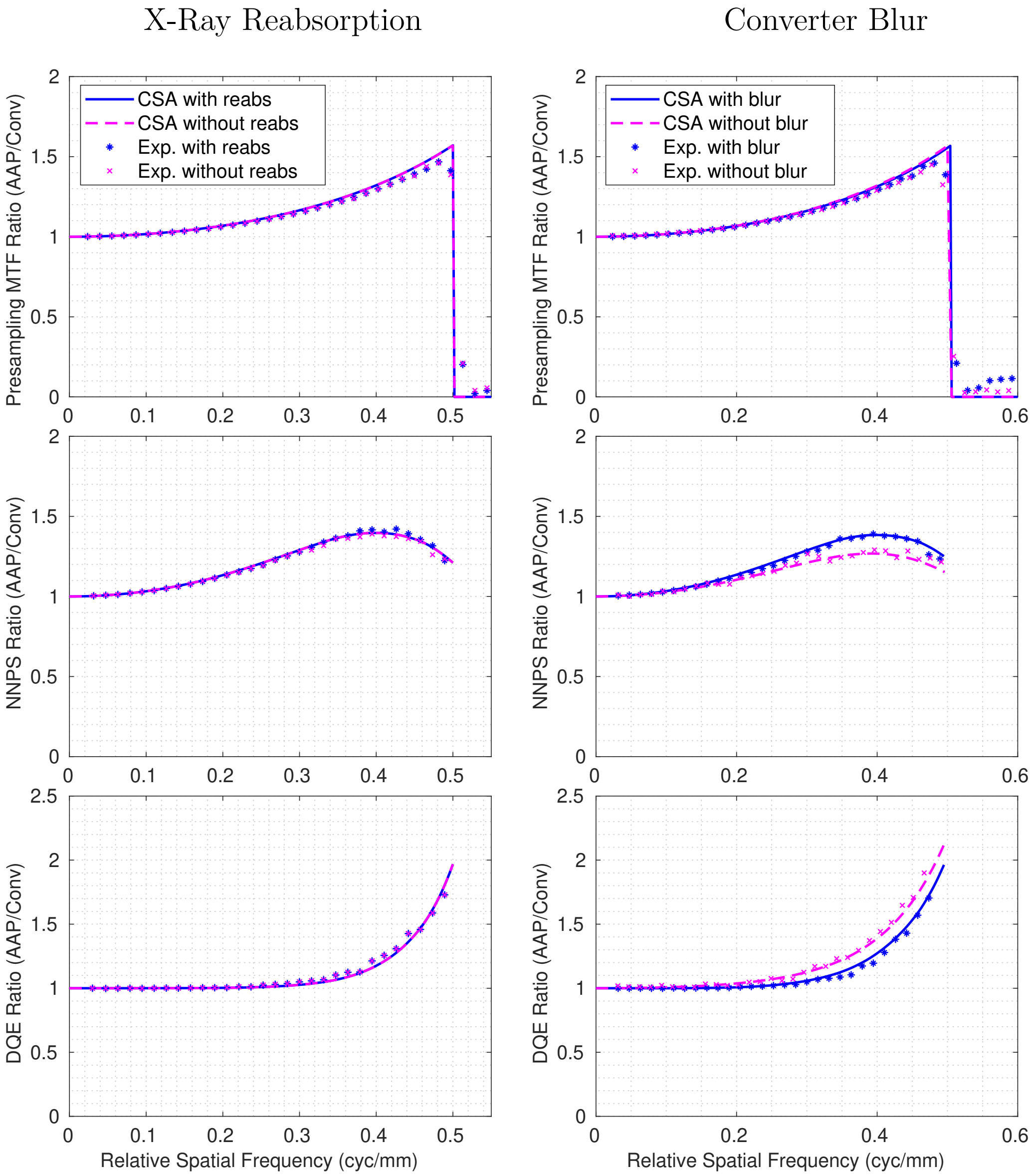

Figure 3.10: Theoretical and experimental results of presampling MTF, NNPS and DQE of conventional to AAP ratios showing effects of reabsorption (left column) and converter blur (right column). High-frequency MTF and DQE was improved for all cases with the AAP approach. Reabsorption did not effect DQE ratio whereas converter blur did, and greater DQE ratio was observed for the case without converter blur.

and without reabsorption, NNPS ratio is greater than unity for high frequencies due to little noise aliasing in conventional images with our detector. DQE ratios for cases with and without reabsorption are similar indicating that DQE improvement with the AAP design does not depend on reabsorption. On the right column, NNPS ratio for the case without blur approaches unity at high frequencies due to the presence of noise aliasing. The case without converter blur has a greater DQE ratio than with blur, indicating that DQE improvement with the AAP design depends on converter blur.

3.4 Discussion

The effect of x-ray reabsorption and converter blur on the AAP design were investigated using a simple-atom CSA model of x-ray interactions that differs by no more than 2% to a complex-atom model for energies up to 100 keV and elements as heavy as Pb.[15] Additionally, our model includes polyenergetic x-ray beams to account for energy-dependent optical gain factors.[25] Experiments comparing cases with and without reabsorption or blur were done using the same x-ray detectors so to allow for direct comparison. The use of different x-ray beams to investigate reabsorption in Fig. 3.8 may cause differences in x-ray interaction depths, however these differences have been shown to not have a significant effect on MTF of columnar CsI.[26, 27, 28] The AAP approach uses a rectangular low-pass filter because it is optimum at attenuating noise aliasing contributions without reducing image frequency power. Although other filter without a sharp cut-off could be used to eliminate aliasing, they would also reduce MTF below the image cut-off frequency.

Relative improvement (such as 1.5× greater MTF near the image cut-off frequency) may be independent of reabsorption and blur, absolute improvement is not and the AAP design does not recover degradation caused by reabsorption or blur in the converter. Equation 3.18 shows that the AAP approach improves DQE in proportion to aliased power in a conventional detector. Reabsorption of characteristic x-rays in CsI has minimal impact on noise aliasing, whereas stochastic blur in the converter layer reduces both MTF and NNPS at high-frequencies, resulting in reduction of aliasing. Detector 1 used in this work has a substantial amount of blur which explains the sub-optimal improvement in DQE for both cases with and without reabsorption. We expect that a detector with minimal blur would achieve close to optimal DQE improvement even with x-ray reabsorption. Detector 2 used for converter blur experiments showed substantial DQE improvement even when pixels were correlated, indicating that the AAP design can provide a benefit even when there are some noise correlations.

3.5 Conclusion

The AAP design offers improved high-frequency MTF and DQE over conventional design by using a micro-element sensor and eliminating noise aliasing. Compared to conventional design near the image cut-off frequency u_c, the AAP design has:

1. Greater MTF by a factor of 1.5× and removal of signal aliasing. If the MTF value is low, this improvement may not be substantial.
   - MTF improvement with the AAP design is not effected by x-ray reabsorption or converter blur.
   - MTF improvement only depends on the AAP filter kernel, micro-element aperture and pixel aperture.
2. Greater presampling NPS below u_c due to the high bandpass of the micro-elements, and elimination of noise aliasing by use of the AAP low-pass filter.
   - At conventional pixel sizes, x-ray reabsorption does not effect noise aliasing and results in the same NPS for conventional and AAP designs.

  - Converter blur reduces the amount of noise aliasing, resulting in greater NPS with the AAP design.

3. Greater DQE by as much as a factor of 2.5× due to greater MTF and reduction of noise aliasing.
   - DQE improvement is not effected by x-ray reabsorption. With a high resolution converter layer, 2.5× DQE improvement is achievable.
   - DQE improvement is reduced by converter blur, providing up 1-2.5× improvement.

The AAP design improves high-frequency MTF and DQE for applications such as radiography, mammography and fluoroscopy provided a low-noise micro-sensor array is used and converter blur is less than pixel size.

3.6 Acknowledgments

The authors are grateful to Terenz Escartin for assistance acquiring x-ray images and to the Canadian Institutes of Health Research (Operating Grant MOP 133596), Natural Sciences and Engineering Research Council (Discovery Grant XXX) and NSERC PGS-D scholarship for financial support.

3.7 Appendix

3.7.1 CSA model of x-ray interactions in the converter layer

We have shown previously that signal and noise transfer through photoelectric, coherent and incoherent interactions for a specified x-ray energy can be described using a single generalized x-ray-interaction simple-atom model.[14] Results for a broad spectrum of x-ray energies are determined as a sum weighted by the spectral shape. The model for each interaction consists of three parallel paths describing liberation of secondary quanta under three conditions: (A) a primary interaction with no subsequent emission or scatter; (B) an interaction followed by emission or scatter but no reabsorption; and (C) an interaction with reabsorption of an emission or scatter photon. The probabilities for each path depend on x-ray energy. For example, below a K-edge energy the probability of following paths B or C may be zero in a photoelectric interaction. This model considers only one edge energy over the range of x-ray energies. For high-Z materials this could be an L shell rather than the K shell. We refer to the characteristic emission as a scatter photon in a photoelectric interaction.

The number of liberated secondary quanta is given as the sum of all paths for each interaction type. For interaction x where x indicates photoelectric, incoherent or coherent, the distribution of liberated secondary quanta is given by

$$\tilde{\mathrm{q}}_{\mathrm{x}}(x) = \tilde{\mathrm{q}}_{\mathrm{x,A}}(x) + \tilde{\mathrm{q}}_{\mathrm{x,B}}(x) + \tilde{\mathrm{q}}_{\mathrm{x,C}}(x). \tag{3.19}$$

Due to the physics of x-ray interactions, secondary quanta are spatially correlated which has important implications for signal and noise transfer and detector performance. The CSA model of this generalized interaction has been described previously[14] and we summarize only the important relationships here. For example, the mean number of liberated secondary quanta per unit area $\bar{q}_{\mathrm{x}}$ for a given interaction is:

$$\bar{q}_{\mathrm{x}} = \bar{q}_{\mathrm{o}} P_{\mathrm{x}} \left[(1 - s_{\mathrm{x}}) \bar{g}_{\mathrm{x,A}} + s_{\mathrm{x}} \left(\langle \bar{g}_{\mathrm{x,B}} \rangle_{E'} + \langle r_{\mathrm{x}} \bar{g}_{\mathrm{x,C}} \rangle_{E'} \right) \right] \tag{3.20}$$

where P_{x} is the probability of interaction x occurring (depending on interaction coefficients), s_{x} is the probability the interaction produces a scatter photon, $\bar{g}_{\mathrm{x}}$ is the mean quantum gain (secondary quanta liberated per interaction) for each path, r_{x} is the probability the scatter photon is reabsorbed (see Fig. 3.11a)[15] and $\langle \rangle_{E'}$ indicates an average weighted by the energy spectrum of scatter photons (important for Compton scatter only

Parameter	PE	COH	INC
s_{x}	$P_{\mathrm{K}}\omega_{\mathrm{K}}$ for $E > E_K$; else 0	1	1
$\bar{g}_{\mathrm{x,A}}$	E/w	0	0
$\bar{g}_{\mathrm{x,B}}$	$(E - E_{\mathrm{K}})/w$ for $E > E_{\mathrm{K}}$; else 0	0	$(E - E')/w$
$\bar{g}_{\mathrm{x,C}}$	E_{K}/w for $E > E_{\mathrm{K}}$; else 0	E/w	E'/w

Table 3.3: Probability of an interaction producing a scatter photon (s_{x}) and average quantum gain ($\bar{g}_{\mathrm{x}}$) parameters in the generalized x-ray interaction model where E is incident x-ray photon energy, E_{K} is K-edge energy, P_{K} is the K-shell participation fraction, ω_{K} is fluorescence yield, w is effective work energy required to liberate one secondary quantum, and E' is Compton-scatter photon energy. It is assumed the K characteristic emission energy is approximately equal to the K-edge energy.

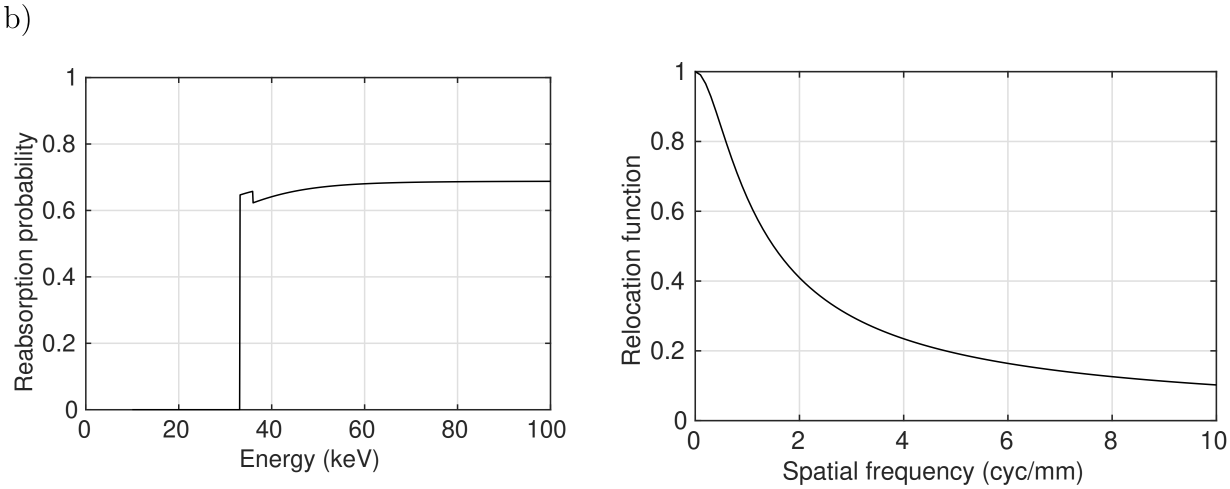

Figure 3.11: (a) CsI K-characteristic x-ray reabsorption probability r_{pe} and (b) relocation function $\mathrm{R_K}$ of a 50 keV x-ray in CsI.[15]

as the scatter photon from photoelectric and coherent interactions have a specific energy for a stated x-ray energy). Table 3.3 and Fig. 3.11 give parameters used in the general x-ray interaction model.

The NPS of the liberated secondary-quanta distribution from interaction type x is given by:[14]

$$\begin{aligned}\mathrm{W_x}(u) \quad &= \quad \bar{q}_{\mathrm{o}} P_{\mathrm{x}} \Big\{ (1 - s_{\mathrm{x}}) \left(\bar{g}^2_{\mathrm{x,A}} + \sigma^2_{g_{\mathrm{x,A}}} \right) + s_{\mathrm{x}} \left[\left\langle \bar{g}^2_{\mathrm{x,B}} + \sigma^2_{g_{\mathrm{x,B}}} \right\rangle_{E'} + r_{\mathrm{x}} \left\langle \bar{g}^2_{\mathrm{x,C}} + \sigma^2_{g_{\mathrm{x,C}}} \right\rangle_{E'} \right] \\ &\qquad +2\, s_{\mathrm{x}} \left\langle r_{\mathrm{x}}\, \bar{g}_{\mathrm{x,B}}\, \bar{g}_{\mathrm{x,C}} \mathrm{R_x}(u) \right\rangle_{E'} \Big\}\end{aligned}$$

where $\mathrm{R_x}(u)$ is the Fourier transform of the normalized reabsorption probability density function (see Fig. 3.11b)[15] and $\sigma^2_{\tilde{g}_\mathrm{x}}$ is the variance of $\tilde{g}_\mathrm{x}$. Conversion from incident x-ray photons to liberated secondary quanta has an OTF given by:[14]

$$\mathrm{T}_\mathrm{x}(u) \quad = \quad \frac{\left[(1-s_\mathrm{x})\bar{g}_{\mathrm{x,A}} + s_\mathrm{x}\left[\langle\bar{g}_{\mathrm{x,B}}\rangle_{E'} + \langle r_\mathrm{x}\bar{g}_{\mathrm{x,C}}\mathrm{R}_\mathrm{x}(u)\rangle_{E'}\right]\right]}{\left[(1-s_\mathrm{x})\bar{g}_{\mathrm{x,A}} + s_\mathrm{x}\left[\langle\bar{g}_{\mathrm{x,B}}\rangle_{E'} + \langle r_\mathrm{x}\bar{g}_{\mathrm{x,C}}\rangle_{E'}\right]\right]}$$

The combined liberated secondary-quanta from all x-ray interactions is given by the summed contributions:

$$\begin{aligned}
\tilde{\mathrm{q}}_\mathrm{r}(x) &= \tilde{\mathrm{q}}_\mathrm{pe}(x) + \tilde{\mathrm{q}}_\mathrm{coh}(x) + \tilde{\mathrm{q}}_\mathrm{inc}(x) \\
\bar{q}_\mathrm{r} &= \bar{q}_\mathrm{pe} + \bar{q}_\mathrm{coh} + \bar{q}_\mathrm{inc} \\
\mathrm{T}_\mathrm{r}(u) &= \frac{1}{\bar{q}_\mathrm{r}}\Big(\bar{q}_\mathrm{pe}\mathrm{T}_\mathrm{pe}(u) + \bar{q}_\mathrm{coh}\mathrm{T}_\mathrm{coh}(u) + \bar{q}_\mathrm{inc}\mathrm{T}_\mathrm{inc}(u)\Big) \\
\wr(u) &= \mathrm{W}_\mathrm{pe}(u) + \mathrm{W}_\mathrm{coh}(u) + \mathrm{W}_\mathrm{inc}(u)
\end{aligned}$$

where subscript r indicates liberated secondary quanta.

Converter blur corresponds to a random relocation of secondary quanta, such as the effect of optical scatter. We represent this blur as a quantum-scatter operator $*_s$ and associated spread function $b(x)$[21, 20] and assume a constant fraction β of liberated secondary quanta are coupled to the sensor array and interact to contribute to the measured signal. The distribution of interacting secondary quanta is therefore given by:

$$\tilde{\mathrm{q}}_\mathrm{s}(x) \quad = \quad \beta\left[\tilde{\mathrm{q}}_\mathrm{r}(x) *_s b(x)\right], \tag{3.21}$$

and

$$\bar{q}_\mathrm{s} = \beta\bar{q}_\mathrm{r}, \tag{3.22}$$

$$\mathrm{T}_\mathrm{s}(u) = \mathrm{T}_\mathrm{r}(u)\mathrm{T}_\mathrm{b}(u) \tag{3.23}$$

$$\mathrm{W_s}(u) \;=\; \beta^2 \left[\wr(u) - \bar{q}_\mathrm{r}\right] \left|\mathrm{T_b}(u)\right|^2 + \beta\bar{q}_\mathrm{r},$$

where $\mathrm{T_b}(u)$ is the OTF of converter blur (Fourier transform of $b(x)$) and $\mathrm{T_s}(u)$ describes the OTF associated with conversion from incident x-ray quanta to interacting secondary quanta. These results reflect properties of the converter and are used in Eqs. (3.3), (3.4), (3.6) and 3.7 to determine the DQE. At the x-ray energies used in this study, the total number of coherent and incoherent interactions is a few percent of the number of photoelectric interactions and have negligible impact on the model predictions.

3.7.2 OTF and NPS of the AAP design

The OTF and NPS of the AAP design, given by $\mathrm{T_A}$ and $\mathrm{W_A}$ respectively, where the MTF is equal to the absolute value of the OTF, is determined by extending previous work[7] to include the effect of the converter layer.

The micro-element signals are represented as $\tilde{\mathrm{d}}_\epsilon^\dagger$ in the AAP design, consisting of δ-functions on spacing x_ϵ scaled by individual micro-element signals. The corresponding OTF, including spectral aliasing, is given by:

$$\mathrm{T}_{d_\epsilon^\dagger}(u) \;=\; \mathrm{T_s}\left(u\right)\mathrm{T}_\epsilon\left(u\right) + \sum_{j=1}^{\infty} \mathrm{T_s}\left(u \pm \frac{j}{x_\epsilon}\right)\mathrm{T}_\epsilon\left(u \pm \frac{j}{x_\epsilon}\right) \tag{3.24}$$

where $\mathrm{T_s}$ and T_ϵ are OTFs of the converter secondary quanta distribution and micro-element aperture respectively. Signals $\tilde{\mathrm{d}}_\epsilon^\dagger$ are subsequently filtered and evaluated on spacings x_a as described in Sec. 3.2.1.3. The corresponding OTF of the AAP output $\tilde{\mathrm{d}}_\mathrm{A}^\dagger$, including aliasing, is therefore given by:

$$\begin{aligned}
\mathrm{T}_{\mathrm{A}^\dagger}(u) &= \mathrm{T}_{d_\epsilon^\dagger}(u)\mathrm{T}_{\mathrm{f}}(u) + \sum_{l=1}^{\infty} \mathrm{T}_{d_\epsilon^\dagger}\left(u \pm \frac{l}{x_a}\right) \mathrm{T}_{\mathrm{f}}\left(u \pm \frac{l}{x_a}\right) \\
&= \mathrm{T}_{\mathrm{s}}(u)\mathrm{T}_{\epsilon}(u)\mathrm{T}_{\mathrm{f}}(u) + \sum_{j=1}^{\infty} \mathrm{T}_{\mathrm{s}}\left(u \pm \frac{j}{x_\epsilon}\right) \mathrm{T}_{\epsilon}\left(u \pm \frac{j}{x_\epsilon}\right) \mathrm{T}_{\mathrm{f}}(u) \\
&\quad + \sum_{l=1}^{\infty} \mathrm{T}_{\mathrm{s}}\left(u \pm \frac{l}{x_a}\right) \mathrm{T}_{\epsilon}\left(u \pm \frac{l}{x_a}\right) \mathrm{T}_{\mathrm{f}}\left(u \pm \frac{l}{x_a}\right) \\
&\quad + \sum_{l=1}^{\infty}\sum_{j=1}^{\infty} \mathrm{T}_{\mathrm{s}}\left(u \pm \frac{j}{x_\epsilon} \pm \frac{l}{x_a}\right) \mathrm{T}_{\epsilon}\left(u \pm \frac{j}{x_\epsilon} \pm \frac{l}{x_a}\right) \mathrm{T}_{\mathrm{f}}\left(u \pm \frac{l}{x_a}\right). \qquad (3.25)
\end{aligned}$$

By specifying a low-pass AAP filter that suppresses frequencies $|u| > \frac{1}{2x_a}$, satisfying $\mathrm{T}_{\mathrm{f}}(u) = \mathrm{T}_{\mathrm{f}}(u)\Pi(x_a u)$, lines 3 and 4 are suppressed and the result simplifies to Eq. (3.6).

The NPS of micro-element signals $\tilde{\mathrm{d}}_\epsilon^\dagger$ is given by:

$$\mathrm{W}_{d_\epsilon^\dagger}(u) = k_{\mathrm{A}}^2 \frac{\epsilon^2}{x_\epsilon^2} \mathrm{W}_{\mathrm{s}}(u) \left|\mathrm{T}_{\epsilon}(u)\right|^2 + k_{\mathrm{A}}^2 \frac{\epsilon^2}{x_\epsilon^2} \sum_{j=1}^{\infty} \mathrm{W}_{\mathrm{s}}\left(u \pm \frac{j}{x_\epsilon}\right) \left|\mathrm{T}_{\epsilon}\left(u \pm \frac{j}{x_\epsilon}\right)\right|^2 + \frac{\epsilon}{x_\epsilon^2}\sigma_\epsilon^2 \qquad (3.26)$$

and the NPS of the output AAP signal $\tilde{\mathrm{d}}_{\mathrm{A}}^\dagger$ with filter $\mathrm{F}(u) = x_a \mathrm{T}_{\mathrm{f}}(u)$ is given by:

$$\begin{aligned}
\mathrm{W}_{\mathrm{A}^\dagger}(u) &= \mathrm{W}_{d_\epsilon^\dagger}(u) \left|\mathrm{T}_{\mathrm{f}}(u)\right|^2 + \sum_{l=1}^{\infty} \mathrm{W}_{d_\epsilon^\dagger}\left(u \pm \frac{l}{x_a}\right) \left|\mathrm{T}_{\mathrm{f}}\left(u \pm \frac{l}{x_a}\right)\right|^2 \\
&= k_{\mathrm{A}}^2 \frac{\epsilon^2}{x_\epsilon^2} \mathrm{W}_{\mathrm{s}}(u) \left|\mathrm{T}_{\epsilon}(u)\right|^2 \left|\mathrm{T}_{\mathrm{f}}(u)\right|^2 + k_{\mathrm{A}}^2 \frac{\epsilon^2}{x_\epsilon^2} \sum_{j=1}^{\infty} \mathrm{W}_{s}\left(u \pm \frac{j}{x_\epsilon}\right) \left|\mathrm{T}_{\epsilon}\left(u \pm \frac{j}{x_\epsilon}\right)\right|^2 \left|\mathrm{T}_{\mathrm{f}}(u)\right|^2 \\
&\quad + \frac{\epsilon}{x_\epsilon^2}\sigma_\epsilon^2 \left|\mathrm{T}_{\mathrm{f}}(u)\right|^2 \\
&\quad + k_{\mathrm{A}}^2 \frac{\epsilon^2}{x_\epsilon^2} \sum_{j=1}^{\infty} \mathrm{W}_{\mathrm{s}}\left(u \pm \frac{l}{x_a}\right) \left|\mathrm{T}_{\epsilon}\left(u \pm \frac{l}{x_a}\right)\right|^2 \left|\mathrm{T}_{\mathrm{f}}\left(u \pm \frac{l}{x_a}\right)\right|^2 \\
&\quad + k_{\mathrm{A}}^2 \frac{\epsilon^2}{x_\epsilon^2} \sum_{l=1}^{\infty}\sum_{j=1}^{\infty} \mathrm{W}_{\mathrm{s}}\left(u \pm \frac{j}{x_\epsilon} \pm \frac{l}{x_a}\right) \left|\mathrm{T}_{\epsilon}\left(u \pm \frac{j}{x_\epsilon} \pm \frac{l}{x_a}\right)\right|^2 \left|\mathrm{T}_{\mathrm{f}}\left(u \pm \frac{l}{x_a}\right)\right|^2 \\
&\quad + \frac{\epsilon}{x_\epsilon^2}\sigma_\epsilon^2 \sum_{l=1}^{\infty} \left|\mathrm{T}_{\mathrm{f}}\left(u \pm \frac{l}{x_a}\right)\right|^2. \qquad (3.27)
\end{aligned}$$

Similar to above, specifying a low-pass filter that suppresses frequencies $|u| > \frac{1}{2x_a}$ suppresses the last 3 lines above and simplifies to Eq. 3.7. It also shows that a low-pass filter is optimum because it reduces noise terms by eliminating aliasing contribution.

Bibliography

[1] R. Shaw, “The equivalent quantum efficiency of the photographic process,” *J. Photogr.*, vol. 11, pp. 199–204, 1963.

[2] J. C. Dainty, *Image Science: Principles, Analysis, and Evaluation of Photographic-Type Image Processing.* Academic Press, 1974.

[3] A. M. Chiarelli, S. A. Edwards, M. V. Prummel, D. Muradali, V. Majpruz, S. J. Done, P. Brown, R. S. Shumak, and M. J. Yaffe, “Digital compared with film mamography: Performance measure in concurrent cohorts with an organized breast screening program,” *Radiology*, vol. 268, no. 3, pp. 684–693, 2013.

[4] M. J. Yaffe, A. K. Bloomquist, D. M. Hunter, G. E. Mawdsley, A. M. Chiarelli, D. Muradali, and J. G. Mainprize, “Comparative performance of modern digital mammography systems in a large breast screening program,” *Med. Phys.*, vol. 40, no. 12, p. 121915, 2013.

[5] E. Ismailova, K. S. Karim, and I. A. Cunningham, “Apodized-Apreature Pixel design to increase high-frequency DQE and reduce noise aliasing in x-ray detectors,” *Proc. SPIE: Physics of Medical Imaging*, vol. 9412, 2015.

[6] T. F. Nano, T. Escartin, K. S. Karim, and I. A. Cunningham, “A novel x-ray detector design with higher DQE and reduce aliasing: Theoretical analysis of x-ray reabsorption in detector converter material,” *Proc. SPIE: Physics of Medical Imaging*, vol. 9783, 2016.

[7] T. F. Nano, T. Escartin, E. Ismailova, K. S. Karim, J. Lindstrom, H. K. Kim, and I. A. Cunningham, “MTF and DQE enhancement using an apodized-aperture x-ray detector design,” *Med. Phys.*, vol. 44, no. 9, pp. 4525–4535, 2017.

[8] C. C. Scott, S. Abbaszadeh, S. Ghanbarzadeh, G. Allan, M. Farrier, I. A. Cunningham, and K. S. Karim, “Amorphous selenium direct detection CMOS digital x-ray imager with 25 micron pixel pitch,” *Proc. SPIE: Physics of Medical Imaging*, vol. 9033, 2014.

[9] C. C. Scott, A. Parsafar, A. El-Falou, P. M. Levine, and K. S. Karim, “High dose efficiency, ultra-high resolution amorphous selenium/CMOS hybrid digital X-ray imager,” *IEEE Int. Electron Devices Meet.*, vol. 30.6.1, pp. 1–4, 2015.

[10] A. Parsafar, C. C. Scott, A. El-Falou, P. M. Levine, and K. S. Karim, “Direct-conversion CMOS x-ray imager with 5.6um x 6.25um pixels,” *IEEE Electron Device Lett.*, vol. 36, pp. 481–483, May 2015.

[11] H. H. Barrett and W. Swindell, *Radiological Imaging: The Theory of Image Formation, Detection, and Processing.* Academic Press, 1996.

[12] J. Yao and I. A. Cunningham, “Parallel cascades: New ways to describe noise transfer in medical imaging systems,” *Med. Phys.*, vol. 28, pp. 2020–2038, October 2001.

[13] M. Sattarivand and I. A. Cunningham, “Computational engine for development of complex cascaded models of signal and noise in x-ray imaging systems,” *IEEE Trans. Med. Imaging*, vol. 24, no. 2, pp. 211–222, 2005.

[14] S. Yun, J. Tanguay, H. K. Kim, and I. A. Cunningham, “Cascaded-systems analyses and the detective quantum efficiency of single-Z x-ray detectors including photoelectric, coherent and incoherent interactions,” *Med. Phys.*, vol. 40, no. 4, p. 041916, 2013.

[15] G. Hajdok, J. Yao, J. J. Battista, and I. A. Cunningham, “Signal and noise transfer properties of photoelectric interactions in diagnostic x-ray imaging detectors,” *Med. Phys.*, vol. 33, no. 10, pp. 3601–3610, 2006.

[16] C. E. Metz and C. J. Vyborny, “Wiener spectral effects of spatial correlation between the site of characteristic x-ray emission and reabsorption in radiographic screen-film systems,” *Phys. Med. Biol.*, vol. 28, no. 5, pp. 547–564, 1983.

[17] W. Zhao, W. G. Ji, and J. A. Rowlands, “Effect of characterisitic xrays on the noise power spectra and detective quantum efficiency of photoconductive x-ray detectors,” *Med. Phys.*, vol. 28, October 2001.

[18] D. M. Hunter, G. Belev, S. Kasap, and M. J. Yaffe, “Measured and calculated K-fluorescence effects on the MTF of an amorphous-selenium based CCD x-ray detector,” *Med. Phys.*, vol. 39, no. 2, pp. 608–622, 2012.

[19] M. Rabbani, R. Shaw, and R. V. Metter, “Detective quantum efficiency of imaging systems with amplifying and scattering mechanisms,” *J. Opt. Soc. Am. A*, vol. 4, pp. 895–901, May 1987.

[20] I. A. Cunningham and R. Shaw, “Signal-to-noise optimization of medical imaging systems,” *J. Opt. Soc. Am. A*, vol. 16, no. 3, pp. 621–632, 1999.

[21] I. A. Cunningham, “Applied linear-systems theory,” in *Handbook of Medical Imaging: Vol 1, Physics and Psychophysics* (J. Beutel, H. L. Kundel, and R. V. Metter, eds.), Ch 2, pp. 79–159, SPIE Press, 2000.

[22] J. H. Hubbell, P. N. Trehan, N. Singh, B. Chand, D. Mehta, M. L. Garg, R. R. Garg, S. Singh, and S. Puri, “A Review, Bibliography, and Tabulation of K, L, and Higher Atomic Shell X-Ray Fluorescence Yields,” *J. Phys. Chem. Ref.*, vol. 23, no. 2, pp. 339–364, 1994.

[23] J. A. Rowlands and J. Yorkston, “Flat panel detectors for digital radiography,” *Handbook of medical imaging, Chapter 4*, vol. 1, pp. 223–328, 2000.

[24] T. F. Nano and I. A. Cunningham, *Clinical diagnostic and interventional radiology physics with Matlab: a problem solving approach*, ch. Toolkit to manipulate x-ray spectra, dose and physics calculations in medical imaging. CRC Press, 2019.

[25] M. Drangova and J. A. Rowlands, “Optical factors affecting the detective quantum efficiency of radiographic screens.,” *Med Phys*, vol. 13, no. 2, pp. 150–157, 1986.

[26] W. Hillen, W. Eckenbach, P. Quadflieg, and T. Zaengel, “Signal-to-noise performance in cesium iodide x-ray fluorescent screens,” *Proc. SPIE: Physics of Medical Imaging*, vol. 1443, pp. 120–131, 1991.

[27] J. A. Rowlands, W. G. Ji, and W. Zhao, “Effect of depth-dependent modulation transfer function and k-fluorescence reabsorption on the detective quantum efficiency of indirect-conversion flat-panel x-ray imaging systems using csi,” *Proc.SPIE*, vol. 4320, 2001.

[28] A. Howansky, A. R. Lubinsky, S. K. Ghose, K. Suzuki, and W. Zhao, “Direct measurement of Lubberts effect in CsI: Tl scintillators using single x-ray photon imaging,” *Proc. SPIE: Physics of Medical Imaging*, vol. 10132, p. 1013209, 2017.

Chapter 4

Performance evaluation of a Se/CMOS prototype x-ray detector with an apodized-aperture x-ray detector design

We implement that AAP design on a small area prototype sensor (Se/CMOS) with 7.8μm element size and compare AAP and conventional (binned) images with 47μm pixel size. Presampling modulation transfer function (MTF), normalized Wiener noise power spectrum (NNPS) and DQE were measured using a tungsten micro-focus x-ray tube 60 kV spectrum and 85μGy air KERMA incident on the detector. At spatial frequencies near the image sampling cut-off frequency (u_c = 10.6cyc/mm), the AAP design has 1.5× greater MTF and 2.5× greater DQE than conventional designs. Specimen images show improved visualization of fine detail with the AAP design.

This chapter is based on a manuscript in preparation for submission to Journal of Medical Imaging: TF Nano, CC Scott, *Y Li, C Con, KS Karim and IA Cunningham.*

4.1 Introduction

In digital radiography and mammography, high cancer detection rates while using low radiation doses in screening programs have been attributed to x-ray detector designs that are dose-efficient at producing images with high signal-to-noise ratios (SNR).[1, 2, 3] The ability of an x-ray detector to produce high SNR images for a given exposure is quantified by the detective quantum efficiency (DQE) as a function of spatial frequency.[4, 5] A maximum DQE value of unity across all spatial frequencies of interest represents an ideal system (in terms of SNR and quantum efficiency) that is only limited by the Poisson statistics of counting x-ray quanta.[6, 7]

Conventional x-ray detector designs have a 1:1 ratio of sensor element size to image pixel size. High DQE values can be achieved at low frequencies (up to 80%) but DQE is much lower at high frequencies (less than 40%).[8] For a conventional detector with a high-resolution converter layer that is only limited by sensor element aperture size, high-frequency DQE is degraded by 60% due to noise aliasing. Our group has previously developed a novel x-ray detector design, which we call apodized-aperture pixel (AAP), that eliminates aliasing by using using a low-noise micro-sensor array having smaller element size (eg. 5 - 50μm) than pixel size (eg. 50 - 200μm) and applying an anti-aliasing filter that attenuates frequencies above the image cut-off frequency.[9, 10, 11, 12] The AAP design could be useful in improving SNR of fine-detail when smaller pixels do not provide additional clinical benefit[13, 14] or if large image sizes are impractical for storage and display. Implementation of a full-size clinical AAP detector could be made possible by manufacturing a large-area sensor having elements of 10-25μm in size with low-readout noise, such as with complementary metal-oxide semiconductor (CMOS) technology.[15, 16, 17] A pixel-to-element size ratio of 4 has been found to give most of the AAP benefit.

The purpose of this work is to implement the AAP design using a selenium (Se) and CMOS small-area prototype with 7.8μm element size and evaluate MTF and DQE performance up to 10 cycles/mm. We use a cascaded system analysis (CSA) for theoretical comparison between conventional and AAP x-ray detector designs.

4.2 Theory

The DQE [unitless] of an x-ray detector expressed as a function of spatial frequency u [cycles mm^{-1}] is given by:[18, 19]

$$\mathrm{DQE}(u) = \frac{\mathrm{MTF}(u)^2}{K Q_o \mathrm{W}(u)/\bar{d}^2} = \frac{\mathrm{MTF}(u)^2}{\mathrm{W}^{\mathrm{n}}(u)} \tag{4.1}$$

where K [μGy] is the corresponding air KERMA, Q_o [mm$^{-2}\mu$Gy^{-1}] is the number of x-ray quanta per unit area per unit KERMA associated with the spectrum, $\bar{d}$ is mean pixel value that scales linearly with incident number of quanta, MTF(u) [unitless] is the presampling modulation transfer function, W(u) [mm^2] is the image Wiener noise power spectrum associated with uniform exposure K, and $\mathrm{W}^{\mathrm{n}}(u) = K Q_o \mathrm{W}(u)/\bar{d}^2$ [unitless] is the image normalized NPS. All quantities in Eq. 4.1 are measurable, and can be theoretically modeled using cascaded system analysis (CSA) assuming a linear shift-invariant system having wide-sense cyclo-stationary noise.[19] Equations are given in 1-dimension but they can be easily generalized to higher orders.

4.2.1 Se/CMOS micro-sensor array

X-ray photons incident on a detector can be described by a random distribution of points, $\tilde{\mathrm{q}}_0(x)$ [mm^{-1}], with each point represented as a Dirac δ function:[20]

$$\tilde{\mathrm{q}}_0(x) = \sum_{i=1}^{\tilde{\mathrm{N}}} \delta(x - \tilde{x}_i), \tag{4.2}$$

where $\tilde{x}_i$ is the random location of the ith photon out of $\tilde{\mathrm{N}}$ total photons. At diagnostic

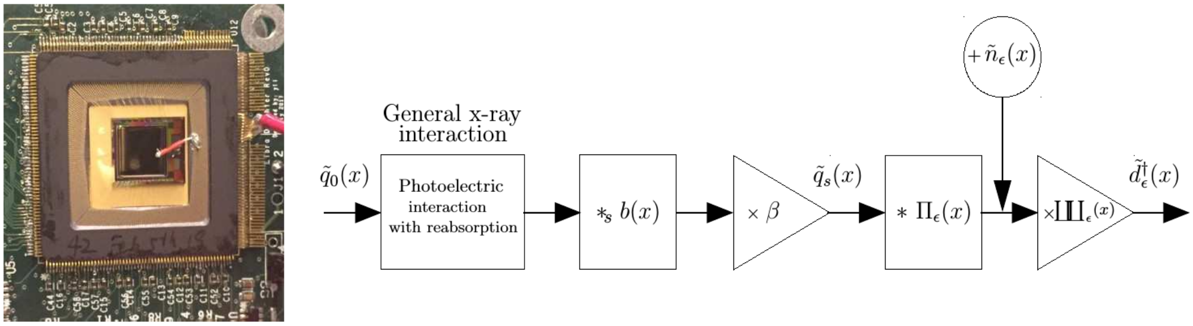

Figure 4.1: Se/CMOS sensor with 7.8μm element size (on the left) has an active area of approximately 1cm^2. The CSA model of the micro-sensor array (on the right) includes x-ray interactions, reabsorption, converter blur $\tilde{\mathrm{b}}(x)$, sensor collection efficiency β, quanta collection in rectangular apertures $\prod_\epsilon(x)$, read-out noise $\tilde{\mathrm{n}}_\epsilon(x)$ and discrete sampling $ш_\epsilon(x)$.

energies, x-rays are most likely to interact in Se via photoelectric interaction that could result in emission/reabsorption of a 12.6 keV characteristic photon. A CSA model is shown in Fig. 4.1 that includes a simple-atom model of x-ray interactions,[21] x-ray reabsorption, and converter blur. Using previously developed descriptions of the quanta distribution released $\tilde{\mathrm{q}}_r(x)$ during x-ray interactions (including reabsorption),[22] the secondary quanta distribution interacting in the sensor array is given by: $\tilde{\mathrm{q}}_s(x) = \beta\left[\tilde{\mathrm{q}}_r(x) *_s \tilde{\mathrm{b}}(x)\right]$, where β is the sensor collection efficiency, $*_s$ is the quantum scatter operator, and $\tilde{\mathrm{b}}(x)$ is the converter blur caused by relocation of quanta. Appendix 4.7.1 gives a summary of the CSA results, including expressions for optical transfer function (OTF) of secondary quanta $\mathrm{T_s}(u)$ and Wiener noise power spectrum $\mathrm{W_s}(u)$ as previously described by Yun et. al.[22]

The output of the Se/CMOS micro-sensor array is given by [mm^{-1}]:

$$\tilde{\mathrm{d}}^\dagger_\epsilon(x) = \sum_{i=-\infty}^{\infty}\left[\tilde{\mathrm{d}}_{\epsilon,i} + \tilde{\mathrm{n}}_{\epsilon,i}\right]\delta(x - i\epsilon), \tag{4.3}$$

where $\tilde{\mathrm{d}}_{\epsilon,i} = k_\epsilon \tilde{\mathrm{q}}_s(x) * \prod_\epsilon(x)\Big|_{x=i\epsilon}$ is the presampling signal and $\tilde{\mathrm{n}}_{\epsilon,i}$ are readout-noise sample values with variance σ^2_ϵ. The mean detector signal gain per secondary quanta interacting in the element is given by k_ϵ, $\prod_\epsilon(x)$ is the sensor element aperture of width ϵ and Dirac-δ functions spatially sample the signal at spacings of ϵ. Mean detector signal is $\bar{d}_\epsilon^\dagger = k_\epsilon \bar{q}_s$, where $\bar{q}_s$ is the mean number of secondary quanta interacting in the sensor.

The presampling MTF of micro-sensor array is given by:[unitless]

$$\mathrm{MTF}_\epsilon(u) = |\mathrm{T_s}(u)|\,|\mathrm{T}_\epsilon(u)| = |\mathrm{T_s}(u)|\,|\mathrm{sinc}(\epsilon u)|\,. \tag{4.4}$$

where $\mathrm{T}_\epsilon(u) = \mathrm{sinc}(\epsilon u)$ is the OTF of the micro-sensor aperture function.

The NPS of the micro-sensor array is given by:[mm-1]

$$\mathrm{W}_{\epsilon^\dagger}(u) \;=\; k_\epsilon^2 \mathrm{W_s}\,(u)\,|\mathrm{sinc}(\epsilon u \pm j)|^2 + k_\epsilon^2 \sum_{j=1}^{\infty} \mathrm{W_s}\left(u \pm \frac{j}{\epsilon}\right)|\mathrm{sinc}(\epsilon u \pm j)|^2 + \frac{1}{\epsilon}\sigma_\epsilon^2. \tag{4.5}$$

The DQE of the micro-sensor array, $\mathrm{MTF}_\epsilon^2(u)/\frac{\bar{q}_o}{\bar{d}_\epsilon^2}\mathrm{W}_{\epsilon^\dagger}(u)$ is therefore given by:

$$\mathrm{DQE}_\epsilon(u) = \frac{|\mathrm{T_s}(u)|^2\,|\mathrm{sinc}(\epsilon u)|^2}{\mathrm{W_s^{(n)}}\,(u)\,|\mathrm{sinc}(\epsilon u \pm j)|^2 + k_\epsilon^2 \sum_{j=1}^{\infty} \mathrm{W_s^{(n)}}\left(u \pm \frac{j}{\epsilon}\right)|\mathrm{sinc}(\epsilon u \pm j)|^2 + \frac{\bar{q}_o}{k_\epsilon^2 \bar{q}_s^2 \epsilon}\sigma_\epsilon^2}. \tag{4.6}$$

where $\mathrm{W_s^{(n)}} = \frac{\bar{q}_o}{\bar{d}_\epsilon^2}\mathrm{W_s}$ is the normalized NPS (NNPS) of the secondary quanta distribution that equals unity for an ideal photon counting detector.

4.2.2 Conventional and AAP designs

A conventional energy integrating x-ray detector has the same pixel size a as sensor element size ϵ. In contrast, the AAP design uses a micro-sensor array (with $\epsilon < a$) and a filter kernel to synthesize images of desired pixel size. Shown in Fig. 4.2 are CSA models that extend the micro-sensor array output to described conventional (left) and AAP (right) designs. The AAP filter f(x) with an OTF $\mathrm{T_f}(u)$ can be implemented on detector firmware, as illustrated in Fig 4.2, so that AAP readout output has the desired

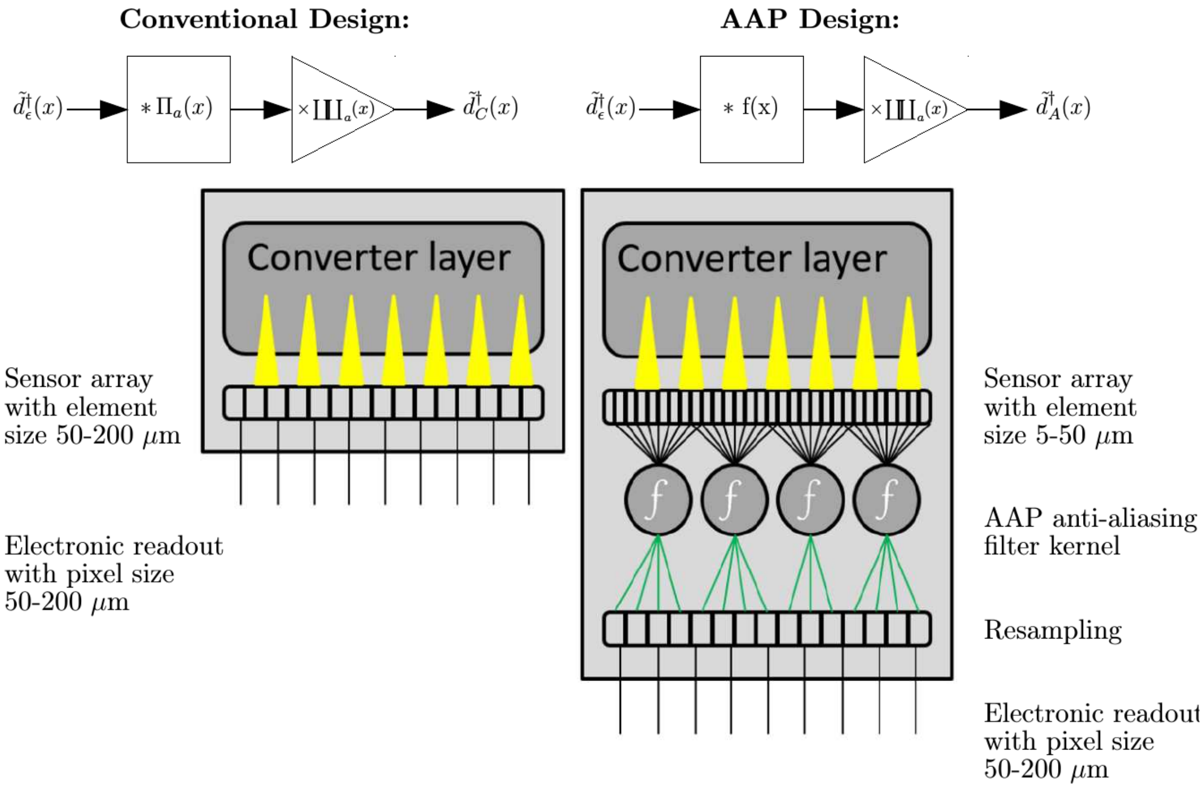

Figure 4.2: CSA models and schematic diagrams of conventional (left) and AAP (right) designs. Enclosed in each detector is a converter layer, sensor array and readout electronics. The AAP detector has a micro-sensor array that allows for acquisition of an oversampled output and on-board filtering to synthesize images of desired pixel size.

	Conventional Design	AAP Design
$\mathrm{MTF}(u)$	$\lvert \mathrm{T_s}(u)\rvert \, \lvert \mathrm{sinc}(au)\rvert$	$\lvert \mathrm{T_s}(u)\rvert \, \lvert \mathrm{sinc}(\epsilon u)\rvert \, \lvert \prod (au)\rvert$
$\mathrm{W^n}(u)$	$\sum_{j=-\infty}^{\infty} \mathrm{W_s}\left(u \pm \frac{j}{a}\right) \mathrm{sinc}^2\left(au \pm j\right)$	$\mathrm{W_s}(u)\mathrm{sinc}^2(\epsilon u) \left\lvert \prod (au)\right\rvert^2$
$\mathrm{DQE}(u)$	$\frac{\left\lvert \mathrm{T_s}(u)\right\rvert^2 \mathrm{sinc}^2(au)}{\sum_{j=-\infty}^{\infty} \mathrm{W_s}\left(u \pm \frac{j}{a}\right)\mathrm{sinc}^2(au \pm j)}$	$\frac{\left\lvert \mathrm{T_s}(u)\right\rvert^2}{\mathrm{W_s}(u)}$

Table 4.1: Theoretical results of presampling MTF, NNPS and DQE for conventional and AAP designs. A rectangular low-pass filter is used for the AAP with cut-off frequency $\pm {}^1/_{2a}$.

image size. Use of an ideal low-pass filter $\mathrm{T_f}(u) = \prod (au)$ attenuates frequencies past $\pm {}^1/_{2a}$ and removes aliasing. Previous proof-of-concept experiments have shown that such a filter results in 1.5× and 2.5× greater high-frequency MTF and DQE respectively with the AAP design.[11]

Detector output from a conventional design is given by [mm^{-1}]:

$$\tilde{\mathrm{d}}^{\dagger}_{\mathrm{C}}(x) = \sum_{i=-\infty}^{\infty} \left[\tilde{\mathrm{d}}^{\dagger}_{\epsilon}(x) * \prod(ax)\right] \delta(x - ia), \tag{4.7}$$

and detector output from the AAP design is given by [mm^{-1}]:

$$\tilde{\mathrm{d}}^{\dagger}_{\mathrm{A}}(x) = \sum_{i=-\infty}^{\infty} \left[\tilde{\mathrm{d}}^{\dagger}_{\epsilon}(x) * \mathrm{f}(x)\right] \delta(x - ia), \tag{4.8}$$

Table 4.1 summarizes presampling MTF, NNPS and DQE equations for conventional and AAP designs. Presampling MTF and NNPS functions are band-limited with the AAP design. DQE of the conventional design includes harmonics of $\mathrm{W_s}$ (shown in the summation term) resulting in reduction due to noise aliasing, while the AAP design eliminates aliasing. In that case of a high resolution converter such as selenium, $\mathrm{T_s}$ and $\mathrm{W_s}$ are approximately unity for all image frequencies. In that case, the AAP design has 1.5× and 2.5× greater MTF and DQE than a conventional design near the image cut-off frequency, respectively.

4.3 Methods

4.3.1 Se/CMOS micro-sensor prototype

A Se/CMOS active pixel sensor with 1k x 1k elements having 7.8μm size and approximately 1cm^2 sensitive area was used to acquire images. The sensor has a 98μm thick Se layer, a 50 nm gold top electrode and is digitized using readout electronics with a 16-bit ADC converter. The x-ray beam used for experiments was generated with a micro-focus x-ray tungsten tube (9μm focal spot, PXS5-928) at 60kV and 2mm of aluminum filtration having an HVL of 1.7mm of aluminum. The x-ray sensor was paced 55cm away from the x-ray focal spot and the DQEPro (DQEInstruments Inc., London, Canada) device's back surface was placed 5cm away from the sensor (Fig. 4.3). At these distances, focal spot blur has a negligible effect on MTF (at most 3-5% near the cut-off frequency). Images were acquired in dynamic mode with 0.136 mAs tube current and 3 second frame integration time with an air KERMA of 85μGy per frame. X-ray spectra were calculated using the Tucker and Barnes model[23] and Fig. 4.3 shows incident and interacting in the sensor (the peak at 12.6 keV are reabsorptions of Se K-characteristic x-rays). The incident number of x-rays for simulated spectrum was 18,786 quanta per mm^2 per μGy.

A non-standard mammography spectrum was used in this study that resulted in 30% quantum efficiency of the x-ray sensor. At mammography energies, the sensor would have an efficiency of 70-80% which is typically of clinical systems.

Images from the prototype micro-sensor array were processed on a lab computer to synthesize conventional (binned) and AAP images with the same pixel size. On a full-size

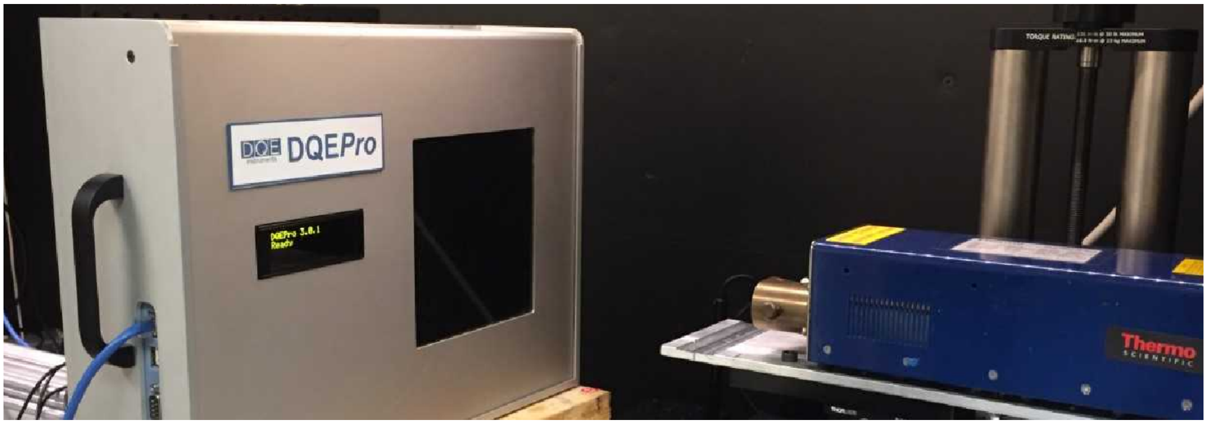

X-rays interacting in the sensor array X-rays output of the micro-focus tube

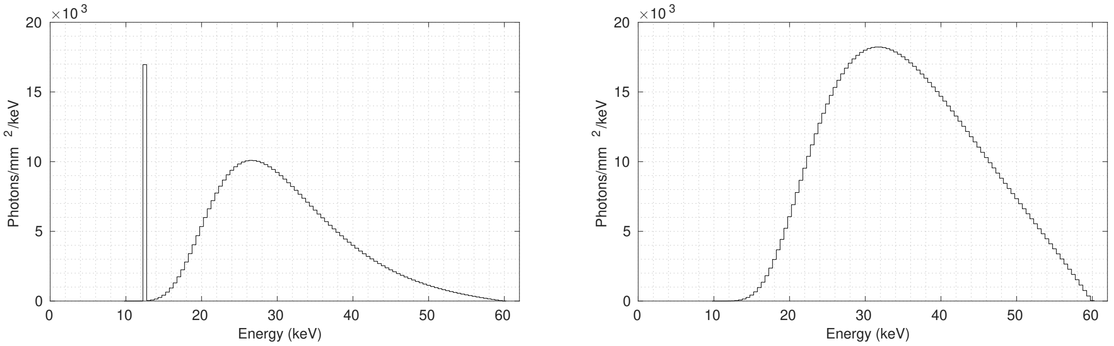

Figure 4.3: The top panel shows the micro-focus x-ray tube (on the right) and the DQEPro device (on the left) placed in front of the Se/CMOS sensor. Simulated spectra are plotted of photons incident on the sensor (right) and interacting in the sensor (left).

detector, it will likely be necessary to implement the AAP algorithms directly on detector firmware due to the extremely large number of micro-sensor elements and corresponding large data-transfer requirements.

4.3.2 Conventional and AAP designs

Comparison between AAP and conventional designs was carried out by generating both conventional and AAP images using the micro-sensor detector output. Conventional images were generated by binning 6 × 6 pixels, and AAP images of the same pixel size were synthesized by applying a rectangular low-pass filter that attenuate frequencies above the image cut-off frequency and resampling at spacings of 47μm (to demonstrate performance at an approximate pixel size used in mammography). Detector performance metrics MTF, NNPS and DQE were measured using conventional and AAP image sets.

4.3.3 Specimen image

An intact dry specimen of a urinary kidney stone was imaged to visually compare binned and AAP images. The specimen was placed 5 cm from the detector and the source-to-image distance was 55 cm. X-ray images of the specimen were log-transformed, inverted and interpolated for display and magnification purposes. Binned and AAP images were synthesized as described above.

4.4 Results

Fig. 4.4 shows the kidney stone specimen (left) and the x-ray image acquired of it using the high-resolution sensor. Fine-detail near edges of the stone's crystalline structure are clearly visible at high resolution.

4.4.1 MTF, NNPS and DQE of conventional and AAP designs

Fig. 4.5 shows theoretical and experimental results of presampling MTF, NNPS and DQE for conventional (left) and AAP (right) designs. Near the image cut-off frequency, $u_c = 10.6$ cyc/mm, MTF of the conventional design is approximately 0.55 and is non-zero for higher frequencies that are aliased. Whereas MTF of the AAP design is 0.85 at u_c ($1.5 \times$ improvement) and frequencies above u_c are attenuated due to the AAP low-pass filter.

Image NNPS measurement are similar for conventional and AAP designs. A flat NPS curve, with both designs, is indicative of uncorrelated image pixel values showing that there are minimal effects from noise correlations (that could be caused by x-ray reabsorption or converter blur) at these frequencies. Electronic readout noise is approximately

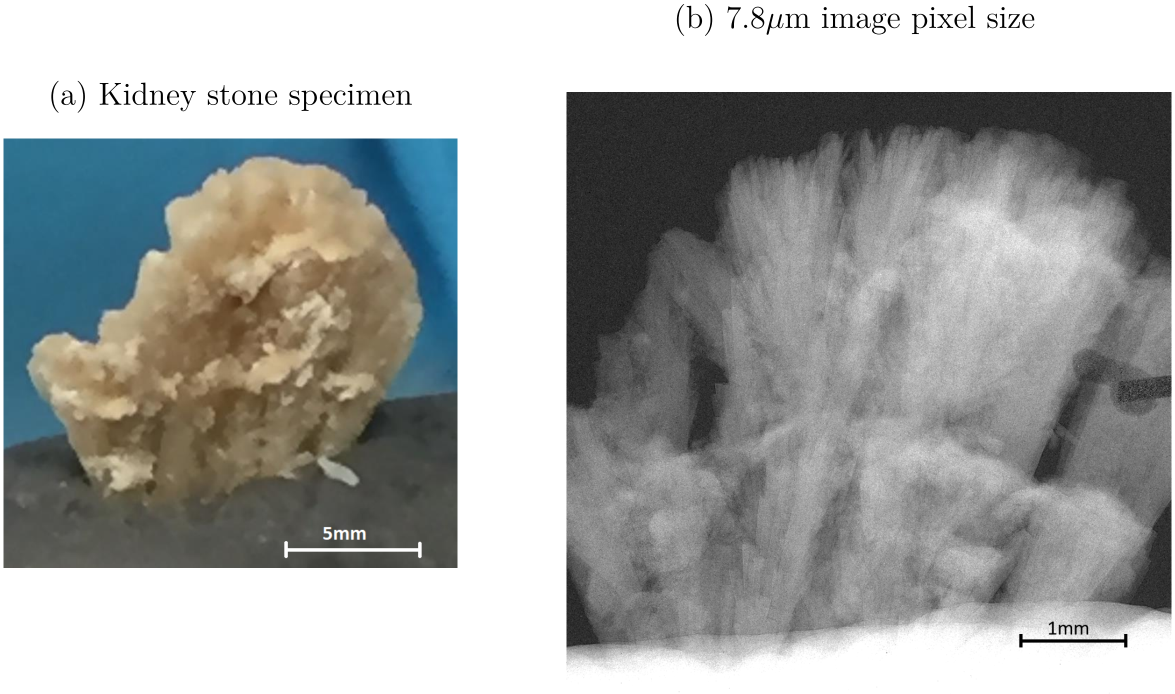
(b) 7.8μm image pixel size

(a) Kidney stone specimen

Figure 4.4: A kidney stone specimen (left) and a high-resolution x-ray image of it acquired with the Se/CMOS sensor.

$^{1}/_{6}$th of total image noise in both designs.

Measured DQE(0) value of 0.3 matches quantum efficiency predictions for Se with the 60kV x-ray spectrum. For conventional design, DQE follows the expected sinc$^2(au)$ response resulting in low DQE at high frequencies. Whereas the AAP design has a flat DQE curve and maintains the same DQE(0) value up to the image cut-off frequency. The AAP design has 2.5× greater DQE than conventional design near 10.6 cyc/mm.

4.4.2 Specimen image

Fig. 4.6 shows conventional and AAP x-ray images of a kidney stone specimen. At first glance, both images might appear very similar due to both conventional and AAP designs having the same DQE values at low frequencies. Upon closer inspection, differences are apparent in areas of fine-detail and near edges due to differences in high-frequency DQE between detector designs. For example, small structures near the top of the stone (white

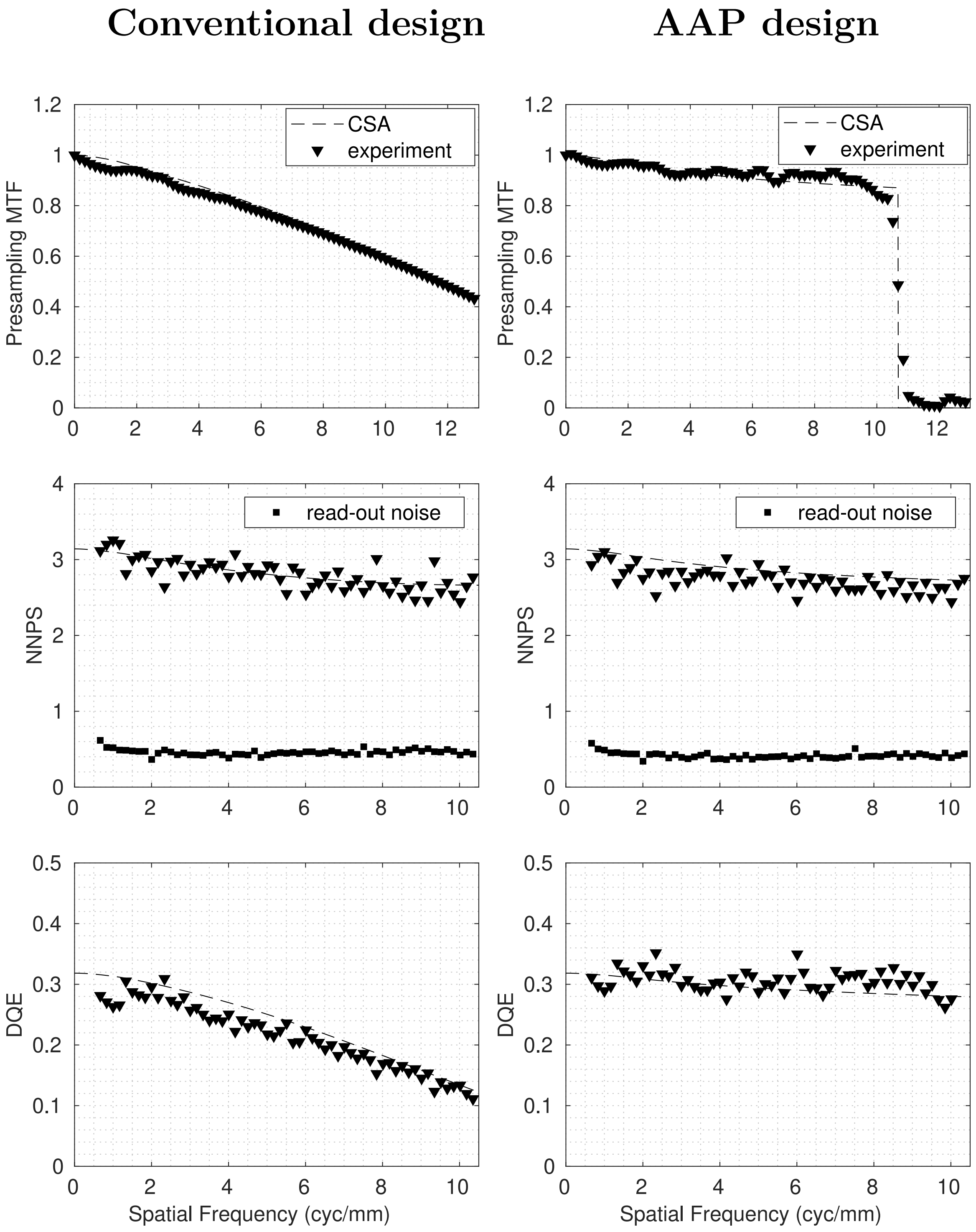

Figure 4.5: Presampling MTF, NNPS and DQE results of conventional (left) and AAP (right) designs showing theoretical CSA and measured results. MTF and DQE of the AAP design is found to be 1.5 × and 2.5 × greater at high-frequencies than conventional design. The DQE curve in the conventional design is reduced with frequency due to noise aliasing, as expected, where as the AAP design has a flat DQE curve across all frequencies.

(a) Conventional image (b) AAP image

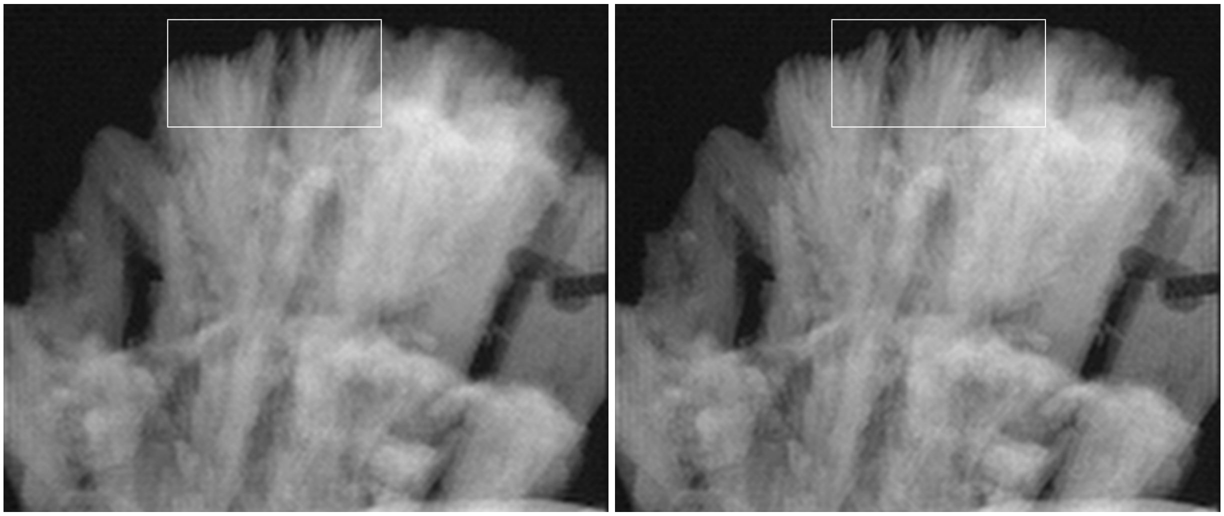

Figure 4.6: Conventional image (left, binned 6 × 6) and AAP image (right) of a kidney stone specimen at 47μm pixel size. The AAP image shows greater visibility of fine-detail (such as in the white box) than conventional. X-ray images have been log transformed, inverted and sinc interpolated for display and magnification purposes.

box) appear sharper and more visible in the AAP image compared to conventional. Sharper edges are also visible in other areas of the AAP image.

4.5 Discussion

This is the first implementation of the AAP x-ray detector design with a small-area micro-sensor array prototype. The AAP design has near-flat MTF and DQE curves up to 10.6 cyc/mm using images having 47μm pixel size (an approximate pixel size used for mammography). At this pixel size, our sensor had uncorrelated pixel values (ie. a flat NPS curve) indicating that there is little effect of converter blur (from charge migration) or x-ray reabsorption. In this case, SNR in a conventional image is limited by pixel aperture size and DQE is reduced at high frequencies from noise aliasing.

CSA results for conventional and AAP designs show excellent agreement for all frequencies (Fig. 4.5). MTF of the conventional design follows an ideal-sinc aperture with size 47μm, and MTF of the AAP design is flat indicating again negligible effects from converter blur and x-ray reabsorption. With such a converter, more than 2.5× improvement is observed at high frequency DQE with the AAP design.

Improvements in MTF and DQE with the AAP design are apparent in specimen images showing high SNR of small structures and fine-detail near edges. Specimen images with the AAP design more accurately represent high-resolution detail of the object being imaged.

4.6 Conclusion

The apodized-aperture pixel (AAP) design is a novel x-ray detector design that makes physical separation between sensor elements and image pixels. Using a micro-sensor array and an anti-aliasing filter, the AAP design removes signal and noise aliasing in images. We show the first implementation of the AAP design using a small-area Se/CMOS micro-sensor array prototype with 7.8μm element size to synthesize images of 47μm pixel size. The impact of the AAP design was 1.5× and 2.5× greater MTF and DQE respectively near the image cut-off frequency of 10 cyc/mm. Specimen images show the potential benefit that the AAP approach could provide at better visualizing fine-detail in images.

4.7 Appendix

4.7.1 CSA equation results summary

Signal and noise properties of secondary quanta released from x-ray interactions in the converter layer have been previously described using a simple-atom model.[22] The model uses a generalized x-ray interaction model consisting of three path that describe liberation of quanta from interactions with: A) no x-ray emission/scatter, B) x-ray emission/scatter but no reabsorption, and C) reabsorption. Liberated quanta for each type of x-ray interaction, $\tilde{\mathrm{q}}_{\mathrm{x}}(x)$, is given as the sum of each path:

$$\tilde{\mathrm{q}}_{\mathrm{x}}(x) = \tilde{\mathrm{q}}_{\mathrm{A}}(x) + \tilde{\mathrm{q}}_{\mathrm{B}}(x) + \tilde{\mathrm{q}}_{\mathrm{C}}(x), \tag{4.9}$$

where $\tilde{\mathrm{q}}_{\mathrm{A}}(x)$, $\tilde{\mathrm{q}}_{\mathrm{B}}(x)$ and $\tilde{\mathrm{q}}_{\mathrm{C}}(x)$ are quanta liberated by each path of a particular x-ray interaction type. The mean number of total liberated quanta is given by:

$$\bar{q}_{\mathrm{x}} = \bar{q}_{\mathrm{o}} P_{\mathrm{x}} \left[(1 - s_{\mathrm{x}}) \, \bar{g}_{\mathrm{x,A}} + s_{\mathrm{x}} \left(\bar{g}_{\mathrm{x,B}} + r_{\mathrm{x}} \bar{g}_{\mathrm{x,C}} \right) \right]$$

where P_{x} is the probability of a photoelectric interaction, s_{x} is the probability that an x-ray will produce an emitted/scattered photon, $\bar{g}_x$ is the mean gain for each path (with variance $\sigma_{\bar{g}}^2$) and r_{x} is the probability the an emitted/scattered photon will be reabsorbed.

For photoelectric interaction, P_{PE} is calculated based on the x-ray probability of interacting in the converter. The probability of an interaction producing a scattered photon $s_{\mathrm{PE}} = P_{\mathrm{K}} \omega_{\mathrm{K}}$ where P_{K} is the K-shell participation fraction and ω_{K} is fluorescence yield. The reabsorption probability r_{PE} and reabsorption relocation function $R_{\mathrm{K}}(u)$ can be calculated using methods described by Hajdok et. al.[21] The mean gain for each path is given by: $\bar{\mathrm{g}}_{\mathrm{PE,A}} = E/w$, $\bar{\mathrm{g}}_{\mathrm{PE,B}} = (E - E_{\mathrm{K}})/w$ for $E > E_{\mathrm{K}}$ else 0, and $\bar{\mathrm{g}}_{\mathrm{PE,C}} = E_{\mathrm{K}}/w$ for $E > E_{\mathrm{K}}$ else 0; where E is the x-ray energy, E_{K} is the characteristic x-ray energy and w is the effective work energy required to liberate one secondary quantum. All gain stages were assumed to have Poisson statistics with $\sigma_g^2 = \bar{g}$.

Bibliography

[1] C. Fink, P. J. Hallscheidt, G. Noeldge, A. Kampschulte, B. Radeleff, W. P. Hosch, and J. Hansmann, "Clinical comparative study with a large-area amorphous silicon flat-panel detector: image quality and visibility of anatomic structures on chest radiography," *Am. J. Roentgenol.*, vol. 178, no. 2, pp. 481–486, 2002.

[2] A. M. Chiarelli, S. A. Edwards, M. V. Prummel, D. Muradali, V. Majpruz, S. J. Done, P. Brown, R. S. Shumak, and M. J. Yaffe, "Digital compared with film mammography: Performance measure in concurrent cohorts with an organized breast screening program," *Radiology*, vol. 268, no. 3, pp. 684–693, 2013.

[3] M. J. Yaffe, A. K. Bloomquist, D. M. Hunter, G. E. Mawdsley, A. M. Chiarelli, D. Muradali, and J. G. Mainprize, "Comparative performance of modern digital mammography systems in a large breast screening program," *Med. Phys.*, vol. 40, no. 12, p. 121915, 2013.

[4] R. Shaw, "The equivalent quantum efficiency of the photographic process," *J. Photogr.*, vol. 11, pp. 199–204, 1963.

[5] J. C. Dainty, *Image Science: Principles, Analysis, and Evaluation of Photographic-Type Image Processing.* Academic Press, 1974.

[6] I. A. Cunningham, W. M. S., and A. Fenster, "A spatial-frequency dependent quantum accounting diagram and detective quantum efficiency model of signal and noise

propagation in cascaded imaging systems," *Medical Physics*, vol. 21, no. 3, pp. 417–427, 1994.

[7] I. A. Cunningham, J. Yao, and V. Subotic, "Cascaded models and the DQE of flat-panel imagers: Noise aliasing, secondary quantum noise and reabsorption," *Proc. SPIE: Medical Imaging*, vol. 4682, pp. 61–72, 2002.

[8] T. Escartin, T. Nano, and I. A. Cunncingham, "Detective quantum efficiency: a standard test to ensure optimal detector performance and low patient exposures," *Proc. SPIE: Medical Imaging*, vol. 9783, March 2016.

[9] E. Ismailova, K. Karim, and I. A. Cunningham, "Apodized-Apreature Pixel design to increase high-frequency DQE and reduce noise aliasing in x-ray detectors," *Proc. SPIE: Medical Imaging*, vol. 9412, 2015.

[10] T. Nano, T. Escartin, K. Karim, and I. A. Cunningham, "A novel x-ray detector design with higher DQE and reduce aliasing: Theoretical analysis of x-ray reabsorption in detector converter material," *Proc. SPIE: Medical Imaging*, vol. 9783, 2016.

[11] T. F. Nano, T. Escartin, E. Ismailova, K. S. Karim, J. Lindstrom, H. K. Kim, and I. A. Cunningham, "MTF and DQE enhancement using an apodized-aperture x-ray detector design," *Med. Phys.*, vol. 44, no. 9, pp. 4525–4535, 2017.

[12] T. Nano and I. A. Cunningham, "Impact of scatter reabsorption and converter blur on MTF and DQE improvements using the apodized-aperture pixel design of x-ray detectors," *Physics in Medicine and Biology*, 2018.

[13] H. Chan, C. Vyborny, H. MacMahon, C. Metz, K. Doi, and E. Sickles, "Digital mammography. roc studies of the effects of pixel size and unsharp-mask filtering on the detection of subtle microcalcifications," *Investigative radiology*, vol. 22, pp. 581–589, July 1987.

[14] M. L. Giger and K. Doi, “Effect of pixel size on detectability of low-contrast signals in digital radiography,” *J. Opt. Soc. Am. A*, vol. 4, pp. 966–975, May 1987.

[15] C. C. Scott, S. Abbaszadeh, S. Ghanbarzadeh, G. Allan, M. Farrier, I. A. Cunningham, and K. S. Karim, “Amorphous selenium direct detection CMOS digital x-ray imager with 25 micron pixel pitch,” *Proc. SPIE: Medical Imaging*, vol. 9033, 2014.

[16] C. C. Scott, A. Parsafar, A. El-Falou, P. M. Levine, and K. S. Karim, “High dose efficiency, ultra-high resolution amorphous selenium/CMOS hybrid digital x-ray imager,” in *IEEE Int. Electron Devices Meet.*, pp. 30.6.1–30.6.4, Dec 2015.

[17] A. Parsafar, C. C. Scott, A. El-Falou, P. M. Levine, and K. S. Karim, “Direct-conversion CMOS x-ray imager with 5.6um x 6.25um pixels,” *IEEE Electron Device Lett.*, vol. 36, pp. 481–483, May 2015.

[18] J. T. Dobbins, D. L. Ergun, L. Rutz, D. A. Hinshaw, H. Blume, and D. C. Clark, “Dqe(f) of four generations of computed radiography acquisition devices.,” *Med. Phys.*, 1995.

[19] I. A. Cunningham and R. Shaw, “Signal-to-noise optimization of medical imaging systems,” *J. Opt. Soc. Am. A*, 1999.

[20] H. H. Barrett and W. Swindell, *Radiological Imaging: The Theory of Image Formation, Detection, and Processing.* Academic Press, 1996.

[21] G. Hajdok, J. Yao, J. J. Battista, and I. A. Cunningham, “Signal and noise transfer properties of photoelectric interactions in diagnostic x-ray imaging detectors,” *Medical Physics*, vol. 33, no. 10, pp. 3601–3610, 2006.

[22] S. Yun, J. Tanguay, H. K. Kim, and I. A. Cunningham, “Cascaded-systems analyses and the detective quantum efficiency of single-Z x-ray detectors including photoelec-

tric, coherent and incoherent interactions," *Medical Physics*, vol. 40, no. 4, p. 041916, 2013.

[23] D. M. Tucker, G. T. Barnes, and D. P. Chakraborty, "Semiempirical model for generating tungsten target x-ray spectra," *Med Phys*, vol. 18, pp. 211–218, 1991.

Chapter 5

Signal-to-noise ratio criteria to suppress Gibbs ringing with the apodized-aperture x-ray detector design

We define a criterion for avoiding Gibbs ringing with the AAP design based on image quantum noise. For contrast-limited features, it is shown that ringing artifacts surpass image noise and may be be visible. An optimized AAP filter with a smooth cut-off frequency transition and cut-off frequency is developed to suppress Gibbs ringing while maintaining 92% of the AAP benefit in MTF and DQE. For noise-limited features, Gibbs ringing is avoided because ringing artifacts are not visible above image quantum noise. Therefore, a low-pass filter with an abrupt cut-off can be used to achieve the most AAP benefit.

This chapter is based on a manuscript in preparation for submission to Medical Physics: TF Nano and IA Cunningham.

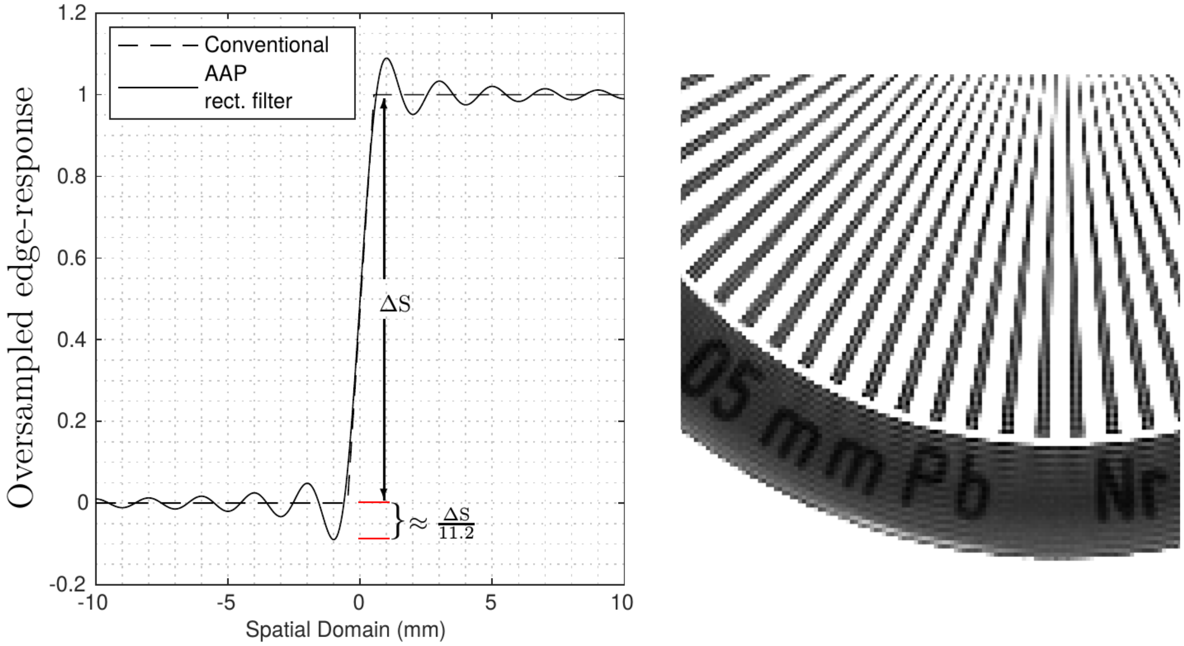

Figure 5.1: Oversampled edge response with conventional and AAP designs (left), and a star-pattern x-ray image (right) with the AAP design. Gibbs ringing is a phenomena that causes artifacts appearing as oscillations emanating from high-contrast edges as a consequence of a sharp low-pass filter with the AAP approach.

5.1 Introduction

X-ray imaging in medicine should produce images with high signal-to-noise ratio (SNR) while maintaining low risk from ionizing radiation to provide medical information for patient benefit. Acquisition of high SNR images while maintaining low x-ray exposures requires high performing x-ray detectors.[1] An x-ray detector's ability to acquire high contrast images in low-noise (or high-contrast) cases is quantified by the modulation transfer function (MTF), whereas detector dose-efficiency in noise-limited images is quantified by the detective quantum efficiency (DQE).[2, 3] Fourier metrics, such as MTF and DQE that are spatial-frequency dependent, are important because they allow one to determine image contrast and SNR for an object of any size. An "ideal" x-ray detector has unity MTF and DQE for all image frequencies and is only limited by the Poisson statistics of counting photons.[4]

We previously described an x-ray detector design, called apodized-aperture pixel (AAP), that uses smaller sensor elements than pixel size to synthesize images where each pixel value is a weighted combination of "micro-sensor" element output.[5, 6, 7] With a high-resolution converter layer, this approach results in a 40% increase in high-frequency MTF and more than double DQE values near the image sampling cut-off frequency u_c. The AAP approach improves MTF and DQE by preserving the micro-element aperture MTF and avoiding aliasing using a low-pass filter (ie. the AAP filter). Suppression of aliasing using a low-pass filter with a sharp cut-off that causes discontinuity, such as rectangular filter that is unity for frequencies below u_c and zero for higher frequencies, can result in ringing known as Gibbs phenomenon.[8, 9] Figure 5.1 shows damped-oscillations in the AAP response of a noise-free edge compared to conventional design, and an x-ray image of a star-patter that has Gibbs ringing near high-contrast edges.

Previous work of the AAP approach used a rectangle low-pass AAP filter to remove aliasing which could cause Gibbs ringing artifacts near high-contrast edges. The objective of this study is to determine an AAP filter that avoids Gibbs ringing while also improving high-frequency MTF and DQE.

5.2 Methods

5.2.0.1 SNR criteria to avoid Gibbs ringing

Gibbs ringing may not be visible in an image if the noise level is greater than the ringing artifact amplitude. The ringing amplitude is greatest at oscillation near the edge, and it is approximately $^{1}/_{10}$th of the signal difference ΔS at the edge as shown in Fig. 5.1. Given a mean pixel value $\bar{d}$ and noise standard deviation $\sigma_{\bar{d}}$, for Gibbs ringing can be avoided when,

$$\frac{\Delta \mathrm{S}}{11.2} \;<\; \sigma_{\bar{\mathrm{d}}}. \tag{5.1}$$

Setting the threshold criteria value equal to the peak amplitude that is closest to the edge ensures that all other peaks are not visible. For an x-ray distribution with mean number of quanta per unit area $\bar{q}_\mathrm{o}$ over the open-side of the edge, $\bar{q}_\alpha = (1-\alpha)\bar{q}_\mathrm{o}$ is the mean number of quanta on the attenuated-side of the edge where α is the attenuation factor. A Gibbs line artifact of length N elements having area a is avoided when the under and overshoot are less than the noise standard deviation, $\sigma_{\bar{d}} = k\sqrt{Na\bar{q}}$, where k is the detector gain and the number of quanta interacting in a sensor follows Poisson statistics.[10] The edge signal difference $\Delta\mathrm{S} = (\bar{d} - \bar{d}_0) = kNa\alpha\bar{q}_\mathrm{o}$ and we can rewrite Eq. 5.1 to give,

$$\frac{kNa\alpha\bar{q}_\mathrm{o}}{11.2} \;<\; k\sqrt{Na\bar{q}_\mathrm{o}(1-\alpha)} \tag{5.2}$$

$$\frac{\alpha}{\sqrt{1-\alpha}} \;<\; 11.2\sqrt{{}^{N}\!/_{a\bar{q}_\mathrm{o}}} \tag{5.3}$$

In the limit of low-attenuating material (as is common in medical imaging), the above equation simplifies to

$$C\sqrt{Na\bar{q}} \;<\; 11.2 \tag{5.4}$$

where C is the contrast of the edge.

Equation 5.4 provides an SNR criteria for when Gibbs ringing becomes visible in x-ray images. It is based on the contrast of an edge and the number of quanta detected by each detector element of area a. This criteria is similar to the Rose-SNR, given by $C\sqrt{A\bar{q}}$,[11, 12] but it differs from it because signal difference is not defined in an area A over many elements. Since ringing occurs in lines parallel to the edge, a similar criterion such as Rose-SNR could be used $C\sqrt{Na\bar{q}}$ where N represents the number of pixels in the line showing ringing. Figure 5.2 shows conventional and AAP edge-response functions with different noise levels. Gibbs ringing is visible for the lowest noise level

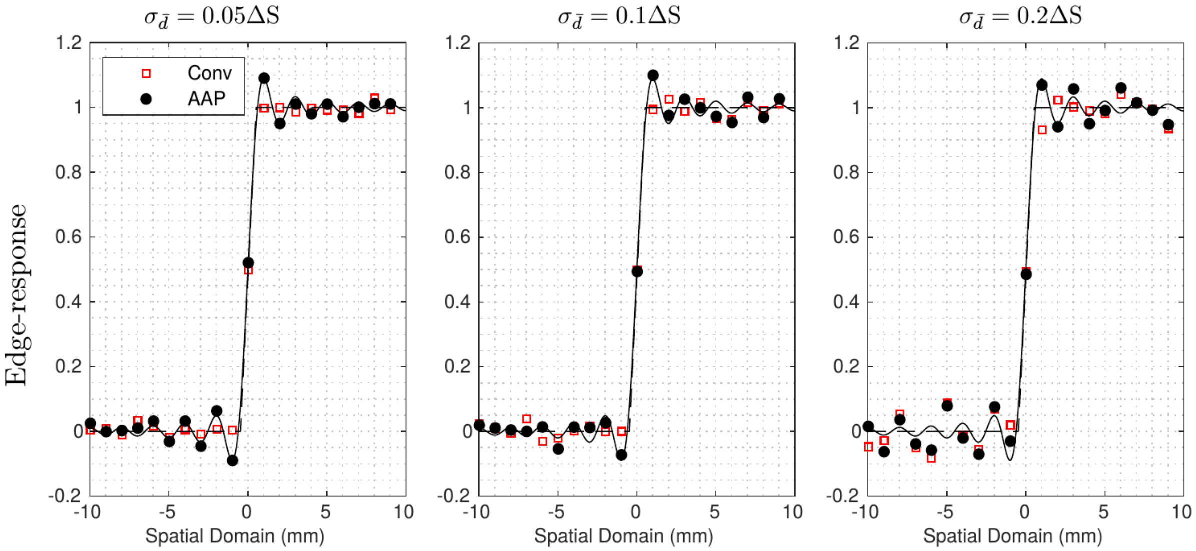

Figure 5.2: Conventional (dashed) and AAP (solid) edge response functions and sampled points (markers) with Gaussian noise having standard deviations of 0.05ΔS, 0.1ΔS and 0.5ΔS where ΔS is the edge signal difference. Gibbs ringing is not visible when noise standard deviation is less than 1/10th of ΔS, as predicted by Eq. 5.4.

and not visible when noise surpasses 1/10th the signal difference of the edge, as predicted by Eq. 5.4. Therefore, medical images that have low-noise and high contrast, such as large calcifications in mammography or sharp bones in radiography, may result in visible Gibbs ringing using the AAP approach.

We validate the criterion for avoiding Gibbs ringing with AAP x-ray images of a star-pattern (Tielung, 0.05 mm Pb thickness, 45 mm diameter, with 2° angled bars) acquired using a clinical mammography system (Hologic Inc.) having a Se converter layer and 0.07 mm sensor elements. Gaussian noise was added to images with a standard deviation equal to a set fraction of edge contrast. AAP images were synthesized to create images with $a = 0.28$ mm using a rectangular low-pass filter as done previously.[7]

We can consider the Gibbs ringing criteria in Eq. 5.4 for typical contrast levels and exposures in medical imaging. The mean number of x-ray quanta incident on a detector $\bar{q} = Q_o X$, where Q_o is the number of photons per unit area per air-KERMA [quanta/mm^2/Gy] of the x-ray spectrum and X is air-KERMA, making $C\sqrt{a\bar{q}} = C\sqrt{aQ_oX}$. A mammog-

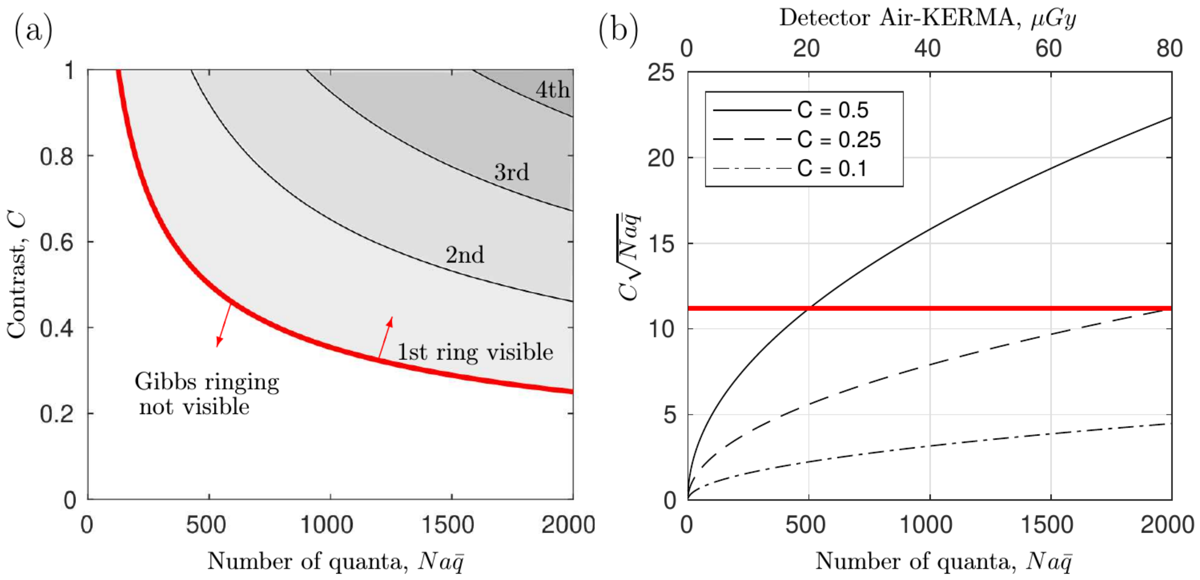

Figure 5.3: (a) A plot showing when Gibbs ringing is visible given image contrast C and number of quanta $\bar{q}$ interacting in a Gibbs line artifact parallel to an edge of length N pixels of size a. For lower contrast or low number of quanta (bottom-left of plot), Gibbs phenomena is not visible. The bold red line is $C\sqrt{Na\bar{q}} < 11.2$ where contrast levels and number of quanta above that line show ringing. (b) Visibility of different contrast levels as a function number of quanta or air-KERMA incident on an x-ray detector. For typical mammography air-KERMA incident on the detector of 10-50μGy, most image contrast levels would not show ringing as they are below the SNR visibility criteria (bold red line).

raphy x-ray spectrum from a molybdenum target at 28kV, using a typical skin entrance air-KERMA of 5mGy,[13] would have an incident air-KERMA of approximately 50μGy on the detector. At this technique, a large calcification (0.5-1mm) in the breast will have a contrast of about $C = 0.5$, a medium sized calcification (0.1-0.2mm) has a contrast of about $C = 0.25$, and soft-tissue lesions have contrast of about $C = 0.1$. Figure 5.3(a) shows the relationship between contrast and number of quanta interacting in the detector that could result in visible Gibbs ringing. Figure 5.3(b) shows a plot of the Gibbs visibility criteria of these three contrast levels as a function of air-KERMA incident on the detector.

For typical mammography exposures, the Gibbs ringing visibility threshold Eq. 5.4 is only passed for contrast $C > 0.25$ as would be achieved for large calcifications. Therefore, we conclude that most medical image features are noise-limited and do not cause ringing artifacts. For higher exposures or non-medical imaging applications with high contrast, ringing could be undesirable in AAP image that use a low-pass filter with an abrupt frequency cut-off.

An AAP filter that does not have a sharp cut-off for reduced Gibbs ringing requires optimization because there is a trade-off between Gibbs reduction and AAP benefit. A filter that has a less abrupt cut-off by attenuating frequencies below the image cut-off will reduce MTF benefit with the AAP approach. On the other hand, a filter that has a less abrupt cut-off by not blocking frequencies above the image cut-off allows some aliasing and reduces DQE benefit with the AAP approach. This trade-off can be investigated by modifying two filter parameters: frequency cut-off smoothness and frequency transition point.

5.2.1 AAP filter with reduced Gibbs ringing

Filter kernels are extensively used for various applications, and as a result, characteristics of common filters (such as side-lobe level, side-lobe fall off, etc.) have been quantified and their benefits have been previously described.[14, 15] Although these characteristics are useful, it is still unclear how such a filter would impact MTF and DQE benefit with the AAP. Therefore, we aim to determine a low-pass filter that suppresses Gibbs phenomena near high-contrast edges while also improving MTF and DQE with the AAP approach.

We investigate the effects of an arbitrary AAP filter by modifying cut-off smoothness s and frequency transition point u_f. We define a generic AAP filter using the following expression,

$$|\mathrm{F}(u)| \;=\; \frac{1}{2}\left[\mathrm{erf}\left(\frac{u+u_\mathrm{f}}{s}\right)-\mathrm{erf}\left(\frac{u-u_\mathrm{f}}{s}\right)\right]. \tag{5.5}$$

For the limiting case when $s \to 0$ and $u_\mathrm{f} = u_c = {}^1\!/\!_{2a}$, Eq. 5.5 becomes the rectangular low-pass AAP filter with a sharp cut-off. This AAP filter expression was chosen for convenience and easy interpretation, but other filter expressions can be used.

5.2.1.1 AAP filter cut-off smoothness

Modification of parameter s in Eq. 5.5 changes the transition slope at cut-off frequency u_c. Figure 5.4 shows the AAP filter for different parameters s in the spatial and frequency domains. As s increases, the cut-off frequency transition becomes smoother in the frequency domain and side-lobes in the spatial domain decrease.

The edge response function for different filters results in reduced oscillations as parameter s increases. Figure 5.5 shows edge responses for AAP filters with s parameters from Fig. 5.4. It is interesting that the first oscillation in the edge-response does not significantly change, although other side-lobes decrease significantly. We show the effect of smoother AAP filters on Gibbs ringing on x-ray images of a star-pattern and Hologic detector. AAP images were synthesized to create images with $a = 0.28$ mm using different AAP filters of varying smoothness.

5.2.1.2 AAP filter cut-off transition

Modification of parameter u_f in Eq. 5.5 changes the location of the filter cut-off frequency (the frequency location where the filter value is 0.5). Figure 5.6 shows the AAP filter for different parameters u_f in the spatial and frequency domains for a given parameter s with some smoothness. As u_f changes the cut-off frequency location in the frequency domain, the main-peak of $\mathrm{f}(x)$ changes in width and the side-lobe amplitude does not change by much. This is clearly shown in the edge-response functions in Figure 5.5. We show the effect of different cut-off frequency locations of the AAP filters on Gibbs ringing on x-ray images of a star-pattern and Hologic detector. AAP images were synthesized to create images with $a = 0.28$ mm using different AAP filters.

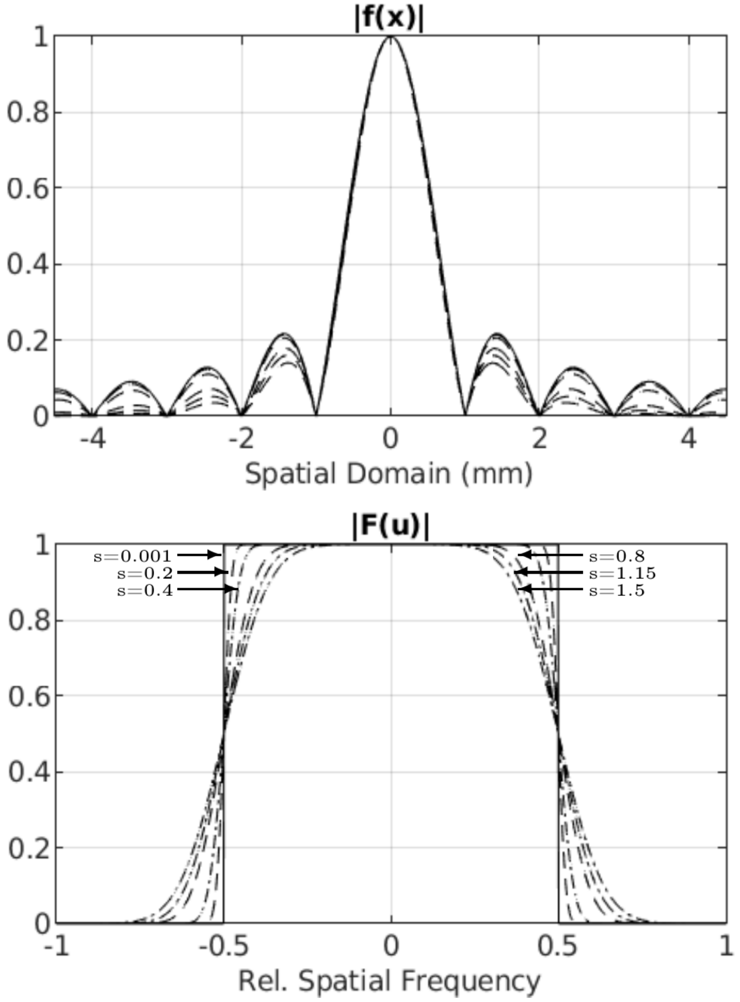

Figure 5.4: AAP filter in the spatial domain (top) and frequency domain (bottom) for different filter cut-off smoothness parameter s. As s increases, the cut-off becomes smoother in the frequency domain and side-lobes of the filter in the spatial domain decrease.

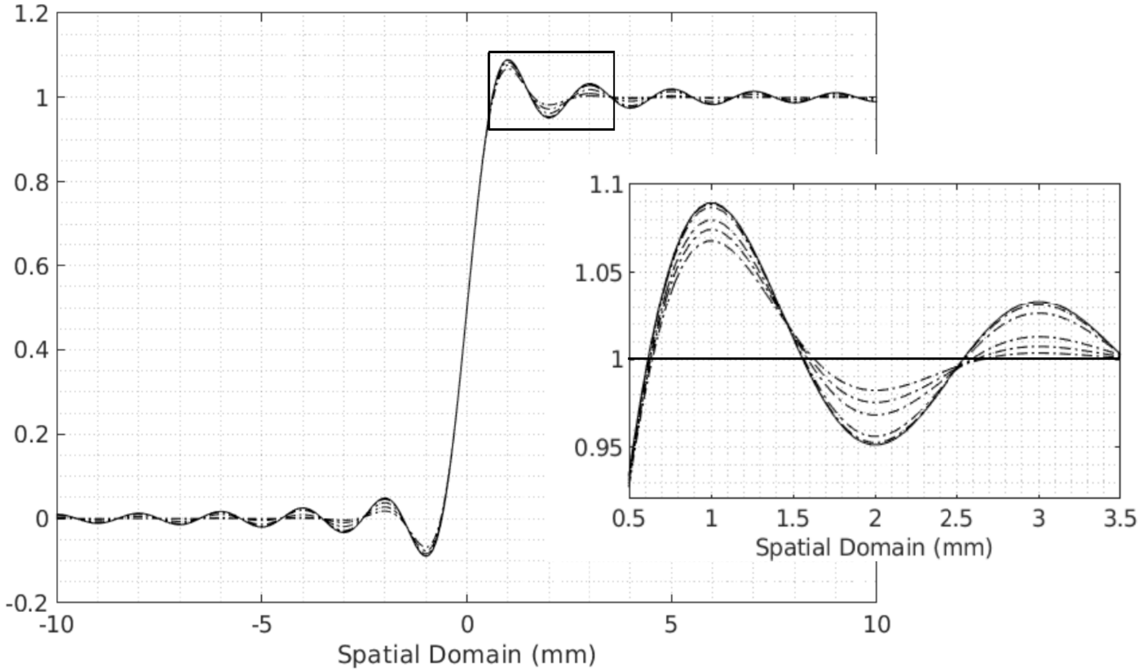

Figure 5.5: Edge-spread function with different AAP filters having increased smoothness s. As cut-off frequency transition becomes smoother, the amplitude of the side-lobes away from the edge are reduced, although the 1st side-lobe does not change.

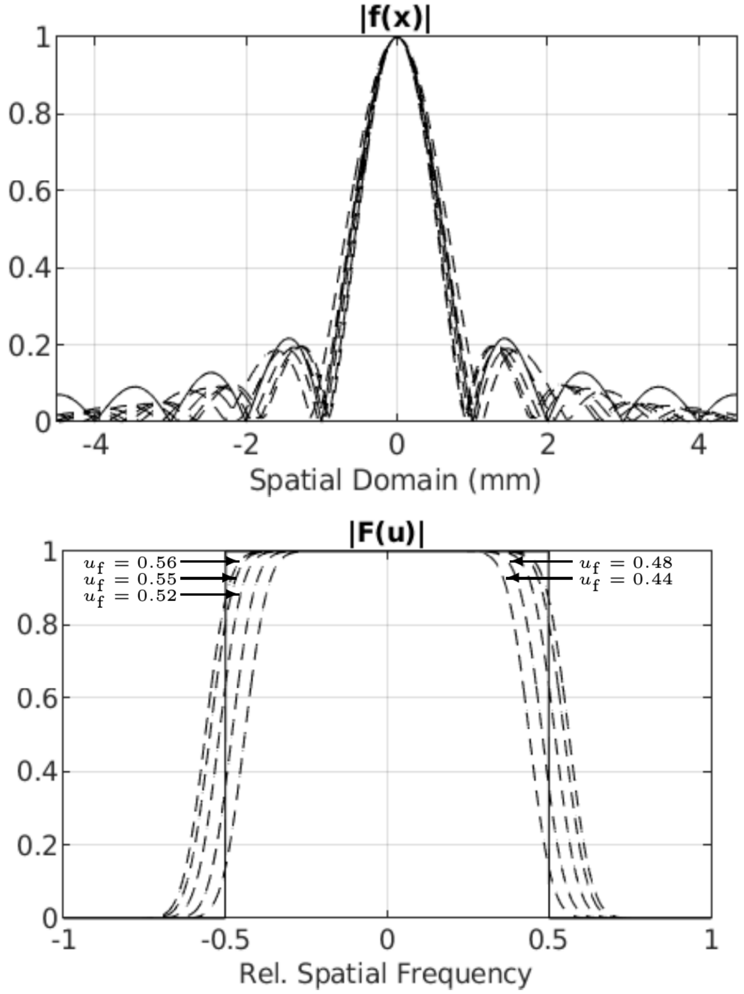

Figure 5.6: AAP filter in the spatial domain (top) and frequency domain (bottom) for different filter cut-off location parameters u_{f} for a set smoothness parameter $s = 0.4$. As u_{f} changes the cut-off frequency location, the main-lobe of f(x) changes in width and the side-lobe amplitude is not affected as much.

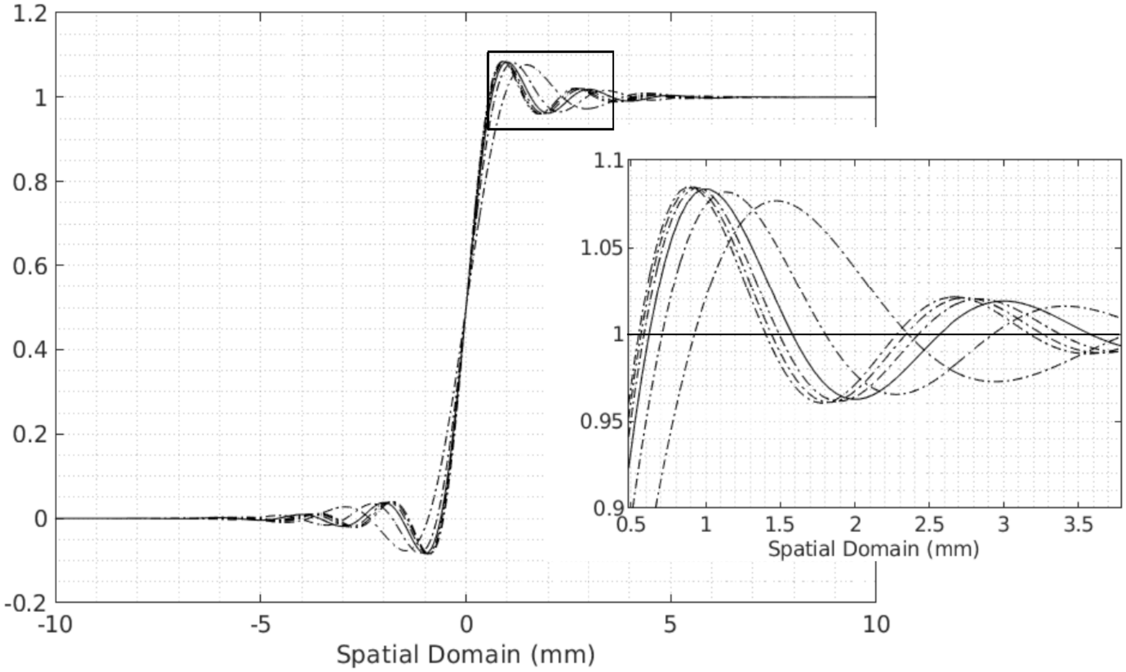

Figure 5.7: Edge-spread function with different AAP filters having different frequency cut-off locations. A change in the frequency cut-off location does not change the under- and overshoot amplitudes, but it spreads them apart or narrows them together.

5.2.2 MTF and DQE benefit

We evaluate the effect of the AAP filter with different parameters for smoothness (s) and cut-off frequency location (u_f) on the AAP design. MTF and DQE curves are most useful as a function of spatial frequency as it shows effects and importance of different frequencies. A way of quantifying frequency-dependent metrics into a single number could be using the integral under the curve for given image frequencies. We define the MTF and DQE benefits with the AAP approach as a percentage,

$$\mathrm{MTF}_{\mathrm{benefit}} = \frac{\int_{-1/2a}^{1/2a} \mathrm{sinc}(\epsilon u)\,|\mathrm{F}(u)|\,\mathrm{d}u - \int_{-1/2a}^{1/2a} \mathrm{sinc}(au)\,\mathrm{d}u}{\int_{-1/2a}^{1/2a} \mathrm{sinc}(\epsilon u)\,\mathrm{d}u - \int_{-1/2a}^{1/2a} \mathrm{sinc}(au)\,\mathrm{d}u} \times 100\% \tag{5.6}$$

$$\mathrm{DQE}_{\mathrm{benefit}} = \frac{\displaystyle\int_{-1/2a}^{1/2a} \frac{\mathrm{sinc}^2(\epsilon u)}{1+\sum_{j=1}^{\infty}\left|\mathrm{F}(u\pm\frac{j}{a})\right|^2}\,\mathrm{d}u - \int_{-1/2a}^{1/2a}\mathrm{sinc}^2(au)\,\mathrm{d}u}{\displaystyle\int_{-1/2a}^{1/2a}\mathrm{sinc}^2(\epsilon u)\,\mathrm{d}u - \int_{-1/2a}^{1/2a}\mathrm{sinc}^2(au)\,\mathrm{d}u} \times 100\%. \quad (5.7)$$

These figures-of-merit are essentially the areas between the AAP and conventional curves. The benefit with the AAP approach for a given filter is 100% when the area under the MTF and DQE curves is equal to the area with a low-pass rectangular AAP filter. The benefit is 0% when the area for a given filter is equal to the area of conventional design.

Experimental validation of the AAP approach using a sharp and smooth cut-off filter was performed using a Se/CMOS active pixel sensor with 1k x 1k elements having 7.8 μm size and approximately 1cm^2 sensitive area was used to acquire images. The sensor has a 98 μm thick Se layer, a 50 nm gold top electrode and is digitized using readout electronics with a 16-bit ADC converter. The x-ray beam used for experiments was generated with a micro-focus x-ray source (9 μm focal spot, PXS5-928) with a stationary tungsten target at 60 kV and 2 mm of aluminum filtration having an HVL of 1.7 mm of aluminum. Images were acquired in dynamic mode with 0.136 mAs tube current and 3 second frame integration time with an air KERMA of 85 μGy per frame.

5.3 Results

5.3.1 SNR criteria to avoid Gibbs ringing

Figure 5.8 shows AAP images of a star-pattern having different amount of noise that are close to the criteria for avoiding Gibbs ringing. When image noise has a standard deviation $\sigma_{\bar{d}} = 0.05\Delta\mathrm{S}$, where $\Delta\mathrm{S}$ is the signal difference between background and edge, then Gibbs phenomena is visible as shown in the left panel. This matches with our

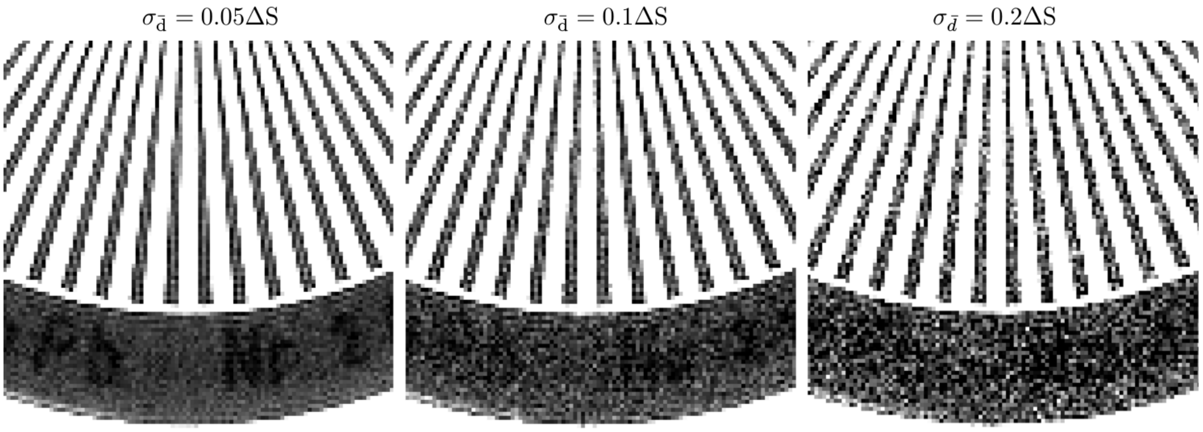

Figure 5.8: Star-pattern x-ray image with simulated Gaussian noise having standard deviation is $0.05\Delta\mathrm{S}$, $0.1\Delta\mathrm{S}$ and $\Delta\mathrm{S}$, where $\Delta\mathrm{S}$ is the signal difference at the edge. The left image shows some ringing, whereas in the other images Gibbs phenomenon is not visible as expected by the Gibbs visibility criteria.

criteria as the ring amplitudes is greater than image noise. When $\sigma_{\bar{d}} = 0.1\Delta\mathrm{S}$, ringing is less visible but it can still be discerned at some locations as shown in the middle panel. However, when $\sigma_{\bar{d}} = 0.2\Delta\mathrm{S}$, ringing is not visible because the ring amplitudes are less than image noise as is predicted by the avoiding Gibbs ringing criteria.

5.3.2 AAP filter with reduced Gibbs ringing

The AAP anti-aliasing filter cut-off smoothness and cut-off frequency are two parameters that can be modified to reduce Gibbs ringing. Below we show the effects on visual Gibbs ringing and AAP improvement for different filter parameters.

5.3.2.1 Filter cut-off smoothness

Figure 5.9 shows theoretical MTF and DQE curves with the AAP approach (black) that implements a different low-pass filter having a smooth cut-off transition for comparison to conventional design (red). The MTF curve is least affected by filter (1) that only slightly attenuates frequencies below the image cut-off ($u_c = 0.5u_s$ where $u_s = {}^{1}\!/_{a}$ is the sampling frequency at spacings of a), and most affected by filter (6) that results in

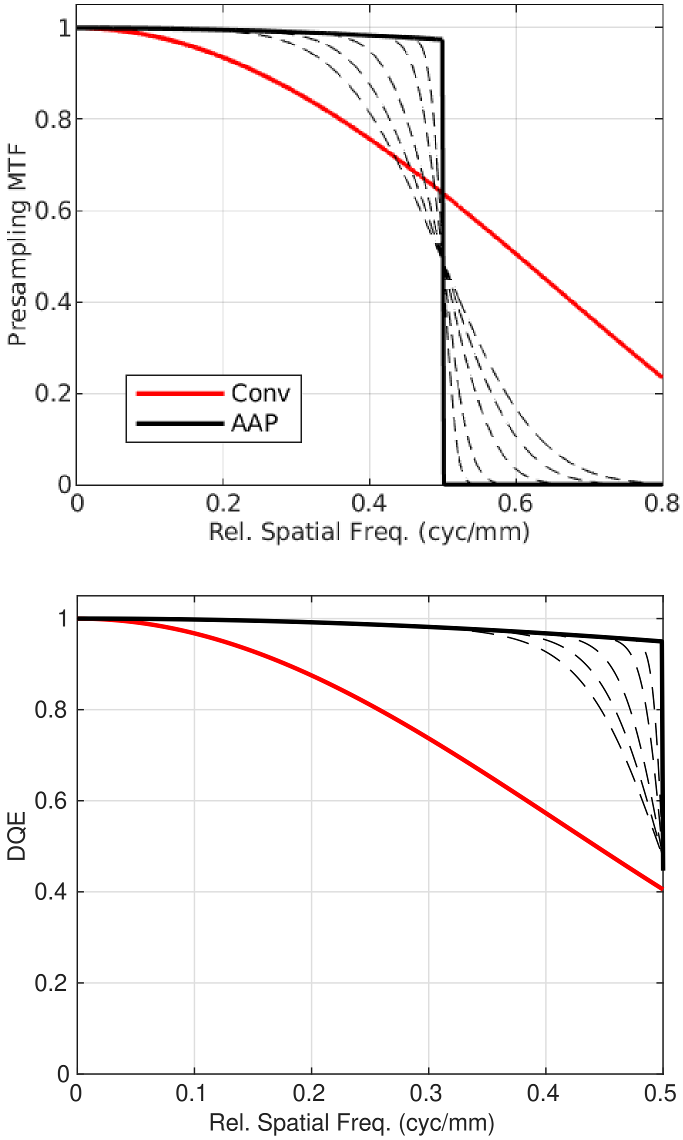

Figure 5.9: MTF and DQE curves with different AAP filter smoothness (black) compared to conventional design (red). Gibbs ringing is reduced with smoother filter cut-off transition, although MTF and DQE benefit can also be reduced.

small MTF improvement with the AAP approach. The DQE curves for different AAP filters are only modestly affected and most of the DQE benefit is lost at a narrow band frequencies near the image cut-off. This reduction is due to a small amount of noise aliasing being allowed by smooth transitioning AAP filters.

Figure 5.10 shows the affect that less abrupt AAP filters cut-off has less Gibbs tining. X-ray images of a star-pattern were synthesized for different filters with increasing smoothness from (1) which is a rectangular low-pass filter to (6) which attenuates high-frequencies the most. The AAP benefit is maximum when using a rectangular low-pass filter, but unfortunately the high-contrast edge of the bar shows severe ringing. Additionally, low-pass filter (6) which shows the least Gibbs ringing would cause a high penalty in DQE benefit. Therefore, an optimum lies between around filter smoothness parameter (3) that only shows the 1st or 2nd overshoot without a large penalty in MTF an DQE.

5.3.2.2 Filter cut-off location

Figure 5.11 shows theoretical MTF and DQE curves with the AAP approach (black) that implements a different low-pass filter having slightly different cut-off transitions. The MTF curve is largely affected when filter cut-off location is below u_c, and the maximum MTF benefit is obtained when the cut-off is above u_c. The DQE curves is least affected when the filter cut-off is below u_c and largely affected at high-frequencies when the filter cut-off is above u_c. The DQE reduction is due to a large amount of noise aliasing being allowed when the filter cut-off frequency is above the image cut-off frequency u_c.

Figure 5.12 shows the affect of a smooth filter having different cut-off frequencies on Gibbs tining on x-ray images of a star-pattern. Filter (1) is a rectangular low-pass filter for references. Filter (2) has a cut-off location below $u_c = 0.5$ and filter (6) has a cut-off location above u_c. The DQE benefit is maximum when using filter (1) because it has the least aliasing, whereas MTF benefit is maximum with filter (6) because it attenuates the least frequencies below u_c. Gibbs ringing is reduced for all filters (2) - (6) because of their

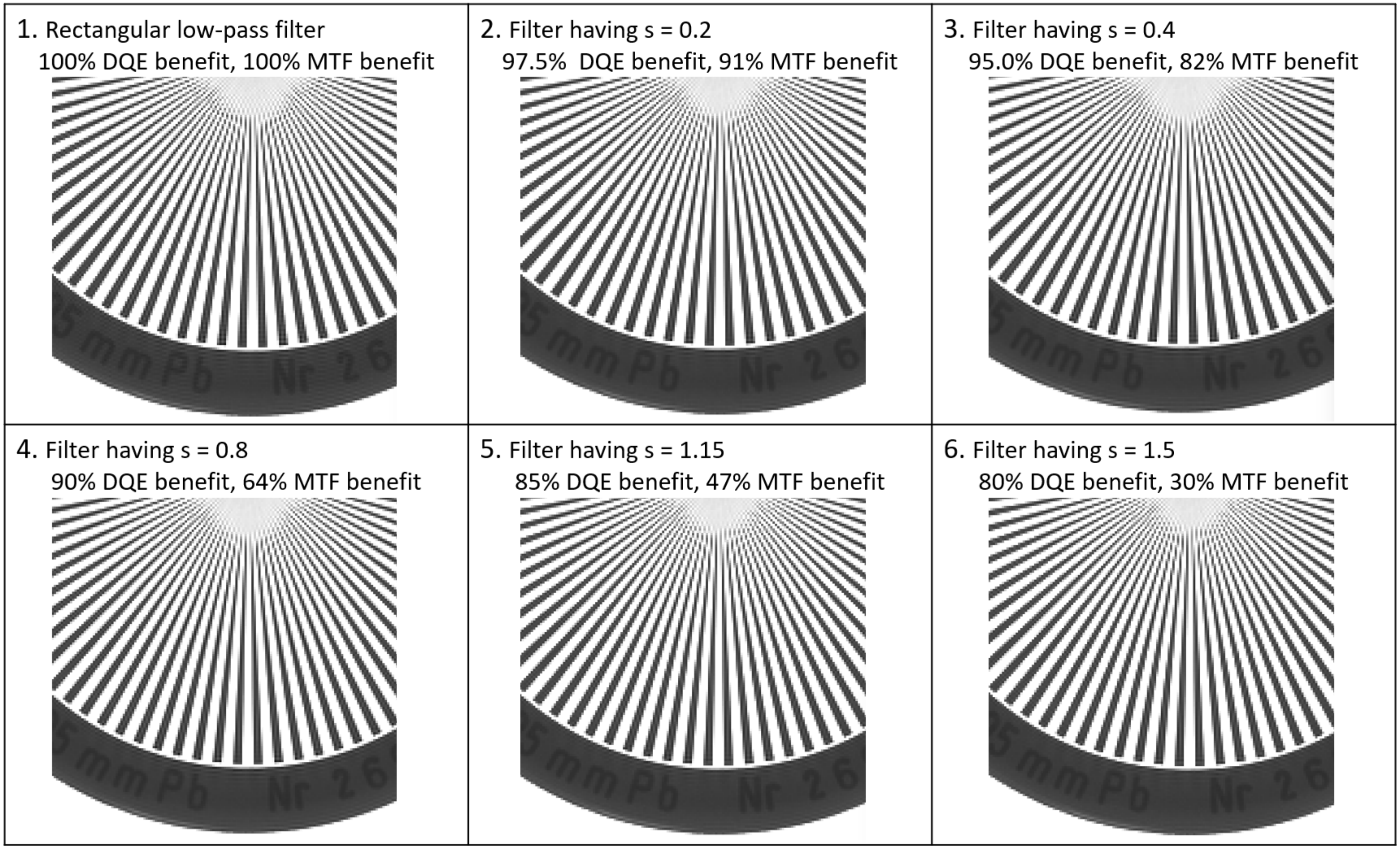

1. Rectangular low-pass filter
100% DQE benefit, 100% MTF benefit

2. Filter having s = 0.2
97.5% DQE benefit, 91% MTF benefit

3. Filter having s = 0.4
95.0% DQE benefit, 82% MTF benefit

4. Filter having s = 0.8
90% DQE benefit, 64% MTF benefit

5. Filter having s = 1.15
85% DQE benefit, 47% MTF benefit

6. Filter having s = 1.5
80% DQE benefit, 30% MTF benefit

Figure 5.10: X-ray images of a star-pattern with the AAP approach for different filter cut-off smoothness. A rectangular low-pass filter (1) shows the most Gibbs ringing while the filter with the smoothest transition (6) has the least ringing. An optimum for reducing ringing and maintaining MTF and DQE benefit with the AAP approach lies around filter (3).

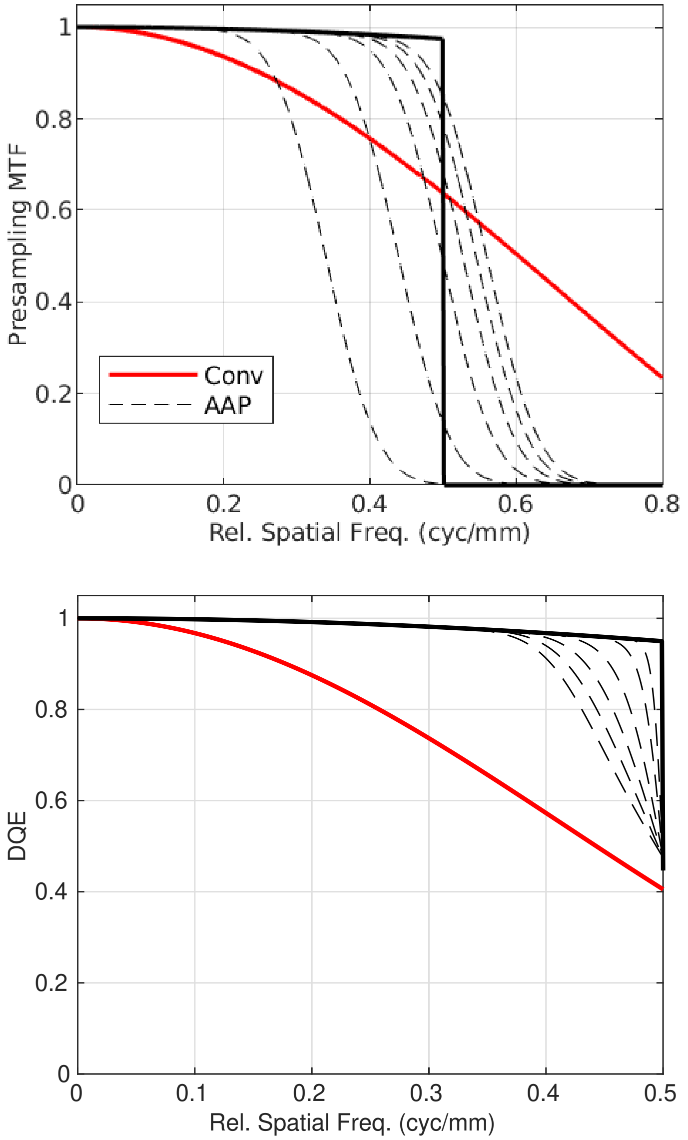

Figure 5.11: MTF and DQE curves with different AAP cut-off transitions u_{f} in frequency (black) compared to conventional design (red). MTF benefit is improved with higher u_{f}, although it results in some noise aliasing that will reduce DQE benefit at high-frequencies.

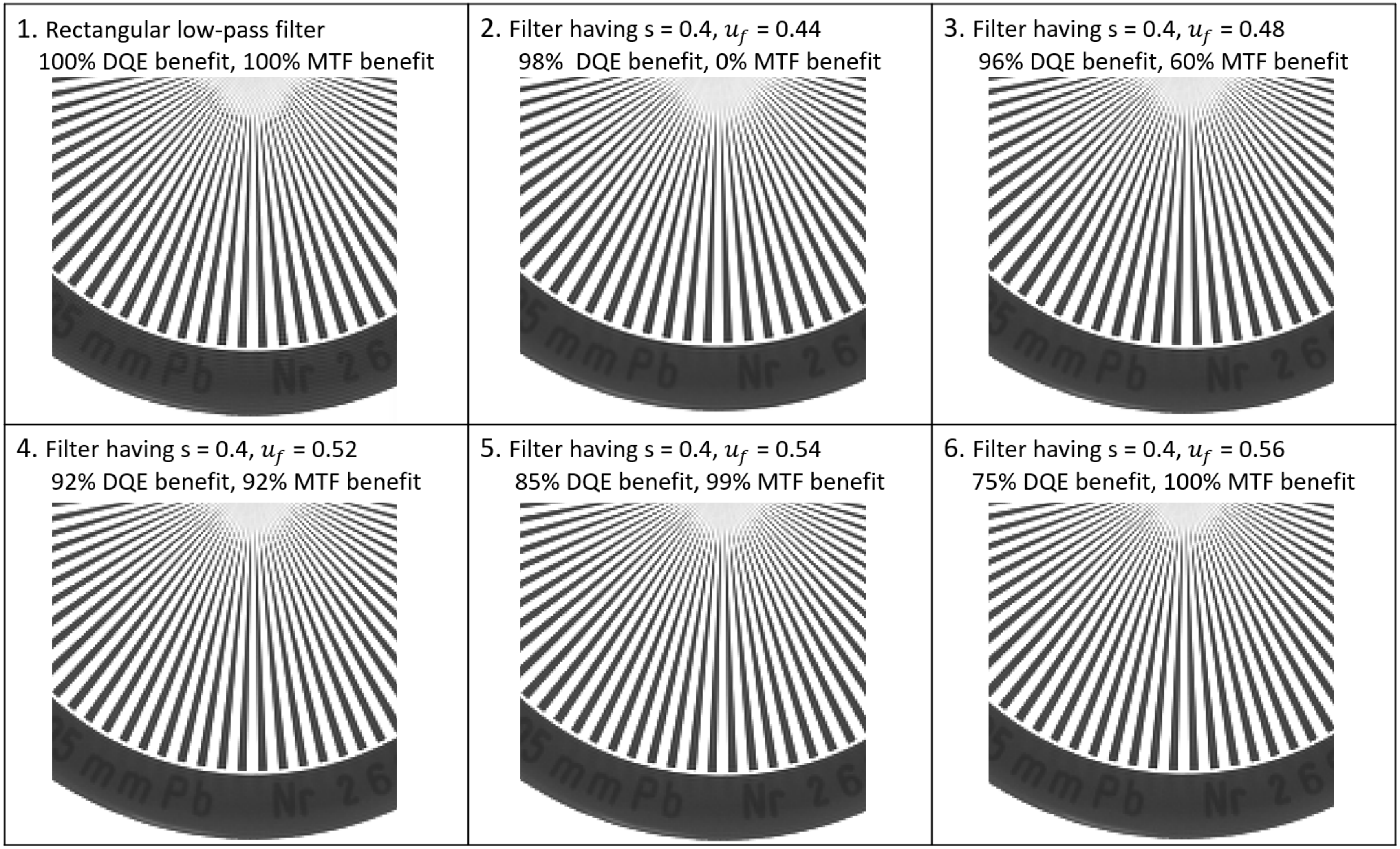

Figure 5.12: X-ray images of a star-pattern with the AAP approach for a smooth filter cut-off with different cut-off frequencies. A rectangular low-pass filter (1) shows the most Gibbs ringing while the filter with the greatest cut-off (6) has the lowest DQE benefit. An appropriate filter that reduces Gibbs ringing while maintaining the highest MTF and DQE benefit with the AAP approach is filter (4).

smooth cut-off frequency transition. Therefore, an appropriate filter that reduces Gibbs ringing while maintaining the highest MTF and DQE benefit with the AAP approach is filter (4).

5.3.3 MTF and DQE benefit

Figure 5.13 shows results of the measured MTF (left) and DQE (right) for the AAP design with an abrupt frequency cut-off (rectangular low-pass) and the modified filter (4) from the previous section. The modified filter has a slightly smoother frequency transition and slightly greater cut-off than a rectangular low-pass. Similar improvements are observed in MTF and DQE with both AAP filters compared to conventional. The AAP approach with the smooth filter has a slightly lower MTF below the image cut-off frequency and slightly greater above the image cut-off that causes aliasing. The small amount of aliasing due to the smooth filter only affects a narrow band of DQE values at the image cut-off frequency.

Figure 5.14 shows the same star-pattern with simulated noise as in Figure 5.8 but images were synthesized using the modified AAP filter that has a slightly smoother and higher cut-off frequency. Gibbs ringing is suppressed in all images and there is a slight "edge-enhancement" effect.

5.4 Discussion

The AAP approach avoids aliasing by band-limiting frequency response to the image cut-off frequency, and this may cause Gibbs ringing near high-contrast edges. We determined an SNR-based criteria for when Gibbs ringing is not visible in an image: $C\sqrt{a\bar{q}} < 11.2$ where C is contrast, a is detector element area and $\bar{q}$ is the mean number of x-rays per mm^2. This criteria is satisfied in medical images when trying to discern low-contrast features using an acceptable low amount of radiation. However, the crite-

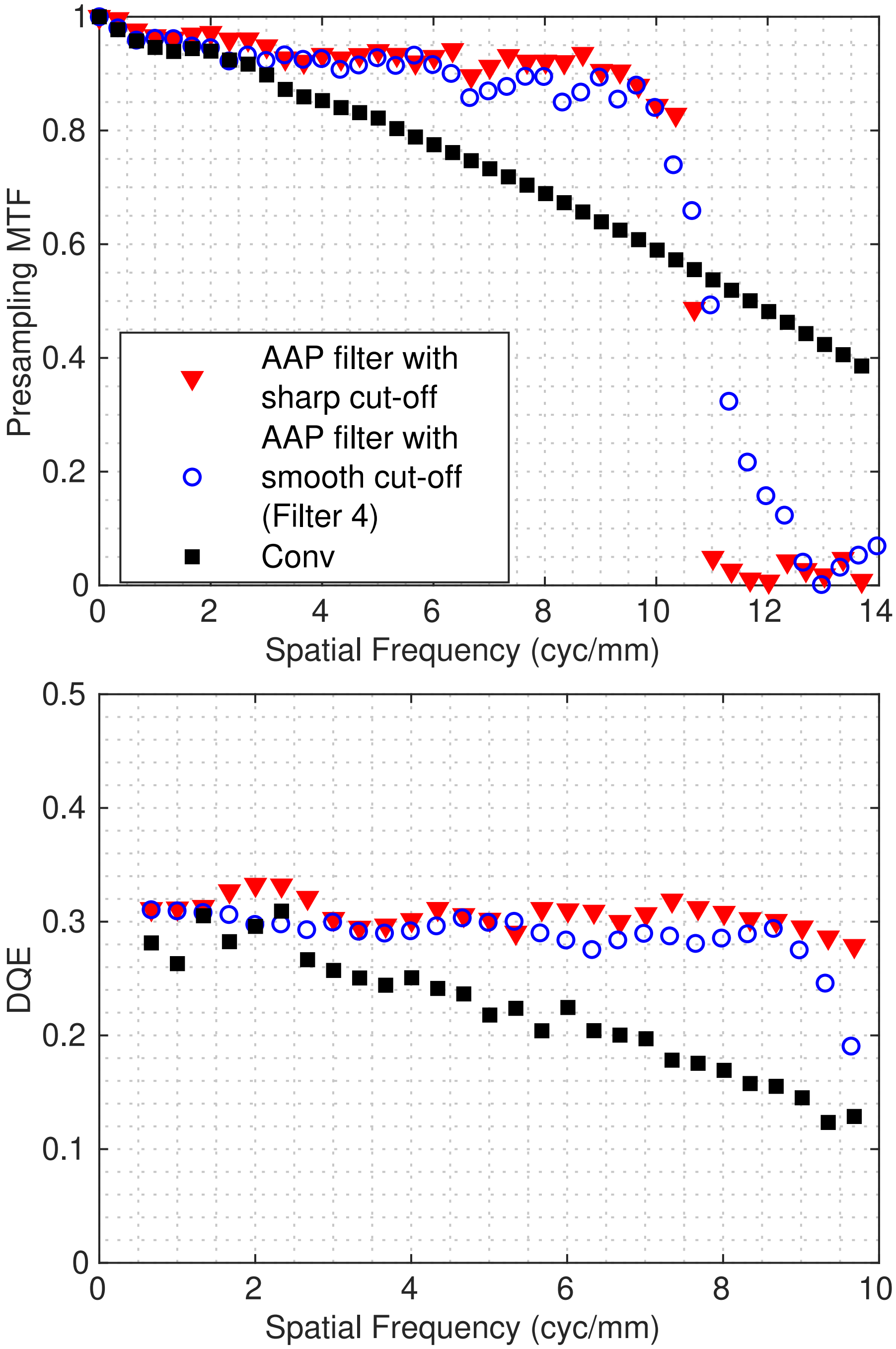

Figure 5.13: Measured MTF (left) and DQE (right) for the AAP design with an abrupt frequency cut-off (rectangular low-pass) and a slightly smooth cut-off (filter 4 from the previous section) compared to a conventional design. The smooth cut-off filter has a small affect on MTF and DQE curves with the AAP approach, providing almost the same improvement at high-frequencies.

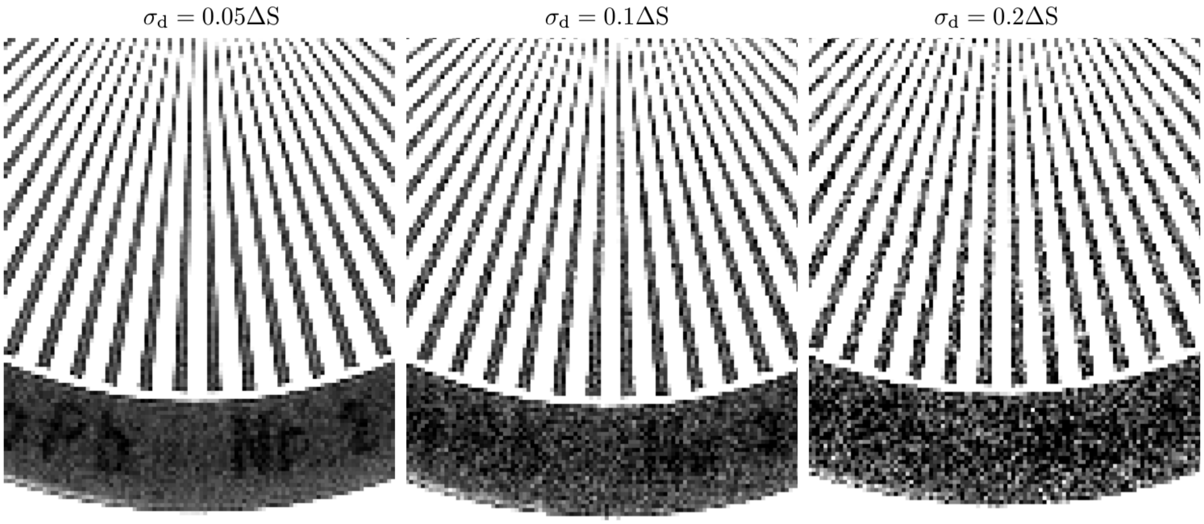

Figure 5.14: The same star-pattern with simulated noise as in Figure 5.8 but images were synthesized using the modified AAP filter that has a slightly smoother and higher cut-off frequency. Gibbs ringing is suppressed in all images and there is a slight "edge-enhancement" effect.

ria for avoiding Gibbs ringing near high-contrast edges is not satisfied. Therefore, we demonstrate a worst-case scenario of Gibbs ringing in AAP images using star-pattern images because they have very high contrast and low noise.

For contrast-limited images, the abrupt cut-off of a rectangular low-pass filter with the AAP approach is not ideal because it would cause Gibbs ringing near sharp edges. We modified the AAP filter by slightly smoothening the cut-off transition ($s = 0.4$) to reduce ringing. However, a smoother filter also reduces the AAP benefit. So we further modified the AAP filter by slightly increasing the filter cut-off frequency ($u_\mathrm{f} = 0.52$) to achieve 92% of the AAP benefit. This modified AAP filter achieves high MTF and DQE at high-frequencies without Gibbs ringing in contrast-limited images. The edge response of the modified AAP filter still shows the 1st under and overshoot, as shown in Figure 5.15, although this might be desirable as it slightly "edge-enhances" the image.

For noise-limited images, the criteria to avoid Gibbs ringing is satisfied as is shown by simulations of noise-limited images in Figure 5.8 where Gibbs ringing is not visible. Therefore, a rectangular low-pass filter should be used to obtain 100% of the AAP bene-

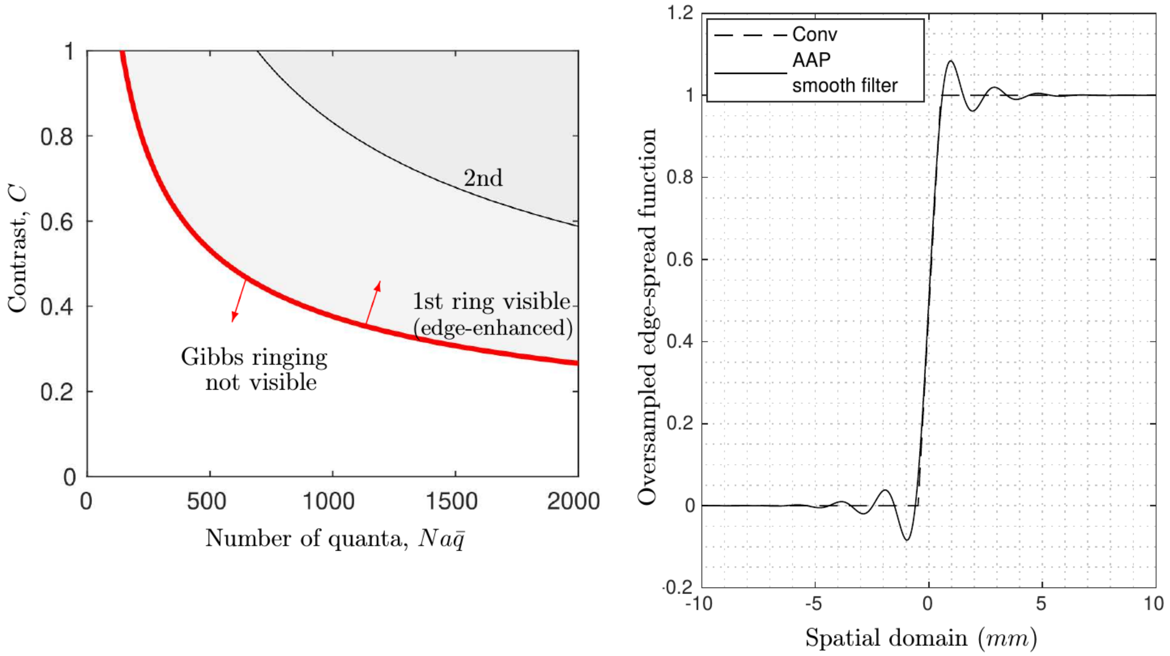

Figure 5.15: A plot showing when avoiding Gibbs ringing criteria for the modified AAP filter (right). This plot shows that many rings are not visible and the 1st side-lobe may not be undesirable as it causes slight "edge-enhancement". An oversampled edge response with conventional and AAP designs (left), showing reduction of oscillations.

fits. In noise-limited image regions, DQE is important for determining detectability so it is important to use an AAP filter that does not cause noise aliasing such as a rectangular low-pass filter with an abrupt cut-off. Adaptive filtering algorithms that detect noise-limited and high-contrast regions could be implemented on-board the AAP detector to select an appropriate filter for a given imaging task, although this would correspond to non-linear post processing.

5.5 Conclusion

The AAP approach improves high-frequency MTF and DQE by implementing an anti-aliasing filter using a micro-sensor array with smaller elements than pixel size. If the AAP anti-aliasing filter has an abrupt cut-off, it result in Gibbs phenomena near high-contrast edges that appear as under- and overshoot artifacts. We define an SNR criteria to avoid Gibbs ringing with the AAP approach, $C\sqrt{a\bar{q}} < 11.2$ where C is contrast, a is detector element area and $\bar{q}$ is the mean number of x-rays per mm^2. This criteria states that Gibbs ringing is not visible for an edge with contrast C when quantum noise is greater than the amplitude of Gibbs overshoot. For contrast-limited images where ringing could occur, we describe a modified AAP anti-aliasing filter that achieves high MTF and DQE at high-frequencies without Gibbs ringing in contrast-limited images. The edge response of the modified AAP filter still show the 1st under and overshoot, as shown in Figure 5.15, although this might be desirable as it slightly "edge-enhances" images. For noise-limited images were ringing is not visible, a rectangular low-pass should be used to obtain 100% of the AAP benefits.

5.6 Acknowledgments

The authors wish to thank Dr. Jan Lindström for providing x-ray image data. The authors also wish to thank Derek Gillies for useful insight and suggestions. We acknowledge financial support from NSERC PGS-D scholarship.

Bibliography

[1] J. C. Dainty, *Image Science: Principles, Analysis, and Evaluation of Photographic-Type Image Processing.* Academic Press, 1974.

[2] R. F. Wagner, K. E. Weaver, E. W. Denny, and R. G. Bostrom, "Toward a unified view of radiological imaging systems. part i: Noiseless images," *Med Phys*, vol. 1, pp. 11–24, 1974.

[3] R. F. Wagner, "Toward a unified view of radiological imaging systems. part ii: Noise images," *Med Phys*, vol. 4, pp. 279–296, 1977.

[4] I. A. Cunningham and R. Shaw, "Signal-to-noise optimization of medical imaging systems," *J. Opt. Soc. Am. A*, vol. 16, no. 3, pp. 621–632, 1999.

[5] E. Ismailova, K. S. Karim, and I. A. Cunningham, "Apodized-Apreature Pixel design to increase high-frequency DQE and reduce noise aliasing in x-ray detectors," *Proc. SPIE: Physics of Medical Imaging*, vol. 9412, 2015.

[6] T. F. Nano, T. Escartin, K. S. Karim, and I. A. Cunningham, "A novel x-ray detector design with higher DQE and reduce aliasing: Theoretical analysis of x-ray reabsorption in detector converter material," *Proc. SPIE: Physics of Medical Imaging*, vol. 9783, 2016.

[7] T. F. Nano, T. Escartin, E. Ismailova, K. S. Karim, J. Lindstrom, H. K. Kim, and I. A. Cunningham, “MTF and DQE enhancement using an apodized-aperture x-ray detector design,” *Med. Phys.*, vol. 44, no. 9, pp. 4525–4535, 2017.

[8] M. Bocher, “Introduction to the theory of fourier’s series,” *Annals of Mathematics*, vol. 7, no. 3, pp. 81–152, 1906.

[9] S. Gottlieb, J.-H. Jung, and S. Kim, “A Review of David Gottliebs Work on the Resolution of the Gibbs Phenomenon,” *Communications in Computational Physics*, vol. 9, no. 3, pp. 497–519, 2011.

[10] I. A. Cunningham, “Applied linear-systems theory,” in *Handbook of Medical Imaging: Vol 1, Physics and Psychophysics* (J. Beutel, H. L. Kundel, and R. V. Metter, eds.), Ch 2, pp. 79–159, SPIE Press, 2000.

[11] A. Rose, “A unified approach to the performance of photographic film, television pick-up tubes, and the human eye,” *J Soc Motion Pict Telev Eng*, vol. 47, no. 4, pp. 273–294, 1946.

[12] A. E. Burgess, “The rose model, revisited,” *J Opt Soc Am A*, vol. 16, no. 3, pp. 633–646, 1999.

[13] S. Dong, T. Chu, J. Lee, G. Lan, T. Wu, Y. Yeh, and J. Hwang, “Estimation of mean-glandular dose from monitoring breast entrance skin air kerma using a high sensitivity metal oxide semiconductor field effect transistor (mosfet) dosimeter system in mammography,” *Applied radiation and isotopes*, vol. 57, no. 6, pp. 791–799, 2002.

[14] Harris, “On the use of windows for harmonic analysis with the discrete fourier transform,” *Proceedings of IEEE*, vol. 66, pp. 51–83, Jan. 1978.

[15] A. Nuttall, “Some windows with very good sidelobe behavior,” *IEEE Transactions on Acoustics, Speech, and Signal Processing*, vol. 29, pp. 84–91, February 1981.

Chapter 6

Conclusions and future work

An overview of the important findings from **Chapters 2 - 5** is provided and a summary of conclusions from each section is presented. ‘study in **Chapters 2 - 5** and suggested future work .

6.1 Overview of research

Breast cancer is the most commonly diagnosed cancer and the leading cause of cancer death world-wide.[1] This disease has an overwhelming financial and social burden on the healthcare system, the individuals affected, and the community as a whole.[2] Prevention of breast cancer remains a challenge, especially because of its association with various genetic and lifestyle-based risk factors. Therefore, detection and treatment is crucial for relieving disease burden. Improvements in breast cancer treatment can provide high 5-year survival rates when early detection is possible,[3] although early detection and discerning benign from malignant disease is difficult. Benign disease is an important indicator of possible future aggressive disease, but it does not necessarily need immediate treatment. A current challenge for disease management falls on accurately differentiating warning signs that should be monitored versus aggressive disease that should be treated immediately.[4] Obtaining such discernment is extremely desirable and motivates further development of imaging techniques to improve specificity and sensitivity of early breast cancer detection.

There are various imaging modalities for the breast that are used clinically and others being developed in research. Each modality has advantages and disadvantages while providing different information that is useful, as summarized in Table 1.1. Screening mammography is the primary modality used for early breast cancer detection in asymptomatic populations.[5, 6] It has been proven to detect cancer at an early stage and reduce mortality when followed by proper treatment.[7] Other imaging modalities that are useful include: tomosynthesis, ultrasound, magnetic resonance imaging, and contrast enhanced imaging. These various techniques are used to provide additional structural and functional information, that improves detection following an abnormal finding with screening mammography. Since mammography is the first line-of-defense against breast cancer and subsequent imaging and clinical decisions are based of this x-ray imaging technique, it is vital that we understand how to provide the best quality x-ray images for a given exposure.

Signal-to-noise ratio (SNR) in mammography mainly depends on x-ray exposure and x-ray detector performance.[8] A large clinical study conducted by the Ontario Breast Screening Program found that not all x-ray detectors have the ability to produce high image SNR for a given exposure.[9, 10] This multi-centre study found that centres using higher performing detector technology had 30% greater cancer detection rates while also using lower exposures. Detector performance is quantified by the modulation transfer function (MTF) and detective quantum efficiency (DQE). Thereby, improving these detector parameters is very important for obtaining high image SNR with the goal of improving cancer detection.

The overarching objective of this thesis work is to redesign the conventional method by which x-ray detectors acquire an image by rethinking image formation to overcome SNR limitations[11] and reduce artifacts that can impede early detection of breast cancer and ultimately patient outcomes. The greatest opportunity for improvement of x-ray detector performance is at high-frequency MTF and DQE values which can be lower by a factor of 10 than at low-frequencies.[12, 13] High MTF and DQE performance at high-frequency is important for clear visibility of small structures and fine-detail, critical markers for early detection. Based on current x-ray detector designs, we identified noise aliasing as the main source of DQE loss at high-frequencies.[14] Therefore, this work aimed to address the following research questions: (1) Can we design a new x-ray detector which eliminates noise aliasing and results in increased high-frequency MTF and DQE? (2) What are the x-ray detector design requirements for achieving an "ideal" x-ray detector in terms of image SNR? (3) With new technology enabling new x-ray detector designs, can we optimize x-ray imaging by improving SNR and providing missing information to current x-ray imaging? The development of an "ideal" x-ray detector would impact mammography screening in two main ways: (1) it allows for use of lower x-ray exposures to obtain the same image SNR as acquired currently, which may make it more feasible to increase screening frequency or increase use of other x-ray imaging techniques; (2) it allows for acquisition of high SNR images, in particular at high frequencies, with the goal of improving cancer detection rates and reducing false positives.

The specific research objectives pertaining to each chapter were: To design an x-ray detector (apodized-aperture pixel, AAP) that uses smaller element size than desired image pixel size and develop a method to synthesize pixels which suppress aliasing for improved MTF and DQE at high-frequencies (**Chapter 2**); to determine the best implementation of the AAP design and identify x-ray detector physics that limit performance (**Chapter 3**); implement the AAP approach using a small-area prototype and show improvement of fine-detail visualization (**Chapter 4**); to optimize the AAP anti-aliasing filter avoiding Gibbs ringing (that can occur near high-contrast edges) while maintaining AAP benefits (**Chapter 5**).

6.2 Summary and conclusions

The AAP design is a new x-ray detector design that eliminates noise aliasing by using a micro-element sensor array and synthesizing smaller pixels of clinically useful size. In **Chapter 2,** we described the development of the AAP approach using a simple cascaded model (without x-ray interactions) of a detector with an ideal converter layer. We compared MTF and DQE performance of the AAP design to those of a conventional detector. It was shown that the AAP approach preserves the MTF of the small sensor elements and attenuates frequencies above the image sampling cut-off frequency. This has the double benefit of improving the MTF by 53% at high frequencies while reducing both signal and noise aliasing, resulting in an increase of DQE by 2.5× at high spatial frequencies. The theoretical model was validated experimentally using a selenium (Se) clinical detector as a proof-of-concept demonstration. A Monte Carlo study and x-ray images of a star-pattern and rat leg showed improved visibility of edges, fine-detail and removal of aliasing artifacts. This work demonstrated that the AAP approach improves high-frequency MTF and DQE resulting in improved SNR of fine-detail for a given exposure.

Previous analysis of the AAP approach was done using an ideal detector model and therefore did not consider x-ray physics in a general converter layer. In **Chapter 3**, we developed a cascaded system analysis (CSA) using a simple-atom model of x-ray interactions that includes effects of stochastic energy-deposition, x-ray reabsorption, quantum scattering and quantum selection in the detector converter layer. We described the impact of x-ray physics on MTF and DQE using cascaded-systems analysis on conventional and AAP x-ray detector designs. It was shown that x-ray reabsorption and converter blur were important factors to consider because they may affect aliasing. A cesium-iodide detector was used to measure DQE of synthesized conventional and AAP images for cases with and without x-ray reabsorption (above and below converter K-edge) and converter blur (small and large pixels). Theoretical models of x-ray spectra below and above converter K-edge show excellent agreement with experiment. We showed that reabsorption has negligible effect on the AAP design, whereas converter blur reduces the AAP benefit because it suppresses aliasing. Therefore, this work demonstrated that the AAP design should be implemented with a high-resolution converter having blurring effects less than pixel size to achieve the most benefit over conventional design.

Following results from **Chapter 3** showing that x-ray reabsorption does not affect the AAP design and that a high-resolution converter layer with little blur provides the most improvement with the AAP approach, our next step was to implement the AAP approach on a prototype with micro-sensor elements. In **Chapter 4**, we used a high-resolution converter layer deposited directly on a complementary metal-oxide semiconductor (CMOS) sensor having micro-sized element size. We described implementation of the AAP approach on a Se/CMOS prototype with 7.8 μm element size and compared AAP and conventional (binned) images with 47 μm pixel size. MTF and DQE was measured using a non-standard clinical spectrum (a tungsten micro-focus x-ray tube with a 60 kV spectrum with 2 mm of added aluminum filtration) but similar air-KERMA was used as in clinical mammography. It was shown that the AAP design has 1.5× greater MTF near the image cut-off frequency (u_c = 10.6 cyc/mm) than conventional design and 2.5× greater DQE. This work demonstrated the first ever implementation of the AAP approach on a micro-sensor array showing a flat-DQE curve up to 10 cyc/mm. In addition, the AAP approach removes signal aliasing which causes partial volume effects causing inconsistent visibility of small structures (such as breast calcifications).

Implementation of the AAP design using an anti-aliasing filter with an abrupt cut-off results in Gibbs ringing (an undesired image artifact) near high-contrast edges. In **Chapter 5**, we investigated the impact the AAP filter has on Gibbs ringing and improvements on MTF and DQE. We defineda SNR criterion to avoid Gibbs ringing with the AAP approach: $C\sqrt{Naq} < 11.2$ where C is contrast, N is the number of elements in a ringing artifact, a is the detector element area and q is the mean number of x-ray per area. Gibbs ringing is not avoided for contrast-limited image regions, thus we described modifying the filter cut-off transition smoothness and frequency cut-off location to eliminate Gibbs ringing while maintaining 92% of the AAP benefit in MTF and DQE. Conversely, Gibbs ringing is avoided for noise-limited image regions, therefore the rectangular low-pass filter can be implemented for 100% AAP benefit. This work demonstrated a fundamental SNR criteria for when Gibbs ringing is visible (applicable to any system that has a band-limited response) and described how to modify the AAP low-pass filter to suppress Gibbs ringing for applications when it is not avoidable.

In summary, we provided: 1) proof-of-concept demonstration of the AAP approach which improves high-frequency MTF and DQE by using a micro-sensor array and anti-aliasing filter; 2) description of x-ray physics limitations with the AAP design, showing that the conditions for best improvement with the AAP design requires a high resolution converter layer and low read-out noise from the sensor; 3) implementation of the AAP approach on a small-area prototype showing 50% MTF improvement and 2.5 × DQE improvement at high-frequencies resulting in a flat-DQE curve up to 10 cyc/mm using a Se/CMOS sensor; and 4) a SNR criteria for avoiding Gibbs ringing and demonstrated suppression of ringing in the AAP design.

6.3 Study limitations

The significant limitations from **Chapter 2-5** are discussed in this section and their implications are further elucidated for each respective chapter.

The work in this thesis is mainly based on (1) Fourier metrics and (2) demonstration of the AAP approach using current detector systems. Use of Fourier metrics is not a limitation, but rather a strength, as they are very useful for providing insight on detector performance. It should be noted however that these metrics only apply for imaging systems that are linear and shift-invariant. Although x-ray detectors are engineered to respond linearly over the entire detector area, these conditions might not always be true (such as when there is image processing turned on). Therefore, one must understand a system's response when interpreting Fourier metrics. Since we do not yet have a full-sized AAP detector, we demonstrate the AAP approach using current detectors by using the full-resolution image as the AAP micro-sensor signal to synthesize larger pixels for AAP images. This is not a limitation in terms of evaluating MTF and DQE, but it is a limitation when visually comparing AAP to current detectors because AAP demo images have larger pixel size (lower resolution) than current clinical images. To make a fair comparison, we created "conventional images" by binning (summing) full-resolution images to create conventional detector images with the same pixel size as the AAP approach. This also has the advantage of comparing two designs using the same detector hardware, which removes any other differences that could affect performance.

In **Chapter 2**, we used a theoretical model to describe the AAP approach and proof-of-concept experiments to demonstrate the potential of the AAP design. This model provides a good understanding of the improvements with the AAP design compared to conventional under simplified conditions. The main limitation is that the theoretical model assumed an "ideal" converter layer without x-ray interactions or blur. This means that MTF and DQE improvements shown here are only applicable only for very high-resolution converter layers that do not degrade DQE for any other factors as well. Since actual detectors rarely behave ideally, one should be aware that the results shown here provide a limiting case of the best MTF and DQE performance.

In **Chapter 3**, we used a theoretical model of x-ray interactions utilizing a simple-atom model that only considers one atomic transition and one interaction per x-ray. This is an approximation that provides results of signal and noise in an image with up to 2% uncertainty.[15, 16] Although this model has been thoroughly validated via Monte Carlo simulations, it is a challenge validating it experimentally. We used a semi-empirical validation to compare noise properties of our detector below and above the detector converter

K-edge. Direct empirical validation is challenging because there are many unknown characteristics/factors about the detector, such as housing material thicknesses and secondary quanta collection efficiency of the sensor. However, obtaining good agreement for two different x-ray beams with different x-ray reabsorption gives confidence that the model is accurate. Our model does not consider Lubberts effects or variations in quantum gain stages. However, these effects are small for high-resolution direct converters such as selenium.[17, 18]

In **Chapter 4**, we implemented the AAP approach on a micro-sensor prototype and showed MTF and DQE improvements for images with typical mammography pixel size (0.05 - 0.1 mm). In addition to showing MTF and DQE comparisons between conventional and AAP designs, we demonstrated how signal aliasing causes partial volume effects that result in inconsistent visualization of specks in mammography phantoms with the conventional design. A limitation in interpreting our results for mammography is that we used a non-standard mammography spectrum and setup due to laboratory constraints. In addition, our x-ray tube has a micro-focus source which is important for high-resolution imaging. Our calculations show that a typical 0.1 mm focal spot size with a source-to-image distance of 60 cm only slightly reduces the micro-sensor MTF at high-frequencies by 5%. A limitation in our demonstration of partial volume artifacts resulting in speck contrast differences is that we simulated sub-element shifts in the object by shifting our sampling grid. This digitally shifts the object, in discrete amounts, whereas ideally we would like to randomly re-position the object on the detector and obtain an image. Our demonstration shows an incomplete representation of the full variability caused by partial volume effects.

In **Chapter 5**, we defined SNR criteria for avoiding Gibbs ringing with the AAP approach and describe a method of modifying the AAP filter the reduce Gibbs ringing while maintaining the benefit of the AAP approach. A limitation of our SNR criteria to avoid Gibbs ringing is that it describes a worst-case scenario. For example, it does not consider detector converter blur, non-uniform noise and anatomical background, all of which would reduce the visibility of Gibbs ringing. Therefore, we believe Gibbs ringing would not be an issue in medical imaging yet it could occur in non-medical applications. A limitation in our optimization of the AAP filter that suppresses Gibbs ringing is that we started with a fixed analytic expression with 2-degrees of freedom (parameters s ad u_{f}). Other filter shapes could be found that provide different benefits to MTF or DQE. Additionally, we only used one object as an example to show the effects of Gibbs ringing and its suppression.

6.4 Future directions

6.4.1 DQE improvement that results in an observable image difference

Since the overall goal of my research is to develop a high-DQE detector design, it is important to understand how much of a DQE improvement is necessary to make an observable difference in an image. However, it is not known how much DQE improvement at low or high frequencies results in a noticeable difference in x-ray images. Therefore, the objective of this proposed future work is to determine what DQE increase is required to make a noticeable improvement in image quality.

Image quality is object dependent, in addition to depending on x-ray detector performance and x-ray exposure.[19] To isolate the impact of the x-ray detector, we study image quality of a Rose phantom (having disks of various diameter and contrast) for a given number of x-ray quanta incident on the detector. A Monte Carlo simulation was done of Rose phantom images with a uniform background and uncorrelated noise. Different x-ray detector DQEs were modeled as being flat (frequency independent) but having different quantum efficiency. A total of 110 images were simulated from detectors with different DQEs with the same number of x-ray quanta incident. We developed a

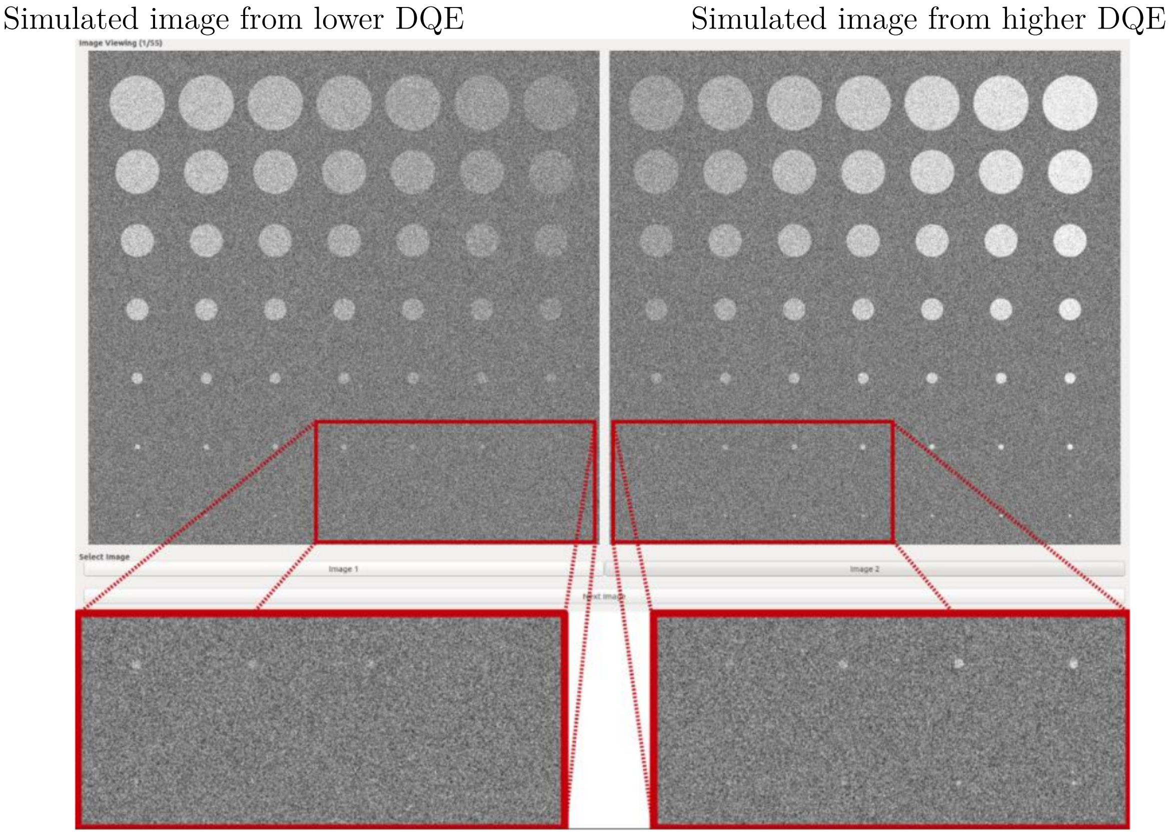

Figure 6.1: Two-alternative forced-choice study to determine the minimum DQE improvement that would result in an observable difference in SNR. Simulated Rose-phantom images from x-ray detectors with different DQEs were displayed side-by-side with synchronized window and leveling.

graphical user interface (GUI) in C++ (GCC4.8.2, Qt5.2.1) to simultaneously display image pairs (left and right) corresponding to two combinations of DQE values, as the two-alternative forced-choice (2AFC) study shown in Figure 6.1. Ten graduate student volunteers were asked to select which image had more visible disks. Participants had the freedom to adjust image window and level, although the GUI was synchronized to update the window and level in the opposite image for a fair comparison. Images were randomized, participants were asked to view the images at least 50cm away from the screen and 110 images were shown to each participant.

For different DQE ratios (right over left), Figure 6.2 shows the relative frequency in which the right image was selected as the higher quality image. The curve shows an

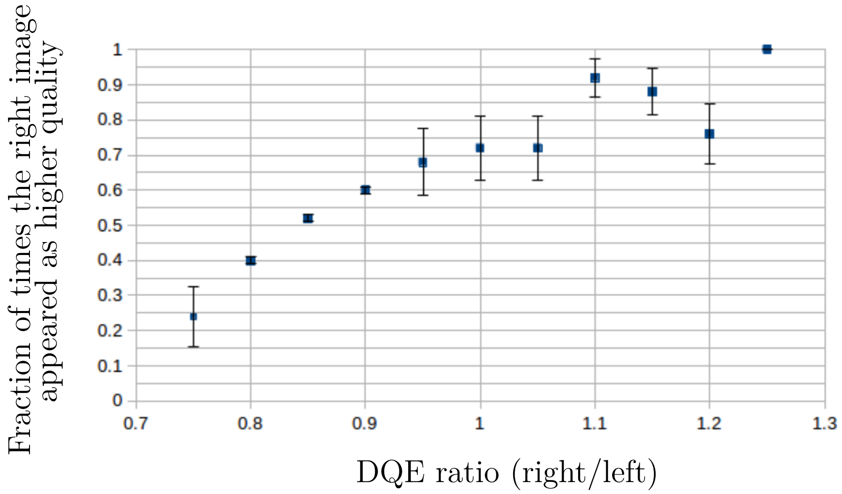

Figure 6.2: Fraction of times the right-hand imaging chosen by an observer as having more visible disks for different DQE ratios of right-to-left imaging systems. The curve has an approximately sigmoidal response that is similar to the detectability index for an ideal observer. A 10% DQE improvement was required to make a noticeable difference in image SNR for observers.

approximately sigmoidal response as would be expected for an ideal observer in a uniform background.[20, 21] The DQE ratio of 1 means the DQE was the same for left and right, and since the fraction of times the right side was selected is 0.7 means there is a bias toward the right image. This bias could be due to most of the participants being right-handed. The fraction of times the right image was selected is significantly different when DQE ratio is 0.9 and 1.1, meaning that a DQE increase or decrease of 10% is needed to change observer performance. The implication is that new detector designs should improve DQE across all frequencies by at least 10% to provide an observable increase in image quality.

In conclusion, observer selection of simulated x-ray images corresponding to different detector performance shows that a 10% DQE improvement (or more) results in a noticeable difference on image quality. Comparisons of Rose phantom images does not allow for analysis of spatial-frequency dependent image quality. Future studies could be done similar to here but DQE differences could be made at either low, mid or high frequencies. Additionally, other tasks besides the Rose phantom in a uniform background could be investigated (such as correlated noise, anatomical background and detection of lesions of varying sizes) for a better understanding of the detector performance needed to improve decision making of challenging diagnostic tasks.

6.4.2 Ultrahigh-resolution imaging of microcalcifications in mammography

An additional benefit of having higher resolution in mammography is to provide more morphological information about microcalcifications. Microcalcification morphology is an indicator of breast cancer aggressiveness.[22, 23, 24] However, calcifications can be as small as only a few image pixels in current mammography which makes it extremely challenging to differentiate between a round smooth shaped calcification versus an irregular shaped calcification. Figure 6.3 shows x-ray film images containing calcifications from malignant and benign cancer cases at mammographic resolution (left panels) and at high specimen imaging resolution (right panels).

We propose developing an x-ray detector that has the ability to acquire high SNR images at ultrahigh resolution (10-25 μm) than current mammography pixel size (50-100 μm). Image SNR is tested clinically using phantoms (such as CDMAM) that allow for detectability scoring of disks in a uniform background. Our objective is to investigate SNR and detectability scoring in images from conventional and ultrahigh-resolution designs.

An x-ray detector prototype having selenium (Se) directly deposited on a complementary metal-oxide-semiconductor (CMOS) sensor with 7.8 x 7.8 μm element size was used to acquire images of phantoms and microcalcification samples from breast biopsies. A 60 kV x-ray beam from a tungsten tube with 2 mm of aluminum filtration was used to acquire images at 85 μGy incident air-KERMA on the sensor.

High SNR images of microcalcifications were acquired using a Se/CMOS prototype with 7.8 μm element size. Figure 6.4 shows better visualization of calcification morphology at ultra-high resolution. At smaller pixel size, the image noise is greater as there are fewer quanta interacting in each element than with larger pixels. Even though

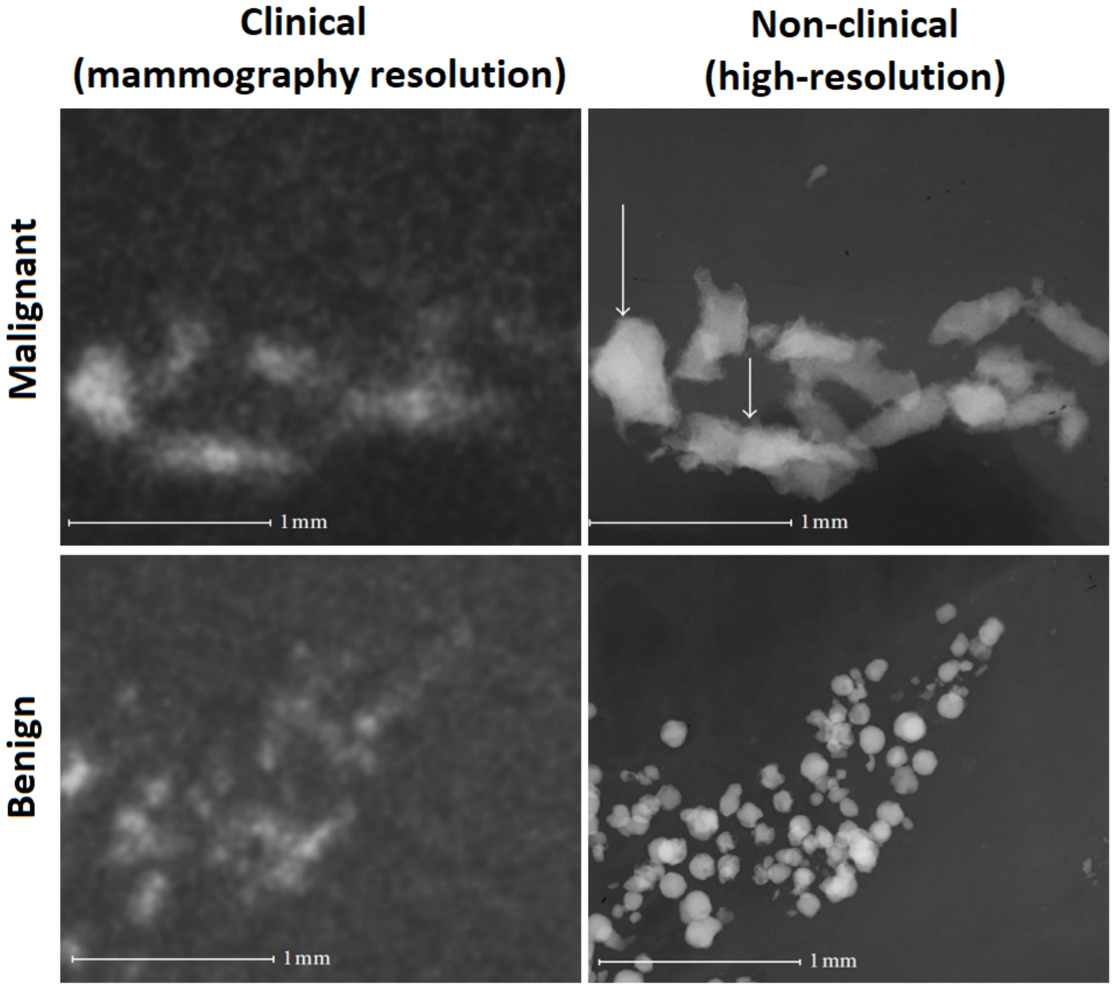

Figure 6.3: Micro-calcifications from malignant (top) and benign (bottom) cases acquired with a mammography system (left) and high-resolution specimen x-ray imaging (right). Both malignant and benign calcifications were categorized as high-risk (BIRADS 4 or 5) but high-resolution images show clear morphological differences related to malignancy (confirmed by histology). Modified from Langen et. al., Rad. Res. Prac., 526293, 2012. Permission to reproduce provided in Appendix.

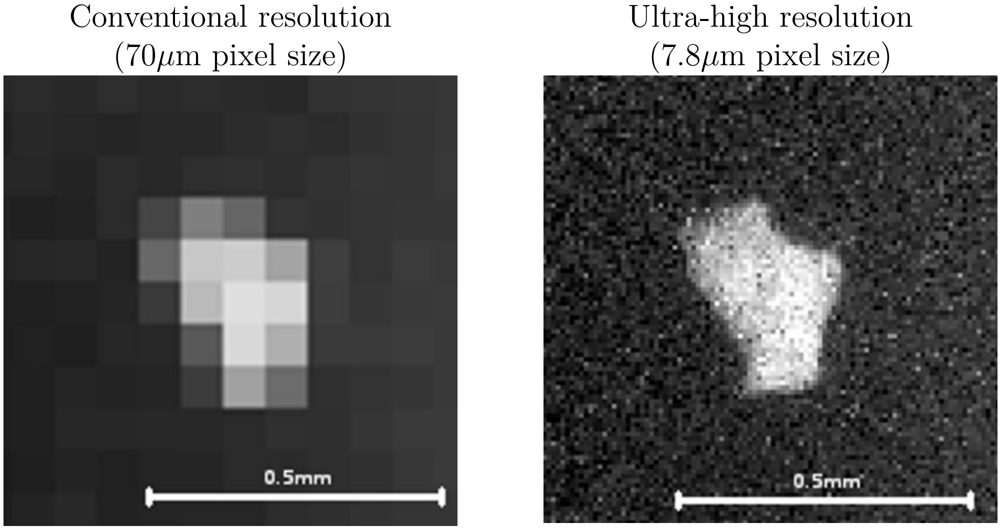
Conventional resolution (70μm pixel size)

Ultra-high resolution (7.8μm pixel size)

Figure 6.4: X-ray images of a microcalcification obtained during a breast biopsy shown at current mammography resolution, 0.07mm pixel size (left), and at 10× higher resolution, 0.007mm pixel size (right). There is poor morphological information in the conventional image because only a small number of pixels make up the calcification, whereas higher resolution more clearly shows texture and shape of the calcification.

there is greater quantum noise, it is still possible to clearly visualize calcifications at high-resolution because the sensor has extremely low readout noise.

We are proposing using detectors with high resolution sensors clinically. When large file sizes cannot be transfered, displayed or stored, then the AAP approach can be used to improve visibility of fine-detail and small structures. If one is not limited by those factors, we propose using ultrahigh resolution where there are microcalcifications. We've demonstrated that CMOS sensors can be used to acquire ultra-high resolution images of microcalcification with high SNR.

[I'd like acknowledge the help of Kalan Lynn and Dr. Muriel Brackstone for providing biopsy samples in this preliminary study.]

6.4.3 Impact of the AAP design tomosynthesis and computed tomography

Flat-panel detectors are used for cone-beam computed tomography (CBCT) in various applications, including breast imaging, as there have been much interest in breast CBCT.[25, 26] The main advantages of CBCT over typical fan-beam CT[27] are quicker acquisition times and lower radiation dose. However, a main limitation of CBCT is poor image quality due to large amounts of scattered radiation because x-rays are interacting in a larger field-of-view in the patient. To overcome this limitation, anti-scatter grids can be used that allow for primary beam transmission while blocking the scatter radiation. For applications that use stationary grids which are not fixed to the detector, "grid-lines" in the image can be difficult to avoid due very small grid motion. These artifacts make the image unusable, as shown in Figure 6.5 (left), thus they must be removed. Typically grid-line suppression can be done via different methods,[28] but if the gird-line frequency is above the image sampling cut-off frequency of the image then the AAP approach can be used to reduce the artifact.

We used a previously developed 2-dimensional anti-scatter grid manufactured from a cobalt-chrome alloy using laser melting.[29] The grid has septa spacings of 1.1mm and septa width of 0.1mm; it was place in front of an x-ray detector (DRX-Plus, Carestream) having 0.139 pixel size. To demonstrate and compare AAP performance with CBCT, we created conventional projections that were binned 4×4 and AAP projections with the same size (0.556mm). Figure 6.5 shows phantom objects and grid lines mainly caused by aliasing of the small grid spacings. Anti-aliasing with the AAP approach drastically suppresses the grid artifact.

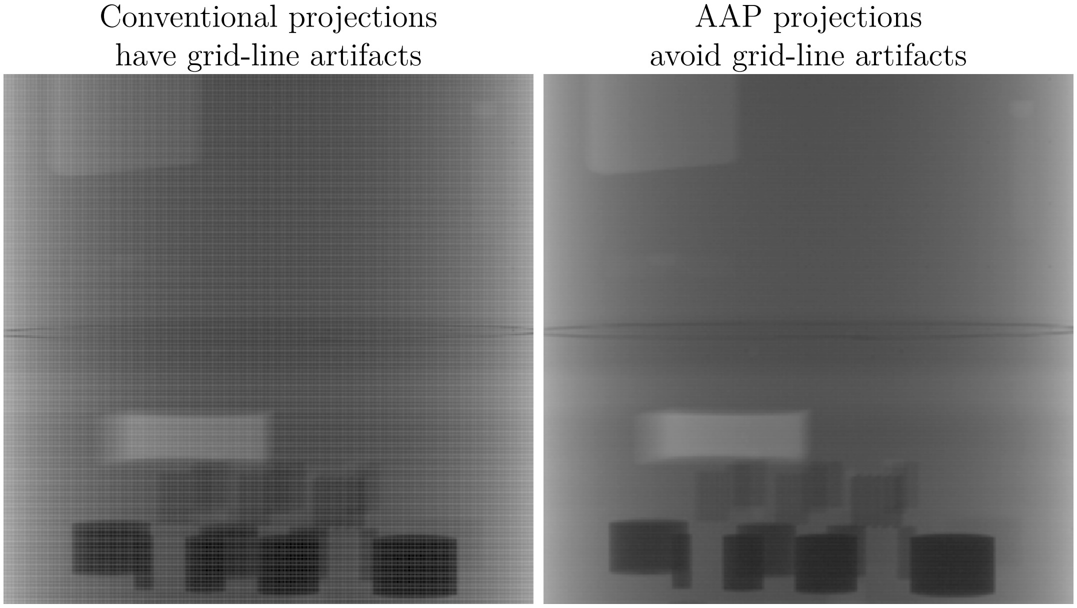

Figure 6.5: A cone-beam CT projection of a phantom with an anti-scattering grid placed in front of the detector. The image on the left is a conventional image with 0.56mm pixel size (binned 4 × 4) and the image on the right is an AAP image synthesized with the same pixel size. The conventional image has a pronounced grid artifact caused mainly by aliasing of the small grid spacings. Anti-aliasing with the AAP approach drastically suppresses the grid artifact.

AAP and conventional projections were reconstructed using the same algorithm (Parker weighted Feldkamp, Davis and Kress (FDK) back-projection algorithm) with isotropic voxels 0.139mm is size.[30] Figure 6.6 shows reconstructed slice with conventional projections (left) and AAP projections (right). Ring artifacts with the conventional design obstruct visibility of all bar-patterns, whereas these artifacts are greatly suppressed with the AAP approach. The image cut-off frequency for both AAP and conventional images is 0.9cyc/mm and the fundamental grid frequency is 0.91cyc/mm. Although the fundamental frequency is above the Nyquist cut-off and should be aliased, incomplete removal of the grid-lines with the AAP could be due to the fundamental frequency having some width (and spectral power) below the image cut-off 0.9cyc/mm. We expect that a slightly higher frequency grid, or smaller pixels, would completely remove the grid artifact.

We show grid-line reduction as an example of the possible benefits with an AAP detector used for CBCT reconstruction. It would be interesting to investigate image quality

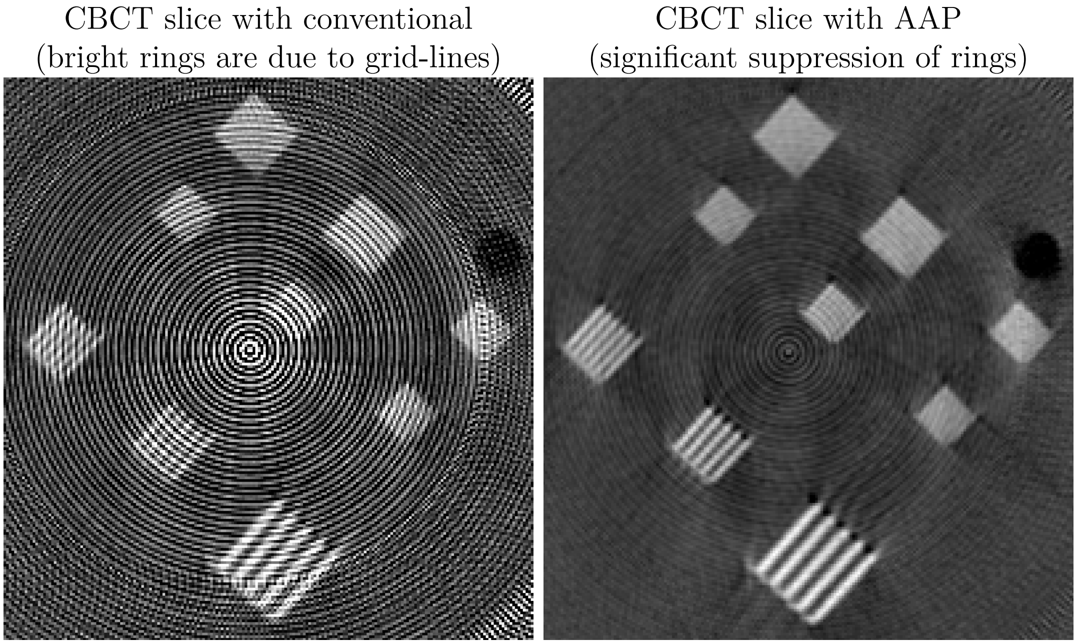

CBCT slice with conventional
(bright rings are due to grid-lines)

CBCT slice with AAP
(significant suppression of rings)

Figure 6.6: A cone-beam CT reconstructed slice with conventional projections (left, binned 4 × 4) and AAP projections (right, 4× pixel size) showing resolution bar-patterns. The CT slice with conventional projections has ring artifacts caused by the grid artifact, which are suppressed with the AAP approach.

in CBCT using an AAP detector as it could improve image quality for every projection that could sum to show a large difference in the reconstructed slice. Another 3D imaging application that the AAP detector could provide benefit for is breast imaging using tomosynthesis. Each projection in tomosynthesis is acquired at a fraction of the dose in typical mammography, therefore detectors with high DQE are required as each image is quantum noise-limited. Since the AAP approach improves high-frequency DQE, it could potentially improve visibility of microcalcifications that are currently more difficult to visualize in tomosynthesis than mammography.

[I'd like acknowledge the help of Santiago F. Cobos, a PhD candidate in Dr. David Holdsworth lab, who provided CT data and contributed to image processing.]

6.5 Significance and impact

The significance of this work is in the improvement of x-ray detector technology to achieve what has not been possible to date. Much work has gone into developing x-ray detectors into the impressive devices they are today, having close to ideal dose-efficiency when it comes to visualizing large structures. However, they can be orders of magnitude less efficient at producing high SNR images of fine-detail and small-structures. Detection of fine-detail is crucial for many medical applications, such as mammography, where micro-calcifications are found in over 90% of cancer detected[31, 32] and their morphology can bean indication of cancer aggressiveness.[33] Poor image SNR for a given exposure and the poor image resolution of fine-detail with conventional x-ray systems is due to detector design. Therefore, it is imperative to redesign the way x-ray detectors acquire images to improve dose-efficiency for improved cancer detection.

In this thesis, we have developed a new x-ray detector design that we call the apodized-aperture pixel (AAP). This design is novel over conventional detectors, where one detector element contributes to only one pixel, by using a micro-sensor array to synthesize image pixels using a weighted combination of many detector elements. This detector has the advantage of improving both high-frequency MTF and DQE when used with a high-resolution converter layer. High-frequency MTF is improved by the micro-sensor array aperture and high-frequency DQE is improved by implementation of the anti-aliasing AAP design to avoid noise aliasing. We have shown the design, development and technical performance of the AAP with the goal of manufacturing a full-sized detector for clinical use and evaluation of cancer detection improvements. A cancer center that is equipped with the high performing AAP design has the potential to detect cancer that would be missed and identify aggressive disease that requires immediate intervention.

Bibliography

[1] F. Bray, J. Ferlay, I. Soerjomataram, R. L. Siegel, L. A. Torre, and A. Jemal, "Global cancer statistics 2018: Globocan estimates of incidence and mortality worldwide for 36 cancers in 185 countries," *CA: A Cancer Journal for Clinicians*, vol. 68, no. 6, pp. 394–424, 2018.

[2] N. Mittmann, J. Porter, J. Rangrej, S. Seung, N. Liu, R. Saskin, M. Cheung, N. Leighl, J. Hoch, M. Trudeau, W. Evans, K. Dainty, C. DeAngelis, and C. Earle, "Health system costs for stage-specific breast cancer: a population-based approach," *Current Oncology*, vol. 21, no. 6, 2014.

[3] Cancer Care Ontario, "Screening guidelines and program eligibility," *Cancer Care Ontario*, 2018. Retrieved Dec. 10th, 2018, from https://archive.cancercare.on.ca/pcs/screening/.

[4] K. I. Bland, E. M. Copeland, V. S. Klimberg, and W. J. Gradishar, *The breast: comprehensive management of benign and malignant diseases*. Elsevier Inc, 2017.

[5] E. D. Pisano and M. J. Yaffe, "Digitla mammography," *Radiology*, 2005.

[6] E. D. Pisano, C. Gatsonis, E. Hendrick, M. Yaffe, J. K. Baum, S. Acharyya, E. F. Conant, L. L. Fajardo, L. Bassett, C. D'Orsi, R. Jong, and M. Rebner, "Diagnostic performance of digital versus film mammography for breast-cancer screening," *New England Journal of Medicine*, vol. 353, no. 17, pp. 1773–1783, 2005.

[7] D. A. Berry, K. A. Cronin, S. K. Plevritis, D. G. Fryback, L. Clarke, M. Zelen, J. S. Mandelblatt, A. Y. Yakovlev, J. D. F. Habbema, and E. J. Feuer, “Effect of screening and adjuvant therapy on mortality from breast cancer,” *New England Journal of Medicine*, vol. 353, no. 17, pp. 1784–1792, 2005. PMID: 16251534.

[8] J. T. Bushberg and J. M. Boone, *The essential physics of medical imaging.* Lippincott Williams & Wilkins, 2011.

[9] A. M. Chiarelli, S. A. Edwards, M. V. Prummel, D. Muradali, V. Majpruz, S. J. Done, P. Brown, R. S. Shumak, and M. J. Yaffe, “Digital compared with screen-film mammography: Performance measures in concurrent cohorts within an organized breast screening program,” *Radiology*, vol. 268, pp. 684–93, Sep 2013.

[10] M. J. Yaffe, A. K. Bloomquist, D. M. Hunter, G. E. Mawdsley, A. M. Chiarelli, D. Muradali, and J. G. Mainprize, “Comparative performance of modern digital mammography systems in a large breast screening program,” *Medical Physics*, vol. 40, no. 12, pp. 121915–n/a, 2013. 121915.

[11] E. D. Pisano, C. Gatsonis, E. Hendrick, M. Yaffe, J. K. Baum, S. Acharyya, E. F. Conant, and L. L. Fajardo, “Diagnostic performance of digital versus film mammography for breast-cancer screenings,” *New England Journal of Medicine*, vol. 353, p. 1773, October 2005.

[12] C. Schaefer-Prokop, D. De Boo, M. Uffmann, and M. Prokop, “Dr and cr: Recent advances in technology,” *European journal of radiology*, vol. 72, no. 2, pp. 194–201, 2009.

[13] T. Escartin, T. Nano, and I. A. Cunncingham, “Detective quantum efficiency: a standard test to ensure optimal detector performance and low patient exposures,” *Proc. SPIE*, vol. 9783, March 2016.

[14] I. A. Cunningham, J. Yao, and V. Subotic, “Cascaded models and the dqe of flat-panel imagers: Noise aliasing, secondary quantum noise and reabsorption,” *Proc. of SPIE: Physics of Medical Imaging*, vol. 4682, pp. 61–72, 2002.

[15] G. Hajdok, J. Yao, J. J. Battista, and I. A. Cunningham, “Signal and noise transfer properties of photoelectric interactions in diagnostic x-ray imaging detectors.,” *Med. Phys.*, vol. 33, no. 10, pp. 3601–20, 2006.

[16] S. Yun, J. Tanguay, H. K. Kim, and I. A. Cunningham, “Cascaded-systems analyses and the detective quantum efficiency of single-Z x-ray detectors including photoelectric, coherent and incoherent interactions,” *Med. Phys.*, vol. 40, no. 4, p. 041916, 2013.

[17] G. Lubberts, “Random noise produced by x-ray flourescent screens,” *The Optical Society of America*, vol. 58, no. 11, pp. 1475–1483, 1968.

[18] A. Howansky, A. R. Lubinsky, S. K. Ghose, K. Suzuki, and W. Zhao, “Direct measurement of Lubberts effect in CsI: Tl scintillators using single x-ray photon imaging,” *Proc. SPIE: Physics of Medical Imaging*, vol. 10132, p. 1013209, 2017.

[19] A. E. Burgess, B. Worthington, C. E. Metz, C. J. Taylor, C. R. Hill, D. C. Barber, D. E. Kuhl, D. G. Brown, K. J. Myers, M. A. Smith, P. Sharp, P. Wells, R. Brooks, and R. F. Wagner, “Report 54,” *Journal of the International Commission on Radiation Units and Measurements*, vol. os28, pp. NP–NP, 04 2016.

[20] K. J. Myers, H. H. Barrett, M. Borgstrom, D. Patton, and G. Seeley, “Effect of noise correlation on detectability of disk signals in medical imaging,” *JOSA A*, vol. 2, no. 10, pp. 1752–1759, 1985.

[21] H. H. Barrett and K. J. Myers, *Foundations of image science.* John Wiley & Sons, 2004.

[22] E. Lazarus, M. B. Mainiero, B. Schepps, S. L. Koelliker, and L. S. Livingston, “Bi-rads lexicon for us and mammography: interobserver variability and positive predictive value,” *Radiology*, vol. 239, no. 2, pp. 385–391, 2006.

[23] L. Liberman and J. H. Menell, “Breast imaging reporting and data system BI-RADS,” *Radiologic Clinics*, vol. 40, no. 3, pp. 409–430, 2002.

[24] M. Lanyi, *Diagnosis and differential diagnosis of breast calcifications*. Springer Science & Business Media, 2012.

[25] J. M. Boone, T. R. Nelson, K. K. Lindfors, and J. A. Seibert, “Dedicated breast ct: Radiation dose and image quality evaluation,” *Radiology*, vol. 221, no. 3, pp. 657–667, 2001. PMID: 11719660.

[26] K. K. Lindfors, J. M. Boone, T. R. Nelson, K. Yang, A. L. Kwan, and D. F. Miller, “Dedicated breast ct: initial clinical experience,” *Radiology*, vol. 246, no. 3, pp. 725–733, 2008.

[27] B. Ohnesorge, T. Flohr, and K. Klingenbeck-Regn, “Efficient object scatter correction algorithm for third and fourth generation ct scanners,” *European radiology*, vol. 9, no. 3, pp. 563–569, 1999.

[28] B. Münch, P. Trtik, F. Marone, and M. Stampanoni, “Stripe and ring artifact removal with combined wavelet - Fourier filtering,” *Optics express*, vol. 17, no. 10, pp. 8567–8591, 2009.

[29] J.-P. Kruth, L. Froyen, J. Van Vaerenbergh, P. Mercelis, M. Rombouts, and B. Lauwers, “Selective laser melting of iron-based powder,” *Journal of materials processing technology*, vol. 149, no. 1-3, pp. 616–622, 2004.

[30] S. Mori, M. Endo, S. Komatsu, S. Kandatsu, T. Yashiro, and M. Baba, "A combination-weighted feldkamp-based reconstruction algorithm for cone-beam ct," *Physics in Medicine & Biology*, vol. 51, no. 16, p. 3953, 2006.

[31] M. L. Spangler, M. L. Zuley, J. H. Sumkin, G. Abrams, M. A. Ganott, C. Hakim, R. Perrin, D. M. Chough, R. Shah, and D. Gur, "Detection and classification of calcifications on digital breast tomosynthesis and 2d digital mammography: a comparison," *American Journal of Roentgenology*, vol. 196, no. 2, pp. 320–324, 2011.

[32] J. Mordang, A. Gubern-Mérida, A. Bria, F. Tortorella, R. Mann, M. Broeders, G. den Heeten, and N. Karssemeijer, "The importance of early detection of calcifications associated with breast cancer in screening," *Breast cancer research and treatment*, vol. 167, no. 2, pp. 451–458, 2018.

[33] S. O'Grady and M. Morgan, "Microcalcifications in breast cancer: From pathophysiology to diagnosis and prognosis," *Biochimica et Biophysica Acta (BBA) - Reviews on Cancer*, vol. 1869, no. 2, pp. 310 – 320, 2018.

Chapter 7

Permission to reproduce copyrighted material

7.1 Permission to reproduce Figures 1.1 and 6.3

Interested in permission to reuse content from this article?

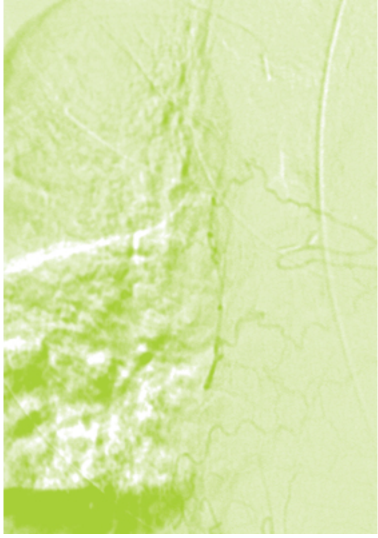

Here are some things to consider:

- Is the original article open access?
- Are you the author of the original article?
- Do you want to reproduce content from the article in a PhD thesis?
- All other queries

Is the original article open access?

Open Access articles in *BJR* and *DMFR* are accompanied by an open access statement on the title page, detailing the type of open access licence.

All *BJR|case reports* and *BJR|Open* articles are published on an open access basis under a creative commons attribution licence (CC BY).

You can read more about our open access policy here

- **Creative commons attribution non-commercial licence (CC BY NC)**

  If the article is open access under a creative commons attribution non-commercial licence (CC BY NC) you are free to reuse, change and build upon the work non-commercially. Your new work must be non-commercial and acknowledge the original source.

- **Creative commons attribution licence (CC BY)**

  If the article is open access under a creative commons attribution licence (CC BY) you are free to reuse, change and build upon the work, even commercially. Your new work must acknowledge the original source.

Are you the author of the original article?

- ***BJR*, *DMFR* and *Imaging***

  Authors of *BJR*, *DMFR* and *Imaging*, articles are free to reuse figures, tables, charts and short sections of text (up to 350 words) from their article in other publications, free of charge providing they cite the original source article.

- ***BJR|case reports* and *BJR|Open***

  BJR|case reports and *BJR|Open* articles are open access under a creative commons attribution licence (CC BY), so authors (and third parties) are free to reuse, change and build upon the work, even commercially. The new work must acknowledge the original source.

Do you want to reproduce content from the article in a PhD thesis?

If you are the author of the original article and wish to reproduce the article in full or in part in your PhD thesis you are free to do so providing you cite the original source article.

If you are not the author of the original article but wish reproduce 1-2 figures, tables, charts and short sections of text (up to 350 words) from a *BJR*, *DMFR* or *Imaging* article, you are free to do so providing you cite the original source article. Requests to reproduce more than 2 figures, tables, charts or larger sections of text must be processed by the copyright clearance centre (see below).

All other queries

All other permission queries are handled by the copyright clearance centre:

- Search for ‘British Journal of Radiology’ or ISSN: 0007-1285; then
- select ‘par per use options’; then
- ‘republish or display content’; then
- you will then be able to select the parameters you require and will be taken through the permission application process.

If you still have questions, please contact publications@bir.org.uk.

=210mm =297mm

This page is available in the following languages:

Creative Commons Legal Code

Attribution 4.0 International

Official translations of this license are available in other languages.
Creative Commons Corporation ("Creative Commons") is not a law firm and does not provide legal services or legal advice. Distribution of Creative Commons public licenses does not create a lawyer-client or other relationship. Creative Commons makes its licenses and related information available on an "as-is" basis. Creative Commons gives no warranties regarding its licenses, any material licensed under their terms and conditions, or any related information. Creative Commons disclaims all liability for damages resulting from their use to the fullest extent possible.

Using Creative Commons Public Licenses

Creative Commons public licenses provide a standard set of terms and conditions that creators and other rights holders may use to share original works of authorship and other material subject to copyright and certain other rights specified in the public license below. The following considerations are for informational purposes only, are not exhaustive, and do not form part of our licenses.

Considerations for licensors: Our public licenses are intended for use by those authorized to give the public permission to use material in ways otherwise restricted by copyright and certain other rights. Our licenses are irrevocable. Licensors should read and understand the terms and conditions of the license they choose before applying it. Licensors should also secure all rights necessary before applying our licenses so that the public can reuse the material as expected. Licensors should clearly mark any material not subject to the license. This includes other CC-licensed material, or material used under an exception or limitation to copyright. More considerations for licensors.▾

Considerations for the public: By using one of our public licenses, a licensor grants the public permission to use the licensed material under specified terms and conditions. If the licensor's permission is not necessary for any reason–for example, because of any applicable exception or limitation to copyright–then that use is not regulated by the license. Our licenses grant only permissions under copyright and certain other rights that a licensor has authority to grant. Use of the licensed material may still be restricted for other reasons, including because others have copyright or other rights in the material. A licensor may make special requests, such as asking that all changes be marked or described. Although not required by our licenses, you are encouraged to respect those requests where reasonable. More considerations for the public.▾

Creative Commons Attribution 4.0 International Public License

By exercising the Licensed Rights (defined below), You accept and agree to be bound by the terms and conditions of this Creative Commons Attribution 4.0 International Public License ("Public License"). To the extent this Public License may be interpreted as a contract, You are granted the Licensed Rights in consideration of Your acceptance of these terms and conditions, and the Licensor grants You such rights in consideration of benefits the Licensor receives from making the Licensed Material available under these terms and conditions.

Section 1 – Definitions.

a. **Adapted Material** means material subject to Copyright and Similar Rights that is derived from or based upon the Licensed Material and in which the Licensed Material is translated, altered, arranged, transformed, or otherwise modified in a manner requiring permission under the Copyright and Similar Rights held by the Licensor. For purposes of this Public License, where the Licensed Material is a musical work, performance, or sound recording, Adapted Material is always produced where the Licensed Material is synched in timed relation with a moving image.
b. **Adapter's License** means the license You apply to Your Copyright and Similar Rights in Your contributions to Adapted Material in accordance with the terms and conditions of this Public License.
c. **Copyright and Similar Rights** means copyright and/or similar rights closely related to copyright including, without limitation, performance, broadcast, sound recording, and Sui Generis Database Rights, without regard to how the rights are labeled or categorized. For purposes of this Public License, the rights specified in Section 2(b)(1)-(2) are not Copyright and Similar Rights.
d. **Effective Technological Measures** means those measures that, in the absence of proper authority, may not be circumvented under laws fulfilling obligations under Article 11 of the WIPO Copyright Treaty adopted on December 20, 1996, and/or similar international agreements.
e. **Exceptions and Limitations** means fair use, fair dealing, and/or any other exception or limitation to Copyright and Similar Rights that applies to Your use of the Licensed Material.
f. **Licensed Material** means the artistic or literary work, database, or other material to which the Licensor applied this Public License.
g. **Licensed Rights** means the rights granted to You subject to the terms and conditions of this Public License, which are limited to all Copyright and Similar Rights that apply to Your use of the Licensed Material and that the Licensor has authority to license.
h. **Licensor** means the individual(s) or entity(ies) granting rights under this Public License.
i. **Share** means to provide material to the public by any means or process that requires permission under the Licensed Rights, such as reproduction, public display, public performance, distribution, dissemination, communication, or importation, and to make material available to the public including in ways that members of the public may access the material from a place and at a time individually chosen by them.
j. **Sui Generis Database Rights** means rights other than copyright resulting from Directive 96/9/EC of the European Parliament and of the Council of 11 March 1996 on the legal protection of databases, as amended and/or succeeded, as well as other essentially equivalent rights anywhere in the world.
k. **You** means the individual or entity exercising the Licensed Rights under this Public License. **Your** has a corresponding meaning.

Section 2 – Scope.

a. **License grant**.
    1. Subject to the terms and conditions of this Public License, the Licensor hereby grants You a worldwide, royalty-free, non-sublicensable, non-exclusive, irrevocable license to exercise the Licensed Rights in the Licensed Material to:
        A. reproduce and Share the Licensed Material, in whole or in part; and
        B. produce, reproduce, and Share Adapted Material.
    2. <u>Exceptions and Limitations</u>. For the avoidance of doubt, where Exceptions and Limitations apply to Your use, this Public License does not apply, and You do not need to comply with its terms and conditions.
    3. <u>Term</u>. The term of this Public License is specified in Section 6(a).
    4. <u>Media and formats; technical modifications allowed</u>. The Licensor authorizes You to exercise the Licensed Rights in all media and formats whether now known or hereafter created, and to make technical modifications necessary to do so. The Licensor waives and/or agrees not to assert any right or authority to forbid You from making technical modifications necessary to exercise the Licensed Rights, including technical modifications necessary to circumvent Effective Technological Measures. For purposes of this Public License, simply making modifications authorized by this Section 2(a)(4) never produces Adapted Material.
    5. <u>Downstream recipients</u>.
        A. <u>Offer from the Licensor – Licensed Material</u>. Every recipient of the Licensed Material automatically receives an offer from the Licensor to exercise the Licensed Rights under the terms and conditions of this Public License.
        B. <u>No downstream restrictions</u>. You may not offer or impose any additional or different terms or conditions on, or apply any Effective Technological Measures to, the Licensed Material if doing so restricts exercise of the Licensed Rights

by any recipient of the Licensed Material.

6. No endorsement. Nothing in this Public License constitutes or may be construed as permission to assert or imply that You are, or that Your use of the Licensed Material is, connected with, or sponsored, endorsed, or granted official status by, the Licensor or others designated to receive attribution as provided in Section 3(a)(1)(A)(i).

b. **Other rights**.

1. Moral rights, such as the right of integrity, are not licensed under this Public License, nor are publicity, privacy, and/or other similar personality rights; however, to the extent possible, the Licensor waives and/or agrees not to assert any such rights held by the Licensor to the limited extent necessary to allow You to exercise the Licensed Rights, but not otherwise.
2. Patent and trademark rights are not licensed under this Public License.
3. To the extent possible, the Licensor waives any right to collect royalties from You for the exercise of the Licensed Rights, whether directly or through a collecting society under any voluntary or waivable statutory or compulsory licensing scheme. In all other cases the Licensor expressly reserves any right to collect such royalties.

Section 3 – License Conditions.

Your exercise of the Licensed Rights is expressly made subject to the following conditions.

a. **Attribution**.

1. If You Share the Licensed Material (including in modified form), You must:

    A. retain the following if it is supplied by the Licensor with the Licensed Material:
        i. identification of the creator(s) of the Licensed Material and any others designated to receive attribution, in any reasonable manner requested by the Licensor (including by pseudonym if designated);
        ii. a copyright notice;
        iii. a notice that refers to this Public License;
        iv. a notice that refers to the disclaimer of warranties;
        v. a URI or hyperlink to the Licensed Material to the extent reasonably practicable;
    B. indicate if You modified the Licensed Material and retain an indication of any previous modifications; and
    C. indicate the Licensed Material is licensed under this Public License, and include the text of, or the URI or hyperlink to, this Public License.
2. You may satisfy the conditions in Section 3(a)(1) in any reasonable manner based on the medium, means, and context in which You Share the Licensed Material. For example, it may be reasonable to satisfy the conditions by providing a URI or hyperlink to a resource that includes the required information.
3. If requested by the Licensor, You must remove any of the information required by Section 3(a)(1)(A) to the extent reasonably practicable.
4. If You Share Adapted Material You produce, the Adapter's License You apply must not prevent recipients of the Adapted Material from complying with this Public License.

Section 4 – Sui Generis Database Rights.

Where the Licensed Rights include Sui Generis Database Rights that apply to Your use of the Licensed Material:

a. for the avoidance of doubt, Section 2(a)(1) grants You the right to extract, reuse, reproduce, and Share all or a substantial portion of the contents of the database;

b. if You include all or a substantial portion of the database contents in a database in which You have Sui Generis Database Rights, then the database in which You have Sui Generis Database Rights (but not its individual contents) is Adapted Material; and

c. You must comply with the conditions in Section 3(a) if You Share all or a substantial portion of the contents of the database.

For the avoidance of doubt, this Section 4 supplements and does not replace Your obligations under this Public License where the Licensed Rights include other Copyright and Similar Rights.

Section 5 – Disclaimer of Warranties and Limitation of Liability.

a. **Unless otherwise separately undertaken by the Licensor, to the extent possible, the Licensor offers the Licensed Material as-is and as-available, and makes no representations or warranties of any kind concerning the Licensed Material, whether express, implied, statutory, or other. This includes, without limitation, warranties of title, merchantability, fitness for a particular purpose, non-infringement, absence of latent or other defects, accuracy, or the presence or absence of errors, whether or not known or discoverable. Where disclaimers of warranties are not allowed in full or in part, this disclaimer may not apply to You.**

b. **To the extent possible, in no event will the Licensor be liable to You on any legal theory (including, without limitation, negligence) or otherwise for any direct, special, indirect, incidental, consequential, punitive, exemplary, or other losses, costs, expenses, or damages arising out of this Public License or use of the Licensed Material, even if the Licensor has been advised of the possibility of such losses, costs, expenses, or damages. Where a limitation of liability is not allowed in full or in part, this limitation may not apply to You.**

c. The disclaimer of warranties and limitation of liability provided above shall be interpreted in a manner that, to the extent possible, most closely approximates an absolute disclaimer and waiver of all liability.

Section 6 – Term and Termination.

a. This Public License applies for the term of the Copyright and Similar Rights licensed here. However, if You fail to comply with this Public License, then Your rights under this Public License terminate automatically.

b. Where Your right to use the Licensed Material has terminated under Section 6(a), it reinstates:

   1. automatically as of the date the violation is cured, provided it is cured within 30 days of Your discovery of the violation; or
   2. upon express reinstatement by the Licensor.

   For the avoidance of doubt, this Section 6(b) does not affect any right the Licensor may have to seek remedies for Your violations of this Public License.

c. For the avoidance of doubt, the Licensor may also offer the Licensed Material under separate terms or conditions or stop distributing the Licensed Material at any time; however, doing so will not terminate this Public License.

d. Sections 1, 5, 6, 7, and 8 survive termination of this Public License.

Section 7 – Other Terms and Conditions.

a. The Licensor shall not be bound by any additional or different terms or conditions communicated by You unless expressly agreed.

b. Any arrangements, understandings, or agreements regarding the Licensed Material not stated herein are separate from and independent of the terms and conditions of this Public License.

Section 8 – Interpretation.

a. For the avoidance of doubt, this Public License does not, and shall not be interpreted to, reduce, limit, restrict, or impose conditions on any use of the Licensed Material that could lawfully be made without permission under this Public License.

b. To the extent possible, if any provision of this Public License is deemed unenforceable, it shall be automatically reformed to the minimum extent necessary to make it enforceable. If the provision cannot be reformed, it shall be severed from this Public License without affecting the enforceability of the remaining terms and conditions.

c. No term or condition of this Public License will be waived and no failure to comply consented to unless expressly agreed to by the Licensor.

d. Nothing in this Public License constitutes or may be interpreted as a limitation upon, or waiver of, any privileges and immunities that apply to the Licensor or You, including from the legal processes of any jurisdiction or authority.

Creative Commons is not a party to its public licenses. Notwithstanding, Creative Commons may elect to apply one of its public licenses to material it publishes and in those instances will be considered the “Licensor.” The text of the Creative Commons public licenses is dedicated to the public domain under the CC0 Public Domain Dedication. Except for the limited purpose of indicating that material is shared under a Creative Commons public license or as otherwise permitted by the Creative Commons policies published at creativecommons.org/policies, Creative Commons does not authorize the use of the trademark “Creative Commons” or any other trademark or logo of Creative Commons without its prior written consent including, without limitation, in connection with any unauthorized modifications to any of its public licenses or any other arrangements, understandings, or agreements concerning use of licensed material. For the avoidance of doubt, this paragraph does not form part of the public licenses.

Creative Commons may be contacted at creativecommons.org.

Additional languages available: Bahasa Indonesia, eesti keel, euskara, Deutsch, Español, français, hrvatski, italiano, latviski, Lietuvių, Nederlands, norsk, polski, português, suomeksi, svenska, te reo Māori, Türkçe, Ελληνικά, русский, українська, العربية, 日本語. Please read the FAQ for more information about official translations.

7.2 Permission to reporduce Chapter 2

JOHN WILEY AND SONS LICENSE
TERMS AND CONDITIONS

Apr 15, 2019

=210mm =297mm

This Agreement between Western University -- Tomi Nano ("You") and John Wiley and Sons ("John Wiley and Sons") consists of your license details and the terms and conditions provided by John Wiley and Sons and Copyright Clearance Center.

License Number	4570480807929
License date	Apr 15, 2019
Licensed Content Publisher	John Wiley and Sons
Licensed Content Publication	Medical Physics
Licensed Content Title	MTF and DQE enhancement using an apodized-aperture x-ray detector design
Licensed Content Author	Tomi F. Nano, Terenz Escartin, Elina Ismailova, et al
Licensed Content Date	Aug 12, 2017
Licensed Content Volume	44
Licensed Content Issue	9
Licensed Content Pages	11
Type of use	Dissertation/Thesis
Requestor type	Author of this Wiley article
Format	Print and electronic
Portion	Full article
Will you be translating?	No
Title of your thesis / dissertation	An apodized-aperture x-ray detector design to improve image quality in mammography
Expected completion date	Jun 2019
Expected size (number of pages)	200
Requestor Location	Western University 1151 Richmond St Unit 3 London, ON N6A 3K7 Canada Attn: Western University
Publisher Tax ID	EU826007151
Total	0.00 CAD
Terms and Conditions	

TERMS AND CONDITIONS

This copyrighted material is owned by or exclusively licensed to John Wiley & Sons, Inc. or one of its group companies (each a"Wiley Company") or handled on behalf of a society with which a Wiley Company has exclusive publishing rights in relation to a particular work (collectively "WILEY"). By clicking "accept" in connection with completing this licensing transaction, you agree that the following terms and conditions apply to this transaction (along with the billing and payment terms and conditions established by the Copyright Clearance Center Inc., ("CCC's Billing and Payment terms and conditions"), at the time that you opened your RightsLink account (these are available at any time at http://myaccount.copyright.com).

Terms and Conditions

- The materials you have requested permission to reproduce or reuse (the "Wiley Materials") are protected by copyright.

- You are hereby granted a personal, non-exclusive, non-sub licensable (on a stand-alone basis), non-transferable, worldwide, limited license to reproduce the Wiley Materials for the purpose specified in the licensing process. This license, **and any CONTENT (PDF or image file) purchased as part of your order,** is for a one-time use only and limited to any maximum distribution number specified in the license. The first instance of republication or reuse granted by this license must be completed within two years of the date of the grant of this license (although copies prepared before the end date may be distributed thereafter). The Wiley Materials shall not be used in any other manner or for any other purpose, beyond what is granted in the license. Permission is granted subject to an appropriate acknowledgement given to the author, title of the material/book/journal and the publisher. You shall also duplicate the copyright notice that appears in the Wiley publication in your use of the Wiley Material. Permission is also granted on the understanding that nowhere in the text is a previously published source acknowledged for all or part of this Wiley Material. Any third party content is expressly excluded from this permission.

- With respect to the Wiley Materials, all rights are reserved. Except as expressly granted by the terms of the license, no part of the Wiley Materials may be copied, modified, adapted (except for minor reformatting required by the new Publication), translated, reproduced, transferred or distributed, in any form or by any means, and no derivative works may be made based on the Wiley Materials without the prior permission of the respective copyright owner.**For STM Signatory Publishers clearing permission under the terms of the STM Permissions Guidelines only, the terms of the license are extended to include subsequent editions and for editions in other languages, provided such editions are for the work as a whole in situ and does not involve the separate exploitation of the permitted figures or extracts,** You may not alter, remove or suppress in any manner any copyright, trademark or other notices displayed by the Wiley Materials. You may not license, rent, sell, loan, lease, pledge, offer as security, transfer or assign the Wiley Materials on a stand-alone basis, or any of the rights granted to you hereunder to any other person.

- The Wiley Materials and all of the intellectual property rights therein shall at all times remain the exclusive property of John Wiley & Sons Inc, the Wiley Companies, or their respective licensors, and your interest therein is only that of having possession of and the right to reproduce the Wiley Materials pursuant to Section 2 herein during the continuance of this Agreement. You agree that you own no right, title or interest in or to the Wiley Materials or any of the intellectual property rights therein. You shall have no rights hereunder other than the license as provided for above in Section 2. No right, license or interest to any trademark, trade name, service mark or other branding ("Marks") of WILEY or its licensors is granted hereunder, and you agree that you shall not assert any such right, license or interest with respect thereto

- NEITHER WILEY NOR ITS LICENSORS MAKES ANY WARRANTY OR REPRESENTATION OF ANY KIND TO YOU OR ANY THIRD PARTY, EXPRESS, IMPLIED OR STATUTORY, WITH RESPECT TO THE MATERIALS OR THE ACCURACY OF ANY INFORMATION CONTAINED IN THE

MATERIALS, INCLUDING, WITHOUT LIMITATION, ANY IMPLIED WARRANTY OF MERCHANTABILITY, ACCURACY, SATISFACTORY QUALITY, FITNESS FOR A PARTICULAR PURPOSE, USABILITY, INTEGRATION OR NON-INFRINGEMENT AND ALL SUCH WARRANTIES ARE HEREBY EXCLUDED BY WILEY AND ITS LICENSORS AND WAIVED BY YOU.

- WILEY shall have the right to terminate this Agreement immediately upon breach of this Agreement by you.

- You shall indemnify, defend and hold harmless WILEY, its Licensors and their respective directors, officers, agents and employees, from and against any actual or threatened claims, demands, causes of action or proceedings arising from any breach of this Agreement by you.

- IN NO EVENT SHALL WILEY OR ITS LICENSORS BE LIABLE TO YOU OR ANY OTHER PARTY OR ANY OTHER PERSON OR ENTITY FOR ANY SPECIAL, CONSEQUENTIAL, INCIDENTAL, INDIRECT, EXEMPLARY OR PUNITIVE DAMAGES, HOWEVER CAUSED, ARISING OUT OF OR IN CONNECTION WITH THE DOWNLOADING, PROVISIONING, VIEWING OR USE OF THE MATERIALS REGARDLESS OF THE FORM OF ACTION, WHETHER FOR BREACH OF CONTRACT, BREACH OF WARRANTY, TORT, NEGLIGENCE, INFRINGEMENT OR OTHERWISE (INCLUDING, WITHOUT LIMITATION, DAMAGES BASED ON LOSS OF PROFITS, DATA, FILES, USE, BUSINESS OPPORTUNITY OR CLAIMS OF THIRD PARTIES), AND WHETHER OR NOT THE PARTY HAS BEEN ADVISED OF THE POSSIBILITY OF SUCH DAMAGES. THIS LIMITATION SHALL APPLY NOTWITHSTANDING ANY FAILURE OF ESSENTIAL PURPOSE OF ANY LIMITED REMEDY PROVIDED HEREIN.

- Should any provision of this Agreement be held by a court of competent jurisdiction to be illegal, invalid, or unenforceable, that provision shall be deemed amended to achieve as nearly as possible the same economic effect as the original provision, and the legality, validity and enforceability of the remaining provisions of this Agreement shall not be affected or impaired thereby.

- The failure of either party to enforce any term or condition of this Agreement shall not constitute a waiver of either party's right to enforce each and every term and condition of this Agreement. No breach under this agreement shall be deemed waived or excused by either party unless such waiver or consent is in writing signed by the party granting such waiver or consent. The waiver by or consent of a party to a breach of any provision of this Agreement shall not operate or be construed as a waiver of or consent to any other or subsequent breach by such other party.

- This Agreement may not be assigned (including by operation of law or otherwise) by you without WILEY's prior written consent.

- Any fee required for this permission shall be non-refundable after thirty (30) days from receipt by the CCC.

- These terms and conditions together with CCC's Billing and Payment terms and conditions (which are incorporated herein) form the entire agreement between you and WILEY concerning this licensing transaction and (in the absence of fraud) supersedes all prior agreements and representations of the parties, oral or written. This Agreement may not be amended except in writing signed by both parties. This Agreement shall be binding upon and inure to the benefit of the parties' successors, legal representatives, and authorized assigns.

- In the event of any conflict between your obligations established by these terms and conditions and those established by CCC's Billing and Payment terms and conditions, these terms and conditions shall prevail.

- WILEY expressly reserves all rights not specifically granted in the combination of (i) the license details provided by you and accepted in the course of this licensing transaction, (ii) these terms and conditions and (iii) CCC's Billing and Payment terms and conditions.

- This Agreement will be void if the Type of Use, Format, Circulation, or Requestor Type was misrepresented during the licensing process.

- This Agreement shall be governed by and construed in accordance with the laws of the State of New York, USA, without regards to such state's conflict of law rules. Any legal action, suit or proceeding arising out of or relating to these Terms and Conditions or the breach thereof shall be instituted in a court of competent jurisdiction in New York County in the State of New York in the United States of America and each party hereby consents and submits to the personal jurisdiction of such court, waives any objection to venue in such court and consents to service of process by registered or certified mail, return receipt requested, at the last known address of such party.

WILEY OPEN ACCESS TERMS AND CONDITIONS

Wiley Publishes Open Access Articles in fully Open Access Journals and in Subscription journals offering Online Open. Although most of the fully Open Access journals publish open access articles under the terms of the Creative Commons Attribution (CC BY) License only, the subscription journals and a few of the Open Access Journals offer a choice of Creative Commons Licenses. The license type is clearly identified on the article.

The Creative Commons Attribution License

The Creative Commons Attribution License (CC-BY) allows users to copy, distribute and transmit an article, adapt the article and make commercial use of the article. The CC-BY license permits commercial and non-

Creative Commons Attribution Non-Commercial License

The Creative Commons Attribution Non-Commercial (CC-BY-NC)License permits use, distribution and reproduction in any medium, provided the original work is properly cited and is not used for commercial purposes.(see below)

Creative Commons Attribution-Non-Commercial-NoDerivs License

The Creative Commons Attribution Non-Commercial-NoDerivs License (CC-BY-NC-ND) permits use, distribution and reproduction in any medium, provided the original work is properly cited, is not used for commercial purposes and no modifications or adaptations are made. (see below)

Use by commercial "for-profit" organizations

Use of Wiley Open Access articles for commercial, promotional, or marketing purposes requires further explicit permission from Wiley and will be subject to a fee.
Further details can be found on Wiley Online Library
http://olabout.wiley.com/WileyCDA/Section/id-410895.html

Other Terms and Conditions:

v1.10 Last updated September 2015

Questions? customercare@copyright.com or +1-855-239-3415 (toll free in the US) or +1-978-646-2777.

Curriculum Vitae

EDUCATION:

2015 - 2019 **Doctor of Philosophy (Candidate)**
Department of Medical Biophysics
The University of Western Ontario, London, Canada
Supervisor: Dr. Ian A. Cunningham
Thesis: A novel x-ray detector to improve high-frequency MTF and DQE

2018 **Master of Science in Clinical Physics (CAMPEP)**
Department of Medical Biophysics
The University of Western Ontario, London, Canada
Program director: Dr. Rob Stodilka

2014 **Bachelor of Science - Honours Physics (Medical Physics)**
Minor in Mathematics and Computer Science
Department of Physics
University of Windsor, Windsor, Canada
Supervisor: Dr. Roman G. Maev
Research: Monitoring and control of sleep architecture using EEG and electrodermal stimulation

POSITIONS:

2017 - 2018 **London Regional Cancer Center**

Teaching Assistant

Department of Medical Biophysics

Course: Biophys 9672 Practical Radiotherapy

Professor: Dr. Kathleen Surry

2016 - 2017 **London Regional Cancer Center**

Quality Assurance Internship

London Health Science Center

Supervisor: Dr. Rob Stodilka

2015 **Robarts Research Institute**

Research Assistant

The University of Western Ontario

Supervisor: Dr. Ian Cunningham

Project: Develop quality assurance and evaluated performance of x-ray detectors

2014 **The Merchant Lab**

Web Developer

Supervisor: Mr. Chad Nantais

Project: Back-end developer for online retail businesses to improve inventory and sales analysis

2014 **Institute of Diagnostic Imaging Research**
Research Assistant
Department of Physics
Supervisor: Dr. Roman G. Maev
Project: Development of a portable ultrasonic transcranial device of high-resolution imaging

2013 **University of Windsor**
Teaching Assistant
Department of Physics
Courses 64-140, 64-141, 64-220
Supervisor: Mr. Aldo DiCarlo

2011 **TRIUMF ISAC Gamma-Ray Spectrometer**
Coop Student
TRIUMF Canada's National Laboratory
Supervisor: Dr. Greg Hackman
Project: TIGRESS (TRIUMF ISAC Gamma-Ray Escape Suppressed Spectrometer) detector calibration

2010 **Windsor Regional Hospital Cancer Center**
Coop Student
Harold E. Johns Scholarship
Supervisor: Mr. Jeff Richer
Project: Commissioning of Siemens Elekta LINAC by measuring neutron flux through door-less maze

HONOURS AND AWARDS:

2018 - 2020	**Postgraduate Scholarship - Doctoral (PGSD2)** Natural Science and Engineering Research Council of Canada (NSERC) Awarded to high-caliber students who are engaged in doctoral programs in the natural science and engineering National ($42,000)
2018	**Alfred Jay Award for Translational Research** Departmet of Medical Biophysics, Western University Awarded annually to a graduate student demonstrating innovation in the development of a clinical diagnsotic or therapeutic procedure during their studies Institutional ($2,000)
2017 - 2018	**Translational Breast Cancer Research Traineeship (TBCRU)** Canadian Cancer Society and Western University Awarded annually to a student working in the field of breast cancer resarch Institutional ($18,000)
2017 - 2018	**Onatrio Graduate Scholarship (OGS)** Western University Awarded to a high-calibre graduate student Provincial ($15,000 - declined)
2017	**Gradaute Student Innovation Scholar (GSIS)** Western University Awarded to a graduate student in science or engineering that is instersted in commercialization Institutional ($3,000)

2016 - 2017 Translational Breast Cancer Research Traineeship (TBCRU)
Canadian Cancer Society and Western University
Awarded annually to a student working in the field of breast cancer resarch
Institutional ($18,000)

2015 - 2016 Postgraduate Scholarship - Masters (CGSM)
Natural Science and Engineering Research Council of Canada (NSERC)
Awarded to high-calibre students who are engaged in masters programs (or 1st year doctorate) in the natural science and engineering
National ($15,000)

2017 - 2018 Onatrio Graduate Scholarship (OGS)
Western University
Awarded to a high-calibre graduate student
Provincial ($15,000 - declined)

PUBLICATIONS, BOOK CHAPTERS AND PRESENTATIONS:

Publications (10 total; 6 first author)

1. **Nano TF.** and Cunningham IA., Signal-to-noise criteria to suppress Gibbs ringing with the apodized-aperture x-ray detector design. *Medical Physics*, 2019 (in preparation)
2. **Nano TF.**, Scott CC., Li Y., Con C., Karim KS., Cunningham IA., An apodized aperture x-ray detector design to improve high frequency DQE and eliminate aliasing: Performance of a small-area Se/CMOS prototype. *Journal of Medical Imaging*, 2019 (in submission)

3. **Nano TF.**, Scott CC., Li Y., Con C., Karim KS., Cunningham IA., Performance evaluation of a Se/CMOS prototype x-ray detector with the Apodized Aperture Pixel (AAP) design, *Proc. of SPIE: Medical Imaging*, 10948-16, 2019
4. Escartin T., **Nano TF.**, and Cunningham IA., Detective Quantum Efficiency Measurements in a Clinical Setting, *Radiology*, 2019 (in submission)
5. **Nano TF.**, Karim, KS., Cunningham IA., Impact of x-ray reabsorption and converter blur on MTF and DQE improvements using the apodized-aperture pixel (AAP) design of x-ray detectors, *Physics in Medicine and Biology*, 2019 (in submission)
6. **Nano TF.**, Escartin T., Ismailova E., Karim KS., Lindstrom J., Kim HK., Cunningham IA., MTF and DQE Enhancement using an AAP X-Ray Detector Design, *Medical Physics*, 44(7), 2017
7. **Nano TF.**, Escartin T., Cunningham IA., A novel x-ray detector design with higher DQE and reduced aliasing: Theoretical analysis of x-ray reabsorption in detector converter material, *Proc. of SPIE: Medical Imaging*, 9783, 2016
8. Escartin T., **Nano TF.**, Cunningham IA., Detective quantum efficiency: A standard test to ensure optimal detector performance and low patient exposures, *Proc. of SPIE: Medical Imaging*, 9783, 2016
9. E. Kwan, C.Y. Wu, N.C. Summers, G. Hackman, T.E. Drake, C. Andreoiu, R. Ashley, G.C. Bal, P.C. Bender, A.J. Boston, H.C. Boston, A. Chester, A. Close, D. Cline, D.S. Cross, R. Dunlop, A. Finlay, A.B. Garnsworthy, A.B. Hayes, A.T. Laffoley, **Nano TF.**, P. Navrátil, C.J. Pearson, J. Pore, S. Quaglioni, C.E. Svensson, K. Starosta, I.J. Thompson, P. Voss, S. Williams, Z.M. Wang, Precision measurements of the electromagnetic dipole strengths in 11Be, *Physics Letters B*, 732, 2014

10. E. Kwan, C. Y. Wu, N. C. Summers, G. Hackman, T. E. Drake, C. Andreoiu, R. Ashley, G. C. Ball, P. C. Bender, A. J. Boston, H. C. Boston, A. Chester, A. Close, D. Cline, D. S. Cross, R. Dunlop, A. Finley, A. Garnsworthy, A. B. Hayes, A. Laffoley, **Nano TF.**, P. Voss, S., Precision measurements of the B(E1) strengths in 11Be, *5th International Conf. on Fission and properties of neutron-rich nuclei (ICFN5)*, 2012

Book Chapters (2 total; 2 first author)

1. **Nano TF.** and Cunningham IA., Clinical Diagnostic and Interventional Radiology Physics with MATLAB: A Problem-solving Approach, Chapter 16: A toolkit to manipulate x-ray spectra in medical imaging, Editor: Johan Sjoberg, Publisher: CRC Press Taylor & Francis Group, 2019
2. **Nano TF.**, Escartin T. and Cunningham IA. , Handbook of X-Ray Imaging: Physics and Technology, Chapter 1.19, Detector Design and Performance in X-Ray Imaging, Editor: Paolo Russo, Publisher: CRC Press Taylor & Francis Group, 2018

Presentations (10 of 22 total; 9 of 18 first author)

1. **Nano TF.**, Scott CC., Li Y., Con C., Karim KS., Cunningham I., Performance evaluation of a Se/CMOS prototype x-ray detector with the Apodized Aperture Pixel (AAP) design, SPIE: Medical Imaging, 2019 (oral presentation)
2. **Nano TF.** and Cunningham IA., Signal and noise performance of the Apodized-Aperture Pixel (AAP) x-ray detector design to increase detective quantum efficiency (DQE), Radiological Society of North America, 2018 (oral presentation)

3. **Nano TF.** and Cunningham IA., Apodized-Aperture Pixel: A novel x-ray detector design to improve cancer detection, 60th Annual Meeting and Exhibition of American Association of Physicist in Medicine, 2018 (oral presentation)

4. **Nano TF.** and Cunningham IA., Identifying signal aliasing in x-ray images with an Apodized Aperture Pixel detector design, Robarts Research Retreat, 2018 (short oral presentation)

5. **Nano TF.** and Cunningham IA., A novel imaging biomarker in x-ray images using identification of signal aliasing with the Apodized Aperture Pixel detector design, London Imaging Discovery Day, 2018 (poster presentation, 1st pace poster award)

6. **Nano TF.** and Cunningham IA., Apodized-Aperture Pixel: A novel x-ray detector design, Imaging Network of Ontario (ImNO) conference, 2018 (oral presentation)

7. Escartin T., **Nano TF.**, and Cunningham IA., Development of a robust tool to determine radiographic detector dose efficiency (DQE) in clinics, London Imaging Discovery Day, 2017 (poster presentation, 1st place poster Award)

8. **Nano TF.**, Escartin T. and Cunningham IA., A Novel X-Ray Detector Design with Improved DQE at High-Frequencies, COMP Winter Imaging School and Mammography Workshop, 2017 (oral presentation)

9. **Nano T.F.**, Escartin T., Stewart E., Cunningham I., Improved Image Quality in X-Ray Images with the Apodized-Aperture Pixel (AAP) Design, London Imaging Discovery Day, 2016 (poster presentation, 1st place poster award)

10. **Nano T.F**, Escartin T., Karim K., Lindstrom J., Kim H., Cunningham I., The new generation of x-ray detectors: higher DQE and reduced aliasing, SPIE Medical Imaging conference, 2016 (oral presentation)